

# **Microstructure and Creep Behavior of Heat-Affected Zone in Grade 91 Steel Weldments**

by

Yiyu Wang

A thesis submitted in partial fulfillment of the requirements for the degree of

Doctor of Philosophy

in

Materials Engineering

Department of Chemical and Materials Engineering

University of Alberta

©Yiyu Wang, 2017

# Abstract

Grade 91 steel is one of the most important 9–12 % Cr creep strength enhanced ferritic (CSEF) steels used in fossil-fuel fired power plants. A narrow heat-affected zone with heterogeneous structures is generated in the base metal, due to non-equilibrium phase transformations during the arc welding processes. This heterogeneous heat-affected zone has been reported to cause short-term creep failures of welded components, such as the infamous Type IV cracking. Two remaining questions associated with the Type IV cracking are: where is the exact fracture location and what structure feature is critically responsible for the failure. Post-weld heat treatment (PWHT) plays a significant role in improving weldments' toughness and maximizing their creep lifetime. How do these PWHT parameters (temperature, holding time) eventually affect creep behavior of the weldments needs a deeper investigation from local structural evolution point of view.

In this work, heterogeneous structures in the heat-affected zone in three thermal stages, including the as-welded, post-weld heat-treated, and crept conditions, have been systematically characterized with advanced microscopy techniques. Non-equilibrium phase transformations in the heat-affected zone, including austenization and martensitic transformation, have been investigated through experimental study and thermodynamic modelling. High-temperature creep rupture mechanisms for Type IV cracking and Type I cracking, have been further analyzed and discussed.

Structures of the heat-affected zone in the as-welded condition in 1-inch-thick pipe weldments and 5-inch-thick heavy section weldments are quantitatively characterized. This as-welded structure analysis provides a foundation for understanding structural evolutions of weldments in the PWHT-ed and crept conditions. A correlation between intercritical heat-affected zone and Type IV creep damaged zone has been built. The Type IV cracking mechanism is understood from a new perspective of the local chemistry at the grain-scale level. The

so-called soft zone responsible for the Type IV cracking has been confidently identified in the ICHAZ in all three thermal stages (as-welded, PWHT-ed, and crept). Finite element analysis further verifies that the ICHAZ, exhibiting the highest first principal stress, the largest stress triaxiality, and the highest creep strain/strain rate, is the most creep-susceptible region when the PWHT temperature is below  $A_1$  temperature of the base metal. In high-temperature creep conditions, weak Cr-depleted ferrite grains in the ICHAZ preferentially deformed, which accelerates creep strength degradation of the ICHAZ. At the mesoscale level, nucleation of creep cavities along the grain boundaries is caused by a high stress triaxiality.

A creep rupture transition from the Type IV cracking in the ICHAZ to the Type I cracking in the fusion zone was observed in the cross-weld samples when the PWHT temperature increases from 600 °C to 840 °C. Structural analysis uncovers that the PWHT-ed fusion zone, resulting in the Type I cracking, also has an intercritical structure of transformed martensite and untransformed tempered martensite. Finite element analysis indicates that the fusion zone becomes the new creep-susceptible region with the largest stress triaxiality and the highest creep strain/strain rate when the PWHT temperature is between the  $A_1$  and  $A_3$  temperatures of the filler metal. It is concluded that the intercritical structure of hard transformed martensite and soft untransformed tempered martensite/ferrite is likely to behave as the most creep-vulnerable structure.

# Preface

The work presented in this thesis was carried out by Yiyu Wang under the supervision of Dr. Leijun Li at the University of Alberta. This work has been funded by Natural Sciences and Engineering Research Council (NSERC) of Canada through a Discovery grant (RES0020431). The welding experiments and creep tests were helped by Dr. Andrew Deceuster and Benjamin Griffiths from the Department of Mechanical & Aerospace Engineering, Utah State University.

Part of this work has been published in peer-review journals. Part of Chapter 3 has been published in the following papers:

Y. Wang, R. Kannan, and L. Li. "Identification and Characterization of Intercritical Heat-Affected Zone in As-welded Grade 91 Weldment". *Metallurgical and Materials Transactions A*, Vol. 47A. 2016, pp. 5680-5684.

Y. Wang, R. Kannan, and L. Li. "Characterization of As-Welded Microstructure of Heat-affected Zone in Modified 9Cr-1Mo-V-Nb Steel Weldment". *Materials Characterization*, Vol. 118, 2016, pp. 225-234.

Y. Wang and L. Li. "Microstructure Evolution of Fine-Grained Heat-Affected Zone in Type IV Failure of P91 Welds". *Welding Journal*, Vol. 95, 2016, pp. 27s-36s.

Y. Wang, R. Kannan, L. Zhang, and L. Li. "Microstructural Analysis of As-Welded Heat Affected Zone of Grade 91 Steel Heavy Section Weldment". *Welding Journal*, Vol. 96, 2017, pp. 203s-219s.

Part of Chapter 4 has been submitted to *Metallurgical and Materials Transactions A* as Y. Wang, R. Kannan, and L. Li. "Correlation between Intercritical Heat-affected Zone and Type IV Creep Damage Zone in Grade 91 Steel". *Metallurgical and Materials Transactions A*, 2017, under revision.

Part of Chapter 5 has been submitted to *Materials Science and Engineering A* as Y. Wang, L. Li, and R. Kannan. "Transition from Type IV to Type I Cracking in Heat-Treated Grade

91 Steel Weldments". *Materials Science and Engineering A*, 2017, under review.

In these published and submitted papers, Yiyu Wang was responsible for conducting experiments, data analysis, and paper writing. Dr. Leijun Li, as the supervisory author, provided advice for experiments and data interpretation, and helped with paper revisions. Rangasayee Kannan's role was to review papers and help with revisions.

*"Knowing others makes you intelligent, knowing yourself makes you wise."*

*-Lao Tzu*

# Acknowledgements

It is a long, but unforgettable journey for me to arrive here at this moment. There are so many people I want to thank for their great company along this trip.

First of all, my sincerest “THANK YOU” goes to my supervisor, Dr. Leijun Li, for his great patience, persistent encouragement, and numerous inspirations through my graduate study. Dr. Li’s rich knowledge, rigorous scholarship, and great personality provide me with an excellent guidance in my research and daily life.

I would like to express many thanks to the members of my dissertation committee, Dr. Patricio Mendez, Dr. Weixing Chen, Dr. Barry Wiskel, and Dr. Adrian Gerlich, and the committee chair Dr. Jinfeng Liu for their patience and consideration. I deeply appreciate the great help from the CME faculties, Dr. Hao Zhang, Dr. Hani Henein, Dr. Douglas Ivey, Dr. Dongyang Li, and the department associate chair Dr. Vinay Prasad. Special thanks to the CME department supports from Lily Laser, Mia Law, Marion Pritchard, and Kevin Heidebrecht. I also acknowledge the technical supports from the NanoFAB staffs, Dr. Eric Flaim, Mr. Peng Li, Dr. Anqiang He, and Dr. Shihong Xu.

I would like to thank my colleagues and friends in our group, Rangasayee Kannan, Neil Anderson, Chris Di Giovanni, and Lieduo Yang. I appreciate their discussions and inspirations. I will cherish those happy hours with them in the lab. I would also like to thank Goetz, Gentry, Narin, Jordan, Cory, Vivek, Mitch, Rebekah, Ying and Louie for their kind help and those wonderful trips to St. John’s, Las Vegas, and Chicago.

I would like to acknowledge the Natural Sciences and Engineering Research Council (NSERC) of Canada for the financial support for this project. Special thanks go to University of Alberta and China Scholarship Council for the scholarships and supporting my student life.

A special gratitude goes to Dr. Lianmeng Zhang, Dr. Qiang Shen, and Dr. Guoqiang Luo from the FGM lab in the WUT for their great support. I am very grateful to my friends,

especially Zhiyong Yin, for helping me enjoy my life in Edmonton.

My family have always being the greatest supporters of my life. I would like to thank my parents, Yude Chen and Zhangju Wang, for their unconditional love and endless patience for so many years. They are the reason who I am right now.

Last but not the least, I would like to express my heartfelt thanks to my lovely wife, Li Fu, for her love, support, and sacrifice. Her encouragement and heart-warming personality always motivate me to overcome any obstacle. Her sweet smile and cheerful attitude make our good and bad days full of sunshine.

**Yiyu Wang**

# Table of Contents

<b>1</b>	<b>Introduction and Literature Review</b>	<b>1</b>
1.1	Introduction . . . . .	1
1.2	Literature Review . . . . .	2
1.2.1	9-12% Cr Creep Resistant Ferritic/Martensitic Steels . . . . .	2
1.2.2	Creep and Deformation Mechanism Map . . . . .	7
1.2.3	Grade 91 Steel . . . . .	10
1.3	Welding of Grade 91 Steel . . . . .	23
1.3.1	Welding Process and Challenge . . . . .	23
1.3.2	Heat-Affected Zone . . . . .	25
1.3.3	Post-Weld Heat Treatment . . . . .	29
1.4	Creep Properties of Grade 91 Steel Weldments . . . . .	32
1.4.1	Macro Creep Rupture . . . . .	32
1.4.2	Formation Mechanisms of Creep Cavities . . . . .	33
1.4.3	Type IV Cracking . . . . .	34
1.4.4	Modeling Creep Behavior of Grade 91 steel weldments . . . . .	37
1.5	Research Objectives . . . . .	40
<b>2</b>	<b>Materials and Methodology</b>	<b>41</b>
2.1	Materials . . . . .	41
2.2	Welding and Post-Weld Heat Treatment . . . . .	42
2.2.1	Welding . . . . .	42
2.2.2	Post-Weld Heat Treatment . . . . .	42
2.3	Mechanical Property Measurement . . . . .	43
2.3.1	High-Temperature Creep Test . . . . .	43
2.3.2	Hardness Test . . . . .	43
2.4	Microstructure Characterization . . . . .	44
2.4.1	Optical Microscopy . . . . .	44
2.4.2	Field-Emission Scanning Electron Microscopy . . . . .	45
2.4.3	Energy Dispersive Spectroscopy . . . . .	45
2.4.4	Electron Backscatter Diffraction . . . . .	46
2.4.5	Auger Electron Spectroscopy . . . . .	47
2.4.6	Image Analysis with ImageJ . . . . .	48

2.5	Thermodynamic Calculation . . . . .	48
2.6	Dilatometry . . . . .	48
2.7	Finite Element Analysis . . . . .	49
<b>3</b>	<b>Microstructure Analysis of As-Welded Heat-Affected Zone in Grade 91 Steel Weldments</b>	<b>50</b>
3.1	As-Welded Grade 91 Pipe Weldment . . . . .	50
3.1.1	Characterization of the as-received P91 base metal . . . . .	50
3.1.2	Microstructure evolutions in the HAZ regions . . . . .	52
3.1.3	Microhardness distribution . . . . .	57
3.1.4	EBSD and EDS analyses on the HAZs . . . . .	58
3.1.5	Study of dissolution of $M_{23}C_6$ carbide by dilatometry . . . . .	63
3.2	As-Welded Grade 91 Heavy Section Weldment . . . . .	74
3.2.1	Characterization of the as-received heavy section block . . . . .	74
3.2.2	Microstructure evolutions in the HAZ regions . . . . .	76
3.2.3	Microhardness distribution . . . . .	83
3.2.4	delta-ferrite in BM and HAZ . . . . .	84
3.2.5	Study of dissolution of delta-ferrite by dilatometry . . . . .	90
3.3	Discussion . . . . .	94
3.3.1	Structural heterogeneity in the as-welded HAZ . . . . .	94
3.3.2	Role of undissolved $M_{23}C_6$ on martensitic transformation . . . . .	97
3.3.3	Behavior of delta-ferrite in block HAZ . . . . .	98
3.4	Conclusions . . . . .	102
<b>4</b>	<b>Correlation between Intercritical Heat-Affected Zone and Type IV Creep Damage Zone in Grade 91 Steel Weldments</b>	<b>104</b>
4.1	Results . . . . .	104
4.1.1	Type IV creep damage . . . . .	104
4.1.2	Soft zone identification . . . . .	105
4.1.3	Instrumented indentation study of the weldments . . . . .	107
4.1.4	Microstructure evolution of the soft zone or ICHAZ . . . . .	110
4.1.5	Characteristic structures of the welds in Type IV cracking . . . . .	117
4.2	Discussion . . . . .	123
4.3	Conclusions . . . . .	130
<b>5</b>	<b>Transition from Type IV to Type I Cracking in Heat-Treated Grade 91 Steel Weldments</b>	<b>131</b>
5.1	Results . . . . .	131
5.1.1	Hardness profile and mapping across the welds after PWHT . . . . .	131
5.1.2	Microstructure of the welds after PWHT . . . . .	137
5.1.3	Creep performance of the cross-weld samples . . . . .	140
5.1.4	Hardness mapping across the HAZ after creep tests . . . . .	142
5.1.5	Microstructure of the welds after creep tests . . . . .	146

5.1.6	Characteristic structures of the welds in Type I cracking . . . . .	150
5.2	Discussion . . . . .	155
5.2.1	PWHT, microstructure, and hardness . . . . .	155
5.2.2	Transition of creep rupture locations . . . . .	157
5.3	Conclusions . . . . .	162
<b>6</b>	<b>Finite Element Analysis of Creep Behavior of Grade 91 Steel Weldments</b>	<b>163</b>
6.1	Results . . . . .	163
6.1.1	Modeling of steady-state creep of the PWHT-ed welds . . . . .	163
6.1.2	Preliminary study of local stress distribution in a crept ICHAZ . . . . .	177
6.2	Discussion . . . . .	181
6.3	Conclusions . . . . .	184
<b>7</b>	<b>Summary and Future Work</b>	<b>185</b>
7.1	Summary . . . . .	185
7.2	Future Work . . . . .	188
	<b>Bibliography</b>	<b>189</b>

# List of Tables

1.1	Operating conditions of fossil fired power plants [2, 3]	3
1.2	Specification of Grade 91 steel in US, Europe, Japan, and China [4, 19].	11
1.3	Chemical composition requirements of Grade 91 steel (P91) by ASTM A213 and A335 (wt.%).	12
1.4	Precipitates in Grade 91 steel	15
1.5	Mechanical property requirements for Grade 91 steel by ASTM A213 and A335.	18
1.6	Typical welding process, filler metal, preheat temperature, interpass temperature, and PWHT temperature used for Grade 91 steel [7, 64].	24
1.7	Peak temperature and microstructural evolution in the HAZ subregions	27
2.1	Chemical composition of Grade 91 base metals and filler metals (wt.%).	41
3.1	Average Vickers hardness of HAZ and BM in as-welded P91 welds.	57
3.2	EBSD grain boundary and grain size analyses on the as-received base metal and CGHAZ, FGHAZ, ICHAZ in an as-welded HAZ.	59
3.3	EBSD KAM and GAM analyses on as-received base metal and CGHAZ, FGHAZ, ICHAZ in an as-welded HAZ.	62
3.4	Critical transformation temperatures determined by the dilatation curve analysis in the simulated HAZ specimens.	66
3.5	EBSD GB and size analysis on 1s-hold, 120s-hold, and 600s-hold specimens.	72
3.6	EBSD KAM and GAM analyses on 1s-hold, 120s-hold, and 600s-hold specimens.	73
3.7	EBSD GB and size analyses on CGHAZ, FGHAZ, and ICHAZ.	79
3.8	EBSD KAM and GAM analyses on CGHAZ, FGHAZ, and ICHAZ.	82
3.9	EDS composition analyses on $\delta$ -ferrite grains in CGHAZ, FGHAZ, ICHAZ, and BM.	86
4.1	EBSD grain boundary and size analyses on the weld PWHT-ed at 760 °C for 2 hours.	118
4.2	EBSD KAM and GAM analyses on the weld PWHT-ed at 760 °C for 2 hours	119
4.3	EBSD grain boundary and size analyses on the crept weld PWHT-ed at 760 °C for 2 hours.	120
4.4	EBSD KAM and GAM analyses on the crept weld PWHT-ed at 760 °C for 2 hours.	122

5.1	EBSD grain boundary and size analyses on the specimen PWHT-ed at 840 °C for 2 hours. . . . .	150
5.2	EBSD KAM and GAM analyses on the specimen PWHT-ed at 840 °C for 2 hours. . . . .	152
6.1	Material property parameters, including Norton parameters A ( $\text{MPa}^{-n}\text{s}^{-1}$ ) and n, Young's modulus E (MPa) at 650 °C are used for FE model in Figure 6.1. These parameters were determined by stress-relaxation tests in a previous work of our group [90]. The samples were PWHT-ed at various temperatures for 2 hours. . . . .	165

# List of Figures

1.1	Creep resistant alloys used in the Subcritical, SC, USC, and A-USC boilers [2] (original by [6]). . . . .	3
1.2	Schematic showing a fossil fired boiler and the typical used materials [4]. . .	4
1.3	The historical development of 9-12 % chromium creep-resistant ferritic/martensitic steels used in boilers [10]. . . . .	5
1.4	Maximum service temperature of 9–12 % Cr steels, based on the 100,000h creep rupture strength of 100 MPa [3]. . . . .	6
1.5	(a) A typical creep curve of strain versus time at constant load and constant elevated temperature. (b) Influence of stress $\sigma$ and temperature T on creep behavior [14]. . . . .	7
1.6	Deformation mechanism map of pure iron with a grain size of 100 $\mu\text{m}$ (by Frost and Ashby [15]). . . . .	9
1.7	The original optimum chemical composition window for Grade 91 steel by ORNL (adapted from [13], original by [18]). . . . .	10
1.8	Continuous cooling transformation (CCT) diagram of Grade 91 steel (T91) [24].	13
1.9	Multi-boundaries of lath martensite in low carbon steels: (a) Schematic graph [25]; (b) SEM image [26]. . . . .	13
1.10	Precipitate distribution in the martensitic matrix of Grade 91 steel: (a) Schematic graph [3]; (b) SEM image. . . . .	15
1.11	Precipitate size in Grade 91 steel during creep at 600 °C and 650 °C [19]. . .	16
1.12	Study of phase transformation in a martensitic 9 wt pct. chromium steel by in-situ X-ray diffraction (XRD) using high energy synchrotron radiation (heating/cooling rate: 10 K/s) (Mayr et al. [37]). . . . .	17
1.13	Creep strength of a T91 steel as a function of creep temperatures [3]. . . . .	19
1.14	Creep strength at 650 °C of Grade 91 steel as a function of tempering temperatures [19]. . . . .	21
1.15	Creep strength and hardness as a function of creep lifetime [13] (original by [60]).	23
1.16	Typical thermal cycles for welding Grade 91 steel [7] (original by [65]). . . .	25
1.17	Schematic structure in a single-pass weldment [66] (original by Savage [67]).	25
1.18	Schematic microstructures in HAZ as a function of peak temperatures during welding (from Mayr [68]). . . . .	26
1.19	$A_1$ temperature as a function of Mn+Ni content in Grade 91 steel [13]. . . .	30

1.20	(a) Charpy impact energies and average Vickers hardness values of different HAZ zones after post-weld heat-treating at various temperatures for 2 hours in Grade 91 steel welds [69]. . . . .	31
1.21	Schematic drawing of cracking modes in steel weldments [4] (original by Schüller et al. [82]). . . . .	32
1.22	Schematic drawing of three fracture mechanisms in a high temperature creep regime ( $>0.3T_m$ ) [4] (original by Ashby et al. [83]). . . . .	33
1.23	(a) Optical graph of the Type IV cracking [86] and (b) creep cavities in the Type IV cracking in a Grade 91 steel weldment. . . . .	34
1.24	Hardness distribution in the Type IV cracking in a Grade 91 steel weld after high-temperature creep tests [74]. . . . .	35
1.25	Structural evolution in the Type IV cracking in a Grade 91 steel weld [74]. . . . .	36
3.1	Typical microstructure of the as-received P91 base metal: (a) In-lens secondary electron image; (b) Magnified image; (c) EDS line scanning across two precipitates marked in (b). . . . .	51
3.2	EBSD analyses of the as-received P91 base metal: (a) In-lens secondary electron (SE) image. (b) Z axis inverse pole figure. (c) Phase map. (d) Kernel average misorientation map. . . . .	51
3.3	Optical cross-section of a P91 steel weldment showing fusion zone, HAZ, and BM. . . . .	53
3.4	Microstructure of the HAZ in an as-welded P91 weld marked by the rectangle 1 in Figure 3.3: (a) Overview of the HAZ from the FZ to BM; (b) CGHAZ; (c) FGHAZ; (d) ICHAZ; (e) BM. . . . .	53
3.5	Microstructure of HAZ in an as-welded P91 weld: (a1), (a2), and (a3) are the CGHAZ. (b1), (b2), and (b3) are the FGHAZ. (c1), (c2), and (c3) are the ICHAZ. . . . .	54
3.6	Microstructure evolutions in the ICHAZ: (a) microstructure of as-received P91 base metal (BM), (b) PAGBs and block boundaries in BM, and (c) a schematic microstructure for BM. (d) microstructure of the ICHAZ, (e) PAGBs and block boundaries in ICHAZ, and (f) a schematic microstructure for ICHAZ. $M_{23}C_6$ carbides along a former PAGB are pointed by white arrows in (d). Black solid lines represent former PAGBs; black dashed lines represent martensite block boundaries; red solid lines represent new PAGBs; and red dash lines represent new martensite packet boundaries. . . . .	56
3.7	Vickers hardness mapping of the cross-section of the as-welded P91 weldment: (a) hardness distribution; (b) correlated hardness indentations. . . . .	57
3.8	EBSD analyses of the CGHAZ: (a) Z axis inverse pole figure (IPF) ; (b) GB map; (c) GAM map with a threshold of $1^\circ$ ; (d) KAM map. . . . .	58
3.9	EBSD analyses of the FGHAZ: (a) Z axis inverse pole figure (IPF); (b) GB map; (c) GAM map with a threshold of $1^\circ$ ; (d) KAM map. . . . .	60

3.10	EBSD analyses of the ICHAZ: (a) Z axis inverse pole figure (IPF) ; (b) GB map; (c) GAM map with a threshold of 1°; (d) KAM map. . . . .	60
3.11	(a) Inverse pole figure of the new PAG in the upper left corner and a former PAG with retained tempered martensite in the lower bottom corner of Figure 3.10a. (b) and (c) shows, respectively, misorientation angle along the two marked dash arrows (AB, CD) across the block boundaries in (a). . . . .	61
3.12	EBSD phase maps show the precipitate distributions in the (a) CGHAZ, (b) FGHAZ, and (c) ICHAZ. . . . .	62
3.13	Equilibrium phase fraction of P91 BM as a function of temperature is calculated by ThermoCalc. . . . .	63
3.14	Thermal history of the simulated HAZ specimens with different holding times by dilatometry. . . . .	64
3.15	A representative heating-cooling dilation curve of the simulated HAZ representing phase transformations. . . . .	64
3.16	An example of heating-cooling curve analysis of the critical phase transformation temperatures in the simulated HAZ specimens. . . . .	65
3.17	Martensite-start $M_s$ temperature of the simulated HAZ specimens. . . . .	66
3.18	Martensitic phase transformation as a function of temperature during cooling in the simulated HAZ specimens. . . . .	67
3.19	Vickers hardness of the simulated HAZ specimens. . . . .	67
3.20	Typical structures of the simulated 1s-hold HAZ specimen. . . . .	68
3.21	Microstructure of the simulated HAZ specimens: (a), (b) 1s-hold; (c), (d) 30s-hold; (e), (f) 60s-hold; (g), (h) 300s-hold. (Red arrows: new PAGBs, Green arrows: old PAGBs). . . . .	69
3.22	PAG size of the simulated HAZ specimens. . . . .	70
3.23	EBSD grain boundary map and IPF of the simulated HAZ specimens: (a) 1s-hold; (b) 120s-hold; (3) 600s-hold. . . . .	71
3.24	KAM distribution of the 1s-hold, 120s-hold, and 600s-hold specimens. . . . .	72
3.25	Optical microstructure of the as-received Grade 91 heavy section block: (a) Tempered martensite matrix. (b) Rod-shaped $\delta$ -ferrite distributes along the PAGBs. . . . .	74
3.26	EBSD analyses of the as-received block base metal: (a) Band contrast map. (b) Grain boundary map. (c) All Euler angle map. (d) IPF in Z direction. (e) KAM map. (f) GAM map. . . . .	75
3.27	Cross-sectional macrostructure of the as-welded heavy section weldment. . . . .	76
3.28	Optical microstructure of the HAZ in an as-welded Grade 91 block weldment: (a) Overview of the HAZ from fusion zone to the base metal; (b) CGHAZ; (c) FGHAZ; (d) ICHAZ; (e) BM. . . . .	77
3.29	SEM images of the HAZ in an as-welded Grade 91 block weldment: (a) BM; (b) CGHAZ; (c) FGHAZ; (d) ICHAZ. . . . .	78
3.30	EBSD grain boundary distribution maps: (a) CGHAZ; (b) FGHAZ; (c) ICHAZ. . . . .	79

3.31 All-Euler maps and IPF in Z direction: (a), (d) CGHAZ; (b), (e) FGHAZ; (c), (f) ICHAZ. . . . .	80
3.32 Local strain distribution illustrated by the KAM maps (a, b, c) and grain average misorientation maps (d, e, e): (a), (d) CGHAZ; (b), (e) FGHAZ; (c), (f) ICHAZ. . . . .	81
3.33 Hardness distribution in the cross-section HAZ specimen in the as-welded condition: (a) Dark-field optical image; (b) hardness contour map; (c) average hardness profile. . . . .	83
3.34 The EBSD band contrast maps (a, b, c) and All-Euler maps (d, e, f) of $\delta$ -ferrite in various regions: (a), (d) BM. (b), (e) FGHAZ. (c), (f) CGHAZ. . . . .	84
3.35 EDS mapping of $\delta$ -ferrite in various regions: (a) BM, (b) FGHAZ, (c) CGHAZ. . . . .	85
3.36 Accumulated concentration of ferrite-stabilizers in $\delta$ -ferrite in HAZ and BM. Composition of the as-received BM (AR-BM) is also shown in the figure. . . . .	87
3.37 Precipitate distribution around $\delta$ -ferrite in various regions: (a) BM, (b) ICHAZ, (c) CGHAZ. . . . .	87
3.38 KAM (a, b, c) and GAM (d, e, f) evaluations of $\delta$ -ferrite in various regions: (a), (d) BM. (b), (e) ICHAZ. (c), (f) CGHAZ. Note: The straight line with high KAM values in (c) is due to a polishing scratch. . . . .	88
3.39 Local misorientation across the $\delta$ -ferrite in various regions: (a) BM, (b) ICHAZ, (c) CGHAZ. . . . .	89
3.40 Calculated equilibrium phase fraction and Scheil solid fraction as a function of temperature of the block base metal by ThermoCalc . . . . .	90
3.41 Thermal curves of the simulated HAZ specimens by dilatometry. . . . .	91
3.42 Vickers hardness of the simulated HAZ specimens. . . . .	92
3.43 EBSD grain boundary map and IPF of the simulated HAZ specimens: (a), (b) 910 °C-ICHAZ; (c), (d) 1060 °C-FGHAZ; (e), (f) 1360 °C-CGHAZ. . . . .	92
3.44 EBSD KAM and GAM maps of the simulated HAZ specimens: (a), (b) 910 °C-ICHAZ; (c), (d) 1060 °C-FGHAZ; (e), (f) 1360 °C-CGHAZ. . . . .	93
3.45 Effects of PAG size [118] and alloying elements [27] on the $M_s$ temperature in low carbon martensitic steels. . . . .	97
3.46 An isopleth of Grade 91 heavy section base metal calculated by ThermoCalc. . . . .	100
3.47 Inlens-SEM images of boundary precipitates between $\delta$ -ferrite and martensitic matrix in (a) BM and (b) CGHAZ. . . . .	100
4.1 Typical creep curve (strain and strain rate) of the Type IV cracking in a cross-weld specimen after PWHT at 760 °C for 2 hours and creep test at 650 °C with a stress level of 70 MPa. . . . .	105
4.2 Hardness distribution across the as-welded weldment along the mid-thickness: (a) Optical figure of the weldment; (b) hardness profile; (c) magnified hardness profile of the HAZ (left side). . . . .	106

4.3	Average hardness profiles across the HAZ in three thermal stages: As-welded; PWHT-ed at 760 °C for 2 hours; Creep failed at 649 hours at 650 °C under a stress of 70 MPa, following a PWHT at 760 °C for 2 hours. There is a hardness vulnerable region (marked by red dash-line rectangle) in the ICHAZ.	107
4.4	The load-displacement curve in three thermal stages: (a) As-welded; (b) After PWHT at 760 °C for 2 hours; (c) After creep test.	108
4.5	Intrumented indentation results: (a) Local hardness and (b) deformation rate of the welds in three thermal stages.	109
4.6	Optical image of the indentations and hardness distribution in as-welded HAZ. Locations associated with the soft zone are marked by #23, #24, #25, and #26.	110
4.7	SE SEM images show structure evolutions in the soft zone and neighbouring zones of as-welded HAZ. Figures (a) to (d) show correlated Locations 23, 24, 25, and 26, respectively. Retained grains are marked by white arrows in the figures.	110
4.8	Local misorientation analyses to distinguish multi-scale boundaries in a location close to Location 25: (a) All Euler map. (b) Line 1 scanning misorientation indicates block and sub-block boundaries in a PAG. (c) Line 2 scanning misorientation inside a fine PAG shows the sub-block boundaries. (d) Line 3 scanning misorientation indicates PAGBs.	111
4.9	EBSD analyses on the soft zone in as-welded HAZ: (a) SE SEM image. (b) Kernel average misorientation (KAM) map. Grains A-G indicate the identified retained tempered martensite.	112
4.10	Statistical measurements of (a) the number density of retained grains and (b) average sizes of re-austenite and retained grains in the Location 23, 24, 25, and 26 (from left to right). The hardness value of each location is also shown in the figure.	113
4.11	Microstructure evolution of the identified soft zones in ICHAZ from Figure 4.3. (a) and (d) As-welded. (b) and (e) After PWHT. (c) and (f) After creep tests.	115
4.12	Evolution of creep cavities in the ICHAZ during the Type IV cracking.	116
4.13	EBSD IPF of the weld PWHT-ed at 760 °C for 2 hours: (a) Fusion zone; (b) CGHAZ; (c) FGHAZ; (d) ICHAZ; (e) Base metal.	117
4.14	KAM distribution in the weld PWHT-ed at 760 °C for 2 hours : (a) Fusion zone; (b) CGHAZ; (c) FGHAZ; (d) ICHAZ; (e) Base metal.	118
4.15	EBSD IPF of the crept weld PWHT-ed at 760 °C for 2 hours: (a) Fusion zone; (b) CGHAZ; (c) FGHAZ; (d) ICHAZ; (e) Base metal.	119
4.16	Local strain distribution in the crept welds: (a) Fusion zone; (b) CGHAZ; (c) FGHAZ; (d) ICHAZ; (e) Base metal.	121
4.17	KAM distribution in the crept welds: (a) Fusion zone; (b) CGHAZ; (c) FGHAZ; (d) ICHAZ; (e) Base metal. The high KAM region in (c) is associated with a creep cavity.	121

4.18	Local chemistry analysis of the as-received base metal and the identified soft zone (ICHAZ) at three thermal stages by mapping C, Cr, and Fe with auger electron spectroscopy. . . . .	123
4.19	Effect of low chromium concentrations (7-10 wt.%) on (a) the Gibbs energy of ferrite and austenite and (b) $T_0$ temperature of ferrite-to-austenite transformation at 820 °C. . . . .	125
4.20	Schematic illustration of microstructure evolution in the ICHAZ in the Type IV cracking. . . . .	128
5.1	Hardness distribution profiles across the weldments in the as-welded condition and after PWHT at various temperatures for 2 hour hold: (a) the entire weldment; (b) the magnified HAZ region. . . . .	132
5.2	Hardness distribution profiles across the weldments in the as-welded (AW) condition and after PWHT at various temperatures for 8 hour hold: (a) the entire weldment; (b) the magnified HAZ region. . . . .	133
5.3	Hardness contour maps of the HAZs after PWHT at various temperatures for 2 hours at: (a) 600 °C; (b) 760 °C; (c) 820 °C; (d) 840 °C. . . . .	134
5.4	Hardness contour maps of the HAZs after PWHT at various temperatures for 8 hours at: (a) 600 °C; (b) 760 °C; (c) 820 °C; (d) 840 °C. . . . .	135
5.5	Average hardness profiles, following the PWHT, from the hardness mapping in Figure 5.3 and Figure 5.4: (a) 2 hours; (b) 8 hours. . . . .	136
5.6	Optical images showing typical microstructure of the specimen after PWHT at 600 °C for 2 hours: (a) Fusion zone; (b) CGHAZ; (c) FGHAZ; (d) ICHAZ; (e) BM. . . . .	138
5.7	Optical images showing typical microstructure of the specimen after PWHT at 840 °C for 2 hours: (a) Fusion zone; (b) CGHAZ; (c) FGHAZ; (d) ICHAZ; (e) BM. . . . .	139
5.8	Creep results of the PWHT-ed cross-weld specimens tested at 650 °C under a stress of 70 MPa. . . . .	140
5.9	Optical images showing the cross-section of the creep-ruptured specimens PWHT-ed at various temperatures for (a) 2 hours and (b) 8 hours. . . . .	141
5.10	Hardness contour maps of the HAZs after PWHT at various temperatures for 2 hours and creep testing at 650 °C under 70 MPa. . . . .	143
5.11	Hardness contour maps of the HAZs after PWHT at various temperatures for 8 hours and creep testing at 650 °C under 70 MPa. . . . .	144
5.12	Average hardness profiles, following the creep tests, from the hardness mapping in Figure 5.10 and 11: (a) 2 hours; (b) 8 hours. . . . .	145
5.13	Microstructure of the cross-section specimen after PWHT at 760 °C for 2 hours and creep test at 650 °C with a stress level of 70 MPa: (a), (b) Fusion zone; (c), (d) CGHAZ; (e), (f) FGHAZ; (g), (h) ICHAZ; (i), (j) BM. . . . .	147

5.14	Microstructure of the cross-section specimen after PWHT at 840 °C for 8 hours and creep test at 650 °C with a stress level of 70 MPa: (a), (b) Fusion zone; (c), (d) CGHAZ; (e), (f) FGHAZ; (g), (h) ICHAZ; (i), (j) BM. . . . .	149
5.15	EBSD analysis on the specimen PWHT-ed at 840 °C for 2 hours: (a) FZ; (b) CGHAZ; (c) FGHAZ; (d) ICHAZ; (e) BM. . . . .	150
5.16	EBSD analysis on the specimen PWHT-ed at 840 °C for 2 hours: (a) FZ; (b) CGHAZ; (c) FGHAZ; (d) ICHAZ; (e) BM. . . . .	152
5.17	EBSD analysis on the crept specimen (PWHT-ed at 840 °C for 2 hours): (a) FZ; (b) CGHAZ; (c) FGHAZ; (d) ICHAZ; (e) BM. . . . .	153
5.18	EBSD KAM and GAM analysis on the crept specimen (PWHT-ed at 840 °C for 2 hours): (a), (b) FZ; (c), (d) ICHAZ. . . . .	154
5.19	Phase fraction as a function of temperature calculated by ThermoCalc: (a) Weld metal; (b) BM. . . . .	155
5.20	An illustration of effects of PWHT temperatures on microstructure evolutions of the HAZ and FZ and creep rupture mode of the weldments. The temperature unit in the figure is °C. . . . .	158
5.21	Microstructure of (a) as-welded ICHAZ and (b) the FZ after PWHT at 840 °C for 2 hours. The untransformed ferritic grains are marked by white arrows in the figures. . . . .	159
5.22	EBSD analysis on the FZ after PWHT at 840 °C for 2 hours: (a) Band contrast (BC) map; (b) Kernel average misorientation (KAM) map. . . . .	160
6.1	Geometry of the 2-D cross-weld model. . . . .	164
6.2	Physics-based mesh and boundary conditions used in the 2-D cross-weld model. . . . .	164
6.3	First principal stress distribution in the welds: (a) PWHT at 760 °C; (b) PWHT at 820 °C; (c) PWHT at 840 °C. . . . .	166
6.4	First principal stress distribution across the mid-thickness of the welds: (a) PWHT at 760 °C; (b) PWHT at 820 °C; (c) PWHT at 840 °C. . . . .	167
6.5	Von Mises stress distribution in the welds after creep tests for 200 h: (a) PWHT at 760 °C; (b) PWHT at 820 °C; (c) PWHT at 840 °C. . . . .	168
6.6	Von Mises stress distribution across the mid-thickness of the welds: (a) PWHT at 760 °C; (b) PWHT at 820 °C; (c) PWHT at 840 °C. . . . .	169
6.7	Stress triaxiality distribution in the welds after creep tests for 200 h: (a) PWHT at 760 °C; (b) PWHT at 820 °C; (c) PWHT at 840 °C. . . . .	170
6.8	Stress triaxiality across the mid-thickness of the welds: (a) PWHT at 760 °C; (b) PWHT at 820 °C; (c) PWHT at 840 °C. . . . .	171
6.9	Stress triaxiality in the centre point of each region as a function of creep time: (a) PWHT at 760 °C; (b) PWHT at 820 °C; (c) PWHT at 840 °C. . . . .	172
6.10	Effective creep strain in the welds after creep tests for 200 h: (a) PWHT at 760 °C; (b) PWHT at 820 °C; (c) PWHT at 840 °C. . . . .	173
6.11	Effective creep strain distribution across the mid-thickness of the welds: (a) PWHT at 760 °C; (b) PWHT at 820 °C; (c) PWHT at 840 °C. . . . .	174

6.12	Effective creep strain rate in the welds after creep tests for 200 h: (a) PWHT at 760 °C; (b) PWHT at 820 °C; (c) PWHT at 840 °C. . . . .	175
6.13	Effective creep strain rate across the mid-thickness of the welds: (a) PWHT at 760 °C; (b) PWHT at 820 °C; (c) PWHT at 840 °C. . . . .	176
6.14	A flow chart shows the steps for generating microstructure-based models for finite element analysis. . . . .	177
6.15	(a) SEM image shows typical microstructure of the ICHAZ in the specimen(PWHT-ed at 600 °C for 2 hours) after creep tests for 650 hours; (b) Post-processed graph (right) highlights the grain boundaries and distributed precipitates; (c) Geometry of the microstructure-based model. . . . .	178
6.16	Three structural components with various strengths, including hard grains, soft grains, and precipitates, used in the microstructure-based model. . . . .	178
6.17	Boundary conditions and mesh used in the microstructure-based model. . . . .	179
6.18	Von Mises stress (MPa), first principal stress (MPa), and stress triaxiality distributions in the structure. . . . .	180
6.19	Optical image of a Type IV cracking and stress triaxiality in the cross-weld model. . . . .	181
6.20	Stress triaxiality distribution in the ICHAZ in the thickness direction (PWHT-ed at 760 °C). . . . .	182
6.21	(a) Stress triaxiality in the structured-based model; (b) A creep cavity nucleated in a grain boundary triple intersection. . . . .	183

# Chapter 1

## Introduction and Literature Review

### 1.1 Introduction

Grade 91 steel, known as modified 9Cr-1Mo-V-Nb steel, is one of the most important 9-12 % Cr creep strength enhanced ferritic (CSEF) steels used in fossil-fuel fired power plants. Fusion welding of Grade 91 steel has been used to produce sound joints. However, rapid heating/cooling and gradient peak temperatures in fusion welding processes cause non-equilibrium phase transformations in the base metal, which results in generating a narrow heat-affected zone (HAZ) between the weld metal and unaffected base metal. Post-weld heat treatment (PWHT) is a common practice to reduce the hardness and residual stress and to improve toughness of weldments. Detailed microstructural evolutions of each individual HAZ sub-regions during different PWHTs have not been well studied. Several creep rupture modes, including Type I cracking and Type IV cracking, have been reported in Grade 91 steel weldments after PWHT. The most common one, the Type IV cracking, has been extensively studied, but several uncertainties remain in understanding its mechanism(s). Further investigations need to be conducted. Modeling creep behavior of Grade 91 steel weldments is worthy of predicting the creep lifetime of these key components. However, it is challenging due to the combination of multiple materials (weld metal, HAZ, and base metal) in one weldment. The inhomogeneous sub-regions in the HAZ introduce more complexities.

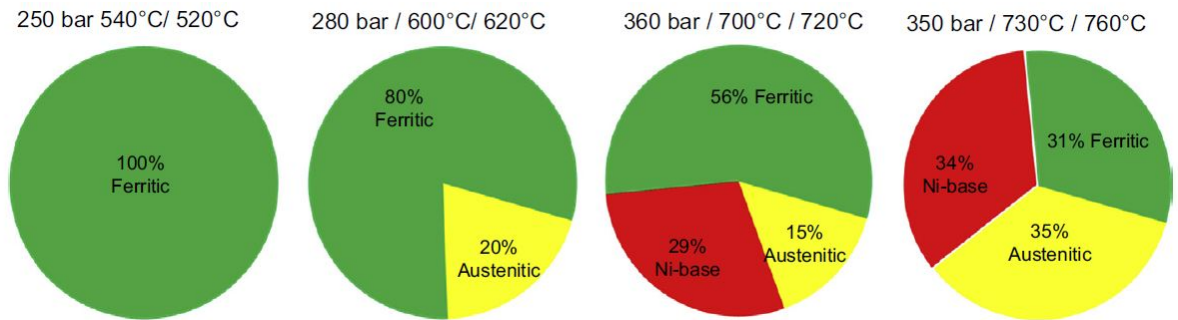
## 1.2 Literature Review

### 1.2.1 9-12% Cr Creep Resistant Ferritic/Martensitic Steels

Fossil fuels became the primary energy source since the Industrial Revolution in the 18th century. Fossil-fuel fired power plants are widely built to generate electric energy around the world. To meet the growing demand of energy, more power plants are being built all over the world, especially China and India in Asia [1]. Based on the used temperature and pressure of water steam, fossil-fuel fired power plants are divided into subcritical power plant, supercritical (SC) power plant, ultra-supercritical (USC) power plant, and advanced ultra-supercritical (A-USC) power plant [2–4]. The operating conditions of these power plants are listed in Table 1.1. The temperature and pressure of the steam are increased to improve thermal efficiency of the Rankine cycle, which eventually reduces the cost of fuel and the use of fuel resources [2, 4]. The subcritical power plants, operating at 540 °C and with a steam pressure of 17 MPa, were widely used in the early 1950s. Later, the technology of the SC power plant became mature and the SC power plants were put into service with a steam temperature up to 600 °C and a steam pressure of 27 MPa in the 1990s [3]. The USC power plants, operating at steam temperature up to 620 °C and steam pressure of 30 MPa, are the state of the art technology in the Europe, Japan, China, and USA [2, 3]. The advanced ultra-supercritical (A-USC) technology is under development for the next generation. Efforts are targeting the thermal efficiency > 50 % , steam temperature 700–760 °C, and steam pressure of 35 MPa for A-USC plants [2, 5].

**Table 1.1:** Operating conditions of fossil fired power plants [2, 3]

Power Plant	Steam Temperature	Steam Pressure	Thermal Efficiency	Note
Subcritical	540 °C	170 bar (17 MPa)	< 38 %	
Supercritical	600 °C	270 bar (27 MPa)	Up to 42 %	Mature technology
Ultra-Supercritical	620 °C	300 bar (30 MPa)	42 %–46 %	State of the art technology
Advanced Ultra-supercritical	700–760 °C	350 bar (35 MPa)	> 50 %	Under development

**Figure 1.1:** Creep resistant alloys used in the Subcritical, SC, USC, and A-USC boilers [2] (original by [6]).

The main components in a coal-fired thermal power plant include the boiler, steam line, steam turbine, and condenser [2]. The boiler consists of water wall, superheater, reheater, header, economizer, and drums. Creep-resistant materials used in these key components are classified into three categories: ferritic/martensitic steels, austenitic steels, and Ni-base alloys [4, 5, 7]. Figure 1.1 shows the relative fractions of these three materials used in the SC, USC, and A-USC boilers. Ferritic/martensitic steels are normally used below 600 °C. Austenitic steels are used between 600 °C and 700 °C. Beyond 700 °C, Ni-base alloys have to be used.

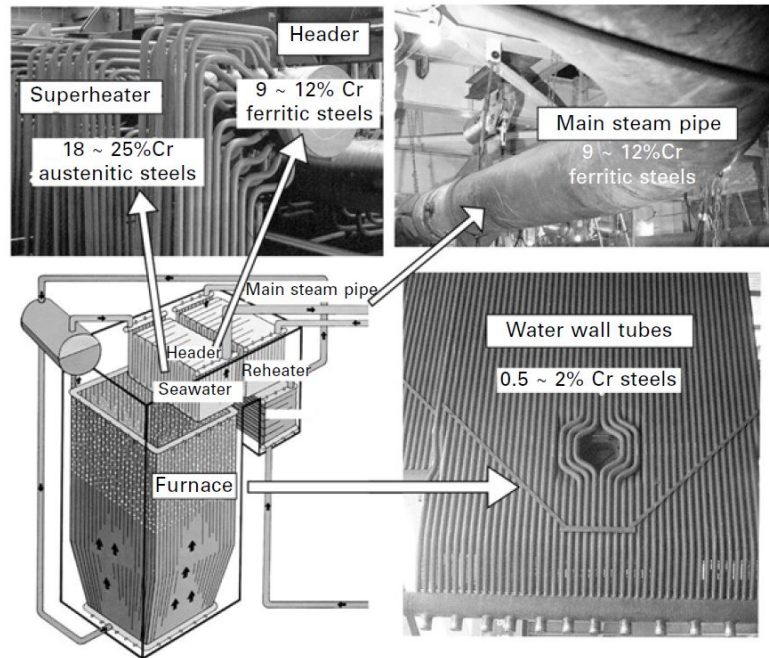


**Figure 1.2:** Schematic showing a fossil fired boiler and the typical used materials [4].

Figure 1.2 shows a schematic of a boiler and the typical used materials in a USC power plant [4]. Water wall tubes (up to 500 °C) are made of 0.5–2 % Cr ferritic steels, such as P22 steel. The materials of superheaters (600 °C) are 18–25 % Cr austenitic steels. 9–12 % Cr ferritic steels, such as P91, E911, and P92 steels, are used in headers (605 °C) and main steam pipes. Some high Cr ferritic steels have similar creep rupture strength with the austenitic stainless steels [8]. In the SC power plants, the ferritic steels have been used for all the components. When the steam temperature increases to 600–620 °C in the USC power plants, 20 % austenitic steels have been used for some key high-temperature components. The austenitic steels used in the USC plants include the Super 304H, AISI 316, AISI 321, AISI 347 [5, 8, 9]. In the A-USC power plants, approximately 30 % Ni-base alloys have to be used to meet requirements of the higher temperatures (700–760 °C) and pressure (35 MPa). The Ni-base alloys, such as Inconel 617, Inconel 740, HR6W, and Haynes 282 are the potential materials for the next generation A-USC plants [2, 7, 9].

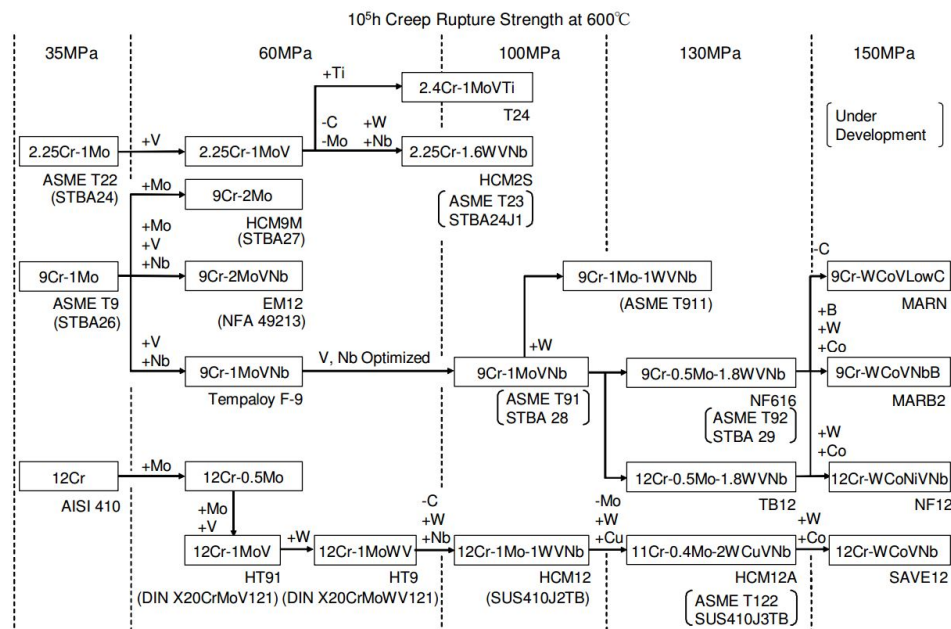


**Figure 1.3:** The historical development of 9–12 % chromium creep-resistant ferritic/martensitic steels used in boilers [10].

9–12 % Cr steels are the most widely used materials in the current USC plants. 9–12 % Cr creep resistant martensitic steels have a similar creep rupture strength with some austenitic steels and a lower (50 %) thermal expansion coefficient than that of austenitic steels [8]. Figure 1.3 shows the historical development of 9–12 % Cr steels. The 100,000-hour creep rupture strength at 600 °C of these steels is also shown in the figure. Alloying elements Mo, V, and Nb were added into 9–12 % Cr steels to further improve their creep strength in 1960s [11]. EM12 (9Cr-2MoVNb) was developed for tubes in France. At the same time, 12Cr-1MoV (X20CrMoV121) was developed for pipes and tubes in Germany [12]. In the late 1970s, the modified 9Cr-1Mo steel (Grade 91 steel) was co-developed by the Oak Ridge National Laboratory (ORNL) and the former Combustion Engineering (later ABBCE, and currently Alstom) [13]. And then the designation of Grade 91 steel (P91 for pipe and plate, T91 for tube) was established in the early 1980s [13]. For 12Cr steels, a further improvement of creep strength was achieved in the HCM12 and HCM12A by adding W and Cu. In the 1990s, E911

(9Cr-1Mo-1WVNb) was developed by adding W into the modified 9Cr-1Mo steel. P92 (9Cr-0.5Mo-1.8WVNb) was also developed by modifying the Mo and W contents [11–13]. For the latest development of 9–12 % Cr steels, including MARN, MARB2, NF12, and SAVE12, B, W, and Co were added or modified to achieve 150 MPa 100,000-h creep rupture strength at 600 °C.

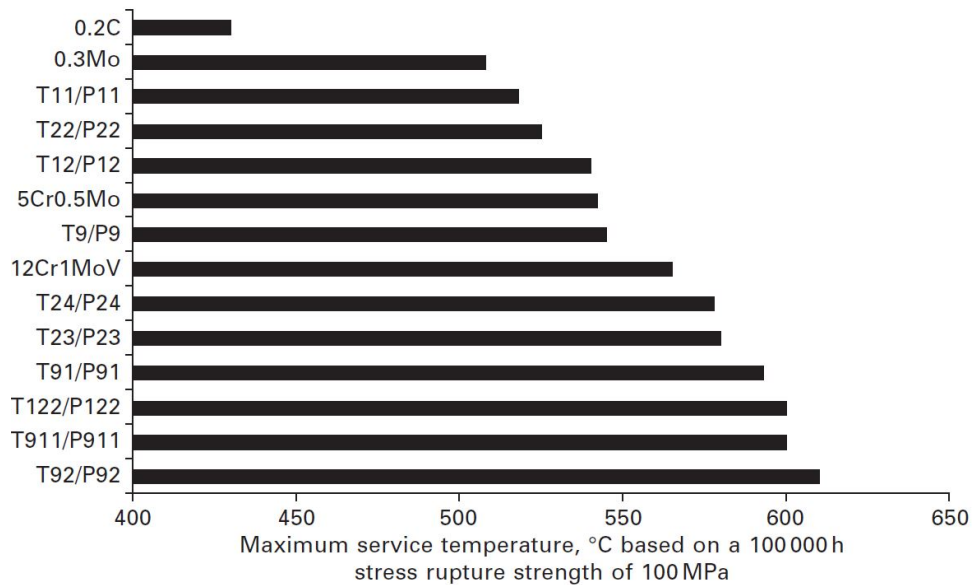


**Figure 1.4:** Maximum service temperature of 9–12 % Cr steels, based on the 100,000h creep rupture strength of 100 MPa [3].

Figure 1.4 compares the maximum service temperature of common 9–12 % Cr steels, based on the 100,000-h creep rupture strength of 100 MPa. It is shown that the maximum service temperature of Grade 91 (T91/P91) steel, E911 (T911/P911) steel, and Grade 92 (T92/P92) steel can reach up to 600 °C. The maximum service temperature Grade 91 steel can even reach to approximately 620 °C.

## 1.2.2 Creep and Deformation Mechanism Map

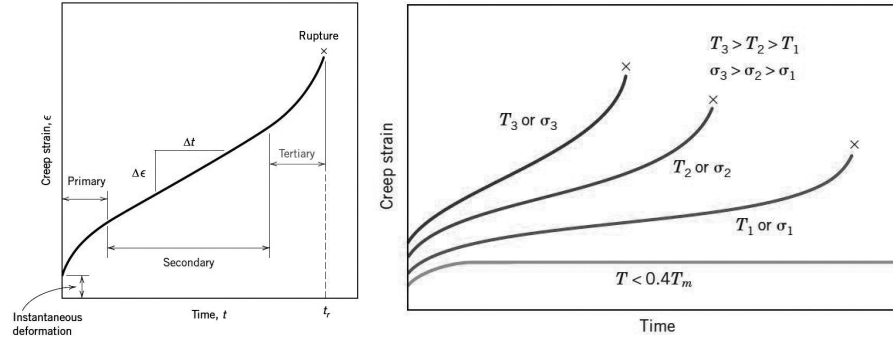


**Figure 1.5:** (a) A typical creep curve of strain versus time at constant load and constant elevated temperature. (b) Influence of stress  $\sigma$  and temperature  $T$  on creep behavior [14].

Creep is a failure of materials due to slow continuous permanent deformation induced by a static load (normally tension) at high temperatures ( $\geq 0.4T_m$ ,  $T_m$  is the melting temperature in K) [14]. Creep is the time-dependent component of plastic deformation [4]. Creep deformation is evaluated by creep strain and strain rate as a function of creep time. The strain and strain rate are expressed as following:

$$\epsilon = \frac{L - L_0}{L_0} \quad (1.1)$$

$$\dot{\epsilon} = \frac{d\epsilon}{dt} \quad (1.2)$$

Where  $L$  is the sample length during test;  $L_0$  is the initial sample length;  $t$  is time.

Figure 1.5a shows a typical creep curve of strain versus time at constant load and elevated temperature. Creep curve of metals and alloys usually contains three stages: the primary creep, secondary creep, and tertiary creep. In the primary or transient creep, the strain rate is quite high and decreases with the increase of time and strain. The secondary creep, also known as steady-state creep, has a constant but minimum strain rate. The secondary creep is the most studied one. The constant strain rate is due to the balance between the rate of

generation of dislocations contributing to hardening and the rate of recovery contributing to softening [4]. The second creep is a thermal-activated process and the strain rate obeys an Arrhenius equation. The steady-state strain rate is normally expressed by the Norton's law (power law) as following:

$$\dot{\epsilon}_s = A\sigma^n = A'\sigma^n \exp(-Q_c/RT) \quad (1.3)$$

where  $\sigma$  is the applied stress;  $n$  is the stress exponent;  $R$  is the gas constant;  $T$  is the absolute temperature;  $Q_c$  is the activation energy for creep;  $A'$  is a material parameter. In tertiary creep, the strain rate exponentially increases. The creep strength decreases dramatically. Necking, cracks, and fracture are usually observed in this stage.

Figure 1.5b schematically shows the influence of stress  $\sigma$  and temperature  $T$  on creep behavior. The general tendency is that the creep strain increases with the increase of temperature and stress. Frost and Ashby [15] developed deformation mechanism maps to show this relationship. It is concluded that for the low-stress creep condition, there are two major deformation mechanisms, the dislocation creep (power law creep) and diffusion creep. Dislocation creep can be further divided into low-temperature power law creep and high-temperature power law creep [4, 15]. Diffusion creep can be further divided into volume diffusion creep (Nabarro–Herring creep) and grain boundary diffusion creep (Coble creep). Figure 1.6 shows an example of deformation mechanism map of pure iron. It shows under a low stress level ( $\sigma/G < 10^{-3}$ ), the deformation mechanism transits from the power law creep to the diffusion flow with the decreasing stress. Furthermore, the deformation mechanism transition from the Coble creep to the Nabarro–Herring creep occurs when the creep temperature increases.

For creep resistant ferritic steels, their service temperature is between  $0.4T_m$  and  $0.55T_m$  and the applied stress is about  $10^{-4}/E$ – $10^{-3}/E$  ( $E$  is Young's modulus) [4]. The creep deformation mechanisms involve high temperature power law creep, Coble creep, and Nabarro-

Herring creep. The constitutive equations of these mechanisms can be expressed by a general form [4]:

$$\dot{\epsilon} = \dot{\epsilon}_0(\sigma/G)^n d^{-p} D \tag{1.4}$$

where  $\dot{\epsilon}_0$  is a characteristic material constant;  $G$  is the shear modulus;  $n$  is the stress exponent;  $d$  is the grain size;  $p$  is the grain size exponent; the  $D$  is the diffusion coefficient. For the high temperature power law creep,  $n=3-5$ ,  $p=0$ , and  $D$  is the volume diffusion coefficient  $D_v$ ; for the Coble creep,  $n=1$ ,  $p=3$ , and  $D$  is the grain boundary diffusion coefficient  $D_{gb}$ ; for the Nabarro-Herring creep,  $n=1$ ,  $p=2$ , and  $D$  is the volume diffusion coefficient  $D_v$  [4, 16, 17].

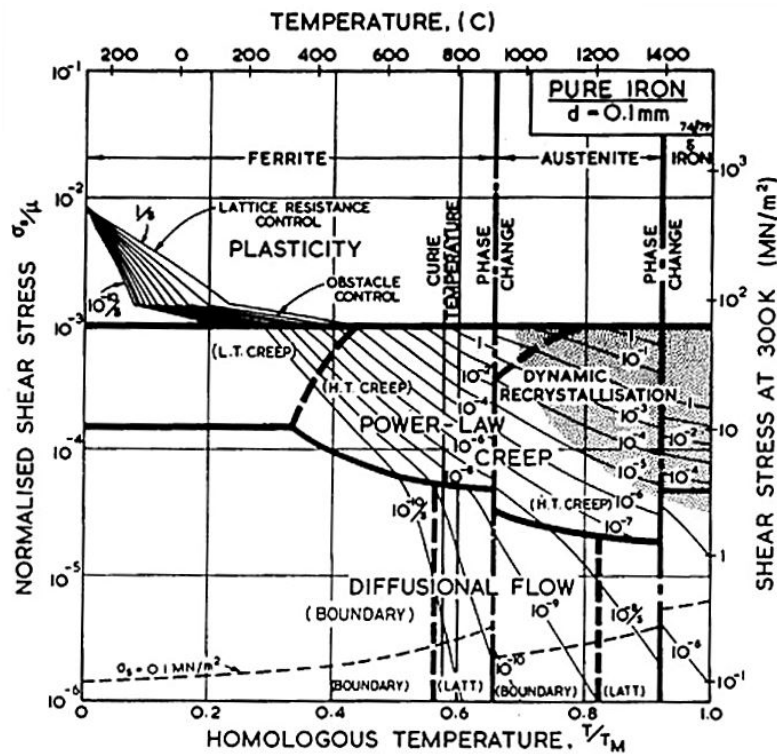


**Figure 1.6:** Deformation mechanism map of pure iron with a grain size of 100 μm (by Frost and Ashby [15]).

### 1.2.3 Grade 91 Steel

#### Specifications

Grade 91 steel, also known as the modified 9Cr-1Mo steel, was co-developed by the Oak Ridge National Laboratory (ORNL) and the former Combustion Engineering (later ABBCE, and currently Alstom) in US in the late 1970s [13]. The original optimum chemical composition window for Grade 91 steel by ORNL is shown in Figure 1.7. The final composition was optimized to achieve the best combination of creep strength, ductility, and toughness. The specification and final chemical composition of Grade 91 steel were established by the ASTM Standard in the early 1980s [13]. The maximum content on Al, Ti, and Zr were changed (or introduced) in the ASME Code in 2006 [13].

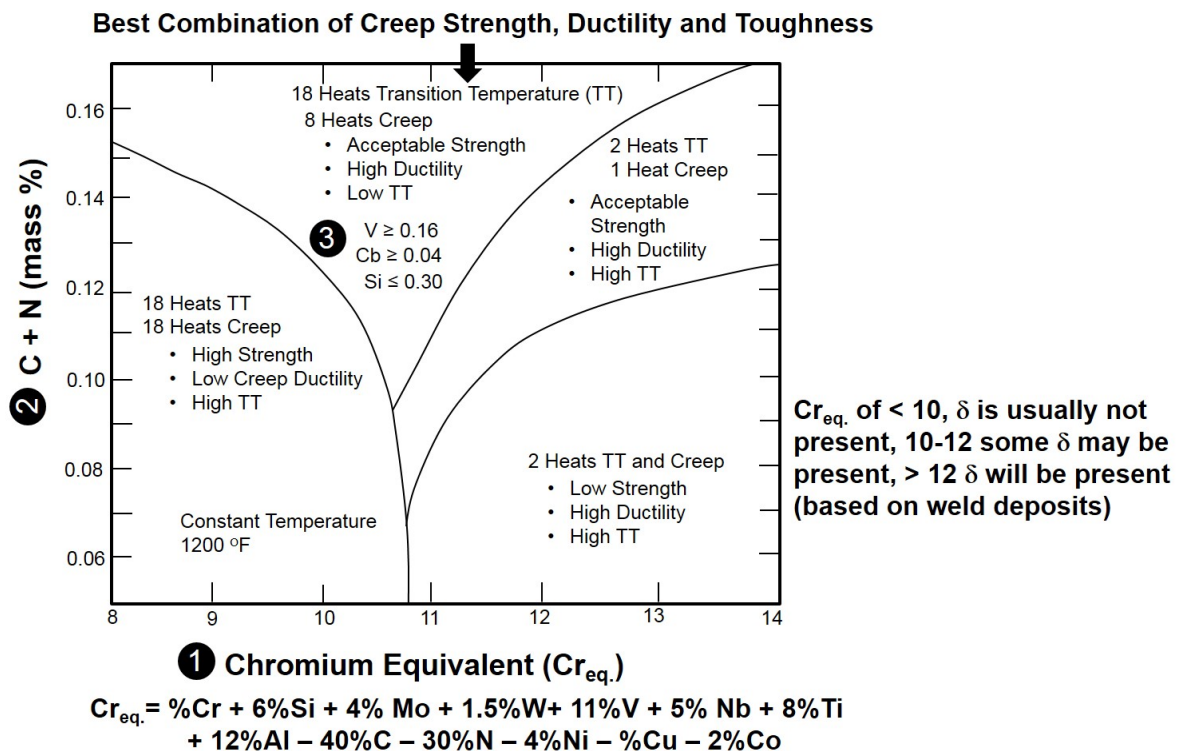


**Figure 1.7:** The original optimum chemical composition window for Grade 91 steel by ORNL (adapted from [13], original by [18]).

**Table 1.2:** Specification of Grade 91 steel in US, Europe, Japan, and China [4,19].

Standard	Designation	Country	Application
ASTM A213	T91	USA	Tubing
ASTM A335	P91	USA	Pipe
ASTM A387	Grade 91	USA	Plate
ASTM A182	F91	USA	Forging
ASTM A217	C12A	USA	Casting
EN 10216-2	X10CrMoVNb9-1	Europe	Tubing, Pipe
EN 10028-2	X10CrMoVNb9-1	Europe	Plate
EN 10222-2	X10CrMoVNb9-1	Europe	Forging
EN 10295	X10CrMoVNb9-1	Europe	Casting
Japanese METI	KA-STBA28	Japan	Tubing
Japanese METI	KA-STPA28	Japan	Pipe
Japanese METI	KA-SCMV28	Japan	Plate
Japanese METI	KA-SFVAF28	Japan	Forging
Japanese METI	KA-SCPH91	Japan	Casting
GB5310-2008	10Cr9Mo1VNb	China	Tubing, Pipe

Grade 91 steel has been used as tubes, pipes, plates, forgings, and castings. The specifications of Grade 91 steel in the USA, Europe, Japan, and China are tabulated in Table 1.2. In USA, there are five ASTM Standards, A213 for tube, A335 for pipe, A 387 for plate, A 182 for forging, and A217 for casting, respectively. The most widely used Grade 91 steels are T91 steel for tubes and P91 steel for pipes. In Europe system, four EN Standards are used to specify tube/pipe, plate, forging, and casting. In Japan, there are also five METI

specifications for each category. In China, GB5310-2008 is the existing national standard used for Grade 91 steel (tube/pipe). The chemical composition of T91 steel and P91 steel specified by the ASTM A213 [20] and A335 [21] is presented in Table 1.3.

**Table 1.3:** Chemical composition requirements of Grade 91 steel (P91) by ASTM A213 and A335 (wt.%).

Materials	C	Cr	Mo	Mn	Si	Ni	Al
T91 steel	0.07-0.14	8.00-9.50	0.85-1.05	0.30-0.60	0.20-0.50	0.40 max.	0.02 max.
P91 steel	0.08-0.12	8.00-9.50	0.85-1.05	0.30-0.60	0.20-0.50	0.40 max.	0.02 max.
Materials	V	Nb	S	P	N	Ti	Zr
T91 steel	0.18-0.25	0.06-0.10	0.010 max.	0.020 max.	0.030-0.070	0.01 max.	0.01 max.
P91 steel	0.18-0.25	0.06-0.10	0.010 max.	0.020 max.	0.030-0.070	0.01 max.	0.01 max.

### Microstructure

Grade 91 steel is a low-carbon martensitic steel. Figure 1.8 shows a continuous cooling transformation (CCT) diagram of Grade 91 steel. It shows that there is no ferrite or bainite formation during continuous cooling from the critical  $A_1$  temperature (810 °C). When the cooling curve hits the martensite-start line, the austenite transforms into martensitic. Martensite-start temperature ( $M_s$ ) is just below 400 °C and martensite-finish ( $M_f$ ) temperature is about 100 °C. Grade 91 steel is considered to have a 100%–martensite structure at ambient temperature. Grade 91 steels are normally used in the normalized-and-tempered condition [22, 23]. Normalizing is performed at 1040–1080 °C to dissolve the nucleated precipitates into matrix [20, 22]. Tempering is performed at 730–800 °C to temper the formed hard martensite and promote the nucleation of fine precipitates [20]. Thus the "as-received" Grade 91 steel has a tempered-martensite structure.

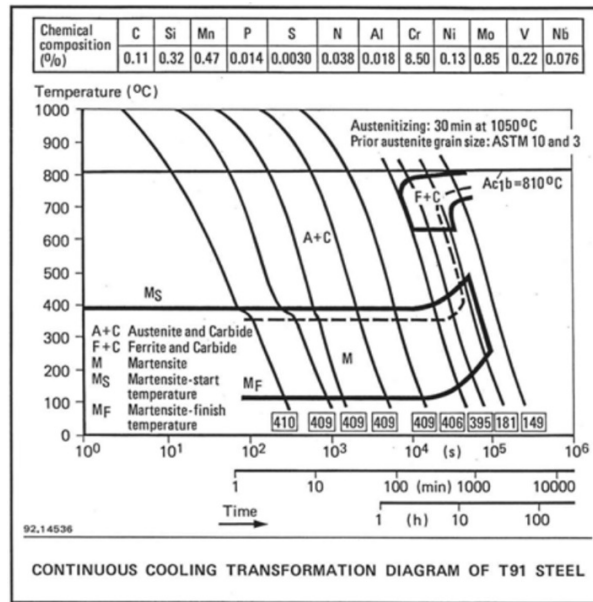


**Figure 1.8:** Continuous cooling transformation (CCT) diagram of Grade 91 steel (T91) [24].

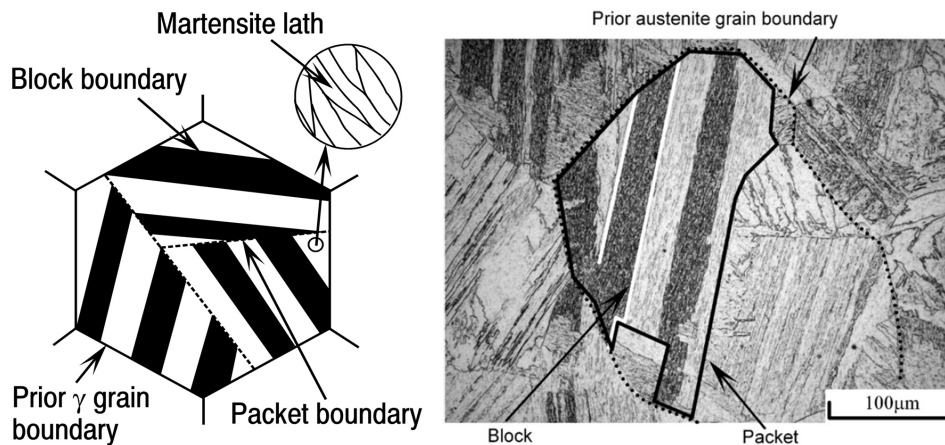


**Figure 1.9:** Multi-boundaries of lath martensite in low carbon steels: (a) Schematic graph [25]; (b) SEM image [26].

After normalizing, martensite forms from the austenite in Grade 91 steel. Martensitic transformation has been studied in massive literatures [25–28]. The morphology of martensite in low carbon steels is lath-like. Multi-boundaries in the lath-martensitic steels include the prior austenite grains boundary (PAGB), packet boundary, block boundary, and lath boundary. The first three are normally high-angle grain boundaries. The lath boundary is low-angle

grain boundary. The schematic and scanning electron microscopy (SEM) structures of lath-martensite in low carbon steels is shown in Figure 1.9. One PAG contains a few packets. One packet consists of several blocks. One block has numerous laths. This multi-boundary structure provides significant boundary strengthening in the Grade 91 steel.

Morito et al. [28] and Kitahara [29] investigated the crystallography and morphology of lath martensite in low-carbon steels by using electron backscatter diffraction (EBSD). Their results show that the orientation relationship between lath martensite and parent austenite follows the Kurdjumov-Sachs (K-S) orientation relationship:

$$(111)_{\gamma} // (011)_{\alpha'} [\bar{1}01]_{\gamma} // [\bar{1}\bar{1}1]_{\alpha'} \quad (1.5)$$

When C concentration is between 0.0026 % and 0.38 %, the sizes of block and packet decrease with the increasing carbon. One packet consists of three blocks with different orientations and each block contains two specific K-S variant groups [28]. Pham et al. [30] evaluated the energetic stability of the boundaries between K-S variants. The K-S variant group with small misorientation up to  $5.5^{\circ} / [001]_{\alpha'}$  has smaller interfacial energy than other K-S variant combinations. Crystallography of the lath martensite in high alloying steels, such as Grade 91 steel, is barely reported. Studying crystallography and morphology of lath martensite in Grade 91 steel helps understanding of its microstructure evolution and creep behavior afterwards.

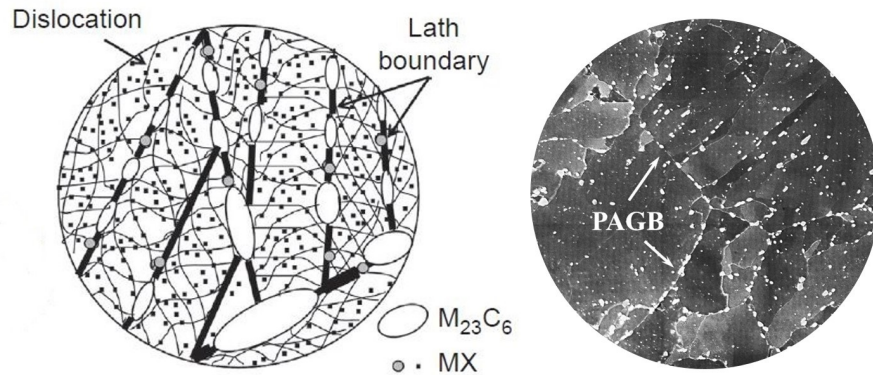


**Figure 1.10:** Precipitate distribution in the martensitic matrix of Grade 91 steel: (a) Schematic graph [3]; (b) SEM image.

**Table 1.4:** Precipitates in Grade 91 steel

Precipitate	Composition	Crystal structure	Distributed locations
M <sub>23</sub> C <sub>6</sub>	Cr <sub>23</sub> C <sub>6</sub> , (Cr, Fe, Mo) <sub>23</sub> C <sub>6</sub>	FCC	PAGB, packet/block/lath boundaries
M <sub>7</sub> C <sub>3</sub>	Cr <sub>7</sub> C <sub>3</sub> , (Cr, Fe, Mo) <sub>7</sub> C <sub>3</sub>	Orthorhombic/Hexagonal	PAGB, packet/block/lath boundaries
MX	V(C,N), Nb(C,N)	FCC	Within martensite lath
Laves phase	(Fe, Cr) <sub>2</sub> Mo	Hexagonal	PAGB, packet/block/lath boundaries
Z phase	(CrVNb)(C,N)	Tetragonal	HAGB after long-term creep

Table 1.4 lists the common precipitates observed in Grade 91 steel. M<sub>23</sub>C<sub>6</sub> carbides (M for Cr, Fe or Mo) and MX carbonitrides (M for V or Nb and X for C or N) are the major ones. Coarse Cr-rich M<sub>23</sub>C<sub>6</sub> carbides distribute along the PAGBs and martensitic packet/block/lath boundaries, and fine MX carbonitrides stay within the martensitic laths. Laves phase, ((Fe, Cr)<sub>2</sub>Mo), an intermetallic compound, is not present in the tempered base metal, but after a long-term creep exposure it precipitates on grain boundaries, especially high angle grain boundaries (HAGBs). Z-phase, abnormally growing on the PAGBs at the expense of MX carbonitrides during long-term creep, is reported to decrease the creep resistance [31–34]. Figure 1.10 shows the schematic and real structure of the tempered martensite in Grade 91 steel. M<sub>23</sub>C<sub>6</sub> carbides distribute along all four types of boundaries. The majority of MX

carbonitrides distribute inside the martensite laths.  $M_{23}C_6$  carbides are much coarser than the MX carbonitrides. The phase fraction of  $M_{23}C_6$  carbides is reported to be around 2 % volume fraction in Grade 91 steel. MX carbonitrides make up about 0.2 % of the volume fraction [4]. Figure 1.11 shows the mean diameter of precipitates in Grade 91 steel during long-term creep at 600 °C and 650 °C [19].  $M_{23}C_6$  carbides coarsened during creep. MX carbonitrides show the highest size stability. A significant coarsening of  $M_{23}C_6$  carbides from 150–180 nm in the as-received condition to 300 nm after creep at 600 °C for more than 100,000-hours is observed in Grade 91 steel [35]. Panait et al. [36] reported there is no significant increase of the size (20–40 nm) of MX carbonitrides in a Grade 91 steel after creep at 600 °C for more than  $10^5$  hours.

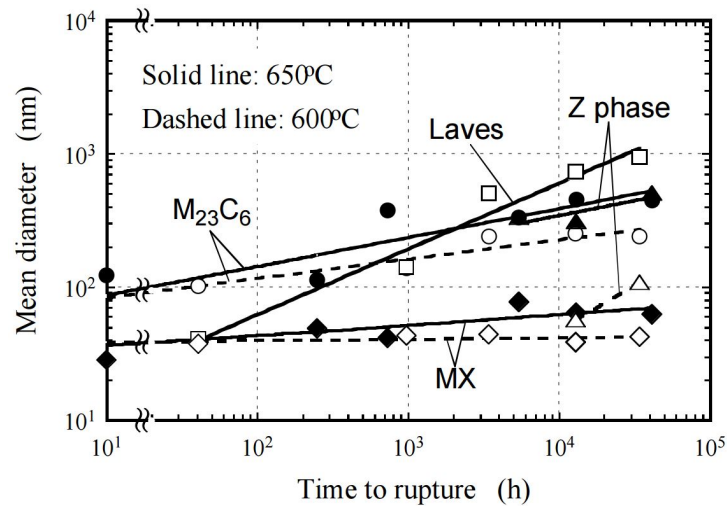


**Figure 1.11:** Precipitate size in Grade 91 steel during creep at 600 °C and 650 °C [19].

Besides the normal tempered martensite structure observed in Grade 91 steel,  $\delta$ -ferrite is also observed in Grade 91 steel, especially in thick heavy sections. During the solidification,  $\delta$ -ferrite is the first phase nucleated from the liquid metal, and then,  $\delta$ -ferrite transforms into austenite during cooling. Due to the high amount of ferrite-stabilizers, Cr, Mo, V, Nb, Si,  $\delta$ -ferrite may not fully transform into austenite. Figure 1.7 indicates  $\delta$ -ferrite will present when the Cr-equivalent is beyond 10. Mayr et al. [37] investigated formation mechanism of  $\delta$ -ferrite

in a 9Cr steel by in-situ X-ray diffraction (XRD) using high energy synchrotron radiation, as shown in Figure 1.12. 2 %  $\delta$ -ferrite was retained when it is cooled to room temperature. The  $\delta$ -ferrite is reported to lower the creep strength of Grade 91 plates [38, 39]. Coarsened precipitates distribute along the boundaries between  $\delta$ -ferrite and tempered martensite [39]. Segregation of alloying elements is observed in  $\delta$ -ferrite [39]. Eliminating or reducing the presence of  $\delta$ -ferrite is normally required to improve creep strength of Grade 91 steel. The mechanism of  $\delta$ -ferrite growth or dissolution in the heat-affected zone has not been reported extensively. Thus it is worthwhile to examine its behavior under the welding thermal cycles.

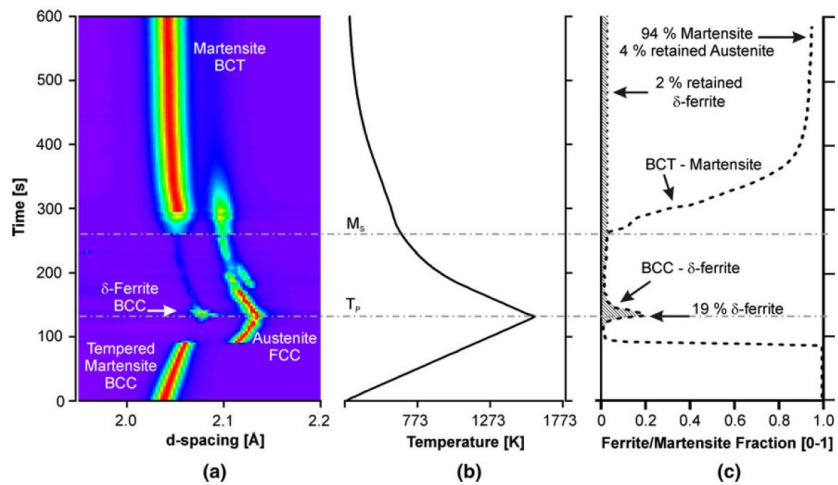


**Figure 1.12:** Study of phase transformation in a martensitic 9 wt pct. chromium steel by in-situ X-ray diffraction (XRD) using high energy synchrotron radiation (heating/cooling rate: 10 K/s) (Mayr et al. [37]).

## Mechanical Property

Mechanical property requirements for Grade 91 steel by ASTM A213 and A335 are tabulated in Table 1.5. The minimum tensile and yield strength are 585 MPa and 415 MPa, respectively. The yield strength of Grade 91 steel can be expressed as:

$$\sigma_y = \sigma_0 + \sigma_{sol} + \sigma_{ppt} + \sigma_{gb} + \sigma_{\rho} \quad (1.6)$$

Where  $\sigma_0$  is the basic lattice hardening,  $\sigma_{sol}$  is the solid solution strengthening,  $\sigma_{ppt}$  is the precipitate strengthening,  $\sigma_{gb}$  is the grain boundary strengthening and  $\sigma_\rho$  is the dislocation strengthening. At the evaluated temperatures, these strengthening mechanisms work together to maintain steel's high creep strength by interacting with dislocations. Maruyama et al. [40] did a review on the strengthening mechanisms of creep resistant tempered martensitic steel.

**Table 1.5:** Mechanical property requirements for Grade 91 steel by ASTM A213 and A335.

Material	Tensile Strength min. MPa (ksi)	Yield Strength min. MPa (ksi)	Elongation in 2 in. or 50 mm min. (%)	Vickers Hardness	Rockwell Hardness
T91	585 (85)	415 (60)	20	196-265 HV	90 HRB-25 HRC
P91	585 (85)	415 (60)	20	196-265 HV	91 HRB-25 HRC

The solid solution strengthening comes from the interstitial solid solute atoms such as C and N and substitutional solute atoms, such as Cr, Mo, and Mn [4, 41]. It is proportional to the square root of alloying concentration ( $\sqrt{C}$ ) [4]. Precipitate strengthening is one of the most important strengthening mechanisms in Grade 91 steel. Precipitates act as barriers and slow down the dislocations cross grain boundaries [36]. The Orowan mechanism is well-recognized by the so-called "Orowan Ring" [4]. The Orowan stress from precipitates is inversely proportional to the inter-spacing between precipitates, which is a function of precipitate volume fraction and size. This quantified relationship can be found in a prior work [42]. Another effect from precipitates is that they slow down recovery of the dislocation substructure and retain the dislocation hardening for longer durations [40]. Grain boundary strengthening is another important strengthening mechanism in martensitic Grade 91 steel. Figure 1.9 shows the multi-scale boundary structures. These boundaries, including PAGBs, packet/block boundaries, lath boundaries and phase boundaries can be climbing obstacles for the movement of dislocations during deformation. The classical Hall-Petch relationship can be

used to quantify this strengthen mechanism [43], but a reliable grain size is quite challenging to measure in martensitic steel. Strengthening from dislocations also plays an important role in maintaining the high creep resistance of Grade 91 steel. Due to the martensitic transformation, a high dislocation density exists in the matrix grains even after tempering heat treatment. It is reported that the dislocation density in the normalized-and-tempered (as-received) Grade 91 steel reaches a magnitude of  $10^{14} \text{ m}^{-2}$  [4, 36, 44].

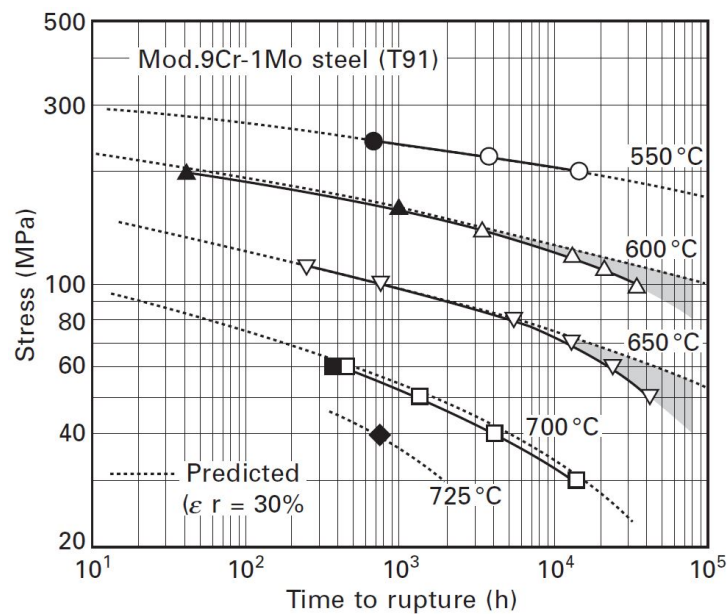


**Figure 1.13:** Creep strength of a T91 steel as a function of creep temperatures [3].

High-temperature creep strength is the most important mechanical property of Grade 91 steels. Figure 1.13 shows creep strength of a T91 steel under different creep temperatures. The  $10^5$ -h creep rupture stress at 550 °C maintains around 200 MPa. The  $10^5$ -h creep rupture stress at 600 °C is about 100 MPa. Once the creep temperature increases beyond 650 °C, the  $10^5$  h-creep rupture stress drops significantly. Loss of creep resistance in Grade 91 steel are caused by the accelerated martrix grain growth and precipitate coarsening at high temperatures.

Many factors that affect creep strength of Grade 91 steel, including concentrations of

alloying elements (C, B, Al, Ni, Cu, S, P, Sn) [41, 45–49, 49, 50], normalizing and tempering parameters [19, 22, 51], have been studied. Abe et al. [41] reported the minimum creep rate increases and the time to rupture decreases with the increasing C content from 0 to 0.05 wt.% in a martensitic 9Cr steel tested at 650 °C and 140 MPa. The time to rupture keeps stable with 0.05–0.15 wt.% C. It is reported that the carbon content at low values (0–0.1 wt.%) affects the precipitation behavior of  $M_{23}C_6$  and MX, and width of martensite laths [45]. Taneike et al. [45] found the absence of  $M_{23}C_6$  when C decreased below 0.002 wt.% and nano-size MX carbonitrides distribute along the grain boundaries. The width of martensitic lath decreases with increasing C content from 0 wt.% to 0.08 wt.%. Liu et al. [52] reported the creep strength of a 9Cr steel is improved by adding boron. B element efficiently slows down the coarsening rate of  $M_{23}C_6$  by B's preferential segregation along PAGBs and lath boundaries and partial replacement of C in  $M_{23}C_6$  carbides. Meanwhile, boron also retards the recovery of the dislocation and delays the grain growth during creep exposure [53]. One challenge of adding B is the formation of BN. B content (< 0.001 wt.%) should be strictly controlled [49]. Magnusson et al. [48] studied the Al content on the creep strength of P91 steel by thermodynamic modeling. Their results indicate that increasing Al content from 0 wt.% to 0.2 wt.% promotes the formation of AlN by consuming VN and the creep strength of the steel decreases. Increasing Ni content up to maximum 0.4 wt.% lowers creep strength of Grade 91 steel due to the enhanced recovery of matrix and tendency to form Z phase [49]. Excessive impurity elements (S, P, Sn) are observed segregating along the subgrain boundaries [49, 50], which reduces creep strength of the steel.

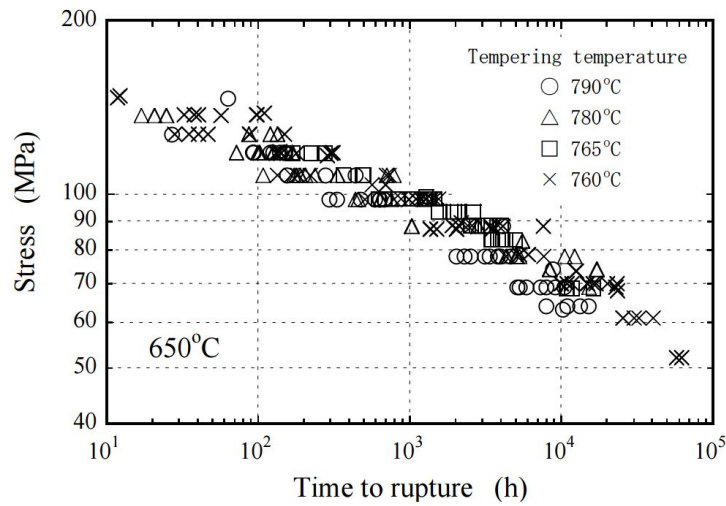


**Figure 1.14:** Creep strength at 650 °C of Grade 91 steel as a function of tempering temperatures [19].

During normalization, the significant microstructural evolutions include austenitization, dissolution of  $M_{23}C_6$  carbides, and homogenization of alloying elements. The normalizing temperature is the key parameter. Totemeier et al. [22] reported the minimum creep rate decreases and the time-to-rupture increases under a creep temperature of 600 °C and a stress level of 145 MPa when the normalizing temperature increases from 850 to 1050 °C. The increasing fraction of transformed austenite (martensite after cooling) with the increasing normalizing temperature is the major contributor to the creep strength improvement. The normalizing temperature should be not too high, otherwise austenite grains grow too fast, which ends with a coarse PAG size. During cooling, wide martensitic laths form at a higher starting-temperature, which lowers creep strength of the steels. Besides the normalizing temperature, tempering temperature has also been reported to affect the final creep resistance of Grade 91 steel. Figure 1.14 shows creep strength of Grade 91 steel as a function of tempering temperatures at 650 °C. The general trend is that the creep stress at the same time-to-rupture decreases with the increasing tempering temperature. The steel after tempering at 760 °C exhibits the longest time-to-rupture (close to 10<sup>5</sup> h). It is believed that excessive coarsening

of  $M_{23}C_6$  carbides is the main reason responsible for this reduced creep strength.

Creep rupture life of Grade 91 steel can be predicted by well-recognized Larson-Miller Parameter (LMP) [54]:

$$LMP = T \cdot (\log t_R + C) \quad (1.7)$$

where  $T$  is the creep temperature (773–973 K) and  $C$  is the Larson–Miller constant. Creep life of this steel decreases with increasing creep temperatures. The Larson–Miller constant  $C$  is a key parameter to predict creep strength. An improper  $C$  may overestimate or underestimate the creep life of steels. It is well known that  $C$  is a function of material itself and creep testing conditions [55]. A wide value range from 20 to 36 of the Larson–Miller constant  $C$  has been reported for Grade 91 steel [22,56,57]. Tamura et al. [55] systematically investigated the Larson–Miller constant  $C$  for 79 heat resistant steels and a recommended Larson–Miller constant  $C$  of 30 was given for Grade 91 steel.

Another well-known formula to predict creep lifetime is the so-called Monkman–Grante (M-G) relationship [58]:

$$\dot{\epsilon}_m^n \cdot t_R = C \quad (1.8)$$

where  $\dot{\epsilon}_m$  is the minimum creep rate,  $t_R$  is the creep rupture time,  $n$  and  $C$  are constants. Constant  $C$  depends on the total elongation of creep [4] and 0.1–0.2 of  $C$  was reported for Grade 91 steel [59]. The minimum creep rate  $\dot{\epsilon}_m$  determines the creep life, which is highly sensitive to applied stress level and internal structures. Degradation of creep strength correlates with the internal microstructure evolution, including recovery and recrystallization of matrix grains, nucleation of new precipitates,  $Z$  phase, and coarsening of precipitates, especially  $M_{23}C_6$ .

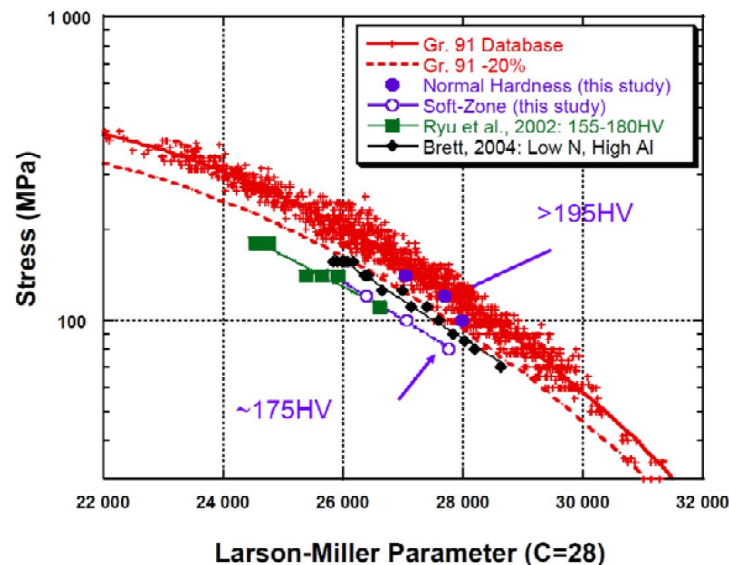


**Figure 1.15:** Creep strength and hardness as a function of creep lifetime [13] (original by [60]).

Hardness is another important property in creep resistant steels. 196–265 HV is required for Grade 91 steel in the ASTM Standard A213 and A335. Hardness can be used as a direct indicator to track microstructural degradation and remaining creep lifetime of Grade 91 steel [61,62]. Figure 1.15 shows the hardness change as a function of creep lifetime. A hardness of about 195 HV means creep strength of the steel is close to its minimum bound of creep rupture strength of 100 MPa. Hardness of 175 HV and under means substantial reduction of creep strength will occur [13].

## 1.3 Welding of Grade 91 Steel

### 1.3.1 Welding Process and Challenge

Welding Grade 91 steel is necessary during fabrication of those steam pipes and headers. Arc welding processes have been widely used in joining Grade 91 steel. A typical thermal cycle for welding Grade 91 steel is shown in Figure 1.16. The typical welding process, filler metal, parameters of preheat, interpass, and post weld heat treatment are listed in Table

1.6. The applied welding processes include gas tungsten arc welding (GTAW), shielded metal arc welding (SMAW), gas metal arc welding (GMAW), flux core arc welding (FCAW), and submerged arc welding (SAW). Codes and guidelines have been published in the the American Welding Society (AWS) and the American Society of Mechanical Engineers (ASME) documents ( D10.10, D10.21, ASME's VIII, B31.1, and B31.3) [7,63]. During cooling, solid-state transformation occurs and a fully martensitic structure forms in the fusion zone, which is highly susceptible to the infamous hydrogen induced cracking (HIC). To avoid the HIC, low-hydrogen consumables are used to weld Grade 91 steel. Typical filler metals for each welding process are presented in Table 1.6. To control the cooling rate of the welds, proper preheat and interpass temperatures should be selected. The preheat temperature is around 150–200 °C and the maximum interpass temperature is around 300–350 °C. A postweld slow cooling (“bake-out”) may be used to prevent the HIC, especially for heavy sections [64].

**Table 1.6:** Typical welding process, filler metal, preheat temperature, interpass temperature, and PWHT temperature used for Grade 91 steel [7, 64].

Welding Process	Filler Metal	Preheat Temperature (°C)	Interpass Temperature (°C)	PWHT Temperature (°C)
SMAW	E9015,16 or 18-B9	Max. 200	Max. 300-350	730-780
GTAW	ER90S-B9	Max. 200	Max. 300-350	730-780
SAW	EB9	Max. 200	Max. 300-350	730-780
FCAW	E91T1-B9	Max. 200	Max. 300-350	730-780
GMAW	ER90S-B9	Max. 200	Max. 300-350	730-780

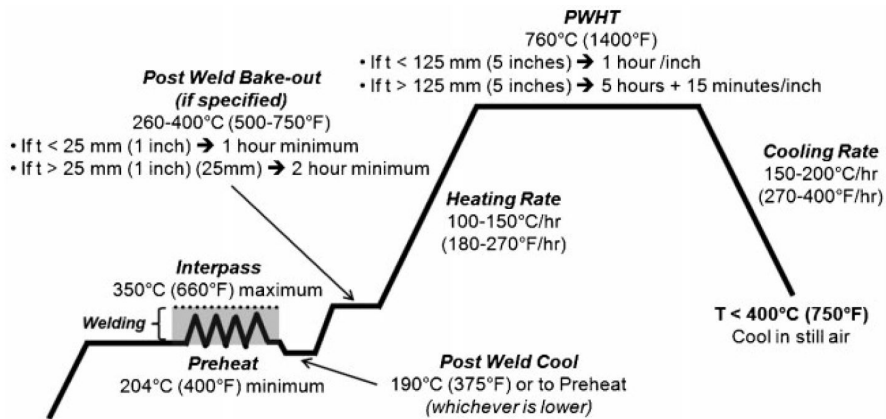


Figure 1.16: Typical thermal cycles for welding Grade 91 steel [7] (original by [65]).

### 1.3.2 Heat-Affected Zone

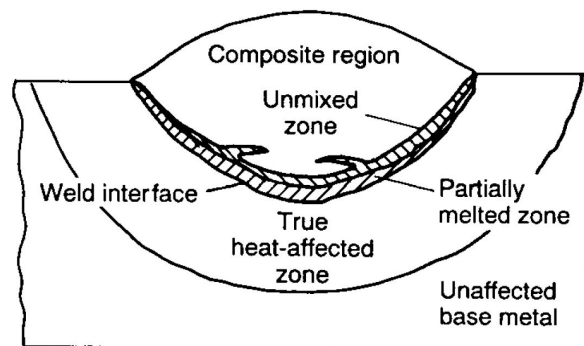
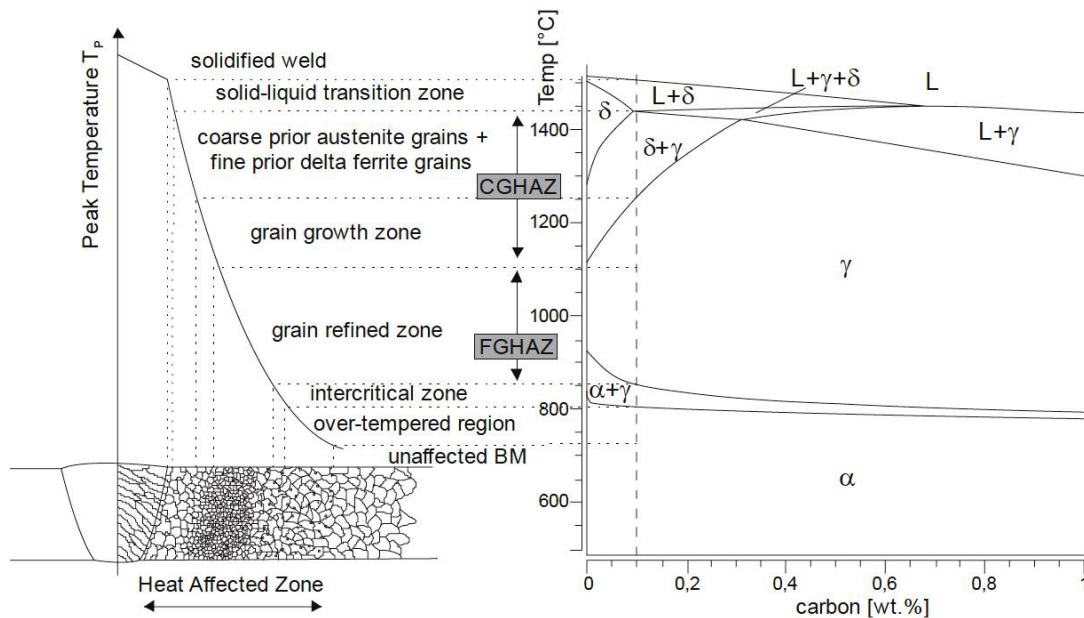


Figure 1.17: Schematic structure in a single-pass weldment [66] (original by Savage [67]).

Figure 1.17 shows a schematic structure of a single-pass weldment. The weldment can be roughly divided into three regions, the solidified fusion zone (FZ) in the center, the heat-affected zone (HAZ) adjacent to the FZ, and the unaffected base metal. The FZ adjacent to the HAZ can be further divided into unmixed zone and partially melted zone. The FZ has a similar composition to the filler metals. The HAZ, unmixed zone, and partially melted zone have the same chemical composition as the base metal.



**Figure 1.18:** Schematic microstructures in HAZ as a function of peak temperatures during welding (from Mayr [68]).

Heat-affected zone is a special region in the weldment. It has the chemistry of base metal and experienced a welding thermal cycle. Every location in the HAZ has its own thermal history (heating/cooling rate and peak temperature), which is different from the conventional thermal cycle for continuous cooling transformation diagram [66]. The heating rate in welding is extremely high and about 300–400 °C/second which depends on the welding process and heat input. The peak temperature ranges from critical  $A_{c1}$  temperature to melting point. Each point in HAZ experiences peak temperatures from a temperature much higher than  $A_{c3}$  (925 °C for Grade 91 steel) to a temperature just above  $A_{c1}$  (818 °C for Grade 91 steel) [69] and cools down to room temperature within a few minutes after thermal cycles. Phase transformations in the HAZ are non-equilibrium, including the diffusive tempered martensite to austenite transformation, diffusionless austenite to martensite transformation, dissolution, nucleation and coarsening of precipitates. A heterogenous structure is formed in the HAZ. A schematic structure in HAZ as a function of peak temperatures during welding is presented in Figure 1.18 [68]. The HAZ is further divided into three sub-regions, coarse-grained HAZ

(CGHAZ), fine-grained HAZ (FGHAZ), and intercritical HAZ (ICHAZ) [70, 71]. The peak temperature ranges and major structural evolutions of these three regions are shown in Table 1.7.

**Table 1.7:** Peak temperature and microstructural evolution in the HAZ subregions

HAZ Subregion	Peak Temperature	Microstructural Evolution
CGHAZ	$\gg A_{C3}$	$\alpha' \rightarrow \gamma$ , $M_{23}C_6$ dissolution, $\gamma$ growth
FGHAZ	$> A_{C3}$	$\alpha' \rightarrow \gamma$ , partial $M_{23}C_6$ dissolution
ICHAZ	$A_{C1}-A_{C3}$	Partial $\alpha' \rightarrow \gamma$ , tempering of untransformed $\alpha'$ $M_{23}C_6$ dissolution and coarsening

### Coarse-Grained Heat-Affected Zone

The CGHAZ is the region experienced a peak temperature from a few hundred degrees higher than the  $A_{c3}$  temperature to the melting point. On-heating, the main microstructural evolution in CGHAZ is the tempered martensite/ferrite to austenite transformation, completely dissolution of the precipitates, and austenite grain growth. For diffusive  $\alpha$  to  $\gamma$  transformation, nucleation and grain growth of austenite in HAZ is closely related to the stability of precipitates at different peak temperatures. The enthalpy of formation of precipitates at room temperature can be used to evaluate their stabilities [70]. The MX (VC, VN, NbC, NbN) carbonitrides have much lower enthalpy of formation ( $< -150$  KJ/mol) than that ( $> 100$  KJ/mol) of the  $M_{23}C_6$  and  $M_7C_3$  carbides, which means MX is more stable than  $M_{23}C_6$  and  $M_7C_3$ . Dissolution of precipitates, especially  $M_{23}C_6$  carbides, accelerates grain growth in the CGHAZ. A homogenization of the dissolved alloying elements also occurs in the CGHAZ. On-cooling, the coarse austenitic grains transformed into martensite in the CGHAZ.

### **Fine-Grained Heat-Affected Zone**

The FGHAZ is the region experienced peak temperatures from just above the  $A_{c3}$  temperature to a few hundred degrees higher than the  $A_{c3}$  temperature. On-heating, low temperature phase tempered martensite/ferrite is also fully transformed into austenite. However, austenitic grain growth is not sufficient due to relative lower peak temperatures. Fine austenitic grains were observed in the FGHAZ.  $M_{23}C_6$  carbides were only partially dissolved. Some  $M_{23}C_6$  carbides even coarsened instead of experiencing dissolution. Coarsening of these un-dissolved precipitates during PWHT and creep is believed to cause creep degradation in the FGHAZ [12, 72]. On-cooling, martensitic transformation also occurred in the FGHAZ. The FGHAZ has been reported as the most-vulnerable region to the Type IV cracking by many researchers [72–74].

### **Inter-Critical Heat-Affected Zone**

The ICHAZ is the region experienced peak temperatures from just above the  $A_{c1}$  temperature to a just below the  $A_{c3}$  temperature. On-heating, partial tempered martensite/ferrite transformed into austenite.  $M_{23}C_6$  carbides were only partially dissolved. Further tempering (recovery/growth) of those un-transformed tempered martensite/ferrite also occurred. On-cooling, austenite transformed into martensite. After welding thermal cycle, a co-existence of newly-formed martensite, tempered martensite/ferrite, coarsened and nucleated  $M_{23}C_6$  carbides, and MX carbonitrides is observed in the as-welded ICHAZ. Strain-free ferrite grains with low dislocation densities were observed in the as-welded ICHAZ [71]. The ICHAZ has also been reported to be responsible for the Type IV cracking by other researchers [12, 75, 76].

### 1.3.3 Post-Weld Heat Treatment

#### PWHT Parameters

Applying a post-weld heat treatment (PWHT) is necessary to reduce the residual stress, to lower the hardness of the FZ and HAZ, and to improve creep strength and toughness of the weldments [77, 78]. The PWHT parameters include temperature and time. Temperature is the critical one. An appropriate temperature helps to balance those mechanical properties mentioned above. When the PWHT temperature is too low, the toughness of the FZ will not increase due to its inefficient tempering effect. The PWHT temperature can not be too high either, otherwise an excessive tempering effect may eventually decrease creep strength of the weldments. AWS Standard D10.10 [79] and ASME Standard B31.1 [80] provide a guideline of PWHT procedures for Grade 91 steels. AWS D10.10 becomes a more practical guideline for performing local PWHT procedures. ASME I & B31.1: Boiler and Pressure Vessel Code requires a PWHT temperature range of 730–775 °C should be followed for Grade 91 steel. Newell et al. [63] further point out that the upper temperature limit is affected by the weld metal composition, especially the total amount of Mn+Ni. Figure 1.19 shows the critical  $A_1$  temperature is a function of Mn+Ni content in Grade 91 steel. Generally, the  $A_1$  temperature decreases with the increasing amount of Mn+Ni content. The highest  $A_1$  temperature can reach 820 ° at a Mn+Ni content of 0.45 wt. %. An the  $A_1$  temperature can be as low as 790 °C. The upper limit of PWHT temperature can be 800 °C when the amount of Mn+Ni is less than 1.0 wt.%. When the amount of Mn+Ni is between 1.0 wt.% and the maximum 1.5 wt.%, PWHT temperature should be controlled within 730– 788 °C [63]. The optimized PWHT parameters of a temperature of 760 °C for 2 hours was reported for Grade 91 pipe steel (P91) by many studies [7, 81]. The ASME Power Piping Code B31.1 [80] specifies the PWHT holding time for Grade 91 steel. 15-min minimum to 1-hour/inch (25 mm) PWHT holding time should be applied for the nominal thickness up to 2 inch (50 mm). When the

nominal thickness is over 2 inch (50 mm), a PWHT holding time of 2 hours plus 15 min for each additional inch should be applied.

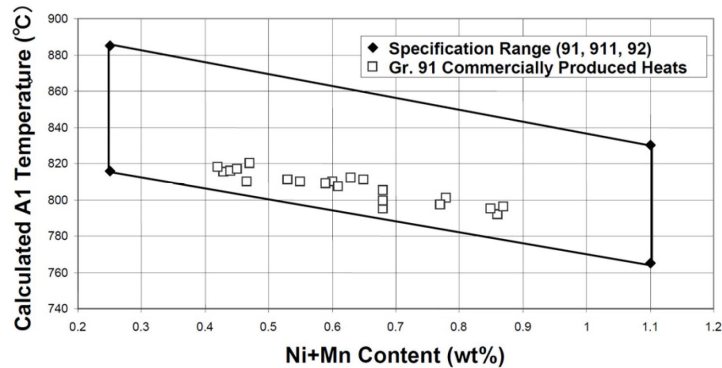


**Figure 1.19:**  $A_1$  temperature as a function of Mn+Ni content in Grade 91 steel [13].

The Charpy impact energy and hardness of Grade 91 steel are a function of PWHT temperatures and times [77, 78]. The general trend is the Charpy impact energy increases and hardness decreases with the increasing PWHT temperature and time. Due to the heterogeneous structures in the HAZ, the subregions of HAZ response differently during PWHT. Silwal et al. [69] studied the toughness and hardness of individual HAZ subregion in P91 steel welds after PWHT at various temperature for 2 hours. Figure 1.20 shows the CGHAZ exhibits the largest impact energy and hardness changes during PWHT. The ICHAZ shows the highest impact energy and the lowest hardness at all PWHT conditions. All three regions exhibit the largest impact energies and the lowest hardness after PWHT at 800 °C for 2 hours.

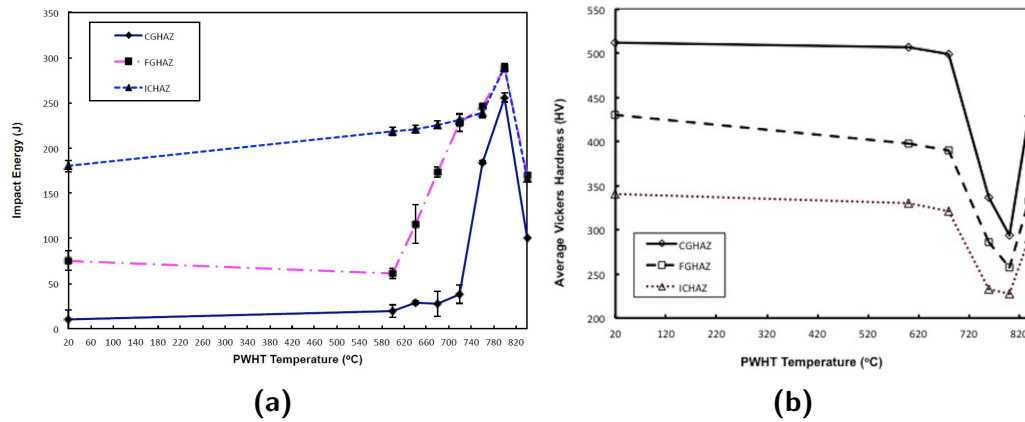


**Figure 1.20:** (a) Charpy impact energies and average Vickers hardness values of different HAZ zones after post-weld heat-treating at various temperatures for 2 hours in Grade 91 steel welds [69].

### Microstructural Evolutions during PWHT

It is well known that the major functions of PWHT includes tempering the microstructure, reducing the residual stress, and increasing toughness by lowering the hardness of the fusion zone and HAZ [7, 77]. However, the heterogeneous as-welded HAZ subregions behavior differently during PWHT. Tempering of untempered martensite by recovering the dislocations is the dominate evolution in the CGHAZ. The large hardness reduction normally observed in the CGHAZ is an evidence for this. Meanwhile, nucleation of  $M_{23}C_6$  carbides also occurs in the CGHAZ. In the FGHAZ, faster grain growth is usually observed in the PWHT-ed sample. This is likely due to the large fraction of recrystallization sites provided by the massive high angle grain boundaries. Coarsening of  $M_{23}C_6$  carbides is also reported in the PWHT-ed FGHAZ. It is known the as-welded ICHAZ has a mixture of newly-formed martensite, un-transformed tempered martensite, and undissolved  $M_{23}C_6$  carbides. More complicated transformations occur in the PWHT-ed ICHAZ. Tempering of those newly-formed martensite, growing of those un-transformed tempered martensite, and coarsening of those undissolved  $M_{23}C_6$  carbides are believed to occur simultaneously in the ICHAZ during PWHT.

## 1.4 Creep Properties of Grade 91 Steel Weldments

### 1.4.1 Macro Creep Rupture

Categorization of creep cracking modes in steel weldments by Schüller et al. [82] is presented in Figure 1.21 [4]. Cracking type is divided by its location and relative orientation within the weldments. Cracks in Type I and II occur in the weld metals. The difference between Type I and II is Type I cracks only stay in weld metal and Type II cracks may propagate into HAZ or even base metal. Both cracking modes are caused by the defects in weld metal, such as un-melted inclusions, pores, microsegregation. Type III cracking, also called reheat cracking, is cracks form in CGHAZ close to fusion line and it may grow into FGHAZ/ICHAZ or base metal. Type III cracking is an intergranular failure due to the segregation of precipitates on the grain boundaries after PWHT, which usually occurs in austenitic stainless steel weldments. Type IV cracking occurs in the narrow FGHAZ or ICHAZ, which is the most common cracking mode in Grade 91 steel weldments.

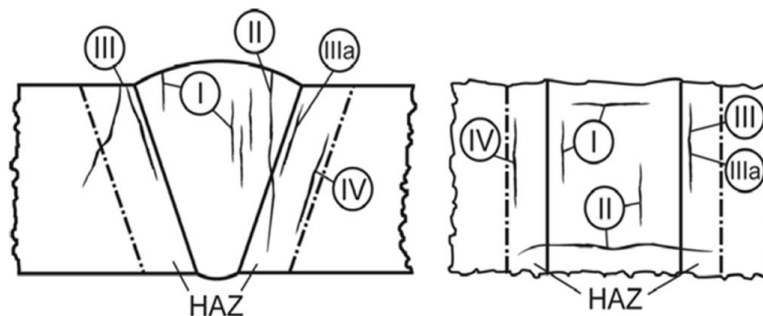


**Figure 1.21:** Schematic drawing of cracking modes in steel weldments [4] (original by Schüller et al. [82]).

### 1.4.2 Formation Mechanisms of Creep Cavities

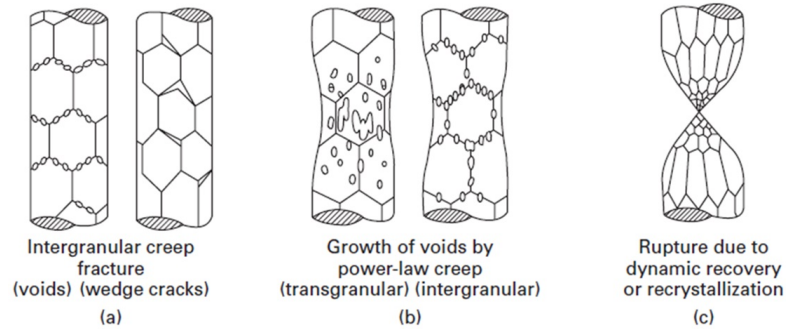


**Figure 1.22:** Schematic drawing of three fracture mechanisms in a high temperature creep regime ( $>0.3T_m$ ) [4] (original by Ashby et al. [83]).

Creep rupture is believed to be caused by the accumulation of creep cavities and micro-cracks. The whole creep cracking process includes the nucleation and growth of fine cavities, connecting of large cavities, formation and growth of micro-cracking, and formation of macro-cracks [84, 85]. Figure 1.22 is a schematic drawing of three fracture mechanisms in a high temperature creep regime, including intergranular creep fracture, mixed intergranular/transgranular fracture by growth of voids, and rupture due to dynamic recovery/recrystallization. Ashby et al. [83] reviewed the fracture mechanism maps for face-center cubic (FCC) metals and alloys. Voids or wedge cracks along the grain boundaries are normally observed in the intergranular creep fracture under low stresses and long-term creep. Grain boundary sliding is considered to be the major mechanism for nucleation of voids and wedge cracks. Growth of voids is by diffusion. Transgranular creep fracture, governed by a power-law creep, occurs when the voids nucleate inside the grains. The inclusions or precipitates inside the grains act as preferential nucleation sites for voids. Rupture due to dynamic recovery or recrystallization at high temperatures is normally observed in FCC metals and most of their alloys [83]. In Grade 91 steel, both intergranular and transgranular failures occur in creep fracture.

### 1.4.3 Type IV Cracking

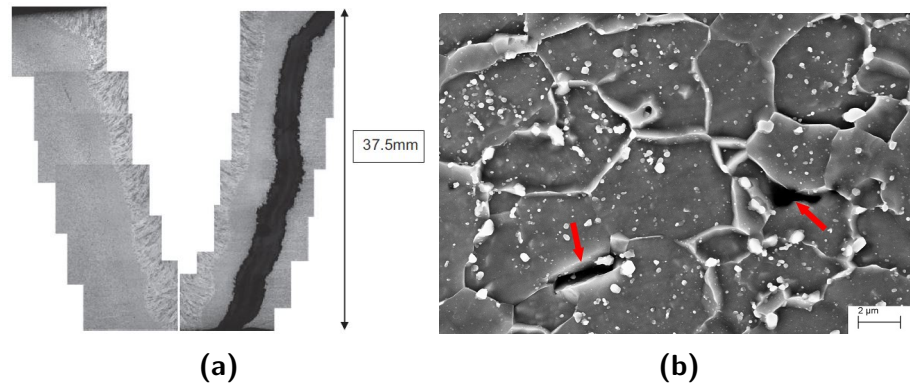


**Figure 1.23:** (a) Optical graph of the Type IV cracking [86] and (b) creep cavities in the Type IV cracking in a Grade 91 steel weldment.

Type IV creep rupture in 9-12 % Cr CSEF steel weldments has been reviewed by Maruyama (2001) [40], Francis (2006) [12], Mayr (2011) [72], Abson (2013) [11], David (2013) [7], Parker (2013) [86] and Abe (2015) [87]. An example of the Type IV cracking in Grade 91 steel weldments is shown in Figure 1.23a. SEM image in Figure 1.23b shows creep cavities formed along the grain boundaries in the cracking regions. It is reported that the Type IV cracking occurred in the outer edge of the HAZ. The susceptible region has been mostly reported in the FGHAZ or ICHAZ. Identifying the exact fracture location of Type IV cracking is challenging with conventional methods, because there is no distinguishable boundary between FGHAZ and ICHAZ. In addition the cracking location is also affected by other factors, such as heat input, groove angle and creep stress level. Which factor is the dominate one is still not clarified. Type IV cracking used to be considered as a “brittle” fracture with a low creep deformation (less than 10 %) of overall gauge length. However, observed large local creep deformation in Type IV cracking indicates the ductile failure character. Parker and Stratford [88] estimated the local creep strain of 20-30 % based on the change of grain shape. It is believed that this high local creep strain is caused by the heterogeneous structures in FGHAZ/ICHAZ. How to quantify this local creep strain and build a relationship with local structures in Type IV

cracking remains a challenge.

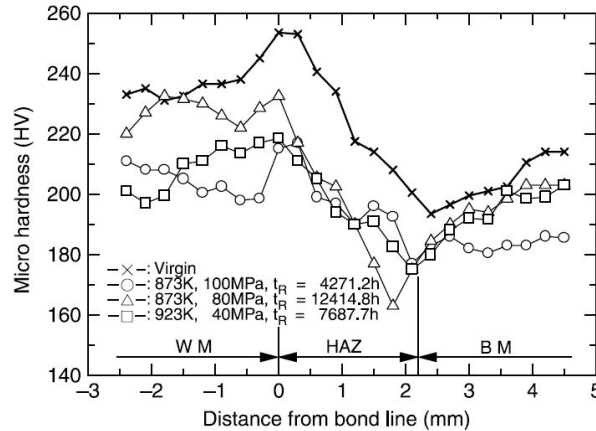


**Figure 1.24:** Hardness distribution in the Type IV cracking in a Grade 91 steel weld after high-temperature creep tests [74].

Many efforts [40, 41, 52] have been made to understand the creep rupture mechanisms of Type IV cracking. David et al. [7] pointed out that determining the weakest region is the major problem to solve the Type IV cracking issue. Hardness measurement is normally used to detect the Type IV cracking susceptible region in the weldments. Figure 1.24 shows a hardness profile across the HAZ in a Grade 91 steel weldments suffering from the Type IV cracking. One common observation of a soft zone in the HAZ has been reported to be highly related with the Type IV cracking by many researchers, as shown in Figure 1.24. Coarse equiaxed grains with low dislocation density and large precipitates in this soft zone has been observed, as shown in Figure 1.25. This soft zone has been correlated to the FGHAZ, ICHAZ, or even over-tempered base metal. To clarify this confusing fact, microstructure and properties of each region need to be well studied. Due to the narrow thickness of each HAZ sub-region, high-resolution tools should be used to quantify their unique structural features.

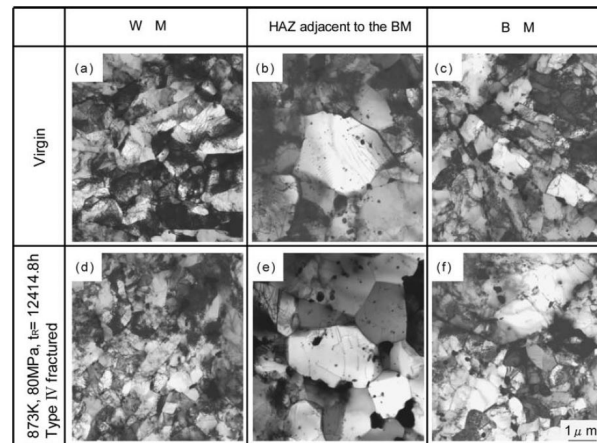


**Figure 1.25:** Structural evolution in the Type IV cracking in a Grade 91 steel weld [74].

Besides the coarsened grains observed in the FGHAZ/ICHAZ, creep cavity density is also higher in the FGHAZ/ICHAZ. These denser cavities cause a degradation of creep resistance in the FGHAZ/ICHAZ. Another observation related with creep cavities is that a higher density of creep cavities (voids) exists in the mid-thickness of the samples. Micro-cracks are firstly observed in the mid-thickness. The HAZ in the mid-thickness has a higher cavity density than in the outer surface [89]. Recently, Li et al. [90] also reported that the ICHAZ with the highest triaxiality factor is more susceptible to the Type IV cracking.

There is a uncertainty remaining on the nucleation time of cavities. Some results show the cavities formed at the primary creep regime. However, other works support the accumulated creep strain in primary creep regime is not high enough to promote formation of cavities and the cavities formed in the secondary creep regime. Besides this uncertainty, there is another conflicting statement of the critical structure factor (coarsening of precipitates or fast grain growth) that leads to lower creep strength in FGHAZ/ICHAZ. Parker [86] claims the local martensitic-transformation-free band is directly responsible for Type IV cracking in Grade 91 weldments. Liu and Abe et al. [52, 91] believe the key to maintaining high creep strength is sufficient boundary strengthening by precipitates. They claimed the undissolved precipitates in FGHAZ/ICHAZ causes a lower concentration of alloying elements,

such as C and Cr in those newly transformed fine austenite grains, which results in the lack of precipitates, especially  $M_{23}C_6$ , along these PAGBs and reduction of the creep strength. Liu et al. [52, 91, 92] reported the elimination of FGHAZ was achieved by adding boron (90 ppm to 130 ppm) in 9Cr-3W-3Co-VNb steel with a reduced nitrogen concentration. They believed the original coarse austenite in base metal were reconstituted through reverse  $\alpha$  to  $\gamma$  transformation during heating and original martensite was also reconstituted during cooling at  $A_{c3}$  in thermal cycle [52, 93]. Coarsening of  $M_{23}C_6$  was retarded by replacing partial carbon with boron in  $M_{23}C_6$ , which stabilizes the recovery and growth of the matrix grains [91]. Thermodynamic study by Song [94] shows the formation enthalpy of  $M_{23}(CB)_6$  is decreased when the carbon is replaced by boron. Why the concentration of boron should be strictly kept from 90 ppm to 130 ppm is still not clarified. Meanwhile, AbdEl-Azim et al. [81] investigated the microstructural instability of FGHAZ of P91 weldments after PWHT and long-term creep at 650 ° C and concluded that the PAG size is the main factor affects the creep behavior of the weldments. They further pointed out the finer the PAG size, as observed in the FGHAZ, the higher the recovery rate of excess dislocations, which leads to higher rates of subgrain growth and precipitate coarsening. A comprehensive understanding about these structural factors, including local martensitic transformation, coarsening of precipitates and recovery/recrystallization of matrix grains, needs to be built to uncover the mechanism of Type IV cracking.

#### 1.4.4 Modeling Creep Behavior of Grade 91 steel weldments

Finite element (FE) modeling is considered a promising approach to predict creep lifetime of a welded joint. Since the secondary creep (steady-state creep) dominates the whole creep lifetime, published research works on modeling creep of the weldments focuses on this stage. The Norton's power law is widely used as the creep constitutive equation in the FE analysis.

Challenges of modeling creep behaviors of a weldment lie in the combination of dissimilar materials, weld metal, HAZ, and base metal. Each materials have their own structures and creep properties. These properties are also a function of PWHT parameters (temperature and holding time) and creep conditions (temperature and stress level). Meanwhile, the HAZ contains sub-regions, CGHAZ, FGHAZ, and ICHAZ. Study of creep behavior of the HAZ is critical because the HAZ usually is the weakest link in the entire weldment. Kimmins and Smith [95] built a simplified strong–weak–strong sandwich model to simulate the WM-HAZ-BM joint and to study its interface stress response under creep. They concluded that a high constraint is built in the weak region when grain boundary sliding is not allowed. If the grain boundary sliding is allowed, this high constraint can be eliminated by the relaxation of interface stress and a large number of cavities nucleated in the weak region which is consistent with the observation in the Type IV cracking. Ogata et al. [89] built a WM-HAZ-BM model and studies the stress distribution in a P91 steel weldment. They pointed out that the triaxial stress states accelerated creep damage evolutions in the HAZ.

To further refine these FE models, creep behavior of each HAZ sub-region should be considered. Due to the narrow thicknesses of each sub-region in the HAZ, creep properties of each region are difficult to obtain directly. To solve this problem, simulated HAZ samples are normally tested instead. HAZ simulation is usually conducted through Gleeble, dilatometer, or other customized furnaces. Shinozaki et al. [96] divided the HAZ into the CGHAZ and FGHAZ in their FE model of a P122 weldment. It is reported that the FGHAZ experienced the highest equivalent strain. Goyal et al. [97] conducted isothermal heat treatment cycles to simulate HAZ samples and to get material properties for each HAZ sub-region. A multi-layer (WM–CGHAZ–FGHAZ–ICHAZ–BM) model and a micro-mechanistic approach were used to investigate the Type IV cracking in a 2.25Cr-1Mo steel weldments. Their results show the ICHAZ experienced the highest stress and strain during creep. Recently Li et al. [90] used stress relaxation tests on simulated Grade 91 HAZ samples through a Gleeble system and

obtained creep properties for each HAZ sub-region. The Type IV cracking was well simulated by inputting these property values into a finite element model. Besides large-scale creep modeling on the entire weldment with creep constitutive equations, meso-scale (grain-scale) creep modeling on the HAZ sub-region, especially ICHAZ, is also significant to understand mechanisms of cavity nucleation and coarsening. More works, such as microstructure-based creep modeling, need to be conducted in this area.

## 1.5 Research Objectives

In this project, microstructural evolution and creep behavior of heat-affected zone in Grade 91 steel weldments are studied. Three main objectives of this research include:

(1) To conduct a detailed microstructural characterization of the HAZ in three successive thermal stages, including the as-welded, post-weld heat treated, and crept. Heterogeneous structures in sub-regions of the HAZ, including matrix grains and dispersive precipitates, are visualized and quantified with advanced microscopy techniques. Non-equilibrium phase transformations in the HAZ, including austenization, dissolution of precipitates, decomposition of delta-ferrite, and martensitic transformation are also analyzed.

(2) To provide a deeper understanding of the infamous Type IV cracking mechanism(s) in 9–12 % Cr creep strength enhanced ferritic steels. A further analysis of the well-characterized structures is to clarify remaining uncertainties in the Type IV cracking, where is it and what is the key responsible structure. Finite element analysis assists in studying local stress and strain distribution in the HAZ during the Type IV cracking.

(3) To evaluate the role of PWHT on structural evolutions of the HAZ and creep rupture behavior of the welds. A correlation between hardness distribution and critical structures is built to compare mechanisms of the Type IV cracking and the Type I cracking. This study is aiming to provide a guidance for welding practice of 9–12 % Cr creep strength enhanced ferritic steels.

# Chapter 2

## Materials and Methodology

### 2.1 Materials

In this study, two Grade 91 steels were used as base metal (BM), Grade 91 pipe steel and Grade 91 heavy section block. Chemical compositions of these two base metals are shown in Table 2.1. The Grade 91 pipe steel (ASTM/ASME A/SA335 P91 [21]) has a 219 mm (8.625 inch) outer diameter (OD) and 29 mm (1.143 inch) thickness. The pipe base metal has been normalized at 1060 °C for 8 min and tempered at 786 °C for 45 min. The Grade 91 heavy section block (ASTM A182 F91 [98]) has dimensions of 127 mm (5 inch) thickness × 228.6 mm (9 inch) width × 304.8 mm (12 inch) length. It had been normalized at 1050 °C for 3.5 h and tempered at 780 °C for 3.5 h following forging.

**Table 2.1:** Chemical composition of Grade 91 base metals and filler metals (wt.%).

Materials	C	Cr	Mo	Mn	Si	Ni	Al	V	Nb	S	P	N
ER90S-B9 GTAW	0.097	8.830	0.928	0.560	0.250	0.307	0.002	0.197	0.064	0.004	0.006	0.030
E91T1-B9 FCAW	0.100	8.830	0.880	0.790	0.280	0.550	0.001	0.200	0.030	0.008	0.020	0.050
Grade 91 Pipe	0.110	8.470	0.940	0.370	0.370	0.080	0.002	0.190	0.071	0.002	0.016	0.048
Grade 91 Heavy Section	0.086	8.890	0.870	0.390	0.330	0.300	0.003	0.220	0.096	0.001	0.020	0.034

## 2.2 Welding and Post-Weld Heat Treatment

### 2.2.1 Welding

Welding of the pipes and blocks was accomplished in our previous project [99]. The used welding parameters are the same for the pipe and heavy section block. Gas tungsten arc welding (GTAW) and flux-cored arc welding (FCAW) were used to deposit the root and filling passes, respectively. The weld joint configuration was a compound-bevel single-groove joint design with a 60° included angle 7/8 high at the bottom of the joint and a 30° included angle maintained through the rest of the joint. ASTM/AWS controlling specifications (AWS A5.28 [100] and AWS A5.29 [101]) and measured compositions of the Grade 91 heavy section block, GTAW filler metal ER90S-B9 (1.2 mm diameter), and FCAW filler metal E91T1-B9 (1.2 mm diameter) are shown in Table 2.1. GTAW parameters used for the root pass were 300 A DC and 1.27 m/min wire feed speed. Deposition of the FCAW filling passes was robotic. FCAW parameters for the filling passes were 1.0 kJ/mm heat input, 0.292 m/min linear travel speed, 27 V arc voltage and 7.62 m/min wire feed speed. The shielding gases used for GTAW and FCAW were pure Argon and mixed 75/25 Argon/ $CO_2$ , respectively. The multiple temper beads were designed to improve toughness of the fusion zone. A preheat temperature of 150 °C and an interpass temperature of 300 °C were selected to avoid common cracking issues, especially the hydrogen-induced cracking (HIC). A 4-hour post-weld bake was also conducted at 400 °C to avoid the HIC.

### 2.2.2 Post-Weld Heat Treatment

Post-weld heat treatment of the weldments was performed in a Cress electric furnace Model C162012/SD. Type-K thermocouples with Pico USB TC-08 data loggers were used to keep the temperature precise in the furnace. The PWHT procedures were following the guidelines of

the ASME B31.1 [80]. The Grade 91 pipe weldments were PWHT-ed at various temperatures and times (600 °C, 760 °C, 820 °C, 840 °C for 2 hours and 8 hours). All PWHT-ed specimens were air-cooled.

## 2.3 Mechanical Property Measurement

### 2.3.1 High-Temperature Creep Test

High-temperature creep tests were performed on the Grade 91 pipe weld joints after PWHT and the as-received base metal. Cross-weld specimens for creep test were extracted from the center of the weldments after PWHT. This cross-weld specimen includes FCAW weld metal, and HAZs on both sides of the weld metal, and the base metal. The rectangular-cross section creep specimen had a cross section of 8.8 × 12.7 mm and an effective gauge length of 84 mm. Creep test was conducted at applied test temperature of 650 °C and engineering stress of 70 MPa (10 ksi). Creep test procedure was conducted following the standard test procedures guided by ASTM E139-06 [102].

### 2.3.2 Hardness Test

#### Vickers Hardness Test

Vickers hardness was measured by using the Wilson VH3300 and Tukon 2500 automated hardness testing systems. A low loading force of 0.5 kgf, a dwell time of 10 seconds, and an inter-spacing of 150 μm were used for hardness data acquisition. Hardness line scanning (Line length: 40 mm) was conducted across the entire weldments at the mid-thickness under the as-welded condition and after PWHT. Microhardness mapping (area: 4.5 mm × 1.5 mm, perpendicular to the fusion line) were conducted on both HAZ specimens under the as-welded condition, after PWHT, and after creep tests. Individual indentations were also used

to measure the hardness in some specific locations, for example  $\delta$ -ferrite grains. Hardness contour maps and the average hardness profiles were post-processed from hardness mapping data sets.

### **Instrumented Indentation Test**

Instrumented indentation test was introduced in 1992 to measure hardness and elastic modulus [103]. Now it has been widely used to evaluate mechanical properties in small scales. Hardness and elastic modulus are measured from the load–displacement curve. The load–displacement curve contains one loading process and one unloading process. Three important parameters, the maximum load  $P_{max}$ , the maximum displacement  $h_{max}$ , and the unloading elastic stiffness  $S=dP/dh$ , are obtained from the load–displacement curve. Calculation of the hardness  $H$  and Young's modulus  $E$  is introduced in Ref. [103]. Instrumented indentation tests were used to evaluate creep behavior of individual HAZ sub-region and to measure their hardness and Young's modulus at room temperature. The tested HAZ samples include one as-welded sample, one PWHT-ed sample, and one sample after creep tests. The used maximum load is 500 mN. The loading and unloading rates are 25 mN/s. The creep (holding) time is 10 seconds.

## **2.4 Microstructure Characterization**

### **2.4.1 Optical Microscopy**

For microstructure characterization, the HAZ specimens were mounted, ground, and polished by using an automatic mechanical polisher. Grit 360, 600, and 1200 SiC sand papers were used for grinding.  $3\ \mu\text{m}/1\ \mu\text{m}$  diamond suspensions,  $0.5\ \mu\text{m}/0.05\ \mu\text{m}$  alumina suspensions, and  $0.02\ \mu\text{m}$  colloidal silica suspension were used for polishing. After polishing, the samples

were cleaned by an ultrasonic machine for 10 min and dried with compressed air. The polished specimens for optical and electron microscope analysis were etched with 10% Nital for 2 to 20 min. Two optical microscopes, Nikon Eclipse MA200 Inverted Microscope and Olympus BX53 Upright Metallurgical Microscope, were used for optical examinations. Both bright-field and dark-field images were captured under magnifications from X50 to X1000.

### **2.4.2 Field-Emission Scanning Electron Microscopy**

Microstructure characterization of the HAZ specimens was conducted on a Zeiss Sigma Field-Emission Scanning Electron Microscopy (FESEM). This FESEM is equipped with a secondary electron detector, an Inlens secondary electron detector, a backscattered electron detector, an energy dispersive spectroscopy detector, and an electron backscatter diffraction detector. Secondary electron detector and Inlens secondary electron detector were used for surface morphology analysis. The backscatter diffraction detector was used to distinguish light and heavy elements with different atomic Z numbers. The energy dispersive spectroscopy detector was used for chemical analysis. The electron backscatter diffraction detector was used for phase identification and crystal orientation measurement.

### **2.4.3 Energy Dispersive Spectroscopy**

Energy Dispersive Spectroscopy (EDS) captures characteristic X-rays that are generated from the specimens when the electrons in the beam interact with the atoms [104]. These characteristic X-rays have specific energies for each element, which is used to determine different elements in the samples. The intensities of these characteristic X-rays are used to quantify concentration of each element. The EDS analyses were conducted on the specimens with a Zeiss Sigma FESEM equipped with an X-Max 150 EDX system under 20 kV accelerating voltage, 60  $\mu\text{m}$  objective aperture, and a work distance of 8.5 mm. The Oxford AztecSynergy

software was used for EDS data acquisition. Both point analysis and element distribution analysis by line scanning and mapping were conducted on the samples.

#### 2.4.4 Electron Backscatter Diffraction

Electron backscatter diffraction (EBSD) technique, an electron microscopy-based technology, has been widely used for identifying phases and measuring crystal orientations [105, 106]. EBSD determines the phase/orientation by measuring the width and angle of the Kikuchi bands generated from the interaction between beam electrons and atoms in the samples. The EBSD analyses on the HAZ were conducted on a Zeiss Sigma Field-Emission SEM (FESEM) equipped with an Oxford AZtec system under 20 kV accelerating voltage, a 60  $\mu\text{m}$  objective aperture and step sizes of 0.05-1.0  $\mu\text{m}$ . The polished sample is tilted into 70°. The BSD and secondary electron detectors were used for imaging. The EDS and EBSD detectors work together to get chemical data and EBSD data simultaneously. The EBSD analyses are conducted based on indexing the 8-11 characteristic Kikuchi bands of crystal orientations and phases. HKL Crystal Structure Database and Inorganic Crystal Structure Database (ICSD) were used for EBSD data acquisition. Post-processing of the EBSD data (reconstructed map) was conducted by using the HKL Channel 5 software package and the ATOM software.

EBSD is an ideal tool to visualize the crystal orientations and phase distribution. Quantitative information, such as phase fraction, grain size, grain boundary distribution, local strain distribution, texture, can be also obtained from EBSD data. In this work, matrix grain orientation was interpreted by the inverse pole figure (IPF) in Z direction (transverse direction, perpendicular to the screen) and all-Euler maps. Low angle grain boundaries (LAGBs, misorientation  $\theta$  below 10°) and high angle grain boundaries (HAGBs, misorientation  $\theta \geq 10^\circ$ ) were distinguished by the scalar misorientation between the adjacent pixels. Grain size of the matrix grains was measured from the grain boundary maps with line-intercept method. Due

to a small distortion in the lattice parameter  $c$  by the low carbon content (below 0.2 wt.%) in the base metal, the martensite matrix is treated as the body-center-cubic (BCC) iron.

Misorientation maps were processed to evaluate and visualize the local strain or deformation magnitude within grains by calculating the kernel average misorientation (KAM) between groups of pixels/kernels within the grains. The GAM is the average misorientation between each neighboring pair of the measured pixels within each grain, which evaluates the local strain of individual grain [106–108]. The internal average misorientation angle within the grain and misorientation between subgrains was measured to categorize the grains. To distinguish the local strain energy difference, matrix grains were classified into recrystallized, substructured, and deformed grains by grain average misorientation (GAM) evaluation with a threshold of  $1^\circ$ . Details of the GAM evaluation is introduced in a previous work [109].

### 2.4.5 Auger Electron Spectroscopy

Auger electron is generated from the surface (about 5 nm in depth) of samples. Auger Electron Spectroscopy (AES) analysis has the advantages of high sensitivity to light elements (such as C, B, O) and high resolution of element concentration difference. Local chemistry analysis was conducted on the as-received base metal and HAZ samples by using the Auger Electron Spectroscopy (JEOL-9500F). The accelerating voltage and emission current for both the SEM and Auger imaging were 10 kV and 10 nA, respectively. Ar sputtering was applied for 60 seconds after the secondary electron imaging and before acquiring the maps to ensure the surface was free from any contamination. The intensity of each pixel in the Auger image was calculated by  $(P-B)/B$ , where  $P$  and  $B$  are the peak and background intensity, respectively. Such intensity definition helps to reduce the edge effect of islands and dots in the microstructure. Point and mapping analyses were conducted to determine element concentration differences in local areas. Mapping of C, Cr, and Fe was on the ICHAZ in three

thermal conditions.

### 2.4.6 Image Analysis with ImageJ

ImageJ software is a powerful and open-source tool used for image analysis [110]. In this work, ImageJ was used for image post-processing, including image format conversion, contrast/brightness adjustment, resizing. Grain size and precipitate size measurements were also conducted with ImageJ.

## 2.5 Thermodynamic Calculation

Thermodynamic calculations were performed using the ThermoCalc<sup>TM</sup> (2016a version) with the TCFE6 database. The equilibrium phase fraction as a function of temperature of the two Grade 91 steel base metals and FCAW filler metal were calculated, respectively. The phases of liquid, BCC-iron, FCC-iron,  $M_{23}C_6$  carbide,  $M_7C_3$  carbide, MX carbonitride, Z-phase, and Laves phase were taken into consideration. Gibbs free energy, equilibrium phase transformation temperature, the isopleth of phase diagram of the Grade 91 steel base metals were also calculated.

## 2.6 Dilatometry

Dilatometry is a well-established technique to study solid-state phase transformation during continuous heating or cooling [111]. The length change of the sample, caused by phase transformations is precisely detected and recorded by a dilatometer. The recorded data can be used to quantify the phase transformation start/finish temperatures, such as  $A_{c1}$ ,  $A_{c3}$ ,  $M_s$ ,  $M_f$  and the transformed phase fraction as a function of temperature. The ASTM A1033-10 [111] describes details of this method. To quantify the phase fraction of the transformation,

the typical line-drawing method is described in the ASTM A1033-10 [111]. Recently a new mathematical method by using dilation curve analysis to quantify phase fraction was proposed by Gibbs and Kamyabi-Gol [112, 113]. Their results show a good consistence with the line drawing method. In this work, this dilation curve analysis was used to quantify the phase fraction of martensitic transformation in the dilatometer-simulated HAZ specimens.

The HAZ simulation experiments were conducted by using a RITA L78<sup>TM</sup> high-speed quench dilatometer for both the pipe and block. The specimen size used in this study is  $\Phi$  4 mm  $\times$  10 mm length. To simulate the microstructure of HAZ sub-regions, the specimens were heated with a heating rate of 100 °C/s to various peak temperatures and cooled down to room temperature with a cooling rate of 20 °C/s. To analyze the effect of carbide dissolution on martensitic transformation, a set of specimens from the pipe were heated up to a peak temperature of 1060 °C for different dwell times, 1 s, 30 s, 60 s, 120 s, 300 s, and 600 s. To investigate the dissolution mechanism of  $\delta$ -ferrite, a set of specimens from block were heated to different peak temperatures, 930 °C, 1060 °C, and 1360 °C.

## 2.7 Finite Element Analysis

Finite element analysis were conducted with the commercial simulation software Comsol Multiphysics<sup>®</sup> to investigate creep response of the weldments after different PWHT conditions. A model consisting of multiple materials, including weld metal, CGHAZ, FGHAZ, ICHAZ and base metal, was built. The mechanical properties of each HAZ sub-region were obtained from a previous work from our group. The Norton's law was used as the constitutive creep mechanics to study the stress and strain distribution in the weldments. A simplified microstructure-based model was also built to study the local stress levels in the ICHAZ during creep tests. The model was extracted from a SEM image by using a Matlab code. The model was studied in the Comsol software.

# Chapter 3

## Microstructure Analysis of As-Welded Heat-Affected Zone in Grade 91 Steel Weldments

### 3.1 As-Welded Grade 91 Pipe Weldment

#### 3.1.1 Characterization of the as-received P91 base metal

A typical microstructure of the as-received P91 BM is shown in Figure 3.1. It has a characteristic tempered lath-like martensite structure in which relatively coarse precipitate (mainly  $M_{23}C_6$ ) along the prior austenite grain boundaries (PAGBs) and martensite packet/block boundaries and fine precipitates homogeneously disperse within the martensitic laths. Fine (V, Nb)(C, N)-type MX carbonitrides homogeneously precipitate within the blocks or on the block boundaries. Measured prior austenite grain size is  $17.9 \mu\text{m}$  with a standard deviation of  $5.02 \mu\text{m}$ . Martensitic blocks with an average size of  $2.1 \mu\text{m}$  are the main substructures within the prior austenite grains. The  $M_{23}C_6$  carbide has an average size of  $144 \text{ nm}$ , and the MX carbonitride has an average size of  $35 \text{ nm}$ .

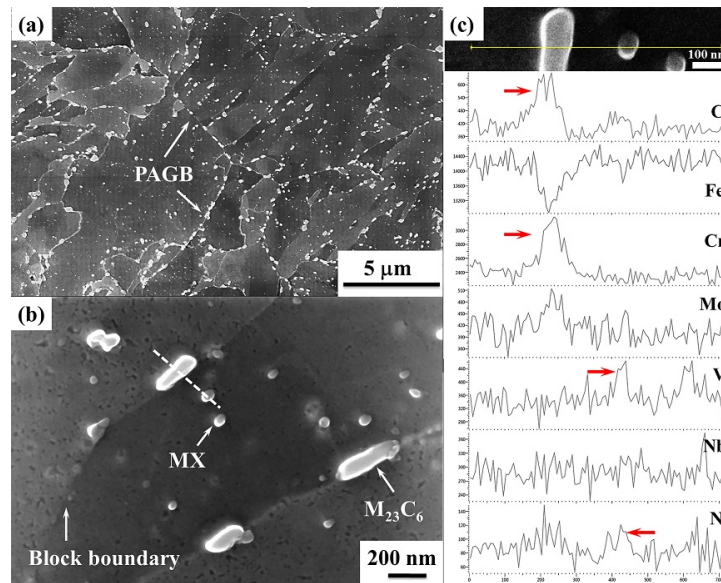


**Figure 3.1:** Typical microstructure of the as-received P91 base metal: (a) In-lens secondary electron image; (b) Magnified image; (c) EDS line scanning across two precipitates marked in (b).

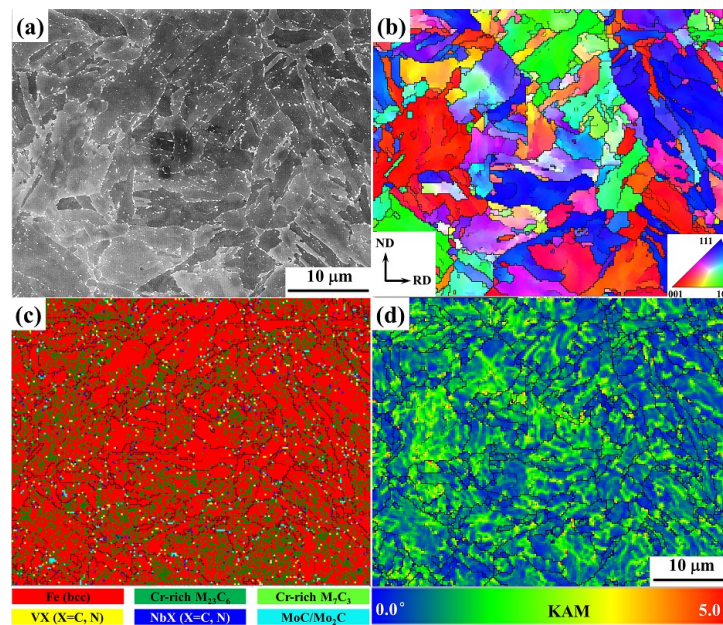


**Figure 3.2:** EBSD analyses of the as-received P91 base metal: (a) In-lens secondary electron (SE) image. (b) Z axis inverse pole figure. (c) Phase map. (d) Kernel average misorientation map.

Results of the EBSD analyses on the as-received BM are presented in Figure 3.2. There are large variations of martensitic block width and length, varying from less than one micrometer

to a few micrometers. Inverse pole figure (IPF) in Figure 3.2b shows the large orientation variations of those tempered martensite in the BM. Phase map in Figure 3.2c illustrates Cr-rich  $M_{23}C_6$  carbides are the main precipitates, distributing along the boundaries (PAGBs, blocks) and inside blocks. However, there is a large density variation of precipitates between blocks. Some blocks contain dense  $M_{23}C_6$  carbides and other blocks have fewer precipitates. MX carbonitrides show a lower fraction and are homogeneously dispersed within the blocks. Kernel average misorientation map (KAM) in Figure 3.2d shows the inhomogeneous distribution of the local strain between the fine blocks and the coarse blocks, with the fine blocks showing a smaller strain and coarser blocks showing a higher strain.

### 3.1.2 Microstructure evolutions in the HAZ regions

Figure 3.3 presents the macro-etched GTAW root pass and multiple FCAW filling passes of the as-welded P91 weldment. FCAW beads in the fusion zone are partially tempered by subsequent beads. The heat affected zone (HAZ) along the fusion line has a uniform width of 3 mm. The typical microstructure of the as-welded HAZ regions marked by rectangle 1 in Figure 3.3 is shown in Figure 3.4. The non-equilibrium HAZ clearly consists of three different sub-zones, including the CGHAZ, FGHAZ, and ICHAZ, as shown in Figure 3.4a. Coarse PAGs with an average size of 20  $\mu\text{m}$  in the CGHAZ are shown in Figure 3.4b. Fine PAGs with an average size of 5  $\mu\text{m}$  in the FGHAZ are shown in Figure 3.4c. The ICHAZ close to the BM consists of a mixture of newly-formed PAGs and coarse tempered grains, as shown in Figure 3.4d.

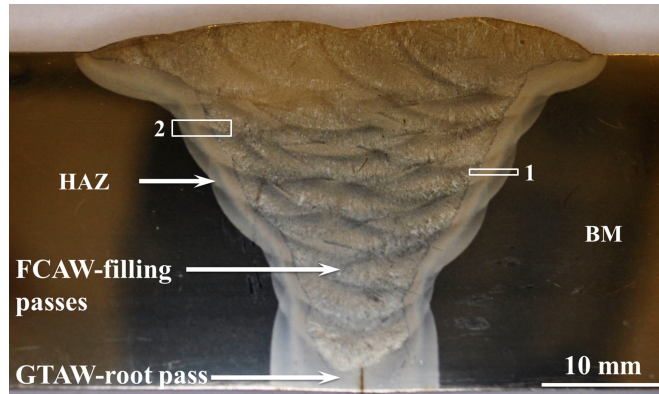


**Figure 3.3:** Optical cross-section of a P91 steel weldment showing fusion zone, HAZ, and BM.

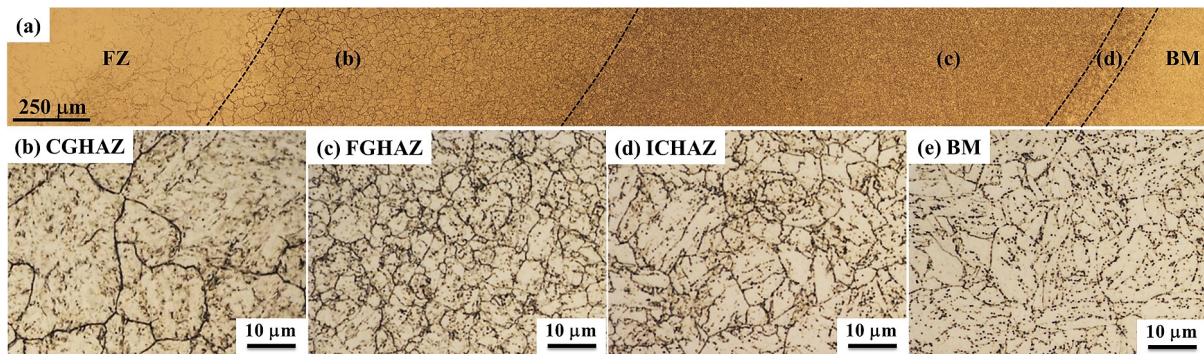


**Figure 3.4:** Microstructure of the HAZ in an as-welded P91 weld marked by the rectangle 1 in Figure 3.3: (a) Overview of the HAZ from the FZ to BM; (b) CGHAZ; (c) FGHAZ; (d) ICHAZ; (e) BM.

Figure 3.5 shows microstructure variations in the CGHAZ, FGHAZ, and ICHAZ. Figure 3.5a1 shows martensitic laths within the coarse equiaxed PAGs in the CGHAZ. Due to higher peak temperatures (much higher than  $A_{c3}$ ), the BM transformed to coarse austenite grains along with the dissolution of former  $M_{23}C_6$  in the CGHAZ during the heating cycles. Figure 3.5a3 shows that the martensitic lath with a higher length/width ratio is the typical substructure in the PAGs. Fine  $M_{23}C_6$  carbides preferentially nucleate on the high-energy boundaries like the PAGBs, lath boundaries, and within some particular laths, as shown in Figure 3.5a3.

Figure 3.5b1 presents a fine equiaxed PAG structure in the FGHAZ. The substructure within these fine PAGs is martensitic laths with a lower length/width ratio, as shown in Figure

3.5b2. Former tempered martensite transformed to austenite without further growth, because the FGHAZ is exposed to a peak temperature  $T_p$  just above  $A_{c3}$  and a short soaking time. Precipitates, especially coarse  $M_{23}C_6$  carbides, do not get enough time to be completely dissolved, as shown in Figure 3.5b2 and Figure 3.5b3. Then undissolved particles further coarsen during the welding thermal cycle. Figure 3.5b3 shows the majority of the undissolved  $M_{23}C_6$  carbides are trapped within the new PAGs. The fine newly-formed  $M_{23}C_6$  distribute on the PAGBs and within some laths in Figure 3.5b3. The ICHAZ presents a mixed structure of new PAGs and retained tempered martensite in Figure 3.5c1. The large size variations of blocks in the BM shown in Figure 3.2b cause this heterogeneous austenitic transformation in the ICHAZ. The undissolved  $M_{23}C_6$  carbides are also observed in the new PAGs, shown in Figure 3.5c2. Figure 3.5c3 shows further tempered martensite and coarsened  $M_{23}C_6$  carbides.

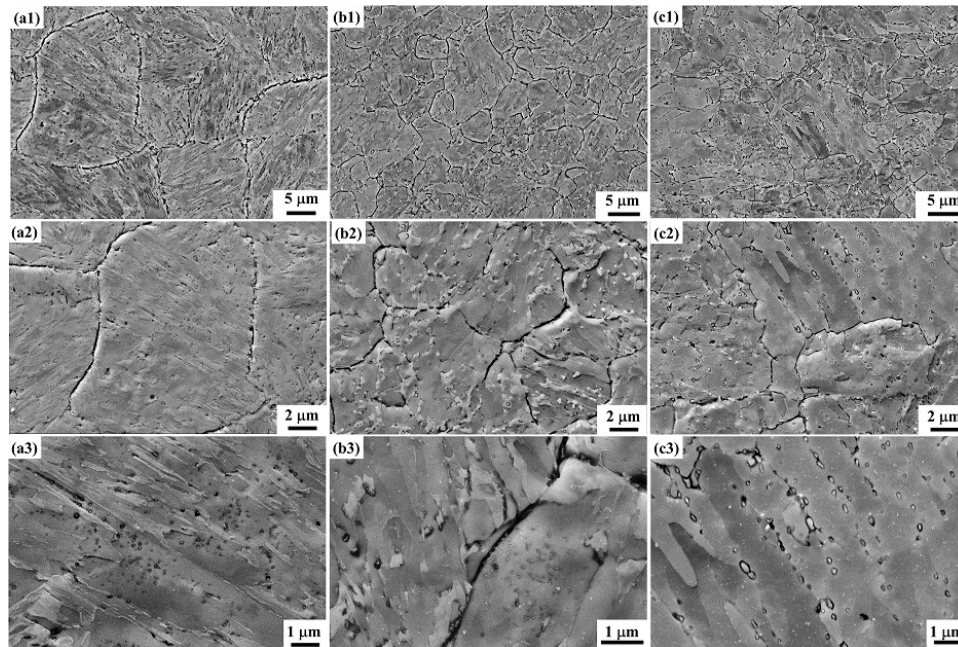


**Figure 3.5:** Microstructure of HAZ in an as-welded P91 weld: (a1), (a2), and (a3) are the CGHAZ. (b1), (b2), and (b3) are the FGHAZ. (c1), (c2), and (c3) are the ICHAZ.

Microstructure of the as-received BM and ICHAZ is compared in Figure 3.6. The PAGBs were determined from the lower-magnified SEM images and optical images, according to the

orientation of martensitic laths and the distribution frequency of precipitates. PAGBs in the tempered BM have migrated, therefore, are not revealed by the Nital etch, but rather are defined by the strings of larger retained  $M_{23}C_6$  carbide particles, as shown in Figure 3.6a. Within these former PAGs are the elongated tempered martensitic blocks. This structural feature is summarized in a sketch in Figure 3.6b. In comparison, those newly formed PAGBs in the as-welded ICHAZ are clearly revealed by the Nital etch. The former PAGBs are still not revealed by Nital etch, but can be reconstructed by tracking the retained  $M_{23}C_6$  carbides on whiter Cr-rich boundaries (indicated by the string of white arrow in Figure 3.6d). The etched continuous boundaries are easily identified as the PAGBs, rather than block boundaries or lath boundaries. By tracking the parallel, retained, precipitates in the middle of Figure 3.6d, the partial austenitic transformation is confirmed. Meanwhile, the equiaxed shape of those newly formed PAGs differs from the the rectangular shape of the tempered martensitic blocks, as shown in Figure 3.6d. Fine martensitic blocks with a short length and small width are observed in the new PAGs (Figure 3.6d). By tracking the locations of former and new PAGBs, austenitization is found to have preferentially nucleated from the former PAGBs. Occasional overlapping of the former PAGBs and new PAGBs is also observed. The microstructure features of ICHAZ are summarized in a sketch in Figure 3.6e. Schematic phase transformation in ICHAZ from BM is also illustrated in Figure 3.6c and 3.6f.

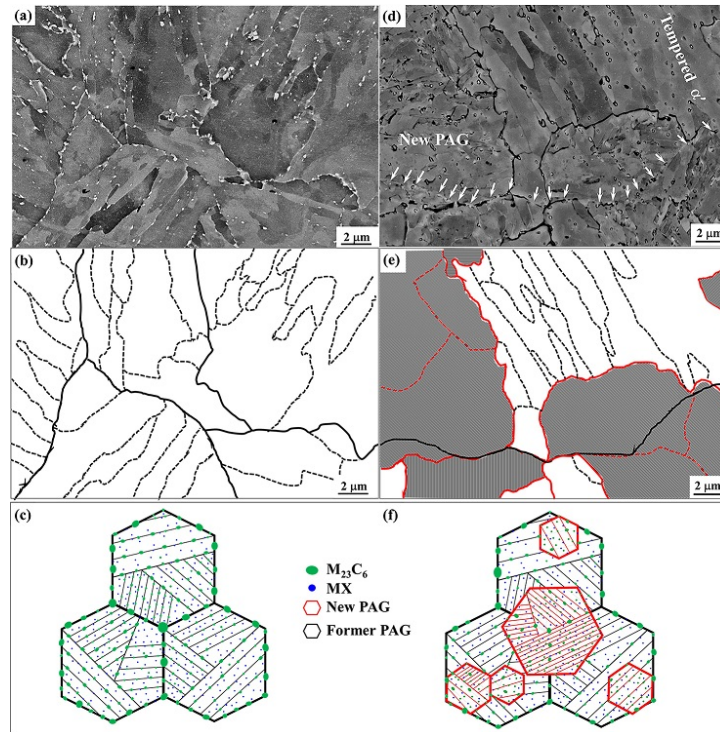


**Figure 3.6:** Microstructure evolutions in the ICHAZ: (a) microstructure of as-received P91 base metal (BM), (b) PAGBs and block boundaries in BM, and (c) a schematic microstructure for BM. (d) microstructure of the ICHAZ, (e) PAGBs and block boundaries in ICHAZ, and (f) a schematic microstructure for ICHAZ.  $M_{23}C_6$  carbides along a former PAGB are pointed by white arrows in (d). Black solid lines represent former PAGBs; black dashed lines represent martensite block boundaries; red solid lines represent new PAGBs; and red dash lines represent new martensite packet boundaries.

### 3.1.3 Microhardness distribution

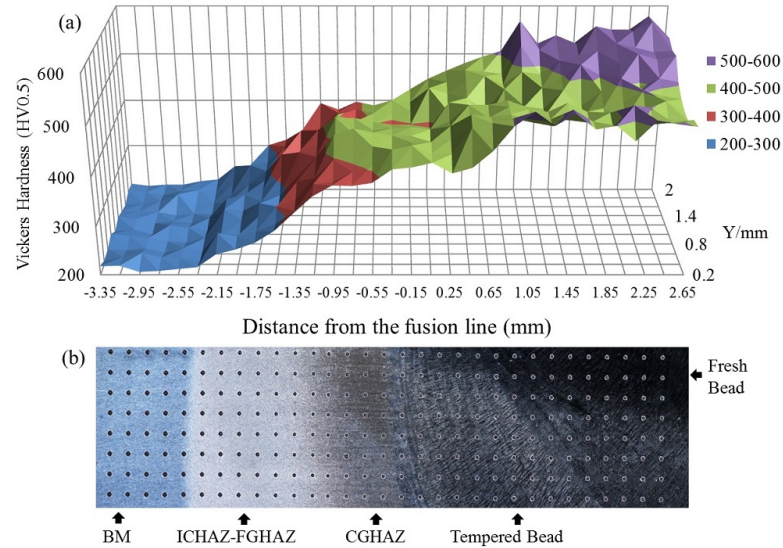


**Figure 3.7:** Vickers hardness mapping of the cross-section of the as-welded P91 weldment: (a) hardness distribution; (b) correlated hardness indentations.

**Table 3.1:** Average Vickers hardness of HAZ and BM in as-welded P91 welds.

Location	CGHAZ	FGHAZ	ICHAZ	BM
Vickers Hardness (HV0.5)	417±31	335±22	228±17	211±11

A microhardness distribution map in Figure 3.7 was reconstructed based on the Vickers hardness values measured from the HAZ (marked by rectangle 2 in Figure 3.3). Average hardness values of the different sub-regions are presented in Table 3.1. Hardness decreases from the fusion zone to the BM. Roughly, five layers with various hardness ranges can be divided, including the BM layer, ICHAZ-FGHAZ layer, CGHAZ layer, tempered bead layer and fresh bead layer (from left to right). The fresh bead has the highest hardness of 503 HV0.5 due to the formation of the fresh martensite. The tempered bead shows a relatively lower hardness of 482 HV0.5 due to the tempering effect from the subsequent beads. In

the HAZ, the CGHAZ exhibits the highest hardness of 417 HV0.5 because of the martensitic substructure within the coarse PAGs. The FGHAZ obtains a lower hardness of 335 HV0.5 due to coarsening of  $M_{23}C_6$  carbides rather than strengthening effect of the finer PAG size and the martensite is lower in carbon and other alloying elements. Because of the mixture structure of fine austenized grains and further tempered martensite laths, the ICHAZ has a comparable hardness of 228 HV0.5 with 211 HV0.5 of BM.

### 3.1.4 EBSD and EDS analyses on the HAZs

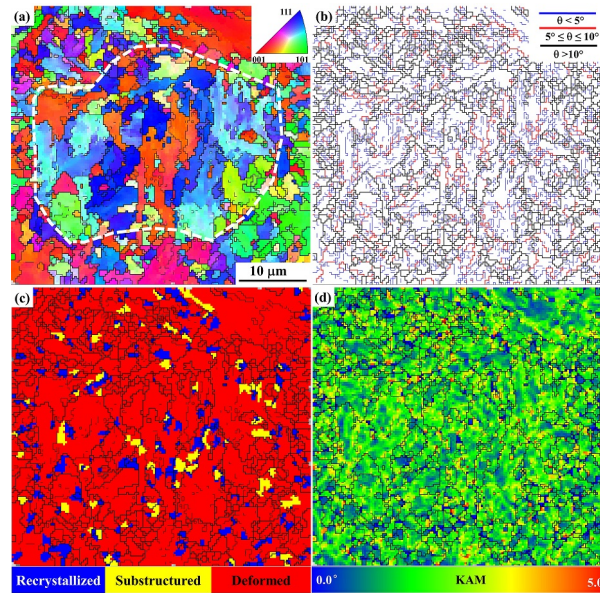


**Figure 3.8:** EBSD analyses of the CGHAZ: (a) Z axis inverse pole figure (IPF) ; (b) GB map; (c) GAM map with a threshold of  $1^\circ$ .;(d) KAM map.

For the CGHAZ, the IPF in Figure 3.8a shows the orientation of a PAG outlined by the white dash line in the center. The PAGB marked in Figure 3.8a was sketched from the low-magnified SEM image. It can be seen that besides the martensitic laths within this PAG, finer grains distribute along the PAGBs. The grain boundary map in Figure 3.8b illustrates the multi-scale boundary structures in the CGHAZ. The normalized frequency of the HAGBs (miorientation  $\theta$

$> 10^\circ$ ) is 29.8 % while the sub-boundaries, such as block boundaries with low misorientation ( $5^\circ \sim 10^\circ$ ) and lath boundaries ( $2^\circ \sim 5^\circ$ ), have a frequency of 70.2 %. The CGHAZ has a comparable grain size of  $2.05 \mu\text{m}$  with  $2.08 \mu\text{m}$  in the BM. GAM map in Figure 3.8c shows the majority of the grains are identified as deformed grains with a relative area fraction of 88.1 %. The fraction of recrystallized grain is only 7.7 %. KAM map in Figure 3.8d shows the high strain levels of the grains in the CGHAZ. These high strain levels or crystal deformations indicate the high degree of the martensite transformation in the CGHAZ.

**Table 3.2:** EBSD grain boundary and grain size analyses on the as-received base metal and CGHAZ, FGHAZ, ICHAZ in an as-welded HAZ.

Location	AR-BM	CGHAZ	FGHAZ	ICHAZ
Grain size by line-intercept method ( $\mu\text{m}$ )	2.08	2.05	1.22	1.32
Grain size standard deviation ( $\mu\text{m}$ )	2.11	1.51	0.76	0.78
HAGB frequency ( $\geq 10^\circ$ , %)	32.4	29.8	34.4	36.6
LAGB frequency ( $< 10^\circ$ , %)	67.6	70.2	65.6	63.4
Ratio of HAGB/LAGB	0.48	0.42	0.52	0.58

The FGHAZ close to the ICHAZ has a typical fine-grained structure with an average block size of  $1.22 \mu\text{m}$ , as shown in IPF (Figure 3.9a). Comparing the grain boundary map in Figure 3.9b with Figure 3.8b, the PAGs in the FGHAZ has fewer substructures with a lower frequency (65.6 %) of LAGBs (misorientation  $\theta < 10^\circ$ ), as shown in Table 3.2 The fraction of the deformed grains decreases into 56.2 %. There are more substructured or partial-recrystallized grains (29.4 %) and recrystallized grains (14.4 %). Those recrystallized grains show a low KAM value. KAM map in Figure 3.9d illustrate the lowered strain level of grains, but larger variations between grains in the FGHAZ, which is different from the uniform-high strain in the CGHAZ.

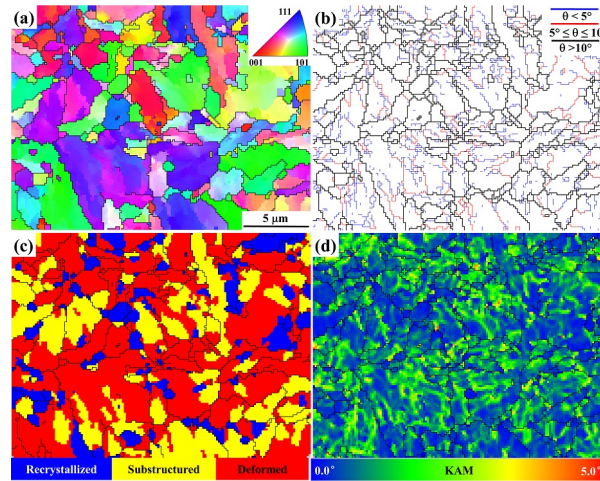


**Figure 3.9:** EBSD analyses of the FGHAZ: (a) Z axis inverse pole figure (IPF); (b) GB map; (c) GAM map with a threshold of  $1^\circ$ ; (d) KAM map.

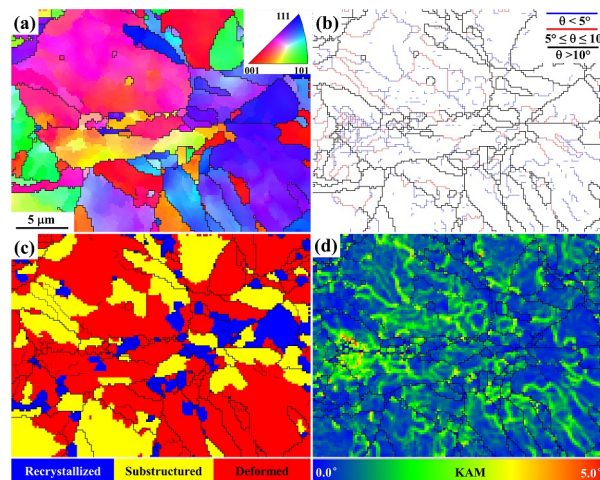


**Figure 3.10:** EBSD analyses of the ICHAZ: (a) Z axis inverse pole figure (IPF) ; (b) GB map; (c) GAM map with a threshold of  $1^\circ$ ; (d) KAM map.

The ICHAZ shows a typical mixed structure of a newly-formed PAG (left-top) and retained tempered martensite (right-bottom) in Figure 3.10a. The grain boundary map in Figure 3.10b presents the new PAG contains substructures within the grain, especially the blocks with low misorientations ( $5^\circ \sim 10^\circ$ ). The new PAG shows a higher KAM value due to the martensitic transformation. However, those retained tempered martensite barely have these blocks due to further tempering effect from the welding thermal cycle. The fraction sum (41.9 %) of

recrystallized grains and substructured grains is comparable with 43.8 % in the FGHAZ, but the ICHAZ shows a lower KAM value ( $0.79^\circ$ ) than  $0.92^\circ$  of FGHAZ due to further tempering effect.

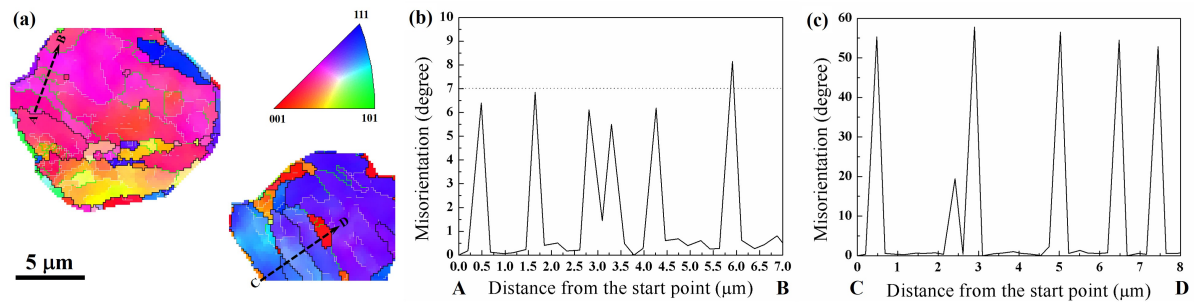


**Figure 3.11:** (a) Inverse pole figure of the new PAG in the upper left corner and a former PAG with retained tempered martensite in the lower bottom corner of Figure 3.10a. (b) and (c) shows, respectively, misorientation angle along the two marked dash arrows (AB, CD) across the block boundaries in (a).

The EBSD results in Figure 3.11 indicate the crystallography of the martensitic laths in the ICHAZ roughly follows the Kurdjumov–Sachs (K-S) orientation relationship (OR) commonly observed in low carbon alloying steels [26, 29]. Figure 3.11c shows that the K-S Group 3 variant pairs with an average boundary misorientation of  $55^\circ$  are identified between the blocks of the tempered martensite retained from BM. The misorientation angle  $55^\circ$  deviates from the ideal  $60^\circ/[011]\alpha'$  Group 3 variant pair in K-S orientation. On the other hand, sub-boundary misorientation analyses show there is one dominant packet in the highlighted new PAG. Only K-S Group 1 variant pairs with an average misorientation angle of  $7^\circ$  are identified within this block. The misorientation angle  $7^\circ$  also deviates from the ideal  $10^\circ$  of Group 1 variant pair in K-S orientation. However, this low misorientation angle agrees with the values reported in Mn-alloying steel by Morito [26]. It is reported the calculated interfacial energy of low-misorientation Group 1 variant pairs decreases when the misorientation angle changes from  $10.5^\circ/[011]\alpha'$  to  $6.5^\circ/[011]\alpha'$  [26]. So this deviation from K-S OR will reduce the interfacial energy from  $582 \text{ mJ/m}^2$  for  $9^\circ/[011]\alpha'$  to  $468 \text{ mJ/m}^2$  for  $7^\circ/[011]\alpha'$  and promote

the preferential growth of Group 1 variant pairs [30]. Reported high frequency (60.1 %) of K-S Group 1 variant pairs [26] also shows the same trend as observed in this work. The fine PAG size maybe the critical reason responsible for this unique structure in the ICHAZ. It is reported that the martensite packet size is close to the PAG size when PAG size is lower than  $10 \mu\text{m}$  in Fe-0.2C alloys [114]. It is possible that some fine PAGs consist of only one single packet (or even one single block) [114].

**Table 3.3:** EBSD KAM and GAM analyses on as-received base metal and CGHAZ, FGHAZ, ICHAZ in an as-welded HAZ.

Location	AR-BM	CGHAZ	FGHAZ	ICHAZ
Normalized KAM value ( $^{\circ}$ )	1.01	1.79	0.92	0.79
Deformed grain frequency (%)	74.9	88.1	56.2	58.1
Substructured grain frequency (%)	18.3	4.2	29.4	30.6
Recrystallized grain frequency (%)	6.8	7.7	14.4	11.3

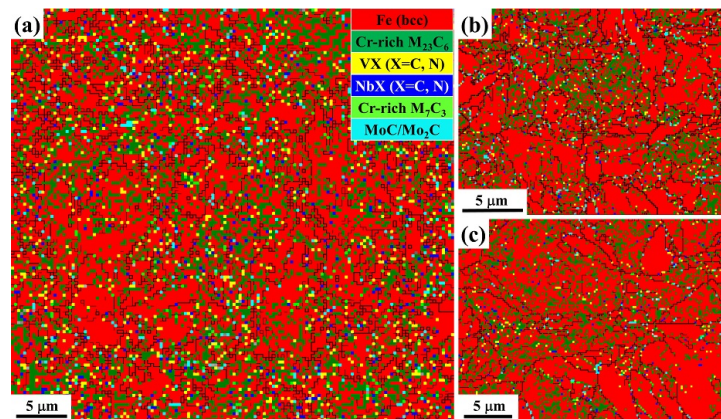


**Figure 3.12:** EBSD phase maps show the precipitate distributions in the (a) CGHAZ, (b) FGHAZ, and (c) ICHAZ.

EBSD phase maps in Figure 3.12 show the distribution variations of the precipitates in three sub-regions of the HAZ, respectively. Precipitates uniformly distribute in the CGHAZ,

which differs from the non-uniform distribution of precipitates in the as-received BM (Figure 3.2c). However, this non-uniform distribution of precipitates from the BM is enhanced in the FGHAZ and ICHAZ. The FGHAZ presents the largest density variation of precipitates. Highly condensed Cr-rich  $M_{23}C_6$  carbides are observed in some specific grains, but some other grains contain few precipitates. In the ICHAZ, there is a higher density of precipitates in the newly formed PAG than that in the retained tempered martensite. Furthermore, more coarse Cr-rich  $M_{23}C_6$  carbides are observed in those new PAGs in Figure 3.12b and 12c. MX, especially VX, shows a higher fraction in the CGHAZ than those in the FGHAZ and ICHAZ.

### 3.1.5 Study of dissolution of $M_{23}C_6$ carbide by dilatometry

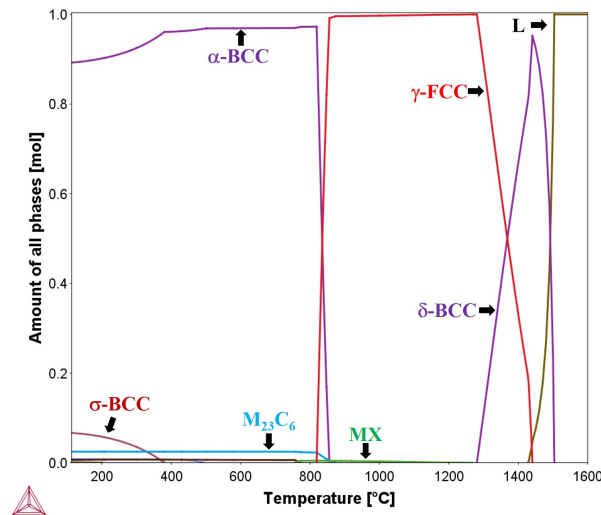


**Figure 3.13:** Equilibrium phase fraction of P91 BM as a function of temperature is calculated by ThermoCalc.

Phase fraction of the base metal as a function of temperature is calculated by ThermoCalc, as shown in Figure 3.13. The stable phases at low temperatures include  $\alpha$ -BCC,  $M_{23}C_6$ , and MX. The calculated critical phase transformation temperatures  $A_1$  and  $A_3$  are 818 °C and 856 °C, respectively.

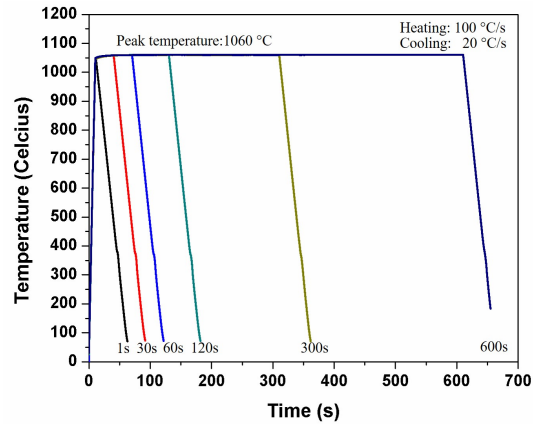


**Figure 3.14:** Thermal history of the simulated HAZ specimens with different holding times by dilatometry.

Based on our previous observation, precipitates (Cr-rich  $M_{23}C_6$  carbides) in the HAZ, especially FGHAZ and ICHAZ, can not be fully dissolved, which may affect the martensitic transformation during on-cooling. To investigate this effect, dilatometer specimens were heated up to FGHAZ peak temperature of 1060 °C and held for different times. Thermal history of the simulated HAZ specimens is shown in Figure 3.14. The heating and cooling rates are 100 °C/s and 20 °C/s, respectively. Holding times are 1 s, 30 s, 60 s, 120 s, 300 s, and 600 s.

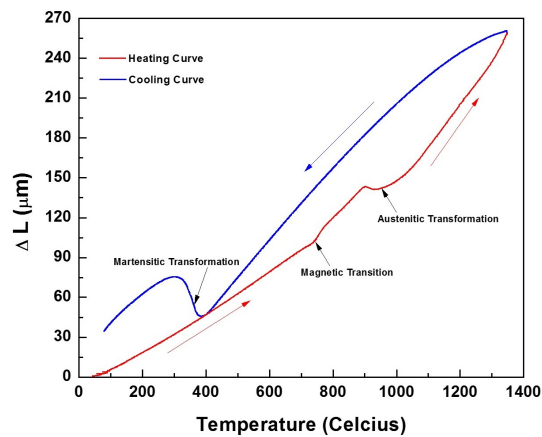


**Figure 3.15:** A representative heating-cooling dilation curve of the simulated HAZ representing phase transformations.

Figure 3.15 demonstrates the typical transformations during heating and cooling. Length change  $\Delta L$  of the specimen is contributed from the thermal expansion and phase transformations. Change of the curve's slope indicates the starting or finish of the transformations. On-heating (red line), the first transformation is the magnetic transformation at Curie temperature. And the following transformation is the austenitic transformation. On-cooling (blue line), martensitic transformation occurs at low temperatures. The transformed austenite grains transform into martensite.

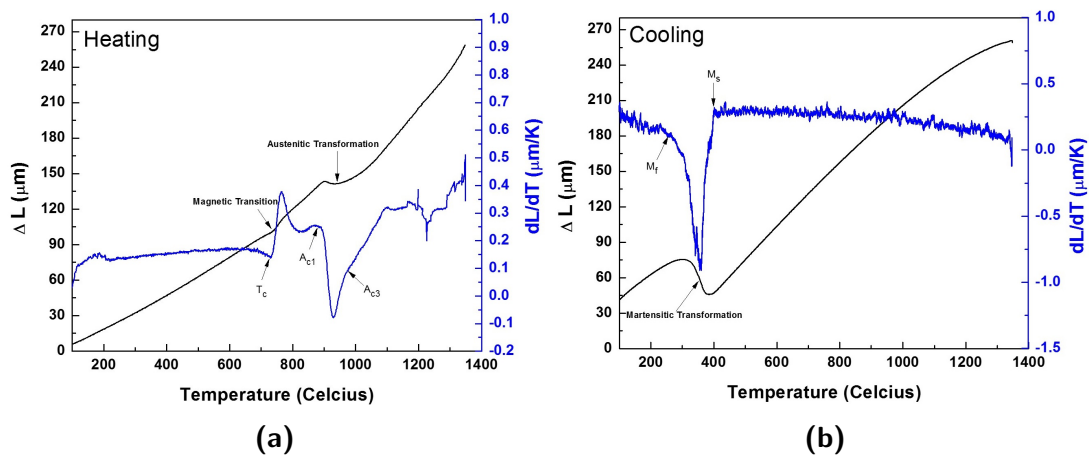


**Figure 3.16:** An example of heating-cooling curve analysis of the critical phase transformation temperatures in the simulated HAZ specimens.

To obtain the precise phase transformation temperatures, heating and cooling curves were analyzed separately. An example of heating-cooling curve analysis of the simulated HAZ is shown in Figure 3.16.  $dL/dT$  is plotted with the temperature. The critical temperatures, Curie temperature  $T_c$ ,  $A_{c1}$ , and  $A_{c3}$  are obtained from the heating curve. The  $M_s$ , and  $M_f$  are obtained from the cooling curve.

**Table 3.4:** Critical transformation temperatures determined by the dilatation curve analysis in the simulated HAZ specimens.

Specimen	$T_c$	$A_{c1}$	$A_{c3}$	$M_s$	$M_f$
1060 °C-1 s	731 °C	877 °C	970 °C	435 °C	280 °C
1060 °C-30 s	731 °C	874 °C	967 °C	433 °C	281 °C
1060 °C-60 s	729 °C	876 °C	973 °C	415 °C	278 °C
1060 °C-120 s	729 °C	879 °C	970 °C	410 °C	250 °C
1060 °C-300 s	730 °C	879 °C	967 °C	394 °C	258 °C
1060 °C-600 s	730 °C	878 °C	972 °C	408 °C	278 °C
Average	730 °C	877 °C	970 °C		

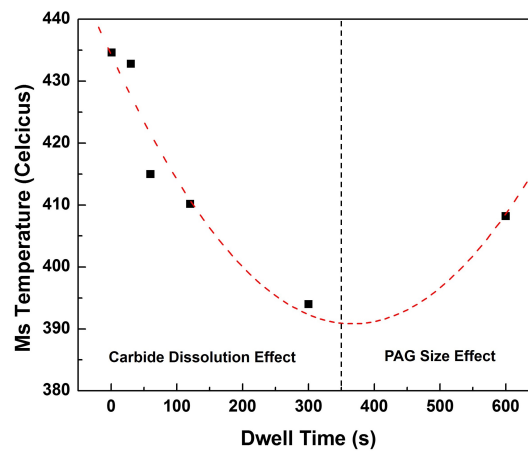
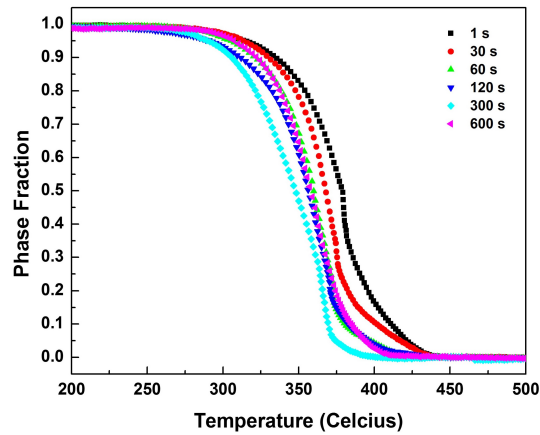
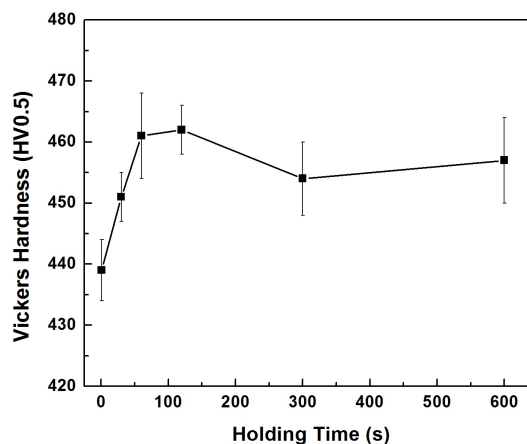
**Figure 3.17:** Martensite-start  $M_s$  temperature of the simulated HAZ specimens.

Table 3.4 summarizes the measured critical transformation temperatures. Apparently the  $A_{c1}$  and  $A_{c3}$  are much higher than the  $A_1$  and  $A_3$  due to non-equilibrium phase transformations. Martensite-start temperature  $M_s$  as a function of holding time is plotted in Figure 3.17.  $M_s$  firstly decreases from 435 °C in the 1s-hold specimen to the lowest value of 394 °C in the 300s-hold specimen and then increases to 408 °C in the 600s-hold specimen.



**Figure 3.18:** Martensitic phase transformation as a function of temperature during cooling in the simulated HAZ specimens.

Figure 3.18 shows the calculated results. It is obvious that the martensite-start temperature varies with different holding times. The martensite-finish temperature is between 260–280 °C. During cooling, austenite starts to transform into martensite at higher temperatures in the specimens with 1s-hold and 30s-hold. The increase of the phase fraction (curve slope) is more rapid in the 30s-hold specimen. The 300s-hold specimen has the lowest martensite-start temperature and the slowest transformation rate.



**Figure 3.19:** Vickers hardness of the simulated HAZ specimens.

Vickers hardness of the simulated specimens are plotted in Figure 3.19. It shows hardness

increases from 439 HV0.5 to 462 HV0.5 when the holding time extends from 1 s to 120 s. However, hardness decreases to 454 HV0.6 when the holding time further increases to 300 s. After 600s-hold, hardness no longer increases or decreases.

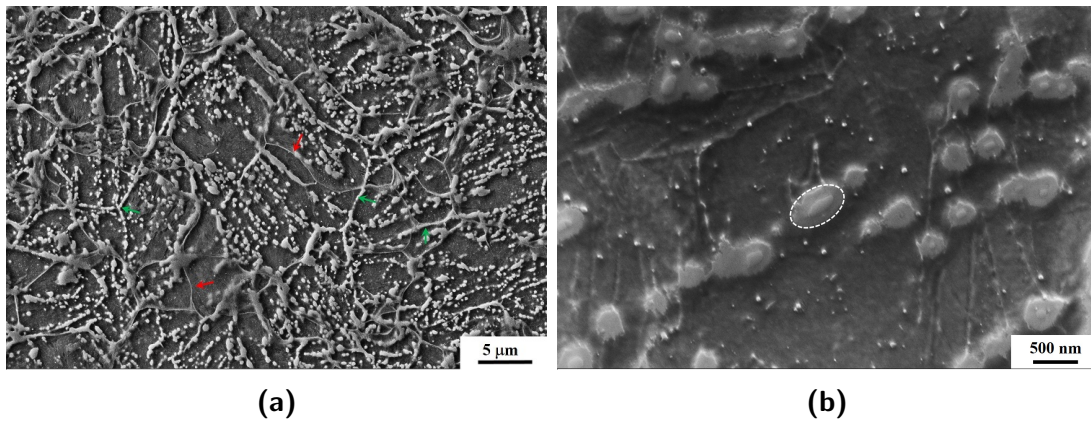


**Figure 3.20:** Typical structures of the simulated 1s-hold HAZ specimen.

Figure 3.20 shows structures of the 1s-hold specimen. Under low magnification, the specimen shows a fine-grained structure with multi-scale boundaries. Coarse particles are also observed. An SEM image at high magnification in Figure 3.20b presents more details of its structure. The first observation is that large numbers of particles are not dissolved and still exist in the specimen. These undissolved particles stay in the previous prior austenite grain boundaries and martensitic packet/block boundaries. The “ghost” prior austenite grain boundaries are marked with green arrows in the figure. New prior austenite grain boundaries are also visualized and marked by red arrows. These boundaries are clean without precipitates. Overlapping of some new prior austenite grain boundary and the previous/old prior austenite grain boundary can be found, but not for majority of the boundaries. The matrix grains are lath martensite. An SEM image with a higher magnification in Figure 3.20b uncovers nature of those coarse particles. Island structures with a outside ring and a central core are the structures of those particles. EDS analyses across these islands identify that these central cores are Cr-Mo-rich  $M_{23}C_6$  carbides. Fine particles without rings are likely the stable MX

carbonitrides.

Formation of those outside rings is due to dissolution of Cr-rich  $M_{23}C_6$  carbides. Dissolution of Cr-rich  $M_{23}C_6$  carbides is a diffusion-controlled process. Dissolution rate is normally controlled by the slower atoms, such as Cr. Movement of substitutional Cr atoms is quite difficult in iron matrix with a similar atom radius. Meanwhile, the holding time of peak temperature is only 1 s. So the diffusion distance of Cr is quite limited. Diffused Cr atoms stay around the original carbides. Thus a ring with a relative higher Cr concentration than the rest matrix has a higher corrosion resistance. When the specimen was etched, the matrix with a lower Cr content was etched and formed those island structures.

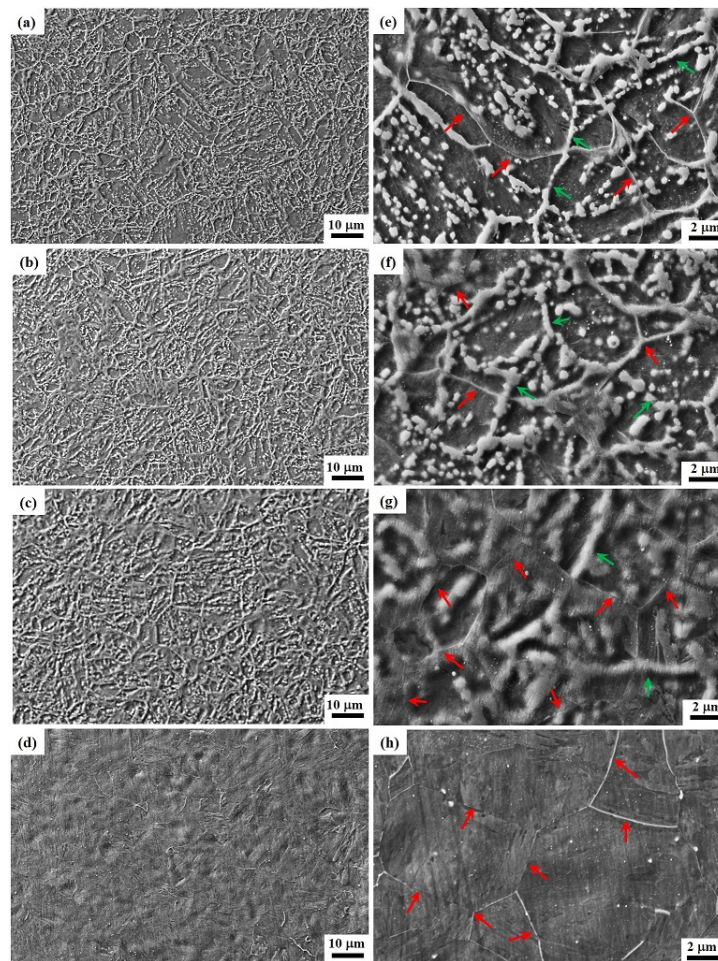


**Figure 3.21:** Microstructure of the simulated HAZ specimens: (a), (b) 1s-hold; (c), (d) 30s-hold; (e), (f) 60s-hold; (g), (h) 300s-hold. (Red arrows: new PAGBs, Green arrows: old PAGBs).

Microstructure of the specimens with 1s-hold, 30s-hold, 60s-hold, and 300s-hold is characterized and shown in Figure 3.21. The 30s-hold specimen shows a similar structure with the 1s-hold specimen. The difference is that there is a lower fraction of those islands in the 30s-hold specimen than that in the 1s-hold specimen. This indicates more precipitates are dissolved with a longer holding time. The measured PAG size is shown in Figure 3.22. The newly-formed prior austenite grain size increases more rapidly from 1s-hold to 60s-hold. After 120s-hold, the increase of PAG size is not significant. The “ghost” prior austenite grain boundaries are still visible in the 30s-hold specimen. When the holding time was extended to 60 s, the structure is dramatically different. Almost no island structure is observed, but some of the “ghost” boundaries with high Cr contents can be seen. It means that Cr-rich  $M_{23}C_6$  carbides are dissolved and diffusion of Cr is still not sufficient or homogenized. In 300s-hold specimen, a full-martensitic structure is observed. The “ghost” boundaries totally disappeared. Fine MX particles are stable and stay inside the grains. It is noticed that morphology of those new prior austenite grain boundaries is pop-out, which indicates they have a higher corrosion resistance and a higher Cr content.

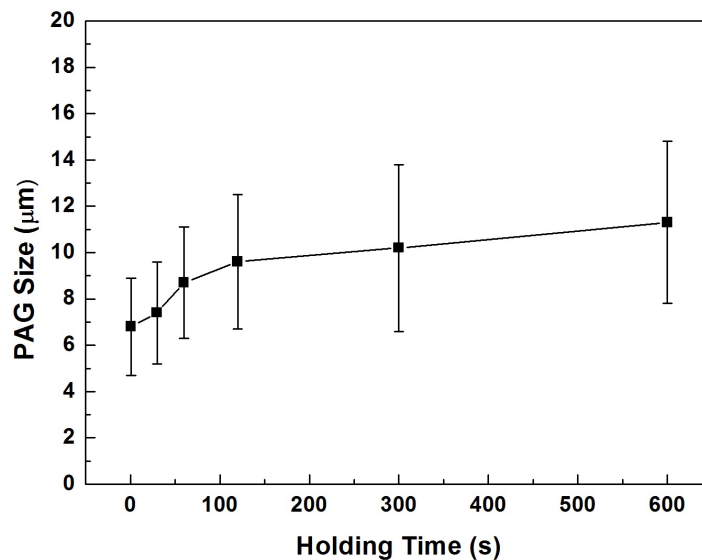
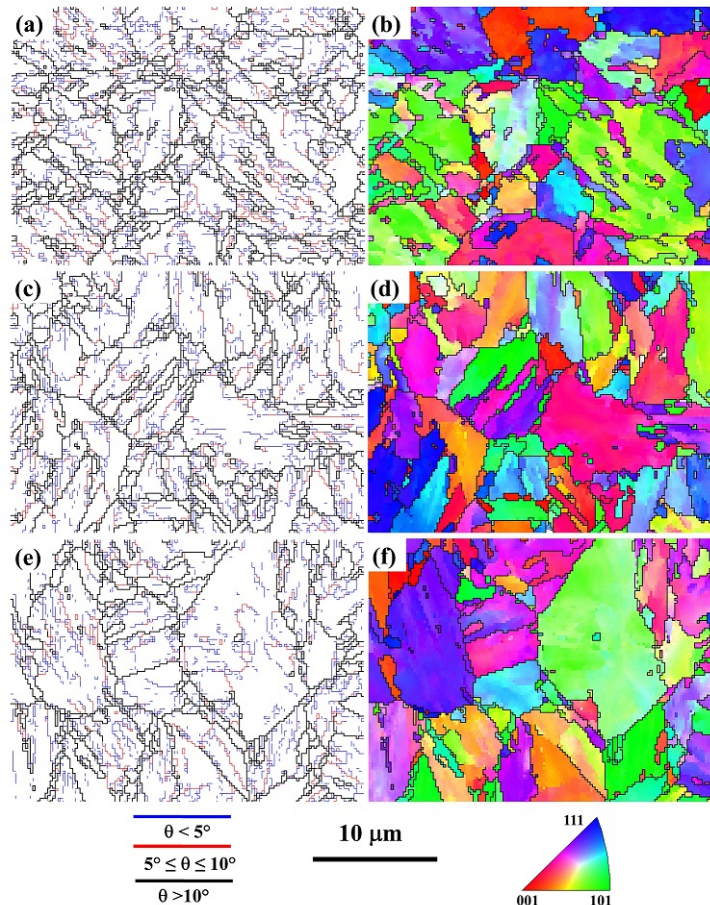


Figure 3.22: PAG size of the simulated HAZ specimens.



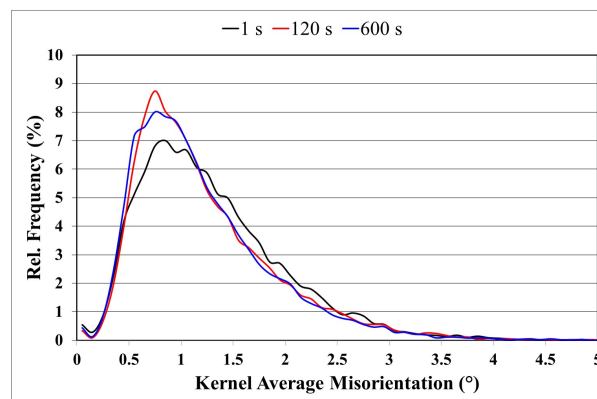
**Figure 3.23:** EBSD grain boundary map and IPF of the simulated HAZ specimens: (a) 1s-hold; (b) 120s-hold; (c) 600s-hold.

Figure 3.23 presents the grain boundary maps and IPF of the 1s-hold, 120s-hold, and 600s-hold specimens. Measured grain size and boundary frequency is tabulated in Table 3.5. High angle grain boundaries (HAGB) shown in Figure 3.23a are prior austenite grain boundaries and martensitic packet/block boundaries. From prior austenite grain size point of view, the grain size of the specimens increases from  $6.8 \mu\text{m}$  in the 1s-hold specimens to  $11.3 \mu\text{m}$  in the 600s-hold specimen. The HAGB frequency is higher with a smaller prior austenite grain size in the specimens. However, from a crystal grain size point of view, the 1s-hold specimen has the largest size of  $1.57 \mu\text{m}$  and the 120s-hold specimen shows the lowest size of  $1.25 \mu\text{m}$ . Besides size differences, morphology of martensite also varies in those specimens. In the

1s-hold specimen, there are more equiaxed grains and not many lath-like grains. However, more lath-like grains are observed in the 120s-hold specimen. In the 600s-hold specimen, both big martensitic blocks and lath-like grains co-exist. Low-angle grain boundary frequency is the highest (74.5 %) in the 600s-hold. These morphology difference is believed to be caused by the PAG size effect and selective formation of blocks.

**Table 3.5:** EBSD GB and size analysis on 1s-hold, 120s-hold, and 600s-hold specimens.

EBSD measurement	1s-hold	120s-hold	600s-hold
Grain size by line-intercept method ( $\mu\text{m}$ )	1.57	1.25	1.48
Grain size standard deviation ( $\mu\text{m}$ )	1.72	1.31	1.71
HAGB frequency ( $\geq 10^\circ$ , %)	28.0	28.7	25.5
LAGB frequency ( $< 10^\circ$ , %)	72.0	71.3	74.5



**Figure 3.24:** KAM distribution of the 1s-hold, 120s-hold, and 600s-hold specimens.

**Table 3.6:** EBSD KAM and GAM analyses on 1s-hold, 120s-hold, and 600s-hold specimens.

EBSD measurement	1s-hold	120s-hold	600s-hold
Normalized KAM value (°)	1.29	1.23	1.20
Deformed grain frequency (%)	80.2	86.7	83.8
Substructured grain frequency (%)	12.1	8.3	12.2
Recrystallized grain frequency (%)	7.7	5.0	4.0

The normalized KAM value and frequencies of three categories of grains by GAM are listed in Table 3.6. The 1s-hold specimen shows the highest inhomogeneity. The 1s-hold specimen has the highest normalized KAM value of 1.29°. KAM peaks in Figure 3.24 shifts towards lower KAM values when the holding time increases from 1s to 600 s. Meanwhile, the frequency of recrystallized grain in the 1s-hold specimen is the highest (7.7 %). These KAM and GAM results imply that the 1s-hold specimen exhibits the largest inhomogeneity of local strain distribution, which indicates the martensitic transformation is different in this 1s-hold. It is believed that the fine PAGs size and inhomogeneous alloying element distribution caused by those undissolved precipitates are likely the main reasons, which is discussed in the following section.

## 3.2 As-Welded Grade 91 Heavy Section Weldment

### 3.2.1 Characterization of the as-received heavy section block

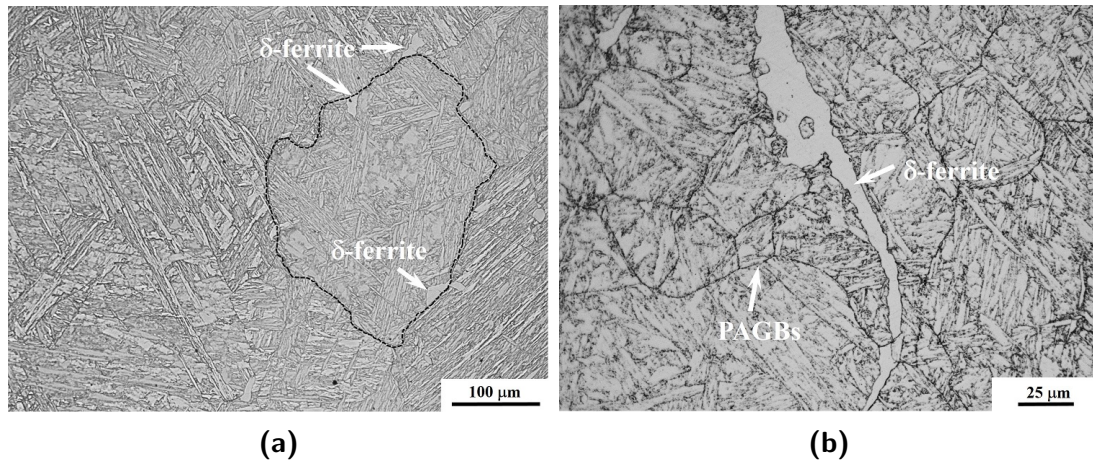


**Figure 3.25:** Optical microstructure of the as-received Grade 91 heavy section block: (a) Tempered martensite matrix. (b) Rod-shaped  $\delta$ -ferrite distributes along the PAGBs.

A typical microstructure of the as-received heavy section BM is shown in Figure 3.25. Comparing with matrix grain structure (20  $\mu\text{m}$  PAG) of the P91 steel, the average PAG size in heavy section material is significantly larger ( $\sim 150 \mu\text{m}$ ). Figure 3.25a shows the  $\delta$ -ferrite grains distribute along the PAGBs. A  $\delta$ -ferrite grain is shown in Figure 3.25b. A few fine PAGs are also observed inside the  $\delta$ -ferrite grain and along the boundary between  $\delta$ -ferrite grain and tempered martensite matrix, which suggests this  $\delta$ -ferrite grain has only partially transformed to austenite during cooling.

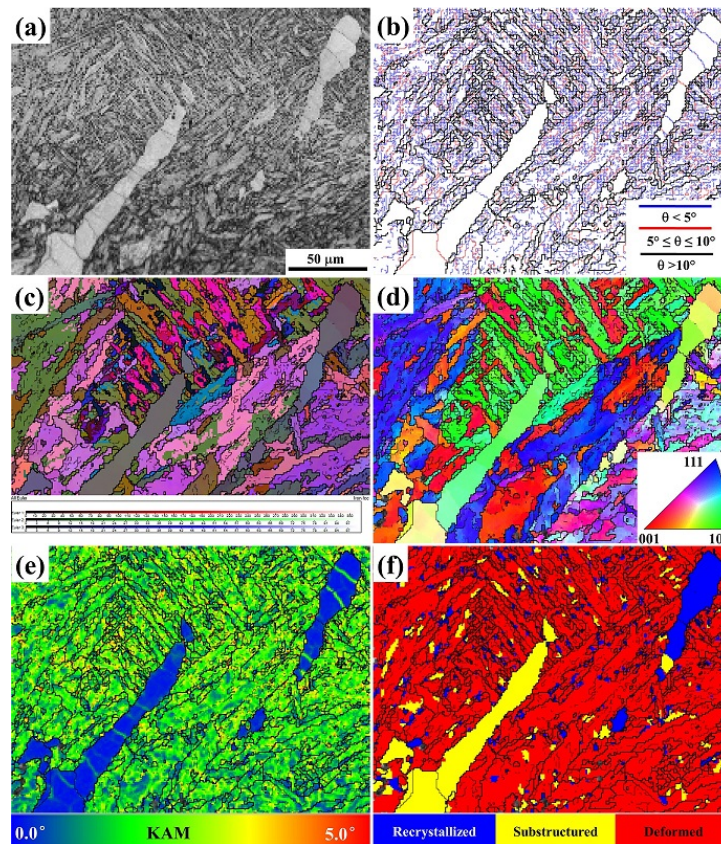
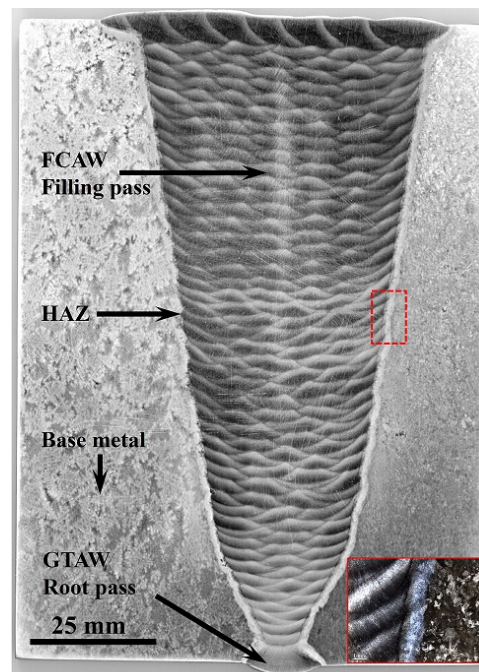


**Figure 3.26:** EBSD analyses of the as-received block base metal: (a) Band contrast map. (b) Grain boundary map. (c) All Euler angle map. (d) IPF in Z direction. (e) KAM map. (f) GAM map.

EBSD band contrast map in Figure 3.26a demonstrates that the brighter and coarser grains are identified as  $\delta$ -ferrite grains and the darker and finer grains are the tempered martensite matrix. The grain boundary map in Figure 3.26b illustrates the boundaries between tempered martensite matrix and  $\delta$ -ferrite grains are identified as high angle grain boundaries. It is observed there are a few sub-boundaries inside the  $\delta$ -ferrite grains that are the low-angle grain boundaries. The all-Euler map in Figure 3.26c indicates dramatic orientation variations between different martensitic blocks; in comparison, the orientations within the  $\delta$ -ferrite grains are similar in all three directions. Secondly, the IPF in Figure 3.26d shows those tempered martensite blocks within one PAG all having similar crystal orientations; in comparison, all

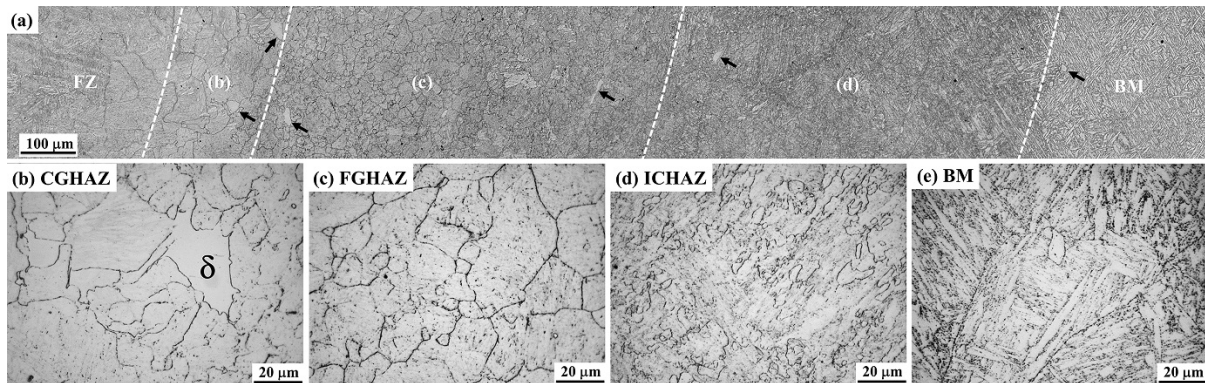
$\delta$ -ferrite grains seem to show the same preferred  $\langle 110 \rangle$  crystal orientation. The KAM map in Figure 3.26e indicates the tempered martensite matrix shows high KAM values, i.e. high local misorientations (strain energy levels); in comparison, the  $\delta$ -ferrite shows invariably low KAM or low strain energy levels. The GAM map in Figure 3.26f shows the majority of the martensitic matrix grains are categorized as deformed grains with high strain energy levels. In contrast, the  $\delta$ -ferrite grains presented are identified as recrystallized or substructured (i.e., partially recrystallized) grains.

### 3.2.2 Microstructure evolutions in the HAZ regions



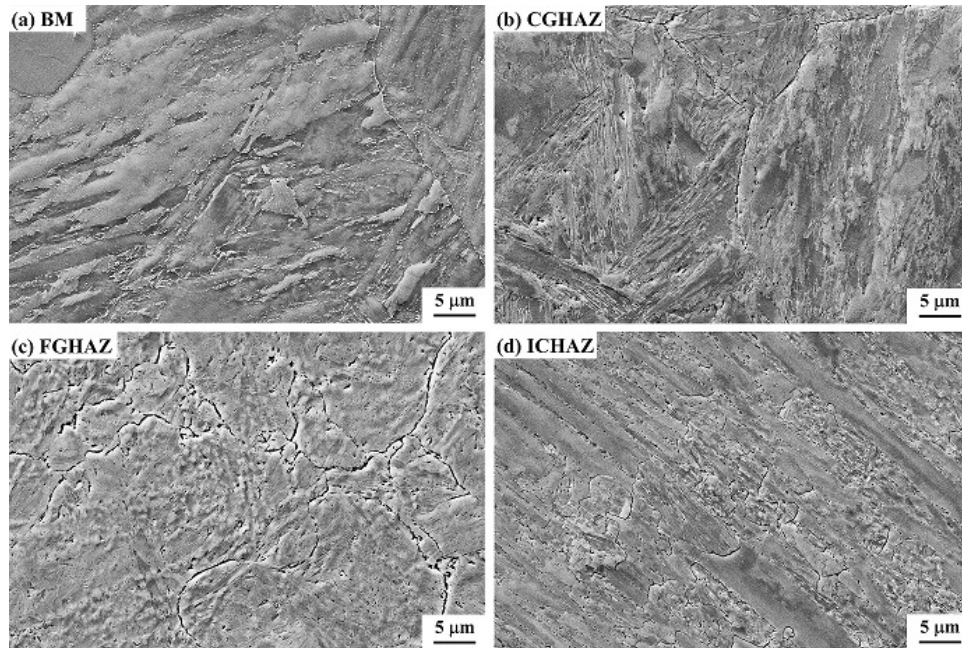
**Figure 3.27:** Cross-sectional macrostructure of the as-welded heavy section weldment.

Figure 3.27 shows macro-etched structures of the entire weldment, including GTAW root pass at the bottom and multiple FCAW filling passes. Width of the HAZ is narrower than 2 mm. A mid-thickness HAZ specimen is chosen to characterize the HAZ structures because creep cavities are normally observed in the mid-thickness HAZ after creep.



**Figure 3.28:** Optical microstructure of the HAZ in an as-welded Grade 91 block weldment: (a) Overview of the HAZ from fusion zone to the base metal; (b) CGHAZ; (c) FGHAZ; (d) ICHAZ; (e) BM.

Figure 3.28 shows structure of the HAZ. Different from the P91 pipe HAZ structures (a wide CGHAZ, a wide FGHAZ, and a narrow ICHAZ), thickness of the CGHAZ is only a few grains wide (0.3 mm width), but thickness (0.7 mm width) of the ICHAZ is much greater. Figure 3.28b shows coarse equiaxed PAGs of the CGHAZ. A  $\delta$ -ferrite grain is also observed in Figure 3.28b. Figure 3.28c shows the relatively fine equiaxed PAGs in the FGHAZ (0.7 mm width). The ICHAZ in Figure 3.28d consists of fine newly formed PAGs and retained tempered martensite blocks from the base metal. The  $\delta$ -ferrite grains marked by the black arrows in Figure 3.28a are observed from the high peak temperature end of the CGHAZ to the low peak temperature end of the ICHAZ. Since the morphology of the  $\delta$ -ferrite grains is close to the equiaxed grains, not the skeletal or thin-string  $\delta$ -ferrite grains retained from the partial  $\delta$ -ferrite-austenite transformation as reported by Maya et al. [37], these  $\delta$ -ferrite grains are believed to be retained from the as-received base metal, rather than newly formed during the welding thermal cycles.



**Figure 3.29:** SEM images of the HAZ in an as-welded Grade 91 block weldment: (a) BM; (b) CGHAZ; (c) FGHAZ; (d) ICHAZ.

SEM image in Figure 3.29a shows that the BM has tempered martensitic blocks with coarse dispersive precipitates along the boundaries. Different from the P91 pipe BM, fine precipitates instead of coarse carbides are observed. The CGHAZ in Figure 3.29b shows a untempered martensitic structure within coarse PAGs. The black cavities inside the PAGs are believed to be locations of the previous coarse precipitates from the base metal. Fine martensitic structure in the FGHAZ in Figure 3.29c is due to martensitic transformation from the newly-formed fine PAGs. “Ghost” tracks of the previous precipitates from the base metal, shown as bright dots, indicative of the previous PAGs in the base metal, can be observed within the newly formed PAGs. Figure 3.29d shows a mixed structure of un-transformed martensitic blocks from the base metal and newly transformed martensite. Coarse precipitates, identified as the Cr-rich  $M_{23}C_6$  carbides [109, 115], are observed along the martensitic blocks, and even inside the transformed PAGs in Figure 3.29d. These carbides are reported to undergo a preferential growth during the PWHT and creep, which provide preferential nucleation sites

for the creep cavities [11, 41, 116].

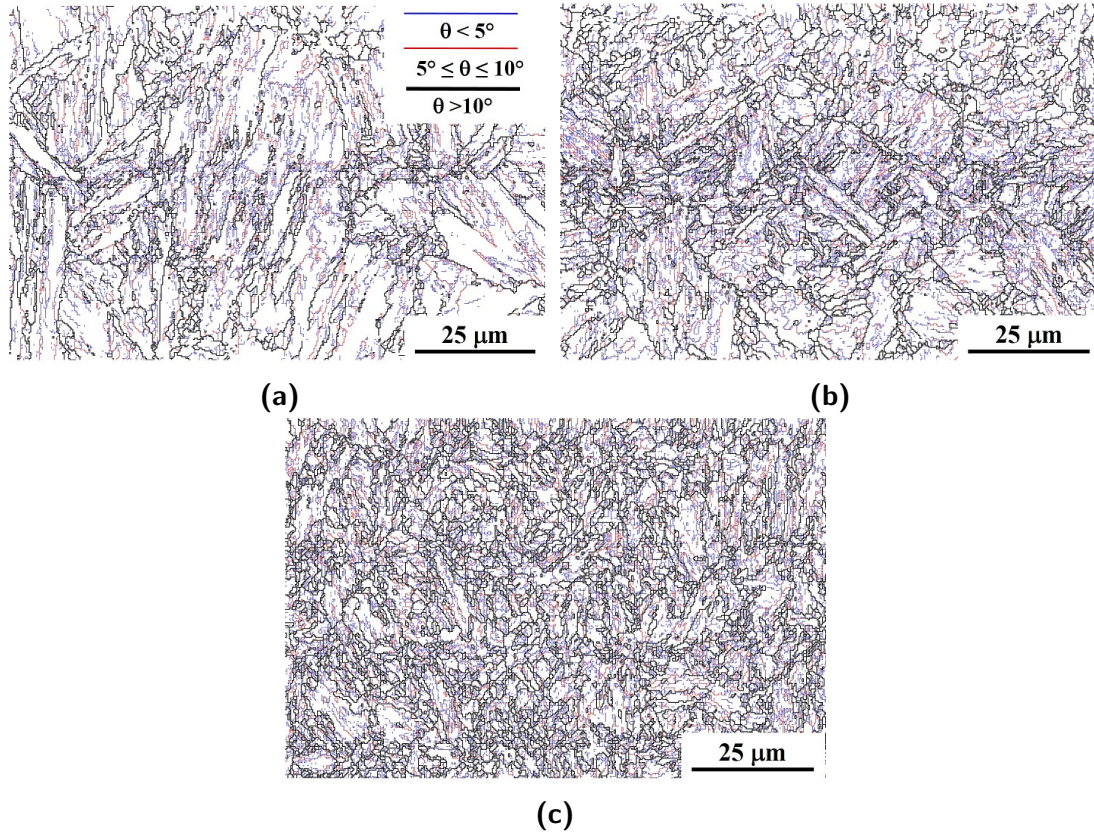


**Figure 3.30:** EBSD grain boundary distribution maps: (a) CGHAZ; (b) FGHAZ; (c) ICHAZ.

**Table 3.7:** EBSD GB and size analyses on CGHAZ, FGHAZ, and ICHAZ.

EBSD measurement	CGHAZ	FGHAZ	ICHAZ
Grain size by line-intercept method ( $\mu\text{m}$ )	2.8	2.4	1.4
Grain size standard deviation ( $\mu\text{m}$ )	3.2	2.6	1.4
HAGB frequency ( $\geq 10^\circ$ , %)	22.9	24.1	31.5
LAGB frequency ( $< 10^\circ$ , %)	77.1	75.9	68.5

Figure 3.30 shows the grain boundary distribution in the CGHAZ, FGHAZ, and ICHAZ, respectively. Figure 3.30a shows the thick martensitic blocks with an average size of 2.8  $\mu\text{m}$  in

the CGHAZ. The FGHAZ obtains a median block size of  $2.4 \mu\text{m}$  (Figure 3.30b). The ICHAZ shows the finest block size of  $1.4 \mu\text{m}$  (Figure 3.30c). Statistical analyses of the HAGB and the LAGB frequencies are tabulated in Table 3.7. Inversely, the CGHAZ has the lowest HAGB frequency of 22.9 %; the FGHAZ has a median HAGB frequency of 24.1 %; the ICHAZ has the highest HAGB frequency of 31.5 %, as shown in Table 3.7.

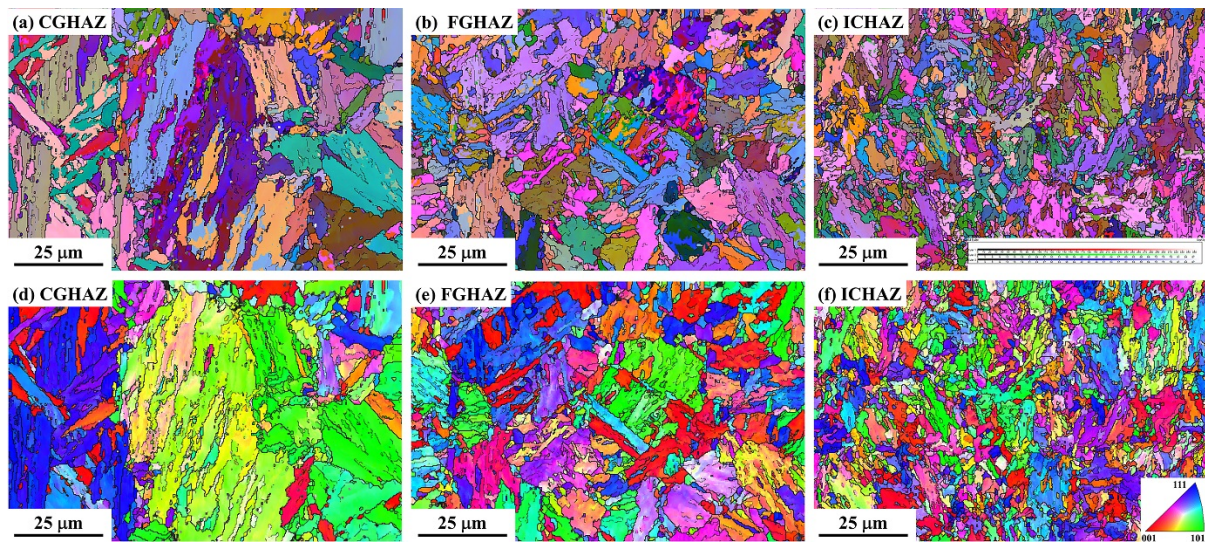


**Figure 3.31:** All-Euler maps and IPF in Z direction: (a), (d) CGHAZ; (b), (e) FGHAZ; (c), (f) ICHAZ.

Figure 3.31a and Figure 3.31d of CGHAZ have fewer colors, which means there are limited orientation variations within the CGHAZ. The FGHAZ (Figure 3.31b and Figure 3.31e) shows more colors, especially for these fine equiaxed grains. Due to fine PAGs formed at lower peak temperatures, the ICHAZ shows the largest orientation variations, as shown in Figure 3.31c and Figure 3.31f. It is reported that martensitic laths in low carbon steels normally follow the Kurdjumov-Sachs (K-S) orientation relationship [26,27]. For low-carbon martensitic steels, six major variants likely form three groups of variant pairs [28]. In the CGHAZ, high length/width martensitic blocks with similar colors/orientations are observed within coarse PAGs. The IPF in Figure 3.31d indicates that there are two main variant pairs (blue-red, green-yellow) between blocks within the PAGs. In the FGHAZ, the high-length/width blocks with a single

color/orientation are still observed, but more equiaxed grains with gradient colors exist in the FGHAZ, as shown in Figure 3.31e. In the ICHAZ, the majority of the matrix grains are fine equiaxed grains or short-length blocks with single color. Those wide blocks are believed to be un-transformed (i.e. not austenitized on heating) tempered martensitic blocks from the original base metal.

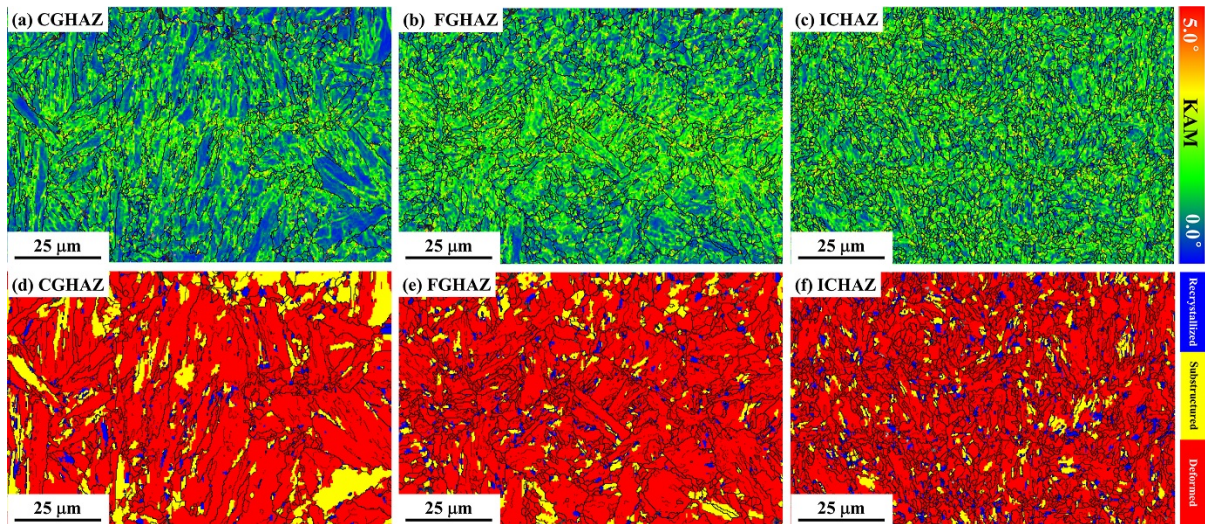


**Figure 3.32:** Local strain distribution illustrated by the KAM maps (a, b, c) and grain average misorientation maps (d, e, e): (a), (d) CGHAZ; (b), (e) FGHAZ; (c), (f) ICHAZ.

Figure 3.32 illustrates local strain energy variations by evaluating the kernel average misorientation (KAM) and grain average misorientation (GAM) in the CGHAZ, FGHAZ, and ICHAZ, respectively. Statistical results are shown in Table 3.8. In summary, all three HAZs show relatively high KAM values and most of the grains are identified as deformed grains, which have high internal strain energies. The CGHAZ shows a non-uniform KAM distribution with some high strained grains (green color) and some low strained grains (blue color) in Figure 3.32a. The blocks with lower KAM values are categorized as the substructured grains (20.4 %, partially recrystallized) in Figure 3.32d. The normalized KAM value in the CGHAZ is  $1.16^\circ$ .

**Table 3.8:** EBSD KAM and GAM analyses on CGHAZ, FGHAZ, and ICHAZ.

EBSD measurement	CGHAZ	FGHAZ	ICHAZ
Normalized KAM value (°)	1.16	1.43	1.47
Deformed grain frequency (%)	75.6	87.0	84.6
Substructured grain frequency (%)	20.4	8.6	7.7
Recrystallized grain frequency (%)	4.0	4.4	7.7

The FGHAZ and ICHAZ show comparable KAM values, 1.43° and 1.47°, respectively, while the ICHAZ shows a more uniform KAM distribution. Both CGHAZ and FGHAZ obtain low frequencies of the recrystallized grains, 4.0 % and 4.4 %. The ICHAZ has a slightly higher frequency (7.7 %) of recrystallized grains, which is contributed from the over-tempered martensite observed in Figure 3.29d. This local strain variation of matrix grains in the CGHAZ, FGHAZ, and ICHAZ may a significant factor for the creep strength reduction in each region during PWHT and creep. It is recommended that the PWHT thermal cycle and creep testing conditions may bring a greater creep strength reduction effect on grains with a high KAM value (i.e., more dislocations), such as the deformed grains in the FGHAZ and ICHAZ.

### 3.2.3 Microhardness distribution

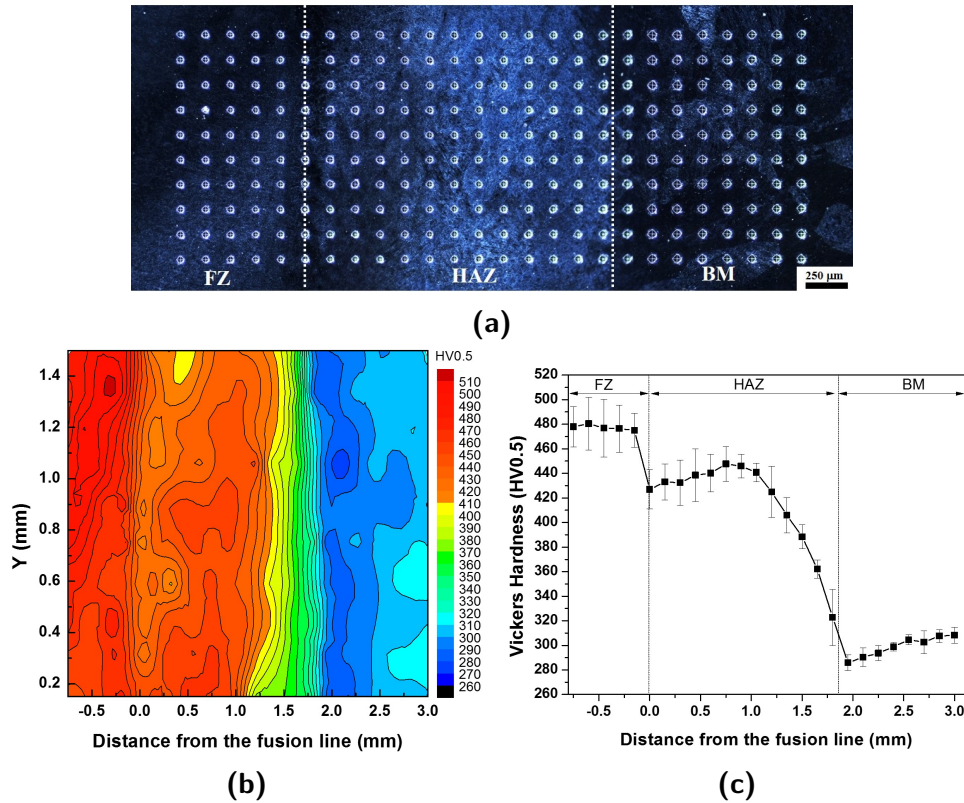


**Figure 3.33:** Hardness distribution in the cross-section HAZ specimen in the as-welded condition: (a) Dark-field optical image; (b) hardness contour map; (c) average hardness profile.

Microhardness mapping was conducted on a cross-sectional HAZ specimen, shown in Figure 3.33a. Hardness contour and average hardness profile are shown in Figure 3.33b and Figure 3.33c, respectively. Fusion zone (FZ) on the left side shows a high and uniform hardness value of 477 HV0.5. Base metal on the right side shows a low and uniform hardness of 304 HV0.5. In contrast, the HAZ has a non-uniform hardness distribution due to the peak temperature gradient. On both sides of the HAZ, either bordering the FZ or the base metal, the denser contour lines can be seen, which means there are larger hardness differences. The CGHAZ close to the fusion line has a relatively lower hardness than that of the CGHAZ neighboring the FGHAZ. This is probably caused by the tempering effect from the subsequent filling passes

on the CGHAZ. The KAM map in Figure 3.32a shows the relatively lower local strain (and proportionally a lower hardness) in the CGHAZ, comparing with that in the FGHAZ which has the highest hardness value of 448 HV0.5. The ICHAZ close to the base metal has a low hardness of 323 HV0.5, but a large deviation (23 HV0.5). The limited martensite from the partially austenitic transformation on-heating, as shown in the Figure 3.29d, and the coarser and more  $M_{23}C_6$  carbides are responsible for the lower hardness value. The hardness difference between the newly transformed martensite and the retained over-tempered martensite leads to the large hardness deviation in the ICHAZ. The softest zone with the lowest hardness of 286 HV0.5 exists in the over-tempered base metal right outside the ICHAZ.

### 3.2.4 delta-ferrite in BM and HAZ

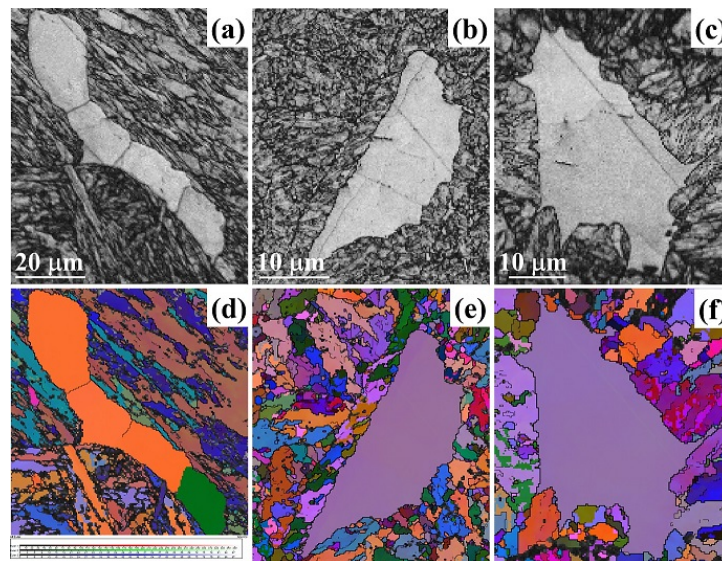


**Figure 3.34:** The EBSD band contrast maps (a, b, c) and All-Euler maps (d, e, f) of  $\delta$ -ferrite in various regions: (a), (d) BM. (b), (e) FGHAZ. (c), (f) CGHAZ.

$\delta$ -ferrite grains are observed in the entire HAZ, including the CGHAZ adjacent to the fusion line, as shown in Figure 3.28a. Figure 3.34 represents the band contrast and all-Euler maps of  $\delta$ -ferrite grains in the base metal, FGHAZ, and CGHAZ, respectively. Based on all-Euler map,

$\delta$ -ferrite grain in the base metal contains subgrains, while  $\delta$ -ferrite grains in the HAZ contain no subgrains. Shape morphology of the  $\delta$ -ferrite grain changes from a high length/width ratio in the base metal to a low length/width ratio in the HAZ. The unique local concave curvatures of the  $\delta$ -ferrite grains in the HAZ seem to show that the growth of PAGs has consumed part of the  $\delta$ -ferrite grains. This reflects the diffusive mechanism of the  $\delta$ -ferrite-to-austenite transformation, which is also reported by others [37, 39].

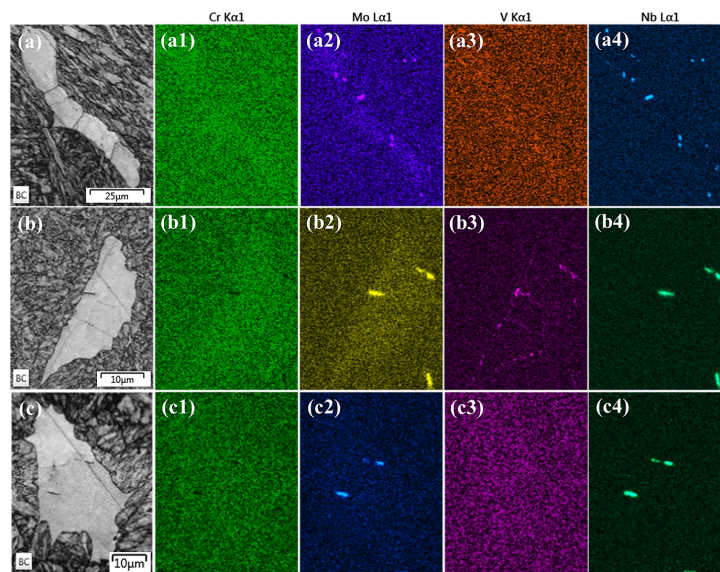


**Figure 3.35:** EDS mapping of  $\delta$ -ferrite in various regions: (a) BM, (b) FGHAZ, (c) CGHAZ.

The EDS mapping in Figure 3.35 shows the distribution of the ferrite-stabilizers, Cr, Mo, V, and Nb, in the  $\delta$ -ferrite grains in the HAZ and base metal. Higher concentrations of Cr, Mo, V, and Nb are observed in the  $\delta$ -ferrite grains in both base metal and HAZ. Distribution of Cr is more homogeneous than Mo, V, and Nb. The particles, rich in Mo and Nb, distribute along the boundaries between  $\delta$ -ferrite grains and PAGs. The Mo and Nb rich particles are also detected inside  $\delta$ -ferrite grains in the CGHAZ, as shown in Figure 3.35c2 and Figure 3.35c4. In Figure 3.35b3, V-rich particles are observed along the boundaries between  $\delta$ -ferrite grains and PAGs. It is also noticed that concentrations (shown by the intensity) of the alloying elements, especially Cr and Mo, in  $\delta$ -ferrite have decreased in the ICHAZ and CGHAZ, compared with

Cr and Mo concentrations in  $\delta$ -ferrite grain of the as-received base metal.

**Table 3.9:** EDS composition analyses on  $\delta$ -ferrite grains in CGHAZ, FGHAZ, ICHAZ, and BM.

Element concentration (wt.%)	Si	V	Cr	Mn	Fe	Ni	Nb	Mo
BM- $\delta$ -ferrite	0.47	0.44	10.65	0.31	85.89	0.13	0.04	2.06
ICHAZ- $\delta$ -ferrite	0.39	0.57	10.52	0.31	86.24	0.22	0.10	1.64
FGHAZ- $\delta$ -ferrite	0.43	0.34	10.41	0.38	86.21	0.23	0.07	1.92
CGHAZ- $\delta$ -ferrite	0.45	0.37	10.34	0.44	86.57	0.18	0.10	1.53

Measured compositions of the  $\delta$ -ferrite grains in both the base metal and HAZ are tabulated in Table 3.9. Cr concentrations inside  $\delta$ -ferrite grains in the base metal are above 10 wt.%, which is higher than the nominal 8.89 wt.% Cr of this alloy. Mo concentrations inside  $\delta$ -ferrite grains in the base metal are above 1.5 wt.%, which is also higher than the nominal concentration 0.87 wt.%. Si, V, and Nb concentrations are higher than their nominal compositions as well. To show how the welding thermal cycles affect the distributions of these alloying elements, accumulated concentrations of ferrite-stabilizers in the  $\delta$ -ferrite grains in HAZ and base metal are shown in Figure 3.36. It can be concluded that ferrite-stabilizer elements are enriched in  $\delta$ -ferrite grains in both the HAZ and base metal, but Cr and Mo concentrations in the HAZ are slightly lower than that in the base metal. Additionally, the accumulated concentration of ferrite-stabilizers slightly decreases from the low peak temperature ICHAZ region to the high peak temperature CGHAZ region, which may be due to greater diffusion coefficients of those elements at higher temperatures. Thus welding thermal cycles seem to have promoted homogenization of these ferrite-stabilizers by accelerating inter-diffusion.

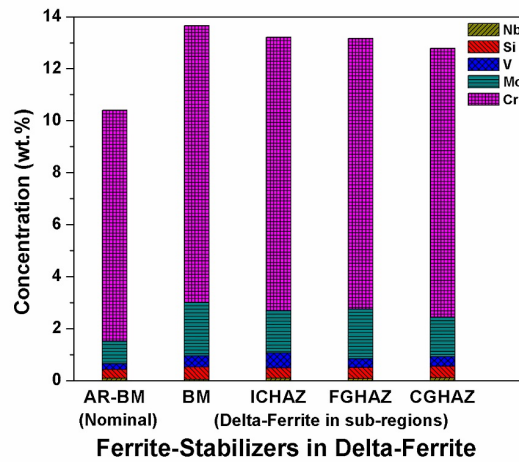


**Figure 3.36:** Accumulated concentration of ferrite-stabilizers in  $\delta$ -ferrite in HAZ and BM. Composition of the as-received BM (AR-BM) is also shown in the figure.

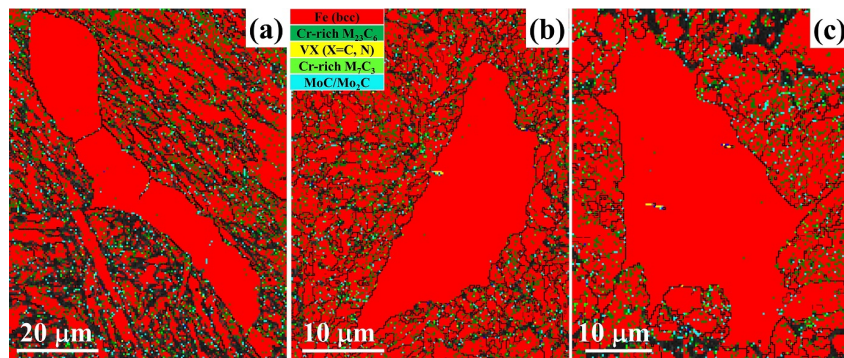


**Figure 3.37:** Precipitate distribution around  $\delta$ -ferrite in various regions: (a) BM, (b) ICHAZ, (c) CGHAZ.

The EBSD phase maps in Figure 3.37 show the precipitate distribution around the  $\delta$ -ferrite grains. It can be seen that a few fine Cr-rich  $M_{23}C_6$  carbides,  $Mo_2C$  carbides and V-Nb-rich MX carbonitrides are detected inside the  $\delta$ -ferrite grains. A large amount of Cr-rich  $M_{23}C_6$  carbides and  $Mo_2C$  carbides are observed along the boundaries between  $\delta$ -ferrite grains and martensitic matrix. This observation agrees with a previous observation by Kimura et al. [38] that segregation of these carbide-forming elements in  $\delta$ -ferrite grains promotes the precipitation along the  $\delta$ -ferrite grain boundaries. Densities of  $M_{23}C_6$  carbides in the CGHAZ and ICHAZ have decreased, comparing with that in the base metal, due to the dissolution

effect from the welding heating cycles.

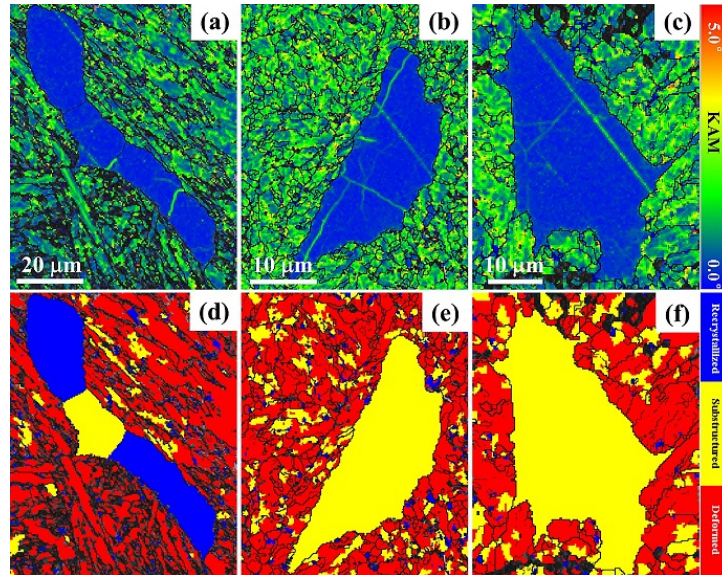


**Figure 3.38:** KAM (a, b, c) and GAM (d, e, f) evaluations of  $\delta$ -ferrite in various regions: (a), (d) BM. (b), (e) ICHAZ. (c), (f) CGHAZ. Note: The straight line with high KAM values in (c) is due to a polishing scratch.

The EBSD KAM and GAM maps in Figure 3.38 show local strain levels in the  $\delta$ -ferrite grains in both the base metal and HAZ. Martensitic matrix in the HAZ shows higher KAM values than that in the base metal. Comparing with tempered martensite matrix,  $\delta$ -ferrite grains in both base metal and HAZ show relatively lower KAM values. However, the GAM maps in Figure 3.38 shows that part of the  $\delta$ -ferrite grains in the base metal is identified as the recrystallized grains due to the previous normalization/tempering heat-treatment, and  $\delta$ -ferrite grains in the ICHAZ and CGHAZ are all substructured grains instead of recrystallized grains. The local line scanning misorientation analyses in Figure 3.39 show there are large misorientation changes across the subgrain boundaries of  $\delta$ -ferrite grain in the base metal. Misorientation variations within  $\delta$ -ferrite grains in the ICHAZ and CGHAZ, however, are larger than that in the base metal. These results seem to indicate local strain levels of  $\delta$ -ferrite grains in the HAZ are higher than that of  $\delta$ -ferrite grain in the base metal. Microhardness measurements on the  $\delta$ -ferrite grains have also verified this conjecture.  $\delta$ -ferrite grains in the

base metal is softer than  $\delta$ -ferrite grains in the HAZ.  $\delta$ -ferrite grains in the base metal have the lowest average hardness value of 240 HV0.05.  $\delta$ -ferrite grains in the FGHAZ and CGHAZ have higher average hardness values of 271 HV0.05 and 289 HV0.05, respectively, although the alloying element concentrations are slightly lower. This hardness comparison agrees with the trend shown in the KAM and GAM data. Higher local misorientation inside  $\delta$ -ferrite grain in the HAZ indicates higher straining (higher dislocation density). These increasing dislocations are believed to have generated by constraints from martensitic transformation during the cooling.

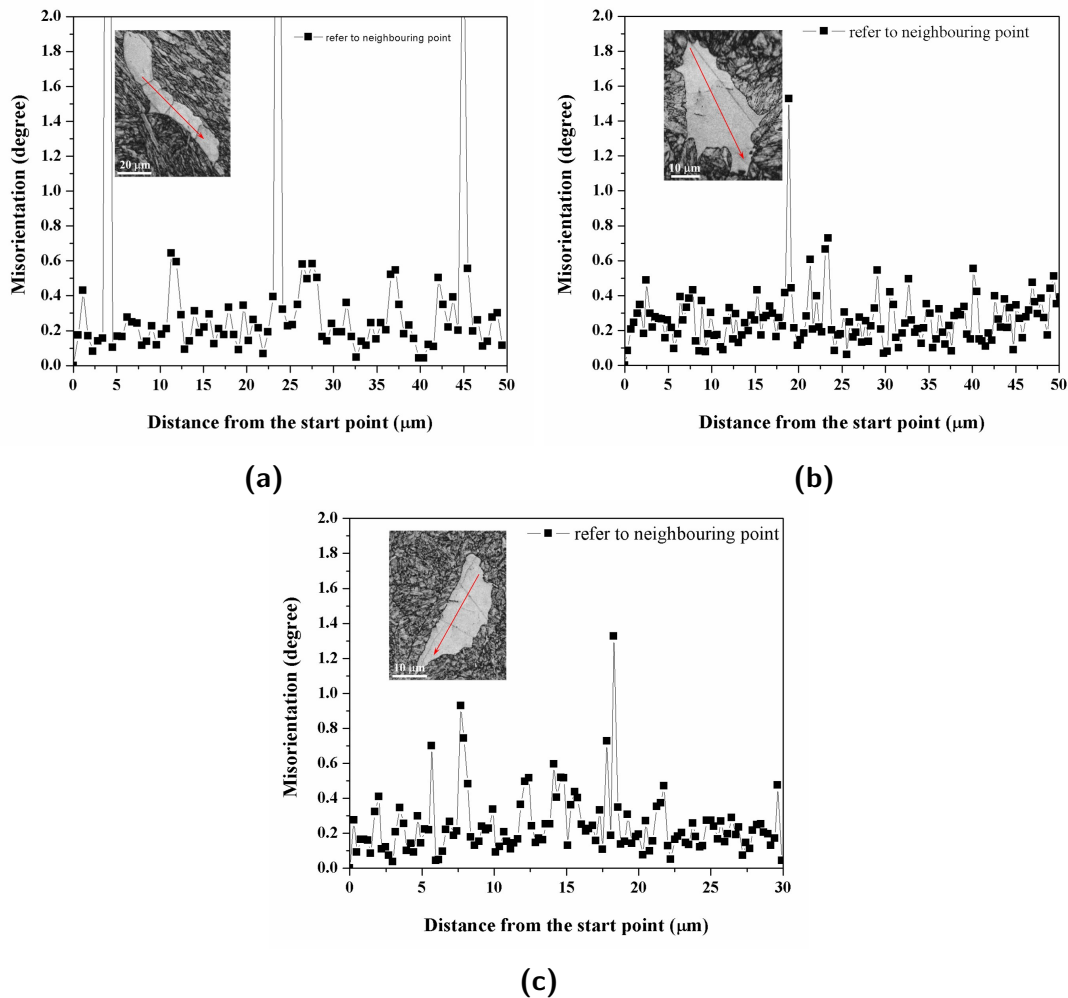


**Figure 3.39:** Local misorientation across the  $\delta$ -ferrite in various regions: (a) BM, (b) ICHAZ, (c) CGHAZ.

### 3.2.5 Study of dissolution of delta-ferrite by dilatometry

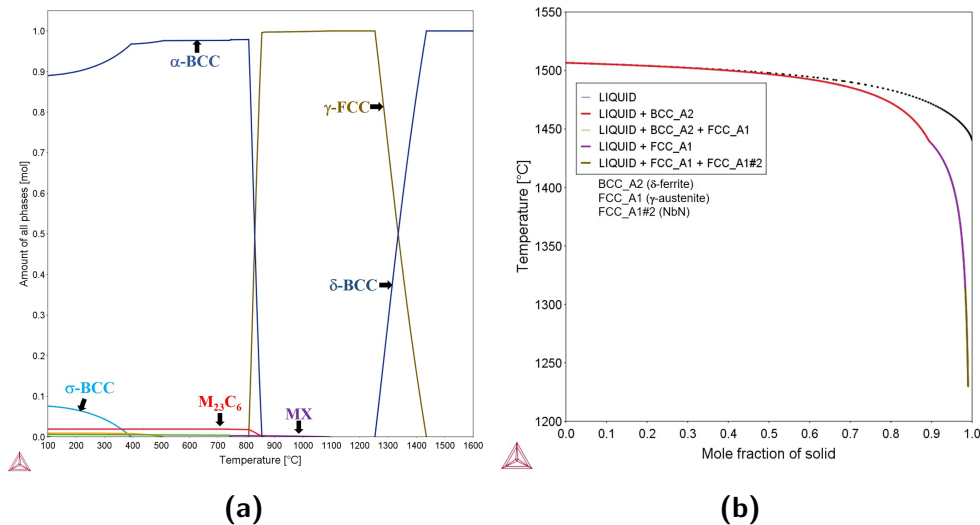


**Figure 3.40:** Calculated equilibrium phase fraction and Scheil solid fraction as a function of temperature of the block base metal by ThermoCalc .

The calculated equilibrium phase fraction and Scheil solid fraction as a function of temperature are shown in Figure 3.40. The graphs show that  $\delta$ -ferrite is the first high-temperature phase nucleated from the molten liquid. During cooling,  $\delta$ -ferrite will transform into  $\gamma$ -austenite. At low temperatures (below 1250 °C),  $\delta$ -ferrite completely transforms into  $\gamma$ -austenite. However, due to non-equilibrium cooling, some  $\delta$ -ferrite may retain at low temperature.  $\delta$ -ferrite was found in the as-received block base metal in Figure 3.25. After welding, some of these retained  $\delta$ -ferrite are also observed in the HAZ, including CGHAZ. Based on the phase fraction calculated in Figure 3.40a, dissolution of  $\delta$ -ferrite should have occurred in the HAZ, but dissolution mechanism of  $\delta$ -ferrite is still unclear. In the following section, dissolution of  $\delta$ -ferrite is studied by using the dilatometry method.

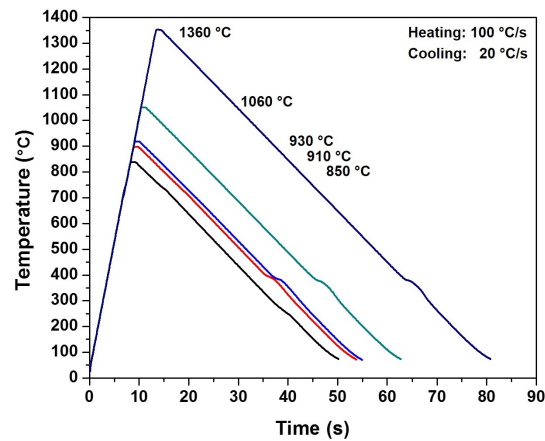


**Figure 3.41:** Thermal curves of the simulated HAZ specimens by dilatometry.

A set of specimens were exposed to different peak temperatures to duplicate heterogeneous HAZ structures. Thermal curves of the simulated HAZ specimens are shown in Figure 3.41. Specimens were heated up to various peak temperatures with a heating rate of 100 °C/s, held for 1s and then cooled to room temperature with a controlled cooling rate of 20 °C/s. Peak temperatures include 1360 °C for CGHAZ, 1060 °C for FGHAZ, 930 °C for ICHAZ-H, 910 °C for ICHAZ-L, and 850 °C for over-tempered base metal (OT-BM). The measured  $A_{c1}$  and  $A_{c3}$  are 895 °C and 955 °C, respectively.

Vickers hardness of the simulated HAZ specimens is plotted in Figure 3.42. Hardness of the simulated CGHAZ is about 440 HV0.5. The FGHAZ has a hardness of 420 HV0.5. Hardness of the ICHAZ-H and ICHAZ-L is among 380-400 HV0.5. The OT-BM increases to 320 HV0.5 from 310 HV0.5 of the BM. The overall hardness distribution of these specimens is consistent with the measured hardness profile in Figure 3.33.

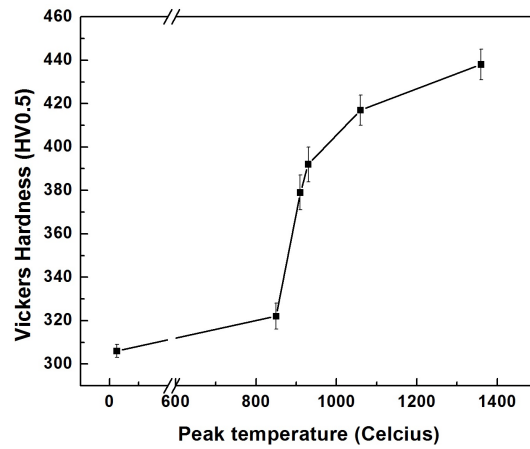


**Figure 3.42:** Vickers hardness of the simulated HAZ specimens.

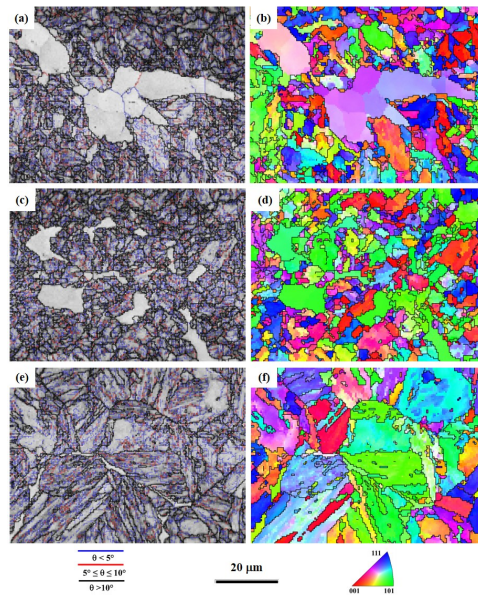


**Figure 3.43:** EBSD grain boundary map and IPF of the simulated HAZ specimens: (a), (b) 910 °C-IHAZ; (c), (d) 1060 °C-FGHAZ; (e), (f) 1360 °C-CGHAZ.

Microstructure of the simulated IHAZ-L, FGHAZ, and CGHAZ specimens are investigated by EBSD. Grain boundary maps and IPFs are presented in Figure 3.43.  $\delta$ -ferrite clusters are observed in the IHAZ-L. IPF in Figure 3.43b shows these plain  $\delta$ -ferrite grains are colored with solid colours, which indicates low misorientation inside the grains. Based on the curvature of  $\delta$ -ferrite grains in the IHAZ-L, it is likely that  $\delta$ -ferrite did not transform into austenite

at 910 °C. Dissolution of  $\delta$ -ferrite is observed in the FGHAZ specimen. Fine  $\delta$ -ferrite grains scatter in the martensitic matrix. In the CGHAZ,  $\delta$ -ferrite skeletons are observed along the prior-austenite grain boundaries. This skeletal morphology implies that these  $\delta$ -ferrite are not the original  $\delta$ -ferrite from the base metal, but the retained newly-formed  $\delta$ -ferrite during simulation. Since the 1360 °C peak temperature is high enough to promote austenite -to- $\delta$ -ferrite transformation, based on our observation, these  $\delta$ -ferrite skeletons exist in the majority of the specimen. To further investigate characteristic features of these  $\delta$ -ferrite, EBSD KAM and GAM maps are post-processed and shown in Figure 3.44. Apparently,  $\delta$ -ferrite grain exhibit a lower strain level than the rest martensite matrix. They are identified as recrystallized, or half-recrystallized grains. Martensite matrix are categorized as deformed grains with a higher strain level. Besides this, the interface between  $\delta$ -ferrite and martensite matrix shows higher strain levels.

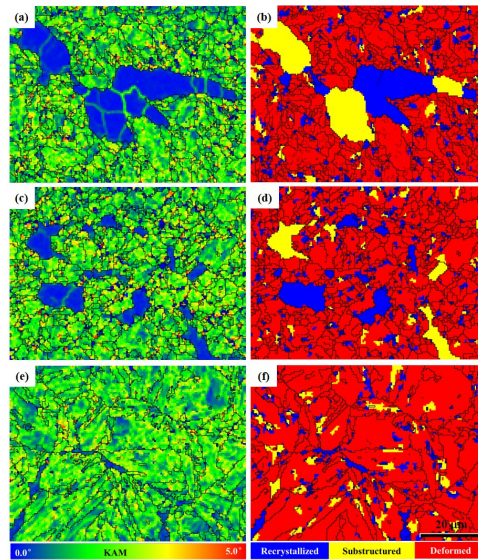


**Figure 3.44:** EBSD KAM and GAM maps of the simulated HAZ specimens: (a), (b) 910 °C-ICHAZ; (c), (d) 1060 °C-FGHAZ; (e), (f) 1360 °C-CGHAZ.

## 3.3 Discussion

### 3.3.1 Structural heterogeneity in the as-welded HAZ

Based on the results above, formation of the non-equilibrium substructures in the HAZ are from two contributors: (1) the dominate structure evolutions caused by the welding thermal cycles and (2) the local structure variations originating from the structural heterogeneities in the as-received BM.

The gradient peak temperatures and soaking times in the HAZ regions determine the heterogeneous nucleation and growth of austenitic grains and the non-equilibrium coarsening/dissolution of precipitates, which leads to the various PAG sizes and the presence of those undissolved  $M_{23}C_6$  carbides. The PAG sizes in the CGHAZ and FGHAZ are 20  $\mu\text{m}$  and 5  $\mu\text{m}$ , respectively. This PAG size difference is quantified by the frequency change of the HGABs from 29.8 % in the CGHAZ to 34.4 % in the FGHAZ. This decreased PAG size from the CGHAZ to the FGHAZ is believed to limit the martensitic transformation during the cooling cycle, which is reflected by the hardness reduction from 417 HV0.5 in the CGHAZ to 335 HV0.5 in the FGHAZ. Bhadeshia [117] and Garcia-Junceda [118] reported that the martensite-start temperature and the number of the possible martensite nucleation sites drop as the PAG size decreases. Morito's work [114] indicate that the block width and packet size decrease by refining the PAG size, and the packet number dramatically reduces when the PAG size is below 10  $\mu\text{m}$  in low carbon steels. EBSD grain boundary map in Figure 3.9b shows the decreased block size and packet number in the FGHAZ with a PAG size of 5  $\mu\text{m}$ . For the local-scale strain distribution, the strain levels in individual grain have a significant effect, which is directly determined by the phase transformations in the welding thermal cycles, especially the martensitic transformation on-cooling. KAM maps in Figure 3.8d and Figure 3.9d indicate that the local strain levels within the grains decrease from the CGHAZ to the FGHAZ and the ICHAZ. The CGHAZ has a higher fraction of deformed grains (88.1

%) and a higher KAM value ( $1.70^\circ$ ) than 56.2 % deformed grains and  $0.97^\circ$  KAM value in the FGHAZ. The welding thermal cycles also affect the behavior of the precipitates. Coarse undissolved Cr-rich  $M_{23}C_6$  carbides are only observed in the FGHAZ and ICHAZ, not in the CGHAZ. Those undissolved carbides are believed to lower the concentrations of the alloying elements, especially the carbon, dissolved in the new PAGs, which also limits the martensitic transformation by reducing the chemical free energy of the PAGs [27]. The fraction of MX carbonitrides, especially VX, is higher in the CGHAZ, as shown in Figure 3.12. Because MX has a much higher stability, they may not be completely dissolved during heating and new MX particles may nucleate during cooling, which contributes to the higher fraction in the CGHAZ. MX carbonitrides have been proved to effectively stabilize the matrix grains by pinning the migration of the mobile dislocations and keep the long-term creep strength of the steel [4, 34, 119].

The structural variations in the BM, including the width difference of the blocks, the non-uniform distribution of the precipitate, and the local strain variations, are believed to further contribute to the inhomogeneity in the HAZ regions. EBSD maps in Figure 3.2 present these inhomogeneous structures in the BM. The non-uniform densities of the precipitates and KAM values within the grains determine the various pinning forces and driving forces for austenitic transformation during heating. This  $M_{23}C_6$  density variation maybe due to the local chemistry difference and promotes the heterogeneous recovery rates of the martensitic blocks during the initial tempering process. Moreover, the effect of this structural variations from the BM affect differently in the CGHAZ, FGHAZ, and ICHAZ due to the gradient thermal cycles. High peak temperatures and long soaking times in the CGHAZ minimize this preferentially austenitic transformation, which results in a more uniform distribution of the precipitates (Figure 3.12a) and homogeneous KAM values (Figure 3.8d) within the grains. However, these heterogeneous structures in the BM take a greater effect in the FGHAZ and the ICHAZ due to the lower peak temperatures and shorter soaking times. Comparing with the structures in the BM,

the FGHAZ and the ICHAZ present even larger density variations of the precipitates (Figure 3.12b and Figure 3.12c) and higher non-uniform KAM distributions (Figure 3.9d and Figure 3.10d).

This following discussion will focus on why the identified soft zone in this as-welded thick heavy section weldment is the over-tempered base metal adjacent to the ICHAZ (Figure 3.33b), not the reported FGHAZ or ICHAZ in the Type IV cracking of the pipe weldments [7, 99]. It is known that hardness in the ICHAZ is a result of two competing effects - the hardness increase due to the martensitic transformation from the new PAGs, and the hardness decrease due to over-tempering of martensite from the base metal. In this work, hardness in the ICHAZ gradually decreases from a higher peak temperature close to the FGHAZ to a low peak temperature close to the base metal, but without a lowest dip, as shown in Figure 3.33c. This indicates the newly transformed martensite on-cooling is the main contributor to hardness in the ICHAZ. For the over-tempered base metal, there is only hardness reduction effect from the welding tempering, which causes the lowest hardness (286 HV0.5). Hardness of the normal Grade 91 base metal after normalizing and tempering is about 210-250 HV0.5, which will not be significantly reduced even after PWHT and creep. Hardness of the P91 base metal reduced only from 230 HV1 (as-welded) to 210 HV1 (PWHT-ed at 760 °C for 2 hours) and 200 HV1 (Crept at 650 °C and 70 MPa for 649 hours). Hardness of 304 HV0.5 of this heavy section base metal is much higher than 211 HV0.5 of the P91 base metal. It seems reasonable to suggest the hardness reduction in the over-tempered base metal of the heavy section is larger than that of P91 pipe, therefore, the softest region is located just outside the ICHAZ of the heavy section weldment.

### 3.3.2 Role of undissolved $M_{23}C_6$ on martensitic transformation

Microstructural analysis of both the as-welded HAZ and simulated HAZ specimens shows that there are a large number of undissolved precipitates (Cr-rich  $M_{23}C_6$  carbides) in the FGHAZ and ICHAZ. These undissolved  $M_{23}C_6$  carbides are reported to coarsen rapidly during post-weld heat treatment and creep service and cause the creep degradation of the welds. Besides their own growth, they also have a great impact on the austenitization on-heating and the subsequent martensitic transformation on-cooling, which also affects the welds' creep resistance in turn.

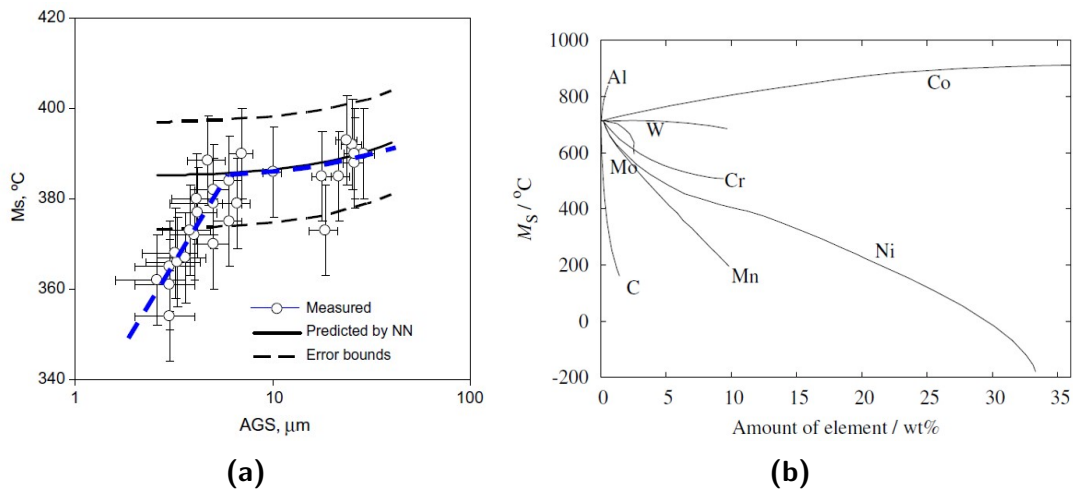


**Figure 3.45:** Effects of PAG size [118] and alloying elements [27] on the  $M_s$  temperature in low carbon martensitic steels.

It is well-known that Zener pinning effect from precipitates slows down the movement of grain boundaries during grain growth. Therefore those undissolved  $M_{23}C_6$  in Figure 3.21a played a role in limiting austenite grain growth. The austenite grain size is a key factor governing martensitic transformation during cooling. Figure 3.45a show the  $M_s$  temperature decreases rapidly with PAG size when it is below 10  $\mu\text{m}$ . Figure 3.22a shows the PAG size in our case is below 10  $\mu\text{m}$ . Meanwhile concentrations of alloying elements in the transformed austenite grains is another critical factor controlling  $M_s$  temperature. Effect of

alloying elements on  $M_s$  temperature is illustrated in Figure 3.45b. Increasing concentrations of carbon and chromium causes a decrease in  $M_s$  temperature. Cr- $M_{23}C_6$  carbide is the major source of C and Cr. Dissolution of Cr- $M_{23}C_6$  carbides will increase the C and Cr contents in high-temperature austenite, which eventually lowers the  $M_s$  temperature.  $M_s$  increase effect from PAG size and  $M_s$  decrease effect from increasing C and Cr alloying element concentrations normally work together and determine the  $M_s$  temperature of martensitic transformation in the FGHAZ and ICHAZ. Figure 3.22 shows increase of the PAG size is not significant even the holding time was extended to 600 s. Thus the  $M_s$  increase effect from PAG size is negligible. Thus, the major factor determining  $M_s$  temperature with a short holding time is alloying concentration effect from the dissolution of  $M_{23}C_6$  carbides.

Figure 3.19 indicates that hardness of transformed martensite is affected by the holding time. Holding time determines dissolution of Cr- $M_{23}C_6$  carbides. Effect of undissolved Cr- $M_{23}C_6$  carbides on hardness of transformed martensite depends on the diffused alloying elements, especially C. Carbon has been approved to directly affect martensite hardness. In low-carbon range, martensite hardness increases as carbon content. Dissolution of Cr- $M_{23}C_6$  carbides promotes more carbon dissolved into high-temperature austenite, which eventually increases transformed martensite hardness. Meanwhile, an inhomogeneous distribution of undissolved Cr- $M_{23}C_6$  carbides is observed in Figure 3.21. This can cause local variations of carbon distribution and martensite hardness differences.

### 3.3.3 Behavior of delta-ferrite in block HAZ

The following part is going to discuss why the  $\delta$ -ferrite grains were formed in the base metal and how retained  $\delta$ -ferrite grains in the HAZ may harm creep resistance of the weldment.  $\delta$ -ferrite formation traces its origin to the initial solidification during the casting process. The Cr equivalent value of 10.81 for this heavy section steel, calculated based on the Equation

3.1, is higher than 10, which shows a high potential for the  $\delta$ -ferrite formation [4].

$$Cr_{eq} = Cr + 6Si + 4Mo + 1.5W + 11V + 5Nb - 40C - 30N - 4Ni - 2Mn - 2Co(\%) \quad (3.1)$$

An isopleth of the studied steel calculated by ThermoCalc using the database TCFE6 is shown in Figure 3.46. It shows that during the solidification, the  $\delta$ -ferrite ( $\delta$ -BCC) is the first phase nucleated from the liquid and then  $\delta$ -ferrite transforms into austenite ( $\gamma$ -FCC) by a diffusive transformation mode. It is our opinion that formation of the high temperature  $\delta$ -ferrite is enhanced with higher concentrations of the ferrite-stabilizers, especially Cr. The left dash lines show that the  $\delta$ -ferrite ( $\delta$ -BCC) completely transforms into austenite ( $\gamma$ -FCC) during a slow cooling at nominal Cr concentration of 8.89 wt.%. However, micro-segregation may cause enrichment of Cr during the initial solidification of  $\delta$ -ferrite ( $\delta$ -BCC). Once the concentration of Cr exceeds the 11.76 wt.% (the right dashed line), a duplex region of  $\delta$ -ferrite ( $\delta$ -BCC) and austenite ( $\gamma$ -FCC) exists beyond the "austenite loop" when the temperature decreases. Those  $\delta$ -ferrite ( $\delta$ -BCC) grains will be retained when the temperature further cools down, which ends with a mixture of ferrite ( $\alpha$ -BCC) and  $\delta$ -ferrite ( $\delta$ -BCC). Measured Cr concentration in  $\delta$ -ferrite grains in the base metal in Table 3.9 is lower than 11.76 wt.%, but accumulated concentration of the ferrite-stabilizers in Figure 3.36 exceeds 11.76 wt.%. Another factor is that the subsequent normalizing and tempering processes may have homogenized (decreased) the as-cast distribution of Cr as well. So it is likely that  $\delta$ -ferrite grain in the as-received base metal has initially formed due to micro-segregation during the solidification. For  $\delta$ -ferrite grains in the HAZ, Cr concentration slightly decreases, but the accumulated concentration of the ferrite-stabilizers is still beyond 11.76 wt.%. This seems to support the contention that a duplex structure ( $\alpha$ -BCC+ $\delta$ -BCC) in the HAZ is thermodynamically stable after cooling.

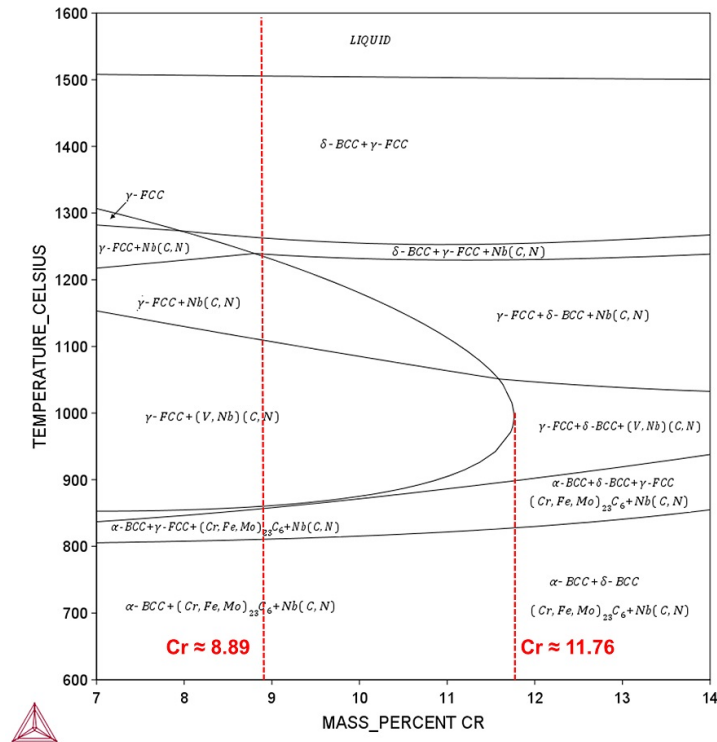


**Figure 3.46:** An isopleth of Grade 91 heavy section base metal calculated by ThermoCalc.

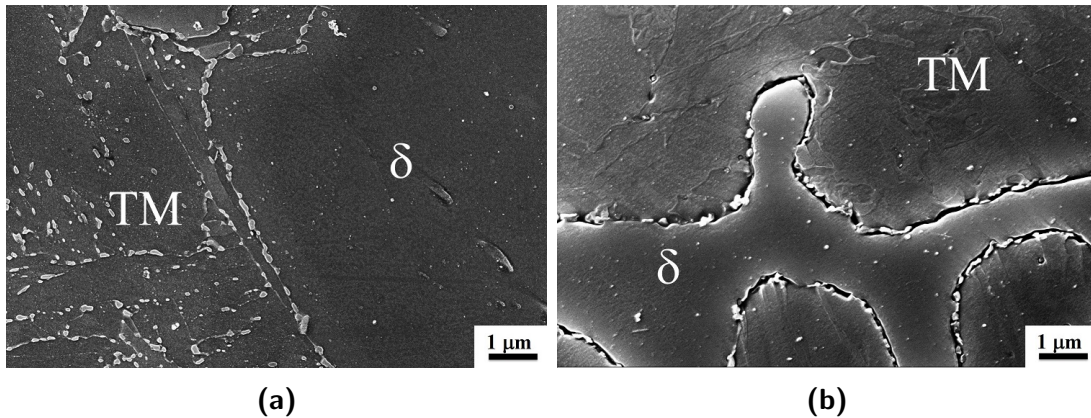


**Figure 3.47:** Inlens-SEM images of boundary precipitates between  $\delta$ -ferrite and martensitic matrix in (a) BM and (b) CGHAZ.

Presence of those  $\delta$ -ferrite grains in the HAZ brings potential harm to the creep strength, as reported by others [37–39]. Figure 3.47 compares the boundary precipitates between the  $\delta$ -ferrite grain and martensitic matrix in the base metal and the CGHAZ. A higher density of

precipitates distributes along the boundaries between  $\delta$ -ferrite grain and martensitic matrix in the base metal. Precipitates along the boundaries between  $\delta$ -ferrite grain and martensitic matrix in the CGHAZ are believed to be the un-dissolved precipitates from the base metal. The EBSD phase map in Figure 3.37c shows those precipitates are the  $M_{23}C_6$  carbides and  $Mo_2C$  carbides. High alloying concentrations in  $\delta$ -ferrite grains, as shown in the EDS maps in Figure 3.35, may promote a preferential coarsening of these carbides during PWHT and high temperature creep service. Coarsened boundary carbides and  $\delta$ -ferrite grains can cause local stress concentration, which provides the preferential nucleation sites for the creep cavities.

Results of the dilatometry studies demonstrate that  $\delta$ -ferrite behaves differently in HAZ temperature range. Dissolution of  $\delta$ -ferrite in the CGHAZ peak temperature range is significant. In the FGHAZ peak temperature range,  $\delta$ -ferrite is also dissolved. However, no dissolution of  $\delta$ -ferrite occurs in the ICHAZ peak temperature. Dissolution of  $\delta$ -ferrite is through diffusive transformation into austenite at high temperatures. At the FGHAZ temperature range, fraction of  $\delta$ -ferrite is decreased as the holding time increases. However,  $\delta$ -ferrite is still retained even when the holding time was extended to 300 s (5 min). Therefore, to improve creep resistance of the HAZ, especially FGHAZ and ICHAZ, the fraction of  $\delta$ -ferrite in the base metal should be carefully controlled. An additional heat treatment is necessary for the base metal.

## 3.4 Conclusions

The as-received pipe base metal exhibits a structure of tempered martensite and coarse precipitates along multi-scale boundaries. Islands of  $\delta$ -ferrite along the PAG boundaries, tempered martensite, and fine precipitates constitute the typical microstructure of the as-received heavy section base metal. Thickness of both the entire HAZ and each sub-region is different in the two welds. A wide ICHAZ ( $\sim 0.7$  mm-thick) is observed in the heavy section weld instead of the narrow ICHAZ ( $\sim 0.4$  mm-thick) in the pipe weld.

Structural heterogeneities in the as-received base metal and the gradient welding thermal cycles contribute to local structure variations in sub-regions of the HAZ. The CGHAZ consists of coarse PAGs with a substructure of martensite laths, fine uniformly-distributed precipitates and a higher fraction of MX carbonitrides. Fine equiaxed PAGs are observed in the FGHAZ. The ICHAZ shows a mixed structure of newly-formed PAGs and retained tempered martensite. Coarse undissolved Cr-rich  $M_{23}C_6$  carbides are only observed in the FGHAZ and ICHAZ, not in the CGHAZ. Martensitic transformation from coarse and fine PAGs contributes to various local strain distributions in the CGHAZ and FGHAZ. In the pipe weld, the FGHAZ close to ICHAZ shows the smallest grain size of  $1.22 \mu\text{m}$  with a high frequency of HAGBs (34.4 %). In the heavy section weld, the ICHAZ has the finest structure with an average martensitic block width of  $1.4 \mu\text{m}$ , the largest local strain distribution with a normalized KAM value of  $1.47^\circ$ , and large frequency (84.6 %) of the deformed grains with higher strain energies. The over-tempered base metal has the lowest hardness value of 286 HV0.5 due to the dominant tempering effect from welding thermal cycles.

The effect of undissolved Cr- $M_{23}C_6$  carbides on martensitic transformation has been analyzed by using the dilatometry method. The undissolved Cr- $M_{23}C_6$  carbides consuming alloying elements, especially C and Cr, lower their concentrations in transformed austenite. Dissolution of Cr- $M_{23}C_6$  carbides did not significantly promote grain growth of austenite on-heating, but

can efficiently lower the  $M_s$  temperature and increase martensite hardness. Structural analysis shows a structure of fine PAGs and undissolved  $M_{23}C_6$  carbides in the simulated specimens exhibits a high inhomogeneous local strain distribution.

Micro-segregation of the ferrite stabilizing elements in the  $\delta$ -ferrite grains, originated from the as-received heavy section base metal, thermodynamically stabilizes its presence in the HAZ after welding. Decomposition of the  $\delta$ -ferrite grains in the HAZ favors precipitation of dense carbides along the boundaries with the adjacent tempered martensite matrix, which is harmful to creep resistance of the HAZ. Dilatometry analysis implies that significant dissolution of  $\delta$ -ferrite only occurs in the CGHAZ region in the heavy section welds.  $\delta$ -ferrite-austenite transformation is a diffusion-controlled process.  $\delta$ -ferrite cannot be fully dissolved in FGHAZ and ICHAZ regions.

## Chapter 4

# Correlation between Intercritical Heat-Affected Zone and Type IV Creep Damage Zone in Grade 91 Steel Weldments

### 4.1 Results

#### 4.1.1 Type IV creep damage

Figure 4.1 shows a typical creep curve of a cross-weld specimen after PWHT at 760°C for 2 hours and creep tested at 650 °C under a stress of 70 MPa. The specimen failed after 649 hours with a total creep strain of 1.2 % over the gage length. The strain rate curve shows it had a short primary creep stage with a high strain rate. The majority of the creep lifetime falls under the secondary creep stage with a strain rate of  $1.3 \times 10^{-3}$  %/h. The short tertiary creep stage exhibits a low strain rate, which indicates that no large creep deformation occurred during the final rupture of the specimen.

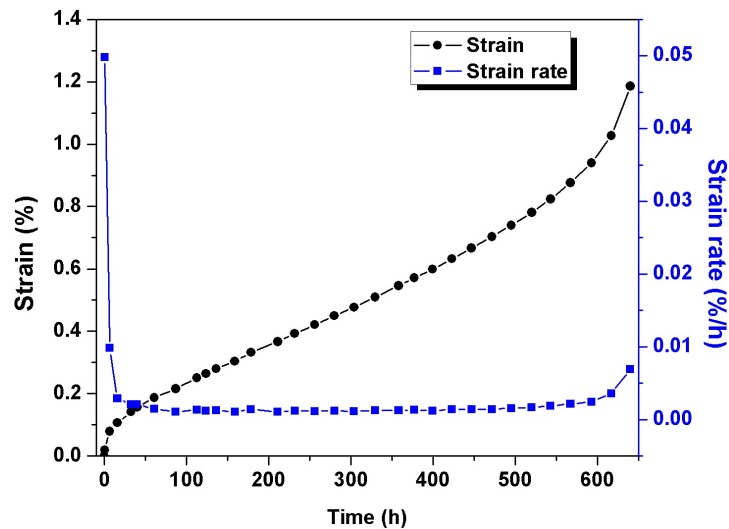


**Figure 4.1:** Typical creep curve (strain and strain rate) of the Type IV cracking in a cross-weld specimen after PWHT at 760 °C for 2 hours and creep test at 650 °C with a stress level of 70 MPa.

### 4.1.2 Soft zone identification

Figure 4.2 shows the hardness distribution across the entire weldment in the as-welded condition. The weld metal shows the highest hardness value due to a higher fraction of the un-tempered martensite formed during cooling. Large hardness variations in the weld metal are observed due to the tempering effect from the subsequent multi-passes. The base metal shows a low and uniform hardness of 230 HV0.5. The base metal adjacent to the HAZ shows a hardness dip ( $< 220$  HV0.5), which is the over-tempered zone. The hardness in the heat-affected zone itself shows a gradual decrease from the weld fusion boundary to the base metal. However, there is a small hardness dip in the HAZ, indicated by the arrow in Figure 4.2b. The magnified graph in Figure 4.2c shows this hardness dip more clearly. Correlating the hardness values to the microstructure at the indentations, this hardness dip is identified to be at the intercritical heat-affected zone (ICHAZ).

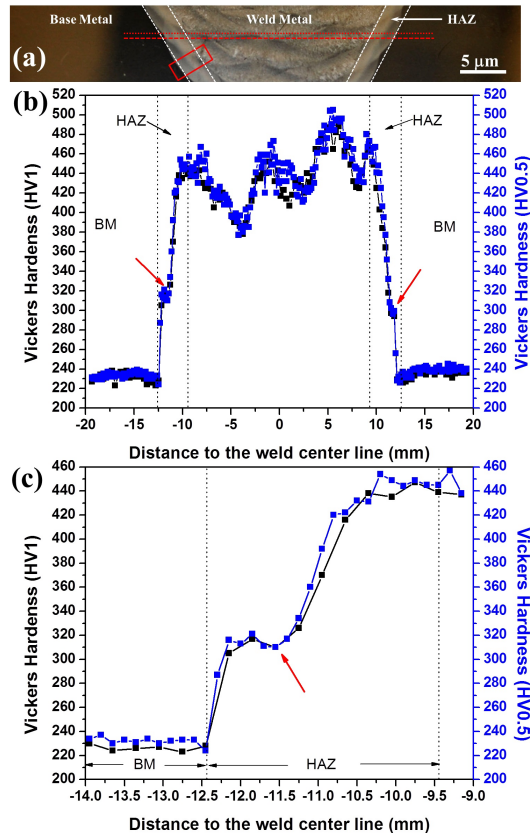


**Figure 4.2:** Hardness distribution across the as-welded weldment along the mid-thickness: (a) Optical figure of the weldment; (b) hardness profile; (c) magnified hardness profile of the HAZ (left side).

The average hardness profiles from the hardness mapping across the HAZ specimens (shown in Figure 4.2a) in three thermal conditions (i.e., the as-welded, PWHT-ed, and crept) are plotted in Figure 4.3 for comparison. The weld metal has the largest hardness decrease following the PWHT and creep, from 450 HV0.5 (as-welded) to 250 HV0.5 (PWHT-ed and crept). The base metal hardness maintains between 210 HV0.5 and 220 HV0.5 without much reduction following PWHT and creep. The HAZ hardness shows the largest changes following the three thermal conditions. A large hardness reduction is observed in the coarse-grained heat-affected zone (CGHAZ), from 425 HV0.5 to 250 HV0.5, following the PWHT. However, a smaller amount of hardness reduction is observed in the CGHAZ after the creep test. The location where the Type IV creep damage is observed in the crept specimen has

a clear hardness dip (marked by the dash-line rectangle in Figure 4.3). This hardness dip in the crept condition seems to be what others refer to as the “soft zone” [7,120]. Comparing the locations for the hardness dips in the three thermal conditions, it is clear the soft zone in the crept condition has its origin in the as-welded and PWHT-ed microstructure. The soft zone, located at 2.0 mm from the fusion line for the weld in this study, shows the lowest hardness value of 174 HV0.5 after the creep test. The most significant finding, however, is the collocation of the soft zone (identified by hardness measurements following the creep) and the ICHAZ (identified by the microstructure observation).

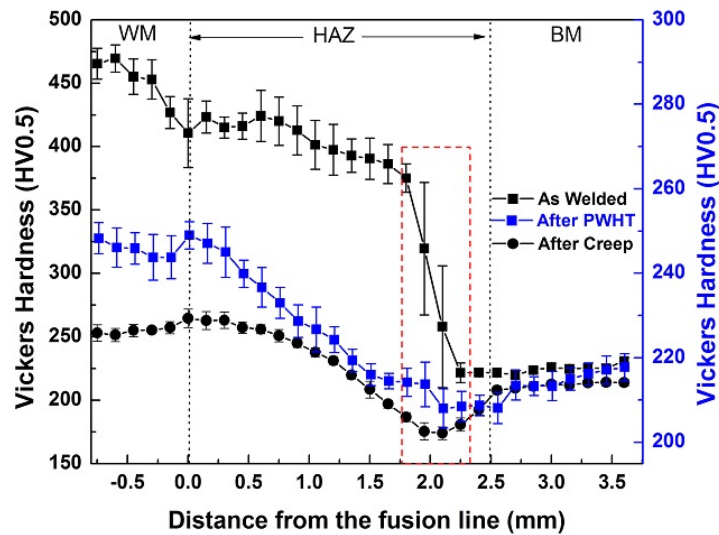


**Figure 4.3:** Average hardness profiles across the HAZ in three thermal stages: As-welded; PWHT-ed at 760 °C for 2 hours; Creep failed at 649 hours at 650 °C under a stress of 70 MPa, following a PWHT at 760 °C for 2 hours. There is a hardness vulnerable region (marked by red dash-line rectangle) in the ICHAZ.

### 4.1.3 Instrumented indentation study of the weldments

Instrumented indentation test was conducted on three HAZ specimens, the as-welded weld, the weld after PWHT-ed at 760 °C for 2 hours, and the PWHT-ed weld after creep tests at 650 °C with a stress level of 70 MPa.

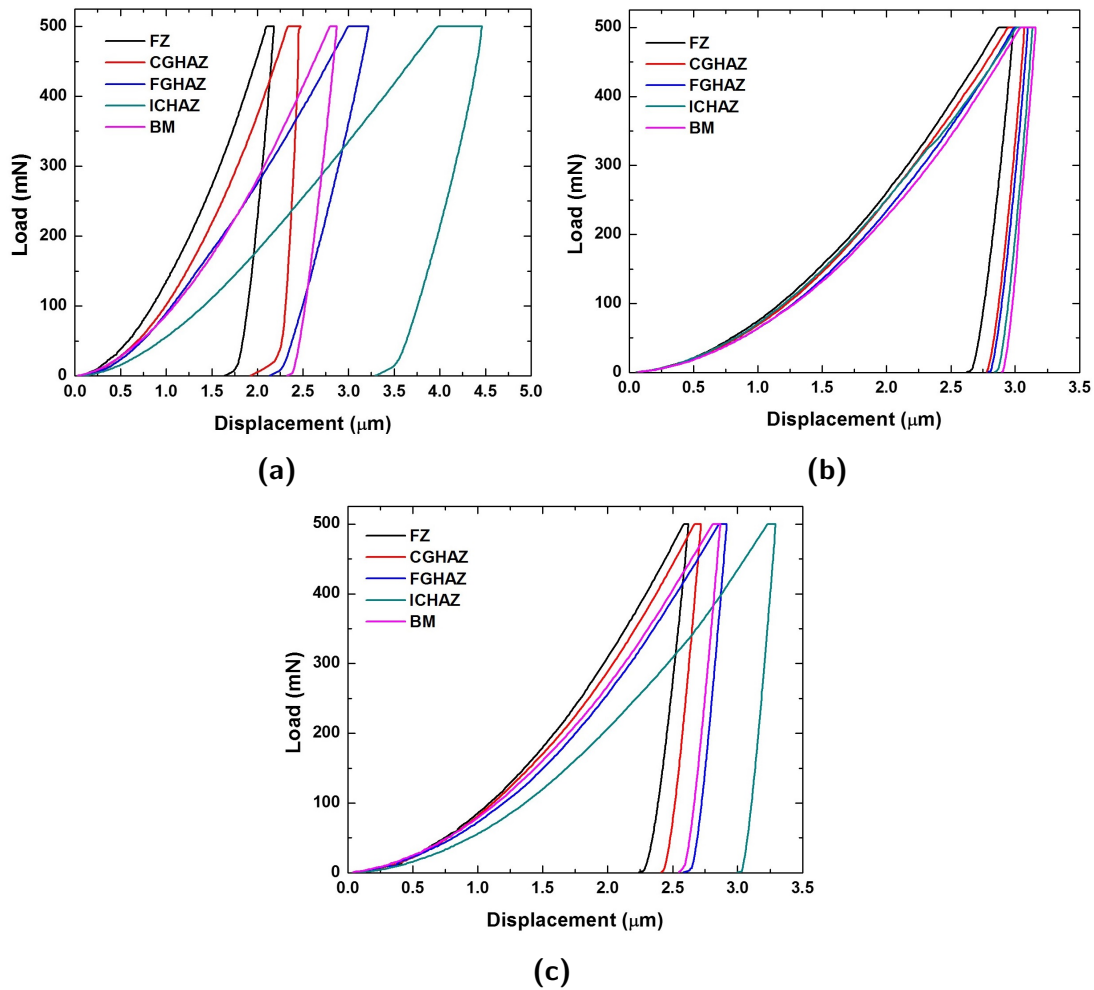
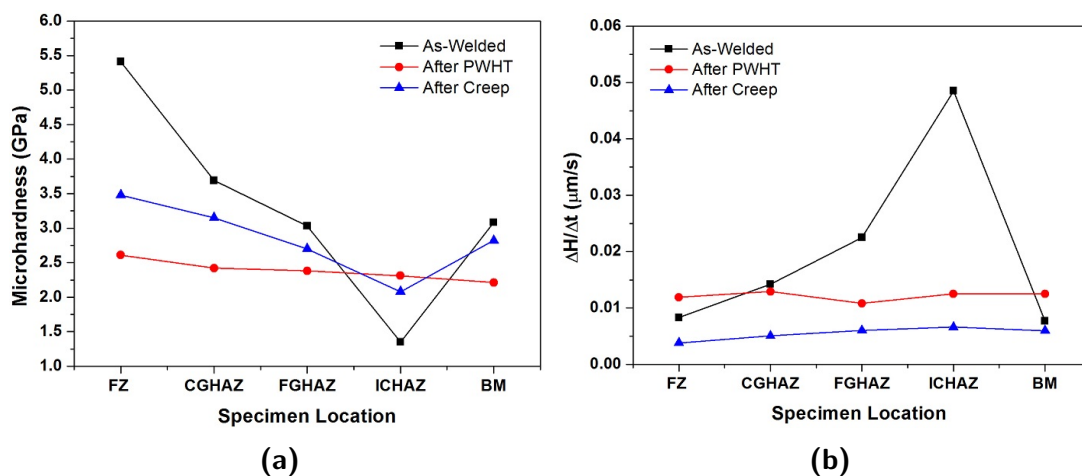


**Figure 4.4:** The load-displacement curve in three thermal stages: (a) As-welded; (b) After PWHT at 760 °C for 2 hours; (c) After creep test.

Figure 4.4 demonstrates the load-displacement curves of the instrumented indentation tests. In the as-welded condition (Figure 4.4a), it is seen that the total displacement and displacement rate are significantly different with each region. The scattered curves indicate that large variations of mechanical property exist these regions. The FZ exhibits the lowest displacement and the ICHAZ shows the largest displacement in all stages, including loading, creep, and unloading. In the PWHT condition (Figure 4.4b), the situation is totally different. All curves pack together, which implies that all regions have similar mechanical properties. In the crept condition (Figure 4.4c), after long-time creep deformation, the curves spread again,

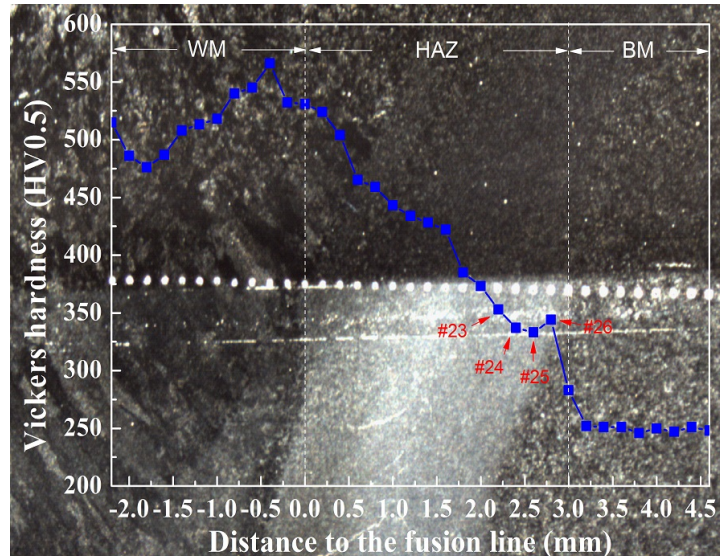
especially the ICHAZ.

The calculated hardness and creep rate from the load-displacement curves are plotted in Figure 4.5. The creep rate defined here is different from the conventional definition of  $\Delta\varepsilon/\Delta t$ . It is evaluated by  $\Delta H/\Delta t$  for the creep stage (H is the depth/displacement of the indenter). In the as-welded condition, hardness decreases from the FZ to the ICHAZ. The FZ has the highest hardness of 5.4 GPa, and the ICHAZ exhibits the lowest hardness of 1.4 GPa. Considering the creep rate in Figure 4.5b, the ICHAZ experienced the highest creep rate of  $0.05 \mu\text{m/s}$  and the FZ and BM has the lowest creep rate of about  $0.008 \mu\text{m/s}$ . In the PWHT-ed specimen, both the hardness and creep rate for each region are quite close, which indicates the entire weld is highly homogenized. In the crept specimen, hardness differences are observed among the FZ and HAZ again. The FZ is still the hardest region and the ICHAZ is the softest region. For the creep rate, there is no significant difference in each region, but the ICHAZ still has the highest creep rate. It is possible that the holding time of 10 s in the creep stage is not long enough to differentiate the creep behavior of each region.

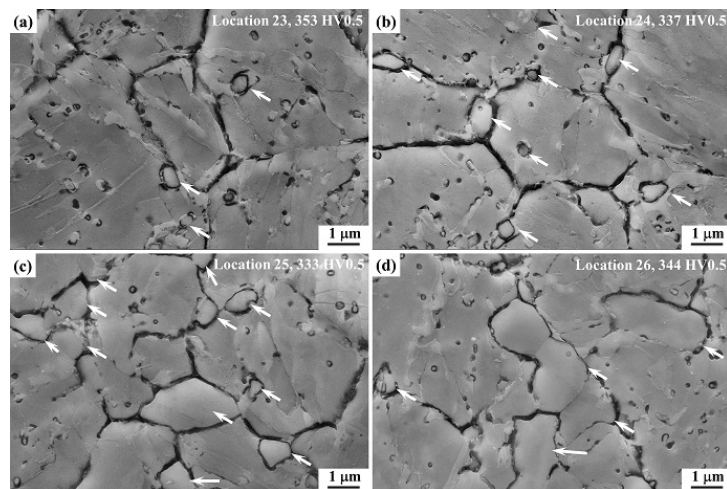


**Figure 4.5:** Instrumented indentation results: (a) Local hardness and (b) deformation rate of the welds in three thermal stages.

#### 4.1.4 Microstructure evolution of the soft zone or ICHAZ



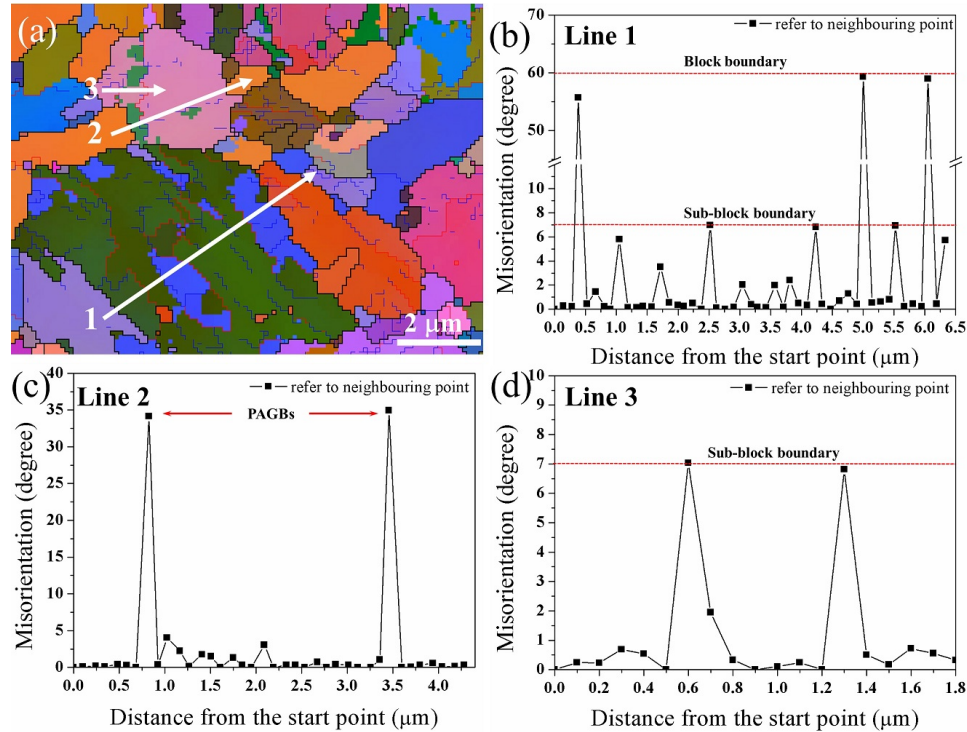
**Figure 4.6:** Optical image of the indentations and hardness distribution in as-welded HAZ. Locations associated with the soft zone are marked by #23, #24, #25, and #26.



**Figure 4.7:** SE SEM images show structure evolutions in the soft zone and neighbouring zones of as-welded HAZ. Figures (a) to (d) show correlated Locations 23, 24, 25, and 26, respectively. Retained grains are marked by white arrows in the figures.

Figure 4.7 shows the progressive structure variations over the four locations (marked by #23, #24, #25, and #26). Two different grain structures co-exist, those containing fine precipitates and substructures, and those not contain any substructure and precipitates (indicated

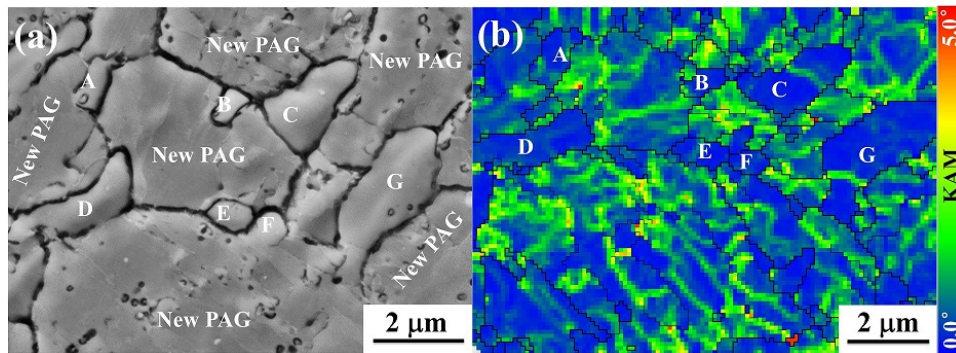
by the arrows in Figure 4.7). The size of the grains without substructures has increased from a higher temperature (Location #23) to a lower temperature (Location #26). It is likely that these two kinds of grains are re-austenitized prior austenite grains and tempered martensite retained from the base metal.



**Figure 4.8:** Local misorientation analyses to distinguish multi-scale boundaries in a location close to Location 25: (a) All Euler map. (b) Line 1 scanning misorientation indicates block and sub-block boundaries in a PAG. (c) Line 2 scanning misorientation inside a fine PAG shows the sub-block boundaries. (d) Line 3 scanning misorientation indicates PAGBs.

The misorientation line scanning in Figure 4.8 shows the various boundaries between the grains near Location #25. Line 1 in Figure 4.8b shows block boundaries with a misorientation of about  $60^\circ$  and sub-block boundaries with a misorientation of  $7^\circ$ . These two special misorientations correspond to the K-S Group 3 variant pair boundary misorientation and Group 1 variant pair boundary misorientation of the fresh lath martensite in low carbon steels and alloy steels [28]. Therefore, the coarse grain with substructures is identified as a re-austenitized grains which subsequently transformed to fresh lath martensite. The high random misorien-

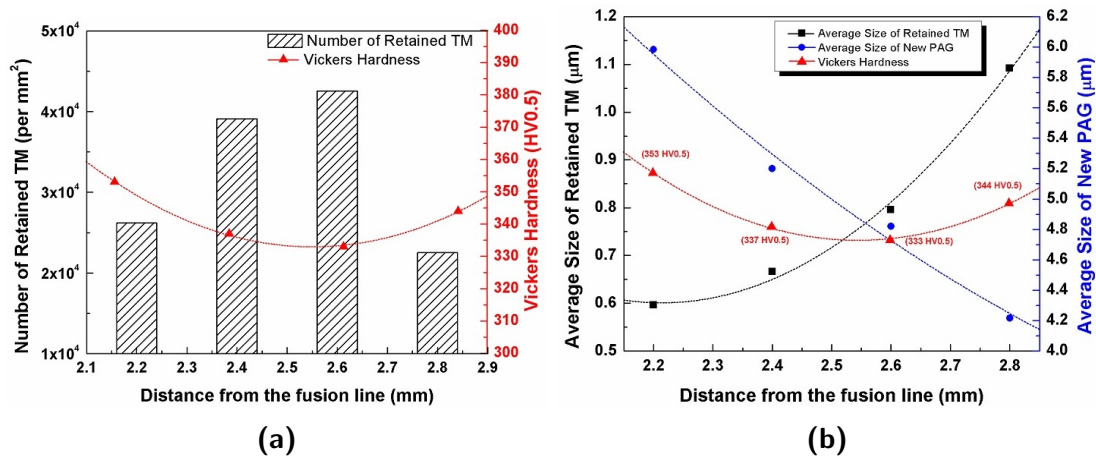
tation ( $35^\circ$ ) along the scan Line 2 (Figure 4.8c), which does not satisfy the typical block or sub-block boundary misorientations in [26], indicates that the two boundaries across the three grains are prior austenite boundaries. The two orange-colored grains (artificial color enhanced to show differences in orientation) at both ends of Line 2 in Figure 4.8a (Grain C and D in Figure 4.9a) have no substructures (or no internal boundaries). They are identified as tempered martensite retained from the base metal. The misorientation scan Line 3 in Figure 4.8d shows the K-S Group 1 variant pairs with a boundary misorientation of  $7^\circ$  inside this pink-colored grain, which implies it belongs to a re-austenitized and martensite transformed grain. Corresponding to the SEM image in Figure 4.9a, it is known that this pink-colored grain is one of two packets in a new prior austenite grain (about  $3\ \mu\text{m}$  size). Inside this packet, there is only one block with several K-S Group 1 variant pairs. This one block feature is different from the typical multi-blocks inside one packet, and is believed to be due to the refinement of the austenite grain sizes. A similar result was reported in a Fe-0.2C-1.5 Mn-1.5V alloy steel with an austenite grain size of about  $2\ \mu\text{m}$  [114].



**Figure 4.9:** EBSD analyses on the soft zone in as-welded HAZ: (a) SE SEM image. (b) Kernel average misorientation (KAM) map. Grains A-G indicate the identified retained tempered martensite.

The kernel average misorientation (KAM) map in Figure 4.9b was used to further differentiate the re-austenitized and retained grains. The KAM map in Figure 4.9b compares the local strain magnitudes inside the grains. All tempered martensite grains retained from the base metal show smaller KAM values or lower plastic strain levels (shown in the blue

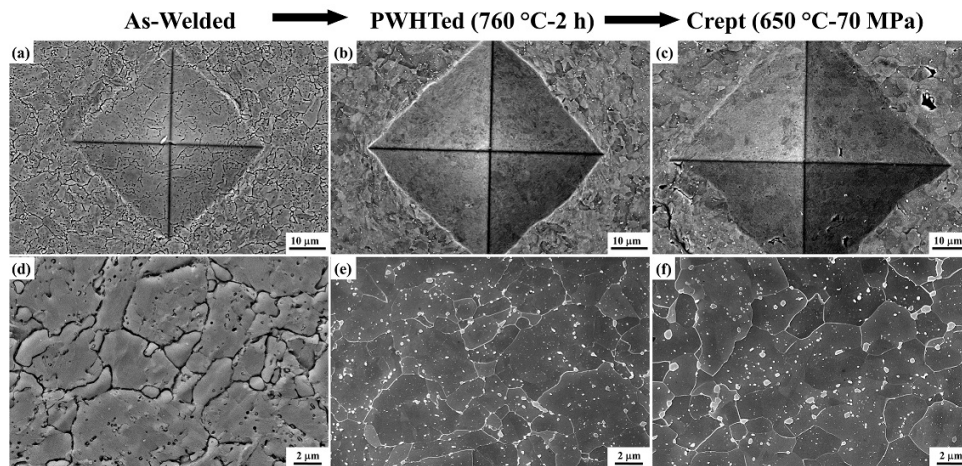
color). These retained grains from the base metal had experienced a tempering process at 786°C for 45 minutes before welding and another tempering process from the welding thermal cycles. The high-density dislocations inside the martensitic laths have been eliminated by recovery/recrystallization. On the other hand, the re-austenitized grains (in green/red colors) show higher local strain levels due to the high dislocation density generated from the martensitic transformation on weld cooling. In our previous results [109], the heat-treated HAZ still exhibits a heterogeneous local strain distribution, even though the strain levels have been decreased during the PWHT.



**Figure 4.10:** Statistical measurements of (a) the number density of retained grains and (b) average sizes of re-austenite and retained grains in the Location 23, 24, 25, and 26 (from left to right). The hardness value of each location is also shown in the figure.

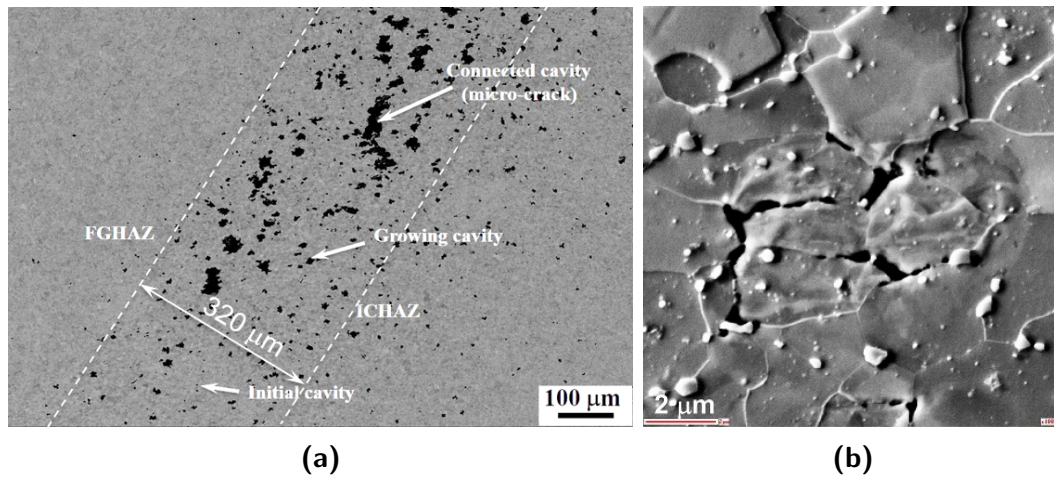
It is verified that the soft zone (near Location #25) is located in the ICHAZ, which has a mixed structure of fresh lath martensite in the re-austenitized grains, and over-tempered martensite grains retained from the base metal. Due to the gradual changes in the peak temperature, the sizes of retained grain have varied accordingly. As shown below, the higher the peak temperature, the smaller the grain size of the retained grains. To further differentiate structures of the Location 25 and three other neighboring locations (Locations 23, 24, and 26), as shown in Figure 4.7, the re-austenite size and retained grain size/number in each

location were measured. The statistically measured number density of the grains from low magnification SEM images are plotted in Figure 4.10. One significant observation is that the density (number) of the retained grains in those four locations shows an opposite tendency with the hardness values. Location 23 (higher peak temperature) has a smaller number of retained grains ( $26,194/\text{mm}^2$ ), the largest re-austenite size of  $5.98 \mu\text{m}$ , and the smallest retained grain size of  $0.60 \mu\text{m}$ , which is also shown in Figure 4.7a. Locations 25 and 24, show the moderate values of re-austenite size and retained grain size, with Location 25 having the highest number of retained grains,  $42,565/\text{mm}^2$ . These examined locations are in the ICHAZ but adjacent the higher temperature region of the HAZ. The peak temperature they experienced is around the  $A_{c3}$ , which is the finish temperature of ferrite-to-austenite transformation. Location 26 (lower peak temperature) has the lowest number of retained grains,  $22,535/\text{mm}^2$ , but the largest grain size of  $1.09 \mu\text{m}$ , and the finest re-austenite size of  $4.22 \mu\text{m}$ . Further away from the fusion line, the experienced peak temperature is closed the  $A_{c1}$ , the start temperature for ferrite-to-austenite transformation. The size of the retained grain is large but the number is fewer. It seems that presence of those retained grains has a significant effect in reducing the hardness at the soft zone. The “martensite-free” band proposed by Parker [86] seems to be the over-tempered grains retained from the base metal, which are essentially ferrite grains. The retained grains are highly recovered and have a low dislocation density, as shown in Figure 4.9b.



**Figure 4.11:** Microstructure evolution of the identified soft zones in ICHAZ from Figure 4.3. (a) and (d) As-welded. (b) and (e) After PWHT. (c) and (f) After creep tests.

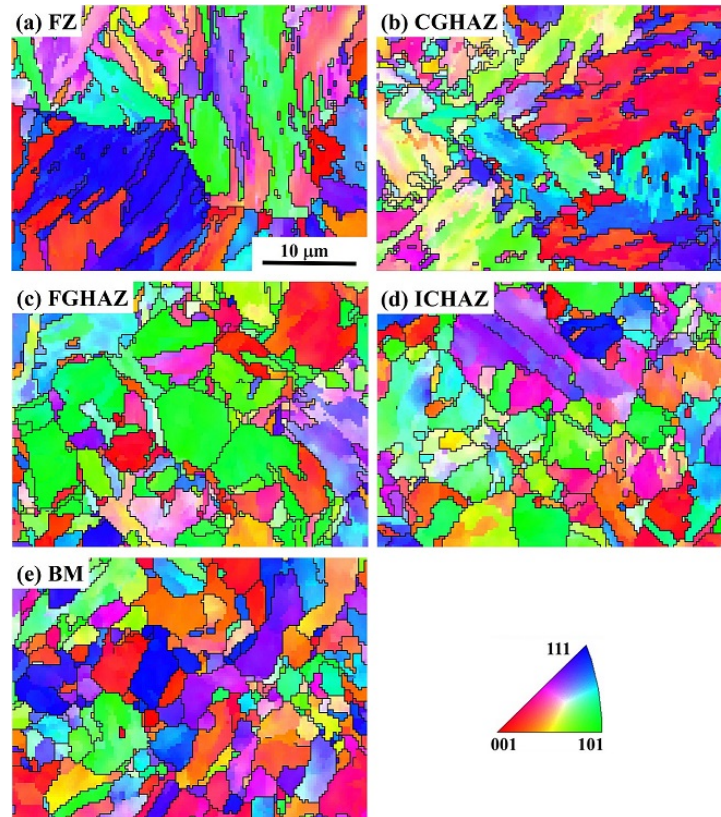
Figure 4.11 compares microstructures of three identified soft zone. In the as-welded condition (Figure 4.11a and 4.11d), average sizes of the matrix grains and  $M_{23}C_6$  carbides are  $1.84 \mu\text{m}$  and  $179 \text{ nm}$ , respectively. The preferential austenitic transformation resulted in a highly heterogeneous structure with various local misorientations and recovery/recrystallization potentials, as shown in Figure 4.9b. Figure 4.11b and 4.11e shows a significant recovery/recrystallization and grain growth of the martensitic laths and retained grains after PWHT. The average grain size increased to  $3.51 \mu\text{m}$  and the hardness decreased ( $206 \text{ HV}_{0.5}$ ) after heat-treating at  $760 \text{ }^\circ\text{C}$  for 2 h. After creep test, a large grain size variation is observed in Figure 4.11e, which is due to the heterogeneous grain growth. Coarsened precipitates (average size  $246 \text{ nm}$ ) are observed not only along the grain boundaries but also inside the grains. Those precipitates inside the grains are believed to have originated from the undissolved  $M_{23}C_6$  carbides observed in the as-welded condition. The coarsened, soft, grains and precipitates lead to a low creep-resistance and a low hardness in the soft zone. It must be noted that the formation of creep cavities in the soft zone is believed to be a compounding contributor to the extremely low hardness  $142 \text{ HV}_{0.5}$  shown in Figure 4.11c.



**Figure 4.12:** Evolution of creep cavities in the ICHAZ during the Type IV cracking.

It is indicated that these soft retained grains mixed with harder re-austenite grains would increase the potential for creep cavity formation by non-uniform shearing. Coarse  $M_{23}C_6$  carbides are believed to cause local stress concentration, especially at the triple points of the grain boundaries between the soft and hard grains [4,68]. Figure 4.12 shows the creep cavities have nucleated around the coarse precipitates at a triple grain boundary junction in the Type IV cracking. It is also observed that the strong boundary between the two deformed grains in the center is free of precipitates (Figure 4.12). This suggests that the presence of the coarse carbides may weaken grain boundaries as well.

### 4.1.5 Characteristic structures of the welds in Type IV cracking

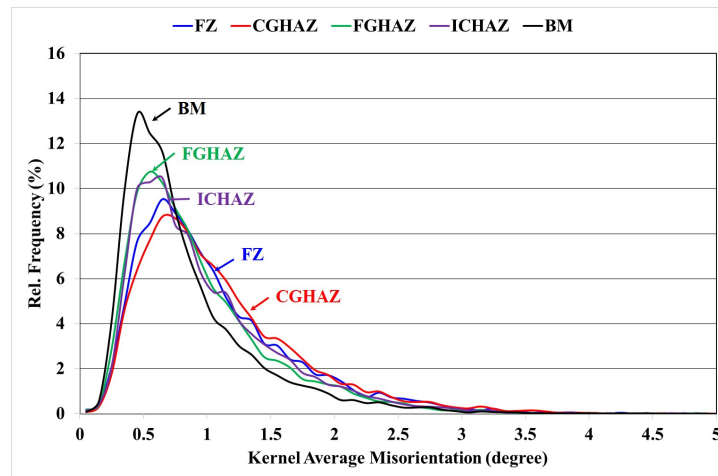


**Figure 4.13:** EBSD IPF of the weld PWHT-ed at 760 °C for 2 hours: (a) Fusion zone; (b) CGHAZ; (c) FGHAZ; (d) ICHAZ; (e) Base metal.

Microstructure of the weld PWHT-ed at 760 °C for 2 h are presented by IPFs in Figure 4.13. The FZ and CGHAZ still show a martensitic structure of lath martensite inside PAGs. The FGHAZ and ICHAZ have a mixed structure of lath-like grains and coarse equiaxed grains. Fine equiaxed grains are observed in the FGHAZ, ICHAZ, and BM. The measured crystal grain size of each region from grain boundary maps is listed in Table 4.1. Different from grain size observed from optical or SEM images, the grain sizes of each region are close between 1.80-2.10  $\mu\text{m}$ . Even the crystal grain size is similar, but larger grain size variations exist in the FGHAZ and ICHAZ. This indicates heterogeneous grain growth in these two regions.

**Table 4.1:** EBSD grain boundary and size analyses on the weld PWHT-ed at 760 °C for 2 hours.

Location	FZ	CGHAZ	FGHAZ	ICHAZ	BM
Grain size by line-intercept method ( $\mu\text{m}$ )	1.80	2.10	1.79	1.95	2.00
Grain size standard deviation ( $\mu\text{m}$ )	1.71	2.56	1.87	1.73	1.53
HAGB frequency ( $\geq 10^\circ$ , %)	35.0	35.7	40.0	37.0	44.2
LAGB frequency ( $< 10^\circ$ , %)	65.0	64.7	60.0	63.0	55.8
Ratio of HAGB/LAGB	0.54	0.55	0.67	0.59	0.79

**Figure 4.14:** KAM distribution in the weld PWHT-ed at 760 °C for 2 hours : (a) Fusion zone; (b) CGHAZ; (c) FGHAZ; (d) ICHAZ; (e) Base metal.

The frequency of KAM values is shown in Figure 4.14. The KAM peak of BM is located in a lower value ( $0.45^\circ$ ). The FGHAZ and ICHAZ show a similar KAM distribution. The KAM peaks of the FZ and CGHAZ shift toward a higher value of  $0.65^\circ$ . The frequencies of deformed, substructure, and recrystallized grains in each region are tabulated in Table 4.2. There is no significant difference between each region, except the BM. This is probably because the martensite in the FZ and HAZ is still in the early stage of tempering. These

tempered martensite with high strain are still identified as deformed grains.

**Table 4.2:** EBSD KAM and GAM analyses on the weld PWHT-ed at 760 °C for 2 hours

Location	FZ	CGHAZ	FGHAZ	ICHAZ	BM
Normalized KAM value (°)	1.06	1.10	0.95	0.98	0.84
Deformed grain frequency (%)	81.0	80.3	79.7	80.9	67.1
Substructured grain frequency (%)	12.6	11.5	11.2	11.8	22.1
Recrystallized grain frequency (%)	6.4	8.2	9.1	7.3	10.8

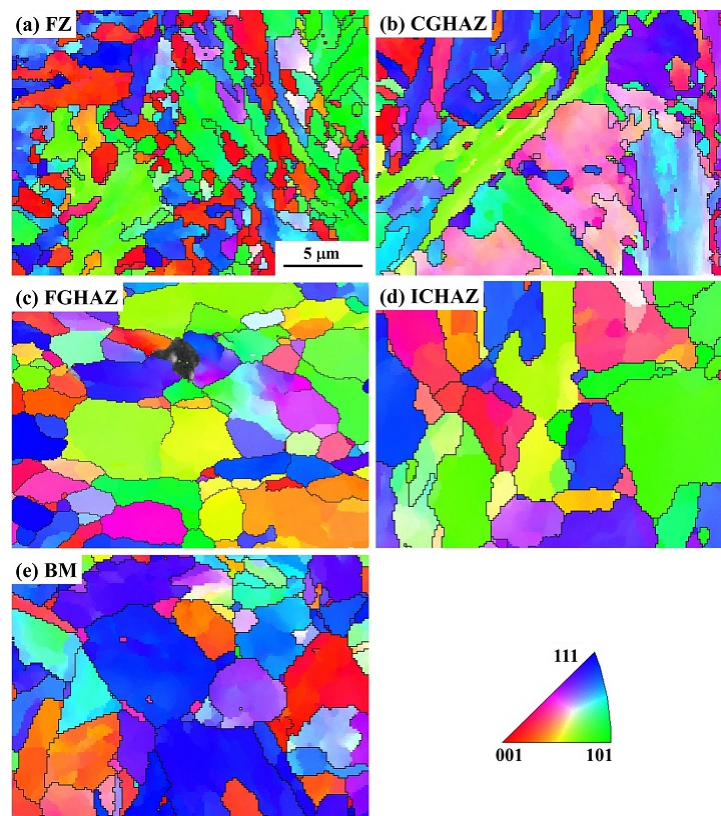


**Figure 4.15:** EBSD IPF of the crept weld PWHT-ed at 760 °C for 2 hours: (a) Fusion zone; (b) CGHAZ; (c) FGHAZ; (d) ICHAZ; (e) Base metal.

A crept weld failed with the Type IV cracking was analysed by EBSD. The weld was

PWHT-ed at 760 °C for 2 hours. It should be noted that the location of the observed FGHAZ is in the transition region between the FGHAZ and ICHAZ. The creep damaged region associated with cavities can be also regarded as the ICHAZ.

EBSD IPFs are shown in Figure 4.15. FZ and CGHAZ exhibit martensitic structures which are different from the equiaxed grains observed in the FGHAZ, ICHAZ, and BM. A number of fine equiaxed grains are also observed in the FZ. These grains are likely recrystallized grains from martensite matrix. The grain sizes of each region measured from EBSD grain boundary maps are listed in Table 4.3. FZ has the finest grain size of 0.92  $\mu\text{m}$ . FGHAZ has the coarsest grain size of 2.16  $\mu\text{m}$ . Relative frequency of the HAGBs and LAGBs in each region is calculated and tabulated in Table 4.3. Due to recrystallization and growth of grains, the FGHAZ and ICHAZ share the highest frequency (about 55.5 %) of HAGBs. The CGHAZ has the highest frequency of LAGBs because of the lath boundaries in martensitic structures.

**Table 4.3:** EBSD grain boundary and size analyses on the crept weld PWHT-ed at 760 °C for 2 hours.

Location	FZ	CGHAZ	FGHAZ	ICHAZ	BM
Grain size by line-intercept method ( $\mu\text{m}$ )	0.92	1.27	2.16	1.87	1.92
Grain size standard deviation ( $\mu\text{m}$ )	0.83	1.43	1.98	1.51	1.73
HAGB frequency ( $\geq 10^\circ$ , %)	44.1	40.2	55.6	55.4	42.7
LAGB frequency ( $< 10^\circ$ , %)	55.9	59.8	44.4	44.6	57.3
Ratio of HAGB/LAGB	0.79	0.67	1.25	1.24	0.75

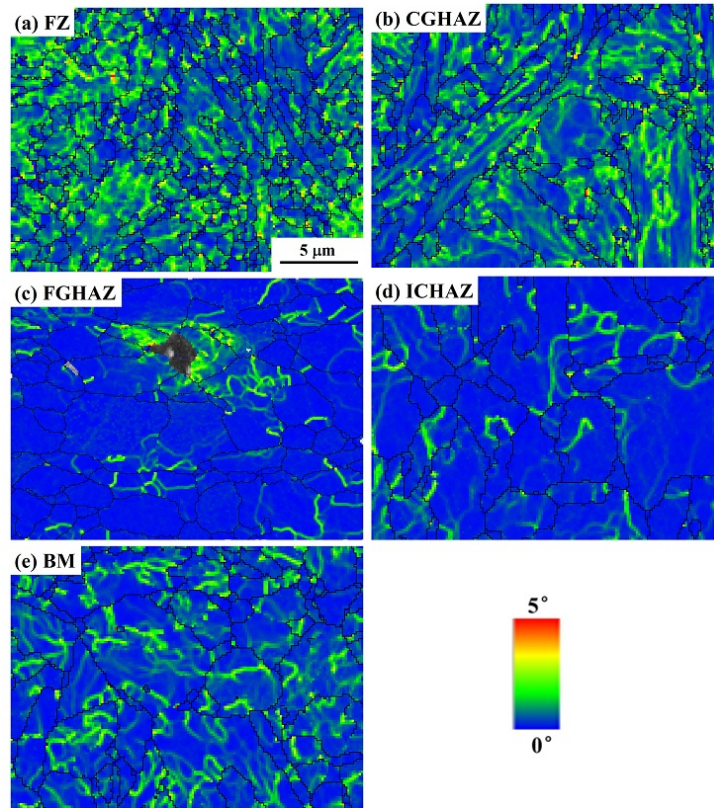


**Figure 4.16:** Local strain distribution in the crept welds: (a) Fusion zone; (b) CGHAZ; (c) FGHAZ; (d) ICHAZ; (e) Base metal.

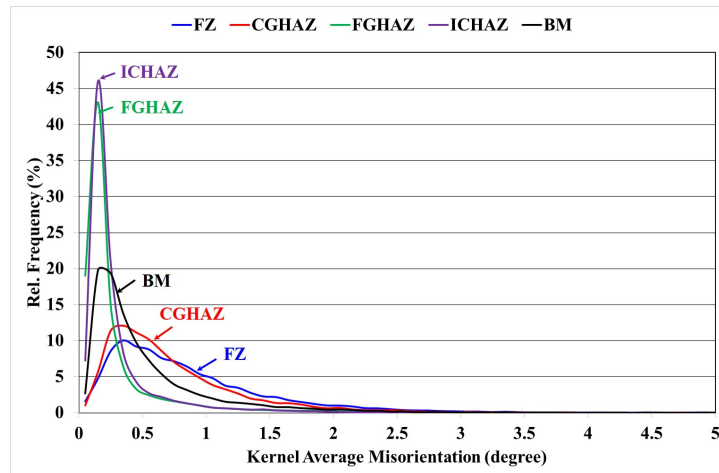


**Figure 4.17:** KAM distribution in the crept welds: (a) Fusion zone; (b) CGHAZ; (c) FGHAZ; (d) ICHAZ; (e) Base metal. The high KAM region in (c) is associated with a creep cavity.

Based on the KAM maps in Figure 4.16, the strain energy of each region can be ranked

this order: FZ > CGHAZ > FGHAZ > ICHAZ. The KAM distribution of each region in Figure 4.17 further confirms this order. The KAM peaks in FZ and CGHAZ shift toward higher values. It should be noted that the high KAM region in the FGHAZ (Figure 4.16c) is associated with a creep cavity. Its high KAM value demonstrates the high local deformation of grains around the cavity. Normalized KAM values from Figure 4.17 are listed in Table 4.4. The FZ has the highest normalized KAM value of  $0.85^\circ$ . The FGHAZ and ICHAZ have the lowest normalized KAM value of  $\sim 0.29^\circ$ .

**Table 4.4:** EBSD KAM and GAM analyses on the crept weld PWHT-ed at  $760^\circ\text{C}$  for 2 hours.

Location	FZ	CGHAZ	FGHAZ	ICHAZ	BM
Normalized KAM value ( $^\circ$ )	0.85	0.73	0.29	0.30	0.52
Deformed grain frequency (%)	53.5	52.0	4.2	3.3	11.6
Substructured grain frequency (%)	31.8	37.7	45.0	62.7	67.9
Recrystallized grain frequency (%)	14.7	10.3	50.8	34.0	20.5

The GAM evaluation was used to quantify the fraction of recrystallized grains in each region. The GAM results are shown in Table 4.4. Area fraction of recrystallized grains in the FZ and CGHAZ are 31.8 % and 37.7 %, respectively, which are lower than the FGHAZ's 50.4 % and ICHAZ's 34.0 %. The total fraction of recrystallized grains and substructured grains are almost equal in the FGHAZ and ICHAZ. The fraction of deformed grains in FGHAZ and ICHAZ is significantly low. These results indicate the structures in the FGHAZ and ICHAZ are highly recrystallized, which corresponds to their low creep resistance.

From a structure point of view, the Type IV cracking occurs in the creep-susceptible region where has the largest grain size, the highest frequency HAGBs, the lowest KAM value, the highest fraction of recrystallized grains, and the largest precipitate-distribution inhomogeneity, and the coarsest precipitate size.

## 4.2 Discussion

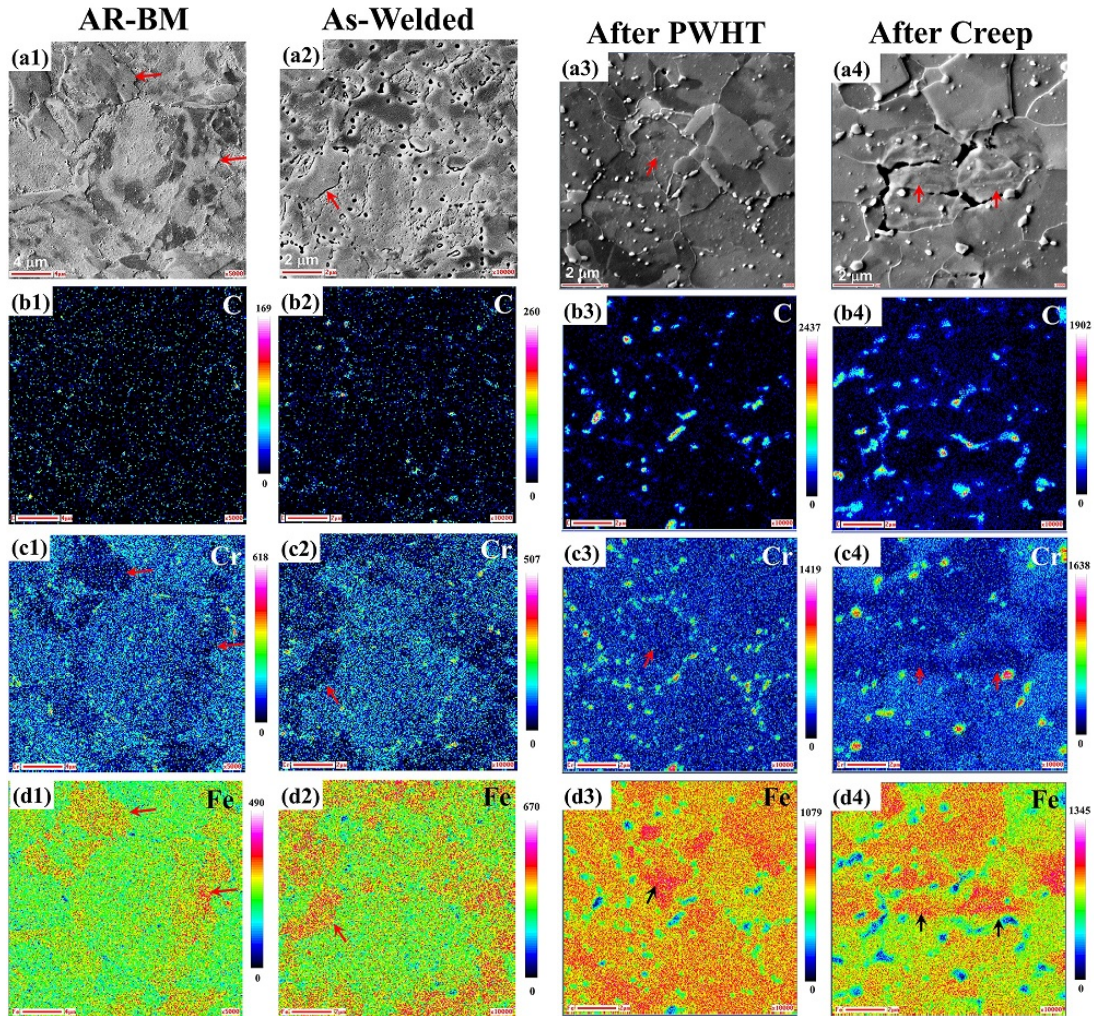


**Figure 4.18:** Local chemistry analysis of the as-received base metal and the identified soft zone (ICHAZ) at three thermal stages by mapping C, Cr, and Fe with auger electron spectroscopy.

In the ICHAZ, which becomes the soft zone after creep, there is a mixture of retained base metal microstructure and newly re-austenitized microstructure. However, it is not clear why only certain grains would transfer into austenite while other close-by grains would not, all under the same welding temperature distribution. Local chemistry analysis was conducted to clarify the mechanism of this preferential re-austenitization. The distribution of the main elements including C, Cr, and Fe is measured in a grain-scale by Auger electron spectrometry.

Both the as-received base metal and the soft zones at three thermal stages are examined. The Auger maps of the C, Cr, and Fe are shown in Figure 4.18.

In Grade 91 steel, carbon and chromium are the dominant alloying elements. It is known that the diffusion of interstitial carbon in steel is orders of magnitude faster than the diffusion of substitutional Cr. In the as-received base metal, the carbon distribution (Figure 4.18b1) is uniform. The high-intensity spots of carbon are corresponding to the precipitated carbides. However, the Cr map in Figure 4.18c1 exhibits large variations in its distribution. This non-uniform distribution exists on two scale levels; the austenite grain level, and the martensitic packet/block level. Firstly, the Cr concentration varies from one austenite grain to another. The austenite grain in the center shows a higher Cr content than the adjacent grains in Figure 4.18c1. Secondly, the martensitic packets inside the same austenite show different Cr concentrations as well. The left packet in the austenite grain in the center has a higher Cr content than that of the right packet. Since Cr is the dominant alloying element, the Fe map in Figure 4.18d1 shows the opposite trend with the Cr. The high Cr intensity spots indicate the Cr-rich carbides. This non-uniform distribution of Cr is likely due to macro-segregation during solidification in the steel making. Zhang et al. [121] observed significant heterogeneity in the distribution of Cr in the solidified Grade 91 weld metal.

After welding, the carbon distribution is uniform in the inter-critical heat-affected zone, as shown in Figure 4.18b2. However, the non-uniform distribution of Cr exists between the retained grains and re-austenitized grains in the soft zone. The grains marked by a red arrow with a lower Cr concentration are the retained grains. The re-austenite grains adjacent to the retained grains exhibit a higher Cr concentration. Sawada et al. [122] reported a non-uniform Cr distribution (4 wt.% difference) between the fine grains and the other matrix grains of an as-welded HAZ. Based on the results of EDS point analysis, the Cr content difference is about 2 wt.% in this work. The undissolved Cr-rich carbides, only observed in the re-austenite grains, may contribute to the Cr heterogeneity. The alloying elements in

the steels have a great impact on the formation of austenite. The tempered martensite-to-austenite transformation potential may be controlled by the slower moving chromium. Chromium is known to be a ferrite-stabilizer at high concentrations ( $>13.4$  wt.%) [123]. However, chromium at low concentrations may become an austenite-stabilizer by widening the austenite loop with a depression of the  $A_3$  temperature [123]. Austin et al. [124] reported the  $A_3$  temperature significantly decreases at low Cr concentrations (0~10 wt. %) with a minimum value at 9 wt.% Cr in a 0.02C alloy steel. The nominal Cr concentration in the Grade 91 steel is 8.47 wt.%, which is in the low chromium concentration range. A hypothesis is that during the welding thermal cycles, the Cr-rich martensite packets observed in Figure 4.18c1 will preferentially transform into austenite that also has a higher Cr concentration (Figure 4.18b2), but the martensite packets with lower Cr will not transform and become the retained grains (Figure 4.18b2).

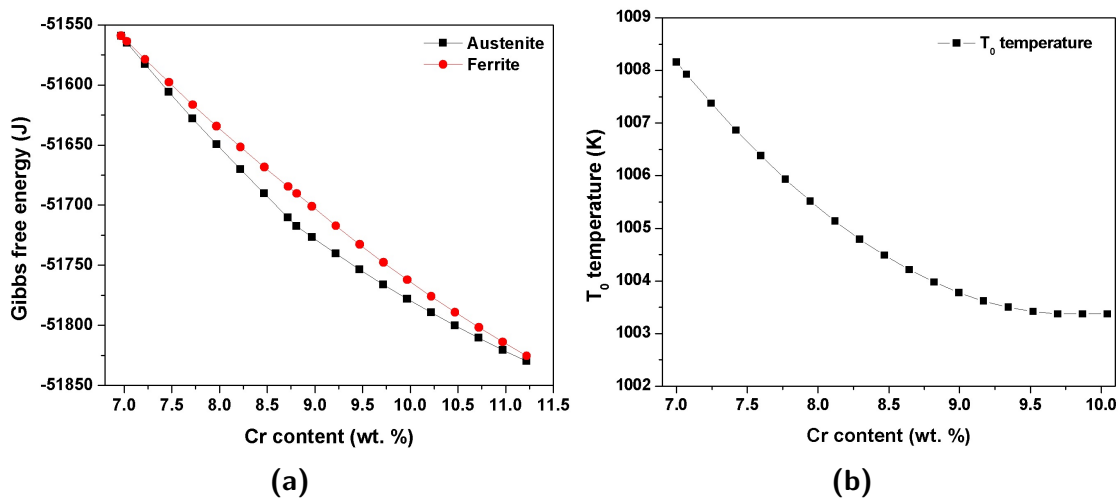


**Figure 4.19:** Effect of low chromium concentrations (7-10 wt.%) on (a) the Gibbs energy of ferrite and austenite and (b)  $T_0$  temperature of ferrite-to-austenite transformation at 820 °C.

To verify this hypothesis, effects of low Cr concentrations on the Gibbs free energy of ferrite and austenite, and the  $T_0$  temperature of ferrite-to-austenite transformation are studied by using ThermoCalc<sup>TM</sup>. The calculated Gibbs free energy of the ferrite and austenite at

820°), just above the critical  $A_1$  temperature of 818°C for the alloy under study, is shown in Figure 4.19a. The lower Gibbs free energy of austenite implies that the austenite is more stable than the ferrite at a Cr range of 7-10 wt.%. The Gibbs free energy difference between austenite and ferrite increases with an increasing Cr concentration above 8.47 wt.%, which indicates that the driving force for the ferrite-to-austenite transformation is increasing with a higher Cr concentration. The  $T_0$  temperature is an index to evaluate the relative stability of ferrite and austenite during transformation.  $T_0$  temperature at low chromium concentrations (7-10 wt.%), calculated with the nominal composition of the test Grade 91 steel, is shown in Figure 4.19b. It shows the  $T_0$  temperature decreases from 735 °C to 730 °C as Cr concentration increases from 7 wt.% to 10 wt.%, which means that thermodynamically the tempered martensite with a lower chromium concentration has a lower potential to transform into austenite. This shows an agreement with our experimental observation. The retained grains in the as-welded soft zone, marked by the red arrow in Figure 4.18c2 has a lower chromium concentration. It is believed that these retained grains have originated from tempered martensite with lower chromium concentrations in the as-received base metal, such as the one marked by a red arrow in Figure 4.18c1. Therefore, grains with higher Cr will preferentially transform to austenite on weld heating.

Figure 4.18c3 shows the heterogeneity of the Cr distribution inside the grains still exists but has relatively decreased due to the PWHT tempering effect. The coarsened carbides exhibit a concentrated Cr content (high-intensity spots in Figure 4.18c3). The grains containing a large number of Cr-rich carbides are more likely to transform into austenite with undissolved carbides (Figure 4.18c3). After the creep test, the chemical analysis was conducted on the location shown in Figure 4.18. The coarsened Cr-rich carbides are identified by the high-intensity spots in Figure 4.18b4 and 4.18c4. Creep cavities seem to be always associated with the Cr-rich carbides at the grain boundaries. Additionally, the chromium distribution in the creep tested specimen is even more non-uniform (Figure 4.18c4), comparing with the

distribution after heat-treatment in Figure 4.18c3. The deformed grains marked by red arrows exhibit low Cr concentrations. It is implied that these Cr-depleted deformed grains have a lower strength than the neighboring grains with higher Cr concentrations. All the results above indicate the distribution heterogeneity in chromium from the base metal has contributed to the heterogeneous phase transformations and microstructural evolution in the ICHAZ, which becomes the creep damaged soft zone. Lowering the micro-segregation of chromium in the grain scale of the base metal might be a direction to improve the creep resistance of the welded 9-12 % Cr creep strength enhanced ferritic steels.

Based on the accumulated evidences/results, a hypothesis of the Type IV cracking mechanism is proposed. This hypothesis is illustrated in Figure 4.20. Details of this hypothesis is described as follows:

(a) Micro-segregation or inhomogeneity of alloying elements, especially C and Cr, exists in both the PAG-scale level and the martensitic packet/block-scale level in the as-received Grade 91 base metal. Those Cr-rich PAGs and packets (darker-yellow grains in 4.20a) exhibit a higher chemical potential to undergo an austenitic transformation on welding-heating.

(b) Under the rapid heating thermal cycle of arc welding, ICHAZ is exposed to peak temperatures between  $A_{c1}$  and  $A_{c3}$  of the base metal. Heterogeneous ferrite-to-austenite transformation occurs in the ICHAZ, which is caused by non-uniform chemical potentials from the micro-segregation in the base metal. Those Cr-rich PAGs and packets with a higher Cr concentration close to 9 wt.% have a higher driving force (a large Gibbs free energy difference between ferrite and austenite) and preferentially transformed into new Cr-rich austenite (darker-yellow grains in 4.20b). During cooling, these transformed austenite grains transform into martensite. Due to the limited short-time exposure of high temperatures, the Cr-depleted ferrite grains do not transform and remain untransformed. Instead, these untransformed grains are over-tempered with low local strain energies. Therefore, after welding, the as-welded soft zone (ICHAZ) has a mixed structure of Cr-rich transformed hard martensite and Cr-depleted

untransformed and over-tempered soft ferrite. Some of the coarse Cr-rich  $M_{23}C_6$  carbides were not fully-dissolved and retained in the structure.

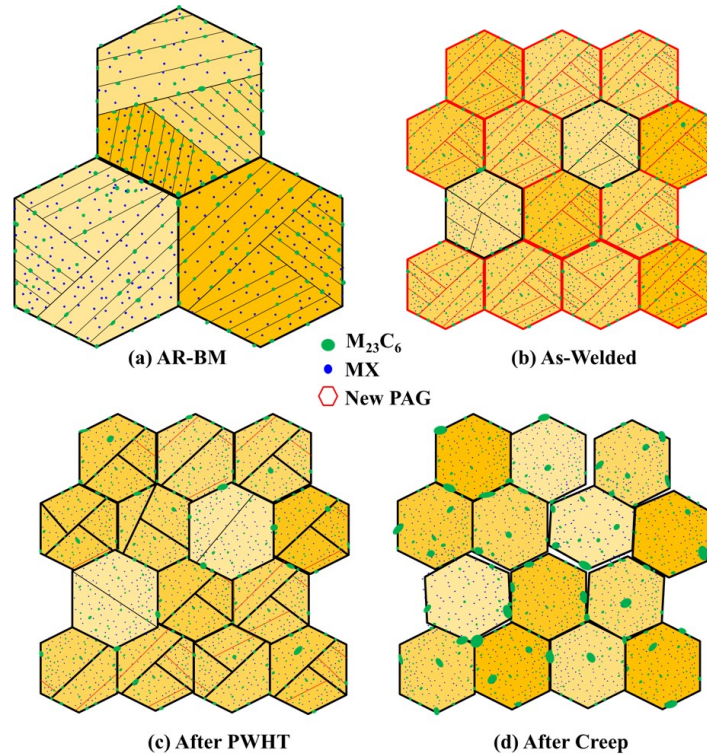


**Figure 4.20:** Schematic illustration of microstructure evolution in the ICHAZ in the Type IV cracking.

(c) In the PWHT condition ( $T < A_{c1}$ ), Tempering (recovery/recrystallization and grain growth) of the Cr-rich transformed martensite and Cr-depleted untransformed ferrite grains occurred in the ICHAZ. Those untransformed soft ferrite grains undergo a preferential grain growth. Meanwhile, the state of those newly-formed martensite changes from the untempered condition to the tempered condition. Meanwhile, the fine Cr-rich carbides (mainly  $M_{23}C_6$ ) nucleated inside those Cr-rich martensite slow down their recovery/recrystallization rate. After PWHT, the Cr-depleted untransformed ferrite grains coarsened and the Cr-rich transformed martensite were just tempered without further grain growth. Those undissolved Cr-rich  $M_{23}C_6$  carbides also coarsened due to a Cr concentration gradient between Cr-depleted

martensite grains and Cr-rich ferrite grains.

(d) During high-temperature creep, these Cr-rich tempered martensite eventually grew into Cr-rich ferrite grains and Cr-depleted ferrite grains further coarsened. The Cr-rich grains exhibit a higher strength due to a higher dislocation density and more precipitation strengthening. Strength mismatch between the weak Cr-depleted grains and strong Cr-rich grains was enhanced along with the ongoing creep process. Coarsening of those undissolved Cr-rich  $M_{23}C_6$  carbides was further promoted due to long-term creep tempering. Under high creep stress in the ICHAZ, creep deformation has to be generated to maintain the creep strength. Locally this creep deformation occurred preferentially in those weak Cr-depleted grains instead of the strong Cr-rich grains. Coarsened hard carbides at the grain boundaries led to local stress concentrations and acted as nucleation sites for creep cavities. Deformation of those Cr-depleted grains enhanced the plastic flow and accumulation of vacancies, which accelerated growth of those nucleated cavities. Then coarsened cavities connected and became micro-cracks, which eventually resulted in the observed Type IV cracking.

## 4.3 Conclusions

Type IV cracking occurred in a narrow creep-susceptible region, named the soft zone, in the HAZ of Grade 91 weldment. The as-welded soft zone in the weldment is positively identified as the ICHAZ. Microstructure evolution of this identified soft zone after heat-treatment and creep test are analyzed. Type IV cracking mechanism is understood from a new perspective of the local chemistry in a grain-scale level. Non-uniform chromium distributions in the austenite grains and martensitic packets of the base metal cause a heterogeneous austenitic transformation in the ICHAZ during welding. This heterogeneous austenitic transformation results in a mixed structure of newly-formed austenite grains, undissolved precipitates, and a number of fine tempered martensite retained from the base metal. These tempered martensite grains from the base metal were retained due to their lower driving force for austenitization from the lower chromium concentrations. The tempering effect of the welding thermal cycles further lowered the hardness of these retained tempered martensite grains. After creep tests, the chromium distribution of the grains became even more non-uniform. The weak Cr-depleted grains have preferentially deformed by the applied creep stress. Coarsened Cr-rich  $M_{23}C_6$  carbides at the grain boundaries may have provided preferred nucleation sites for creep cavities. Deformation of the weak Cr-depleted grains accelerated the coarsening of the nucleated cavities, which eventually resulted in the observed Type IV cracking.

# Chapter 5

## Transition from Type IV to Type I Cracking in Heat-Treated Grade 91 Steel Weldments

### 5.1 Results

#### 5.1.1 Hardness profile and mapping across the welds after PWHT

Figure 5.1 shows the hardness profiles across the entire weldments in the as-welded (AW) condition and after PWHT at various temperatures for 2 hours. Three distinguished regions, the fusion zone, the HAZ, and the base metal, with different hardness magnitudes are observed in Figure 5.1. The fusion zone and HAZ in the as-welded condition show the highest hardness values. The large hardness variations in the as-welded fusion zone are caused by the tempering effects from the multiple filling passes. The fusion zone exhibits the highest hardness, the base metal has the lowest hardness, and the HAZ has a median hardness for all the PWHT temperatures. The fusion zone hardness decreases to the lowest value of 270 HV0.5 after PWHT at 760 °C and then increases after PWHT at 820 °C and 840 °C. The fusion zone after PWHT at 600 °C shows a comparable hardness with the fusion zone after PWHT at 840 °C (approximately 375 HV0.5). Base metal shows a high consistency and a small reduction in hardness (210-245 HV0.5) for all the PWHT temperatures. The magnified

hardness profiles in Figure 5.1b shows that hardness in the HAZ decreases from the coarse-grained HAZ close to the fusion line to ICHAZ close to the base metal. In contrast to the trend exhibited by the fusion zone after different PWHT temperatures, the hardness of the HAZ continuously decreases as the PWHT temperature increases, as shown in Figure 5.1b. Meanwhile, a softened region with a lower hardness is observed in the HAZ close to the base metal in Figure 5.1a. This hardness reduction in the softened region is about 10-20 HV0.5, in comparison to the adjacent base metal, as shown in Figure 5.1b.

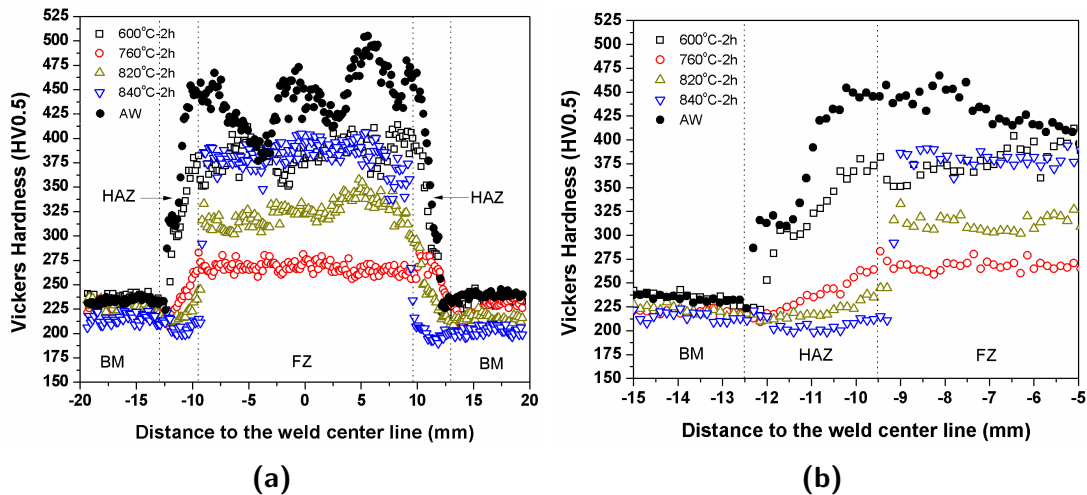


**Figure 5.1:** Hardness distribution profiles across the weldments in the as-welded condition and after PWHT at various temperatures for 2 hour hold: (a) the entire weldment; (b) the magnified HAZ region.

Figure 5.2 shows the hardness profiles across the entire weldments after PWHT at various temperatures for 8 hours. Hardness of the fusion zone shows a similar trend (decreases and increases as the PWHT temperature increases) as with the 2-hour PWHT samples in Figure 5.2a. However, the difference is that the fusion zone after PWHT at 840 °C for 8 hours has a higher hardness of 420 HV0.5 than the fusion zone (360 HV0.5) after PWHT at 600 °C for 8 hours. Hardness of the fusion zone after PWHT at 820 °C slightly increases from 320 HV0.5 for 2 hours to 335 HV0.5 for 8 hours. The fusion zone hardness after PWHT at 760 °C decreases from 270 HV0.5 for 2 hours to 235 HV0.5 for 8 hours. Base metal hardness does

not decrease significantly except with a high hardness after PWHT at 840 °C for 8 hours. Besides the fact that HAZ hardness decreases after a longer PWHT, the HAZ after PWHT at 820 °C for 8 hours shows the lowest hardness instead of the HAZ after PWHT at 840 °C for 2 hours in Figure 5.1b. A softened region with further decreased hardness is observed in the HAZ, especially for the PWHT at 820 °C for 8 hours. The hardness difference between the fusion zone, the HAZ, and the base metal is significantly reduced after PWHT at 760 °C for 8 hours.

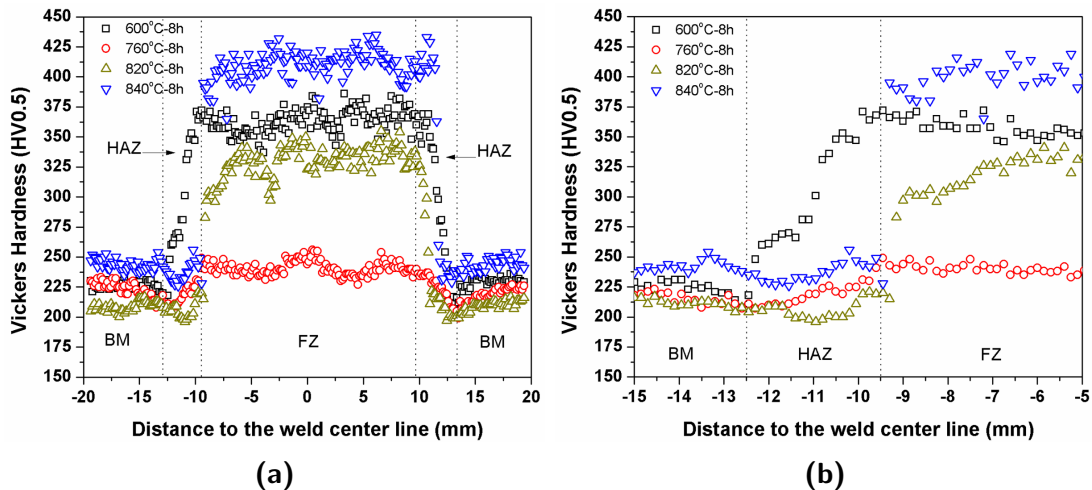


**Figure 5.2:** Hardness distribution profiles across the weldments in the as-welded (AW) condition and after PWHT at various temperatures for 8 hour hold: (a) the entire weldment; (b) the magnified HAZ region.

It is summarized that the hardness sensitivity during the PWHT exhibits a high-to-low order from the fusion zone to the HAZ and the base metal. It is also observed that the hardness of the fusion zone is significantly affected and depends on whether the PWHT temperature is below or above the  $A_1$  temperature (818 °C) for the as-received Grade 91 base metal. When the PWHT temperature is above the  $A_1$  temperature (818 °C), an increase in hardness is observed in the fusion zone, otherwise, a reduction in hardness is observed. However, at a shorter holding time of 2 hours, hardness of the base metal and the HAZ decreases with the increase in PWHT temperature even when the PWHT temperature is above the  $A_1$

temperature (818 °C). The hardness of the base metal and the HAZ only increases after a PWHT at 840 °C for 8 hours.

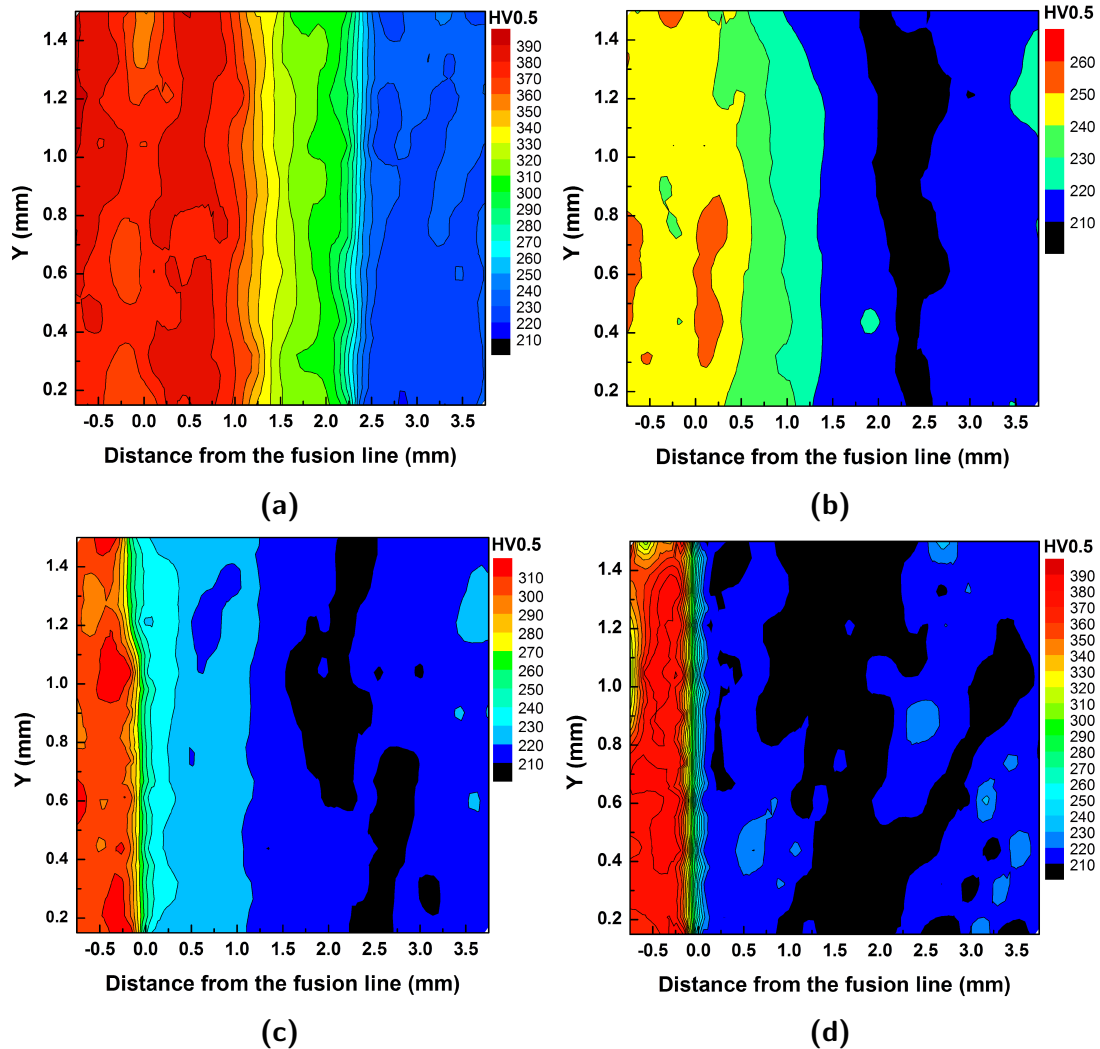


**Figure 5.3:** Hardness contour maps of the HAZs after PWHT at various temperatures for 2 hours at: (a) 600 °C; (b) 760 °C; (c) 820 °C; (d) 840 °C.

To obtain a magnified and more accurate hardness distribution in the HAZ, hardness mapping was conducted across the HAZ with a low indentation load and a narrower inter-spacing. Figure 5.3 shows the hardness contour maps of the HAZ specimens after PWHT at various temperatures for 2 hours. At a low PWHT temperature of 600 °C, the hardness difference between the base metal and HAZ is high, as shown in Figure 5.3a. Clear boundaries

between the coarse-grained HAZ, fine-grained HAZ/ICHAZ, and base metal can be distinguished. However, increasing the PWHT temperature from 760 °C, to 820 °C and finally to 840 °C has homogenized the hardness variations of both the base metal and the HAZ, and has narrowed the hardness difference between the base metal and HAZ as well. A softened region (black region) with a hardness below 210 HV0.5 is observed at 760 °C, 820 °C, and 840 °C. These softened regions consistently appear at a location around 2.0–2.5 mm from the fusion line.

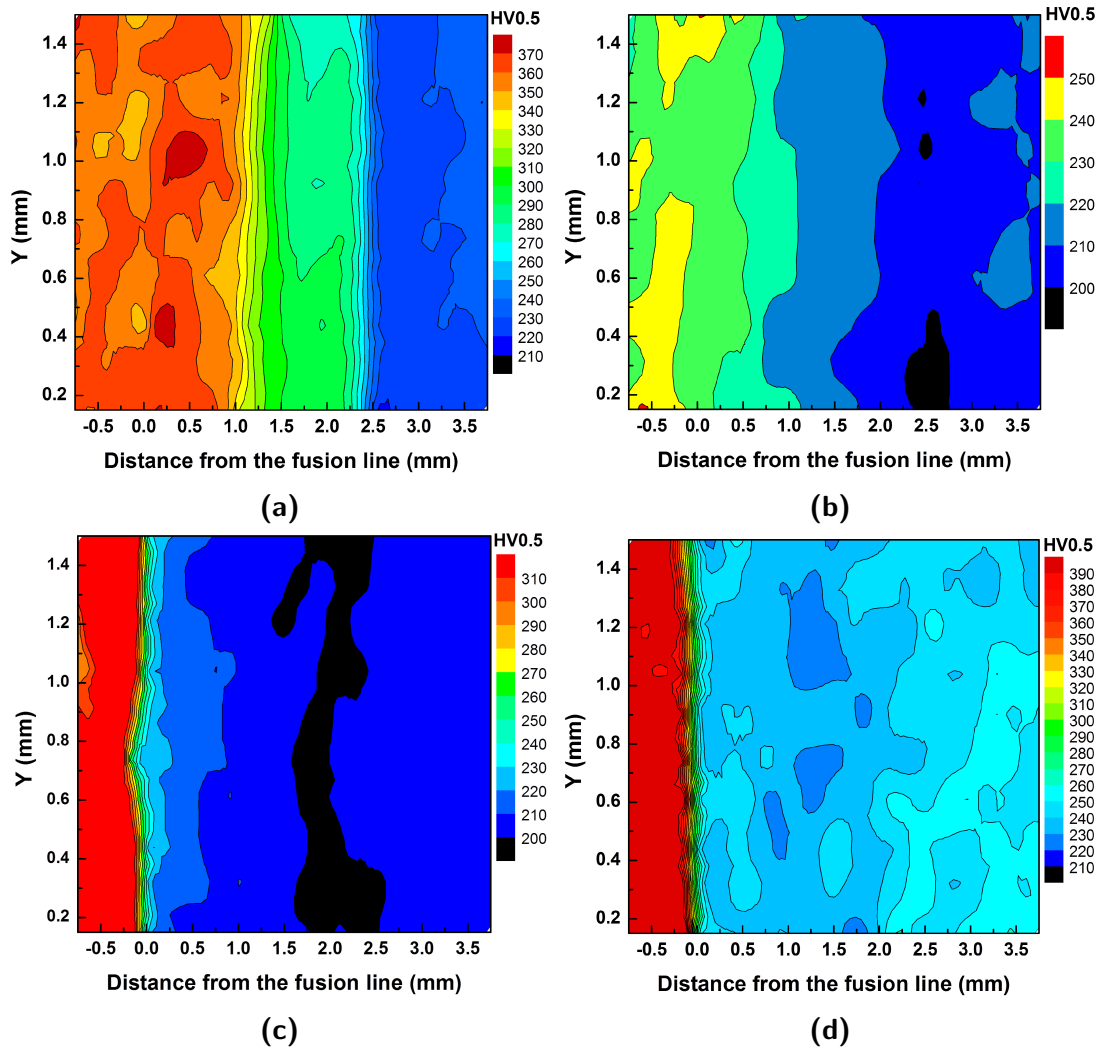


**Figure 5.4:** Hardness contour maps of the HAZs after PWHT at various temperatures for 8 hours at: (a) 600 °C; (b) 760 °C; (c) 820 °C; (d) 840 °C.

Besides the PWHT temperature, PWHT holding time also exhibits its role in affecting the hardness distribution in the HAZ. Figure 5.4 shows the hardness contour maps across the HAZ specimens after PWHT at various temperatures for 8 hours. The homogenization effect on hardness is enhanced, which results in more uniform hardness distributions of the HAZ and the base metal. The entire base metal and HAZ after PWHT at 820 °C has a low hardness of 210-200 HV0.5. However, the HAZ after PWHT at 840 °C has a uniform and higher hardness value of about 240 HV0.5. The softened region with a hardness below 200 HV0.5 is only observed in the HAZs after PWHT at 760 °C and 820 °C. The location of the softened region is consistent with that shown in Figure 5.3. However, the width of the softened region decreases after a longer time PWHT.

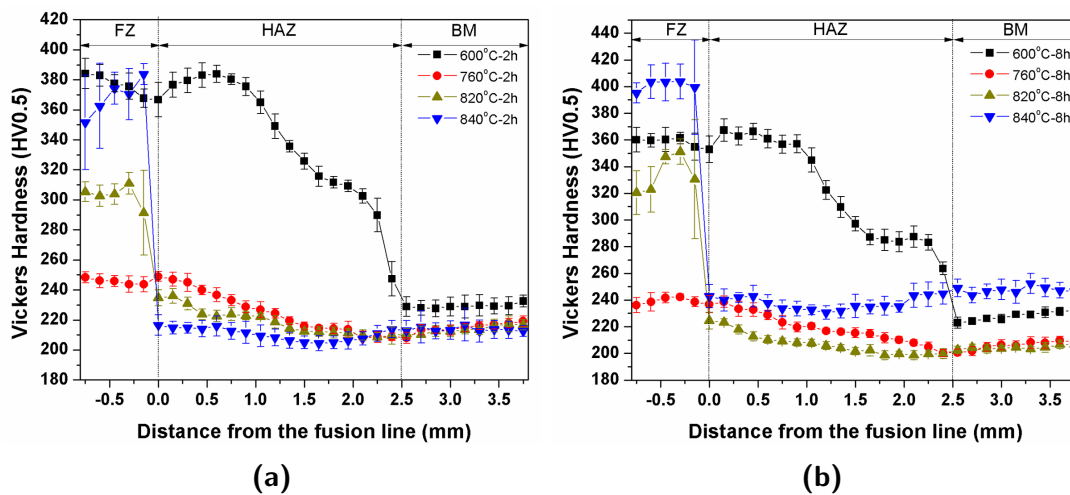


**Figure 5.5:** Average hardness profiles, following the PWHT, from the hardness mapping in Figure 5.3 and Figure 5.4: (a) 2 hours; (b) 8 hours.

Figure 5.5 shows the average hardness profiles from the hardness mapping in Figure 5.3 and Figure 5.4. It is observed that PWHT temperature has a greater effect on tempering the welds than the PWHT holding time. At a low PWHT temperature of 600 °C, the tempering effect on both the fusion zone and HAZ is quite limited even when the PWHT holding time increases from 2 to 8 hours. The PWHT temperatures of 760 °C and 820 °C have a similar

tempering effect on the base metal and HAZ, but not on the fusion zone. The PWHT at 760 °C exhibits a tempering effect on both the HAZ and fusion zone. At 820 °C, hardness of the fusion zone firstly decreases and then increases when the PWHT time increases from 2 to 8 hours. The PWHT at a high temperature of 840 °C causes an opposite effect on the hardness of base metal and HAZ for 2 hours and 8 hours. Figure 5.5a shows hardness of both the base metal and HAZ decreases after PWHT at 840 °C for 2 hours. On the contrary, a hardness increase was observed in the base metal and the HAZ after PWHT at 840 °C for 8 hours. To further clarify these hardness profile results, a detailed microstructure analysis of the PWHT-ed specimens is shown in the following section.

### 5.1.2 Microstructure of the welds after PWHT

Microstructure of the as-welded HAZ was reported in our previous papers [125,126]. The main structural features include the fine-grained HAZ close to ICHAZ has the finest grain structure and coarse un-dissolved precipitates, and the ICHAZ has a mixed structure of newly formed prior austenite grains with high local strains and some fine retained tempered martensite with low local strains. It is reported that the typical structural evolutions during PWHT include recovery/recrystallization of tempered martensite, precipitation and coarsening of carbides and carbonitrides. Figure 5.6 shows the typical structures of the fusion zone, HAZ, and base metal after PWHT at 600 °C for 2 hours. In the grain-scale level, the HAZ and base metal have no significant change in the microstructure and maintain the as-welded structure reported in [125,126]. These structures very likely stay at the early recovery stage with the annihilation and re-organization of dislocations. That is why the hardness values in the HAZ are still high, as shown in Figure 5.5a. However, fine recrystallized grains are observed along the prior austenite grain boundaries in the fusion zone, as shown in Figure 5.6a. These facts indicate the fusion zone has been tempered and recrystallization of the tempered martensite

occurs.

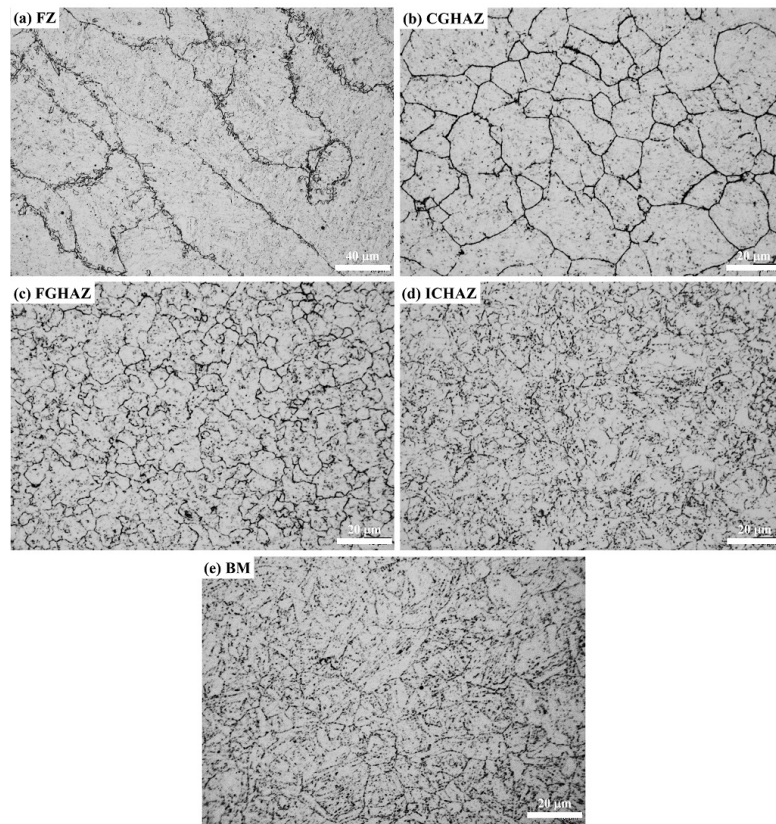


**Figure 5.6:** Optical images showing typical microstructure of the specimen after PWHT at 600 °C for 2 hours: (a) Fusion zone; (b) CGHAZ; (c) FGHAZ; (d) ICHAZ; (e) BM.

Figure 5.7 shows the microstructure of the fusion zone, HAZ, and base metal after PWHT at 840 °C for 2 hours. The fusion zone in Figure 5.7a shows un-tempered martensite grains instead of tempered martensite or fine equiaxed grains, which indicates that a high degree of austenization has occurred in the fusion zone. It is believed that this large amount of un-tempered martensite causes its high hardness as shown in Figure 5.1. Unlike the coarse prior austenite grain structure in Figure 5.6b, the coarse-grained HAZ in Figure 5.7b exhibits a structure of tempered martensite grains and fine nucleated precipitates along the multiple boundaries. A small amount of fine equiaxed grains are also observed in the coarse-grained HAZ. These equiaxed grains are very likely new prior austenite grains nucleated during PWHT.

The fine-grained HAZ in Figure 5.7c has a mixture of coarse tempered martensite grains, fine equiaxed grains, and a large amount of coarsened precipitates. Most of these coarsened precipitates stay inside the grains which likely originate from the un-dissolved  $M_{23}C_6$  carbides observed in the as-welded condition. Moreover, their distribution is not uniform. Some grains have dense carbides, but some grains are free of these coarse carbides. The structure of ICHAZ shown in Figure 5.7d has slightly more fine equiaxed grains and some tempered martensite. Coarsened  $M_{23}C_6$  carbides are also observed in the ICHAZ. The base metal in Figure 5.7e still shows a structure of tempered martensite grains.

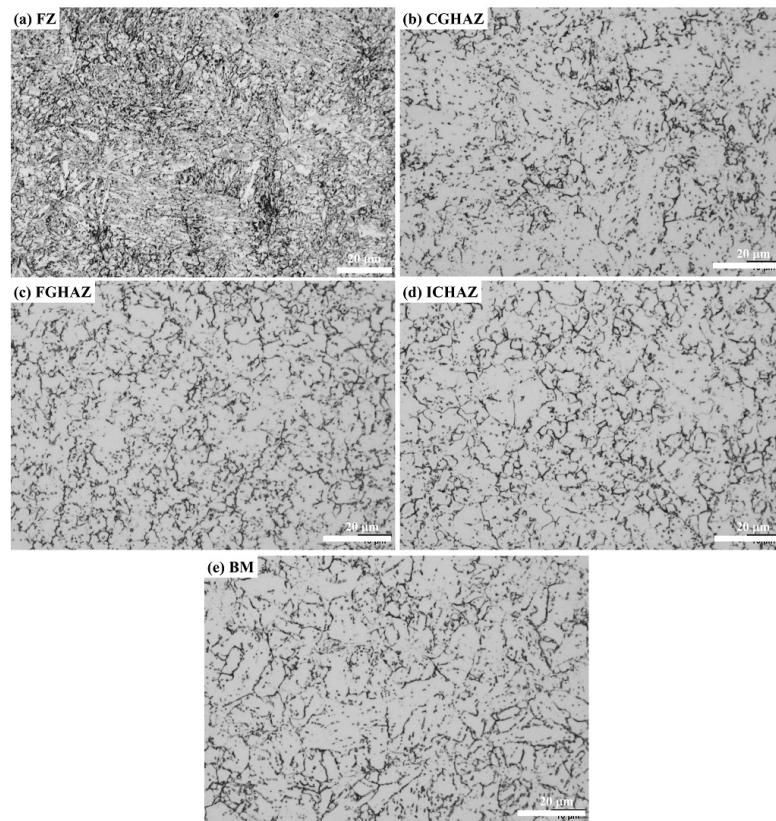


**Figure 5.7:** Optical images showing typical microstructure of the specimen after PWHT at 840 °C for 2 hours: (a) Fusion zone; (b) CGHAZ; (c) FGHAZ; (d) ICHAZ; (e) BM.

### 5.1.3 Creep performance of the cross-weld samples

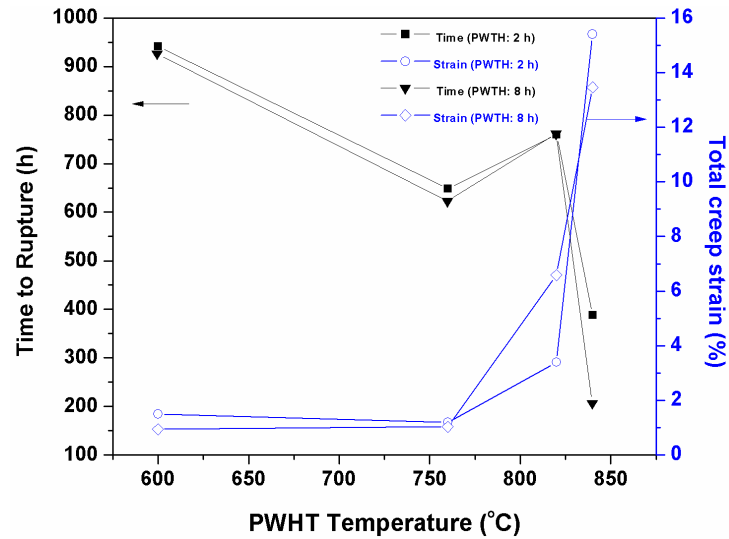


**Figure 5.8:** Creep results of the PWHT-ed cross-weld specimens tested at 650 °C under a stress of 70 MPa.

Figure 5.8 summarizes the creep results of the PWHT-ed cross-weld specimens tested at 650 °C under a stress of 70 MPa. The creep lifetime of the weldments is much shorter (less than 1000 hours) than the reported creep data of the Grade 91 base metal [2, 25]. The creep rupture time sensitively varies with the PWHT temperatures. When the PWHT temperature (below  $A_1$  of the base metal) increases, the rupture time decreases. When the PWHT temperature (above  $A_1$  of the base metal) increases, the rupture time significantly drops. The total creep strain increases as the PWHT temperature increases. The effect of the PWHT holding time on the creep lifetime is insignificant, except when the PWHT temperature is 840 °C. From both high-temperature ( $\geq 650$  °C) creep life and creep strain point of view, PWHT at a lower temperature of 600 °C for 2 hours is the best and should be preferred.

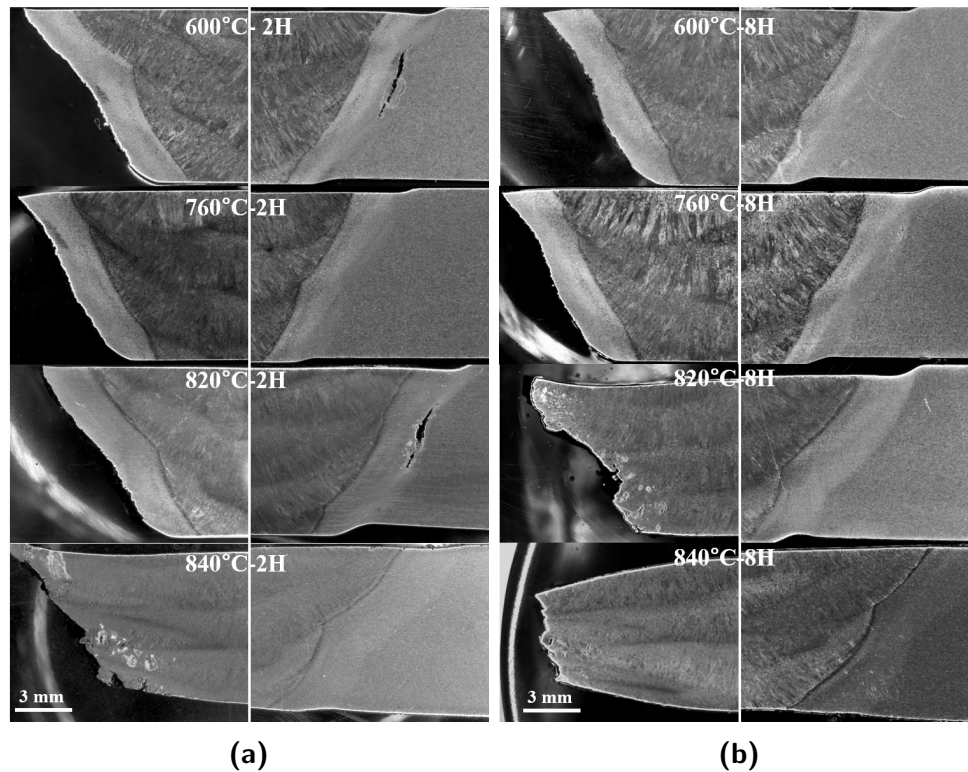


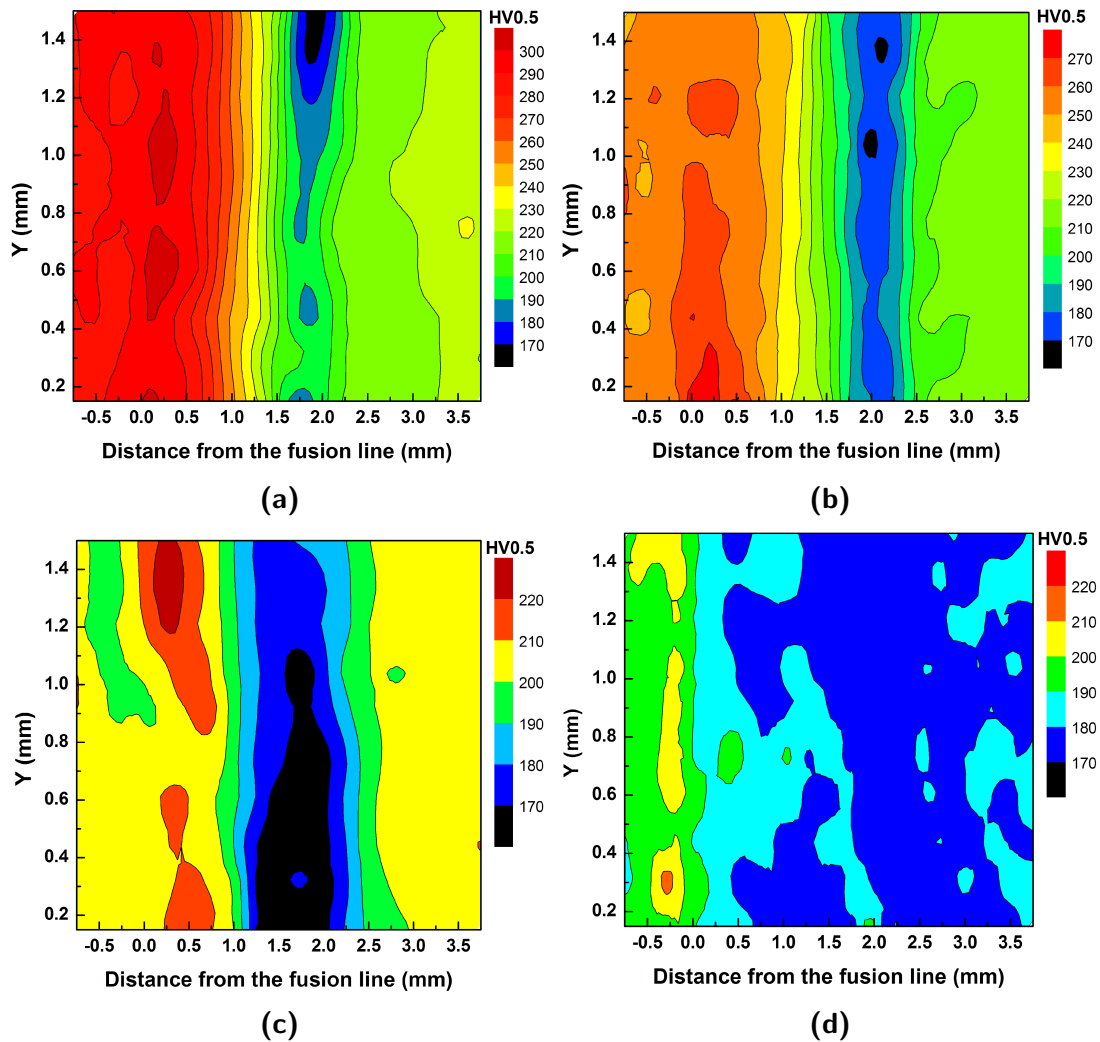
**Figure 5.9:** Optical images showing the cross-section of the creep-ruptured specimens PWHT-ed at various temperatures for (a) 2 hours and (b) 8 hours.

The optical micrographs in Figure 5.9 show the cross-sections of the failed specimens after the creep tests at 650 °C under a stress of 70 MPa. Creep rupture without much necking occurred in the HAZ outside edge close the base metal at PWHT temperatures of 600 °C, 760 °C, and 820 °C, which is identified as the Type IV cracking. Cracks are also observed in the other side of the HAZ. The Type I cracking with obvious necking occurred in the fusion zone of the specimen after PWHT at 840 °C for 2 hours. The specimens after PWHT at 600 °C and 760 °C for 8 hours still failed with the Type IV cracking. However, the specimen after PWHT at 820 °C for 8 hours shows the Type I cracking and a large shear deformation in the HAZ as well. The specimen after PWHT at 840 °C for 8 hours also fractured with the Type I cracking and a significant necking, but without shear deformation in the HAZ. It appears that the PWHT temperature has a greater impact on the creep fracture modes than

the holding time does. At low PWHT temperatures ( $< A_1$  of the base metal), an increase of the holding time has a small effect on the fracture location (Type IV or Type I). At high temperatures ( $\geq A_1$  of the base metal), the effect of holding time on the fracture location becomes more significant.

#### 5.1.4 Hardness mapping across the HAZ after creep tests

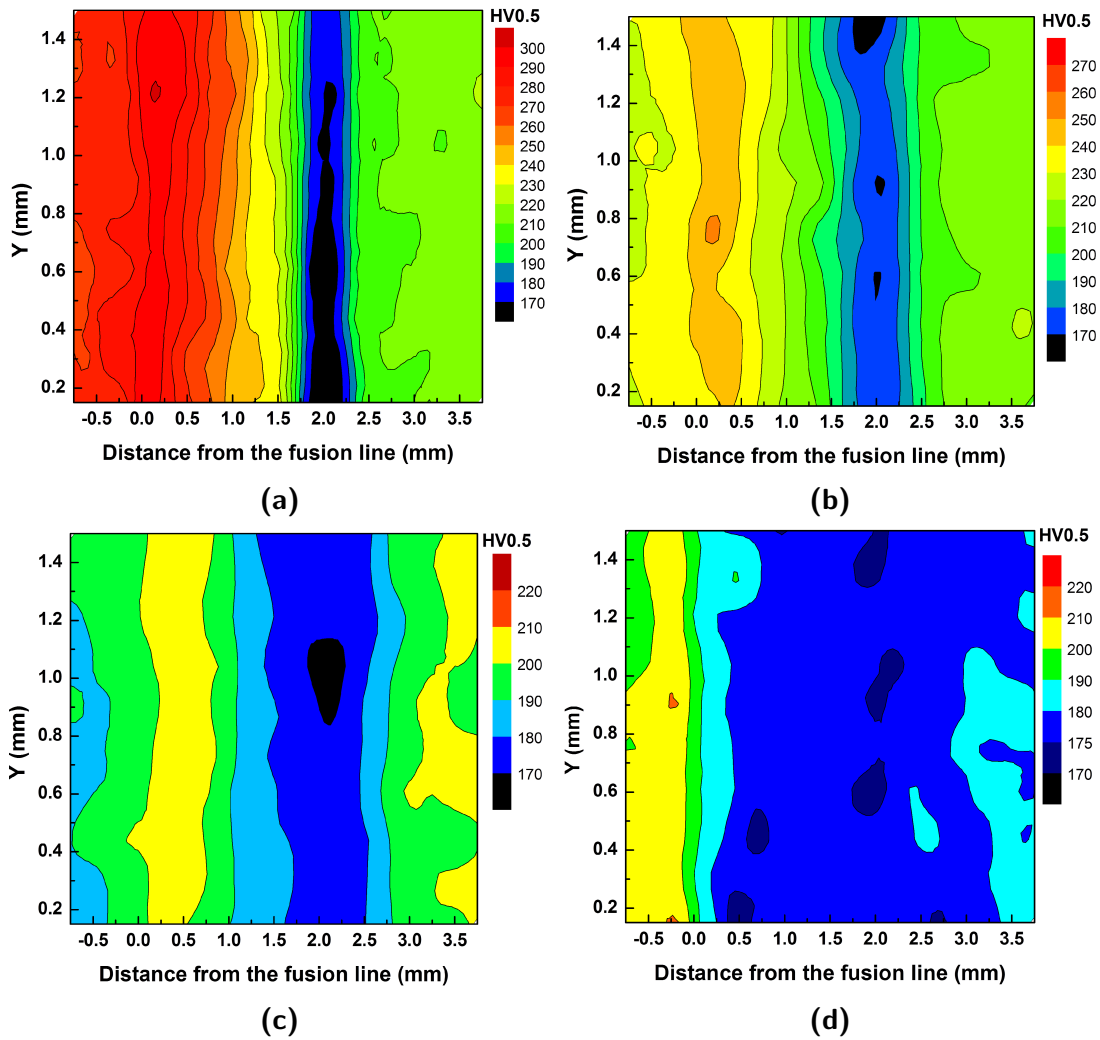
Figure 5.10 shows the hardness contour maps of the 2-hour PWHT-ed specimens after creep test. The hardness gaps in the fusion zone, HAZ, and base metal of the specimen after PWHT at 600 °C for 2 hours is still high. The hardness of the coarse-grained HAZ adjacent to the fusion line is much higher than the ICHAZ adjacent to the base metal. An increase of the PWHT temperature narrows this hardness gap. A softened region with extremely low hardness value is observed at the location with about 2.0 mm distance from the fusion line, as shown in Figure 5.10a, 5.10b, and 5.10c. These softened regions are where the Type IV cracking is observed in Figure 5.9. Hardness distribution of the HAZ in the specimen after PWHT at 840 °C for 2 hours is significantly different, as shown in Figure 5.10d. A homogeneous hardness distribution of the HAZ and base metal is observed. The hardness of fusion zone is slightly higher than that of the HAZ. This feature is correlated with the Type I cracking observed in Figure 5.9.



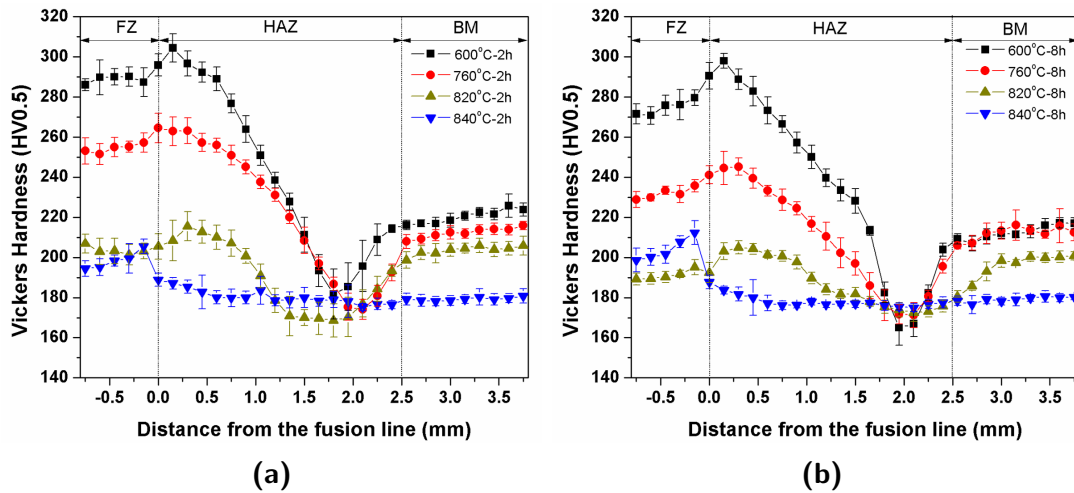
**Figure 5.10:** Hardness contour maps of the HAZs after PWHT at various temperatures for 2 hours and creep testing at 650 °C under 70 MPa.

Figure 5.11 shows the hardness contour maps of the 8-hour PWHT-ed specimens after creep test. The hardness distribution of the HAZ shows a similar trend with that shown in Figure 5.10. Softened regions, associated with the Type IV cracking shown in Figure 5.9, are also observed at 2.0 mm from the fusion line in the specimens after PWHT at 600 °C and 760 °C. Even in the specimen after PWHT at 820 °C failed with the Type I cracking, a softened region is still observed. The large shear deformation in the HAZ shown in Figure 5.9 is correlated with this softened region. It should be pointed out that the hardness value

of this softened region is close to the surrounding area (the difference is less than 10 HV0.5). Figure 5.11d exhibits a highly-uniform hardness distribution in the HAZ and base metal after PWHT at 840 °C.



**Figure 5.11:** Hardness contour maps of the HAZs after PWHT at various temperatures for 8 hours and creep testing at 650 °C under 70 MPa.



**Figure 5.12:** Average hardness profiles, following the creep tests, from the hardness mapping in Figure 5.10 and 11: (a) 2 hours; (b) 8 hours.

Figure 5.12 shows the average hardness profiles from the hardness mappings in Figure 5.10 and 5.11. The fusion zone, the HAZ, and the base metal in the specimen after PWHT at 600 °C underwent the smallest hardness reduction after creep test. In comparison, the specimen after PWHT at a high temperature of 840 °C experienced the largest hardness drop. The detected softened regions (about 2.0 mm from the fusion line), are correlated with the location for the Type IV cracking which is identified as the interface between the fine-grained HAZ and ICHAZ in the subsequent section. After PWHT at high temperatures of 820 °C and 840 °C for a longer time of 8 hours, a uniform hardness distribution of the HAZ is generated after the creep test. Comparing with Figure 5.5 and Figure 5.12, it is implied that even through a homogenized hardness distribution in the HAZ is achieved by a proper PWHT, such as the code-recommended PWHT at 760 °C for 2 hours, the creep condition eventually differentiates the heterogeneous regions in the HAZ through various hardness reduction rates and reveals the creep-susceptible region in the HAZ.

### 5.1.5 Microstructure of the welds after creep tests

Figure 5.13 shows the microstructure of the cross-section specimens after PWHT at 760 °C for 2 hours and creep test at 650 °C with a stress level of 70 MPa. It is known that the specimen fractured with the Type IV cracking, as shown in 9. The fusion zone in Figure 5.13a shows a structure of fine lath-shaped tempered martensite and fine dispersive precipitates along the boundaries. The coarse-grained HAZ in Figure 5.13b consists of coarse tempered martensite, a small amount of fine equiaxed grains, and fine precipitates along the boundaries. The fine-grained HAZ in Figure 5.13c exhibits a dramatically different structure from the other regions, with equiaxed matrix grains. Coarse precipitates (white dots) distribute not only along the grain boundaries, but also inside some grains. Creep cavities nucleated along the grain boundaries are also observed. It should be noted that the location of the observed fine-grained HAZ is in the transition region between the fine-grained HAZ and ICHAZ. The creep damaged region associated with cavities can be also regarded as the ICHAZ. The ICHAZ close to the base metal in Figure 5.13d has a mixed structure of coarse equiaxed grains, wide tempered martensite, and precipitates along the boundaries. The base metal in Figure 5.13e still has the structure of wide tempered martensite and dispersive precipitates along the boundaries. Corresponding with the hardness profile in Figure 5.12a and fracture image in Figure 5.9, these coarse equiaxed grains and coarse precipitates may be the critical causes for the low hardness and the Type IV cracking.

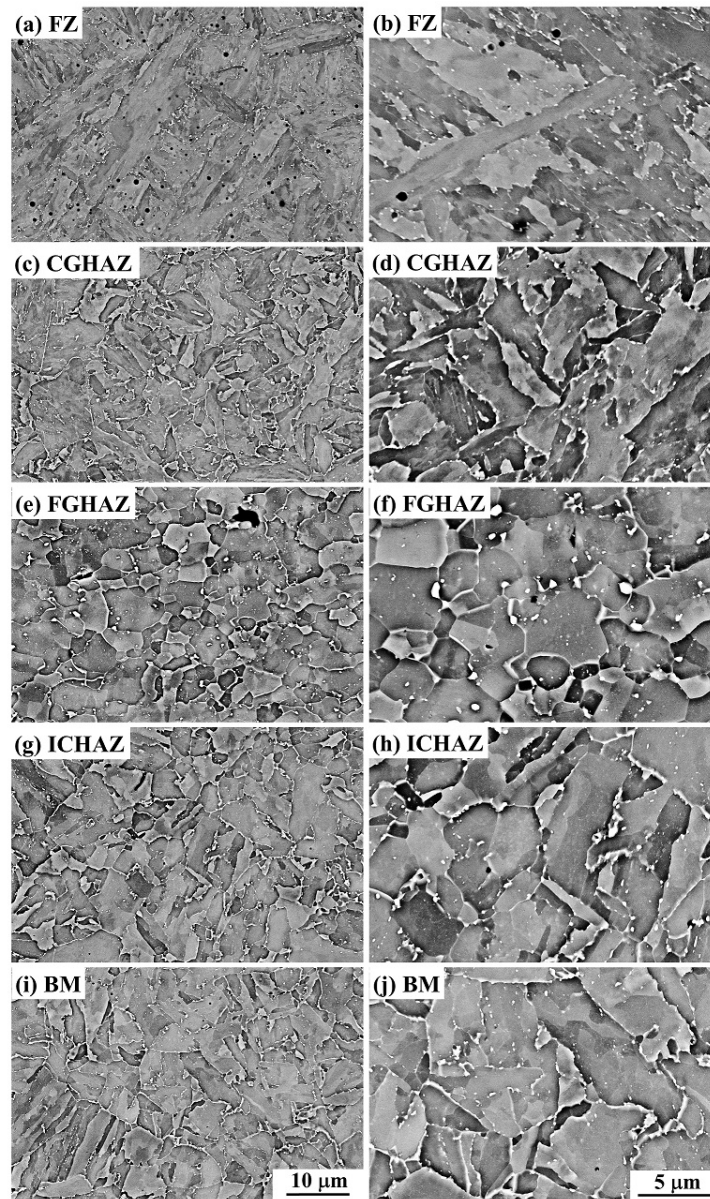


**Figure 5.13:** Microstructure of the cross-section specimen after PWHT at 760 °C for 2 hours and creep test at 650 °C with a stress level of 70 MPa: (a), (b) Fusion zone; (c), (d) CGHAZ; (e), (f) FGHAZ; (g), (h) ICHAZ; (i), (j) BM.

Microstructure of the fractured specimen (PWHT-ed at 840 °C for 8 hours) with the Type I cracking shown in Figure 5.9b is shown in Figure 5.14. The creep fracture has occurred in the fusion zone with many creep cavities observed along the grain boundaries, as shown in Figure 5.14a and 14b. Elongated grains in the horizontal creep stress direction are also

observed in the fusion zone in Figure 5.14a. In Figure 5.14b, a creep cavity has formed with a spherical oxide along the grain boundaries. Coarse precipitates mainly distribute along the grain boundaries as well. The majority of these coarse precipitates are reported to be Cr-rich  $M_{23}C_6$  carbides. The coarse-grained HAZ in Figure 5.14c and 14d exhibits a structure of equiaxed grains and dispersive coarse precipitates. Figure 5.14d shows most of these coarse precipitates are located within the grains rather than along the grain boundaries. The fine-grained HAZ in Figure 5.14e and 14f shows a similar equiaxed grain structure with the coarse-grained HAZ. However, coarser precipitates are observed in the fine-grained HAZ. The structure of ICHAZ in Figure 5.14g and 14h is slightly different from the fine-grained HAZ. Coarse precipitates distribute not only inside the grains, but also along the grain boundaries. The base metal in Figure 5.14a and 14b shows a coarse-grained structure. Precipitates inside the grains indicate the “ghost” prior-austenite grain boundaries and block boundaries. Besides these structures features, a few fine creep cavities are observed in the coarse-grained HAZ, fine-grained HAZ, and ICHAZ, but not in the base metal. The HAZ structures in the Type I cracking is dramatically different from the structures in the Type IV cracking in Figure 5.13. The coarse-grained HAZ, fine-grained HAZ, and ICHAZ show similar structures rather than significant structural variations. Comparable hardness values in Figure 5.12b also confirm this structural similarity. In contrast, the fusion zone exhibits a quite different structure with elongated grains and dense precipitates.

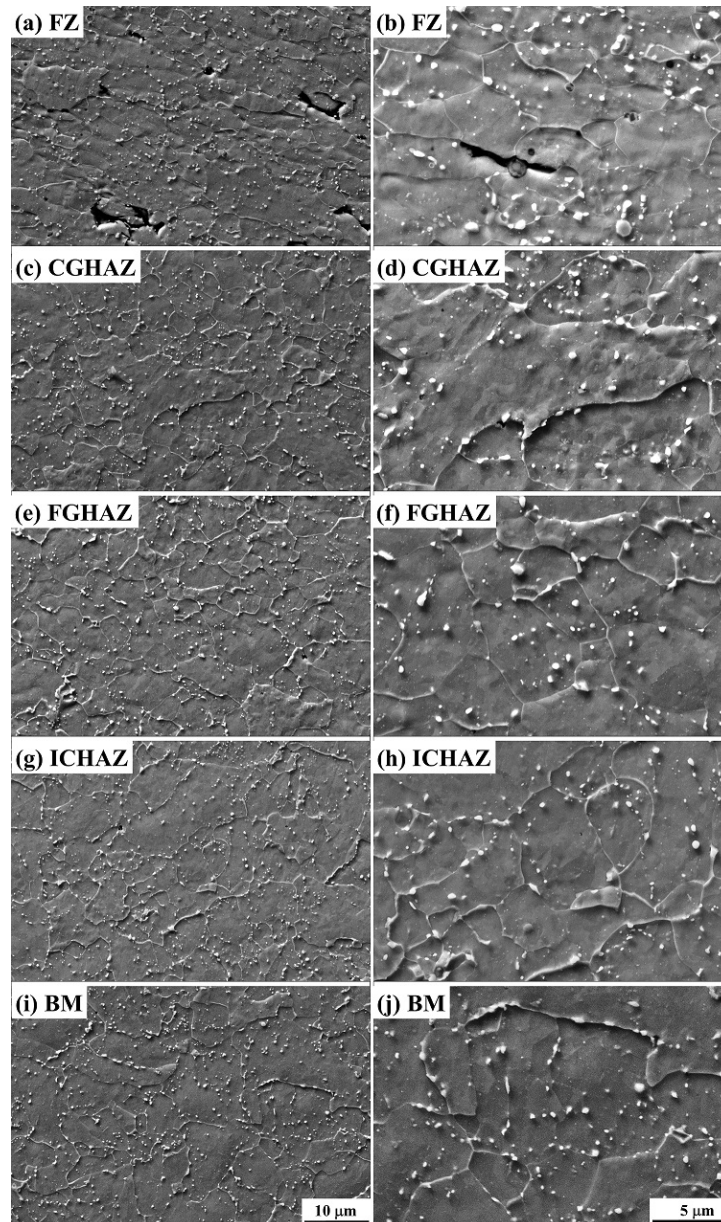


**Figure 5.14:** Microstructure of the cross-section specimen after PWHT at 840 °C for 8 hours and creep test at 650 °C with a stress level of 70 MPa: (a), (b) Fusion zone; (c), (d) CGHAZ; (e), (f) FGHAZ; (g), (h) ICHAZ; (i), (j) BM.

### 5.1.6 Characteristic structures of the welds in Type I cracking

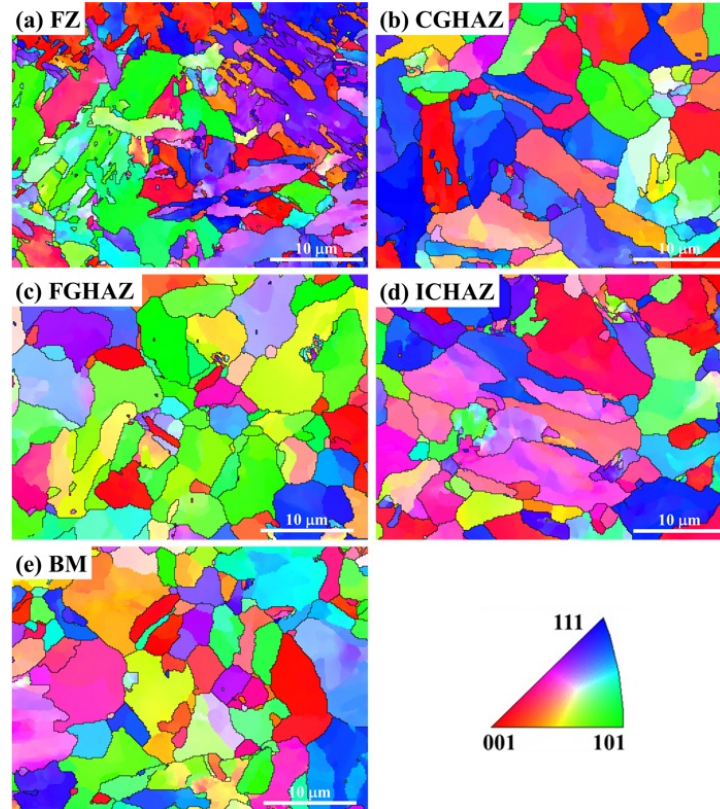


**Figure 5.15:** EBSD analysis on the specimen PWHT-ed at 840 °C for 2 hours: (a) FZ; (b) CGHAZ; (c) FGHAZ; (d) ICHAZ; (e) BM.

**Table 5.1:** EBSD grain boundary and size analyses on the specimen PWHT-ed at 840 °C for 2 hours.

Location	FZ	CGHAZ	FGHAZ	ICHAZ	BM
Grain size by line-intercept method ( $\mu\text{m}$ )	1.61	2.70	2.64	2.73	2.60
Grain size standard deviation ( $\mu\text{m}$ )	1.67	2.32	2.47	2.80	2.32
HAGB frequency ( $\geq 10^\circ$ , %)	36.5	49.2	57.4	44.0	53.4
LAGB frequency ( $< 10^\circ$ , %)	63.5	50.8	42.6	56.0	46.6
Ratio of HAGB/LAGB	0.57	0.97	1.35	0.79	1.15

Microstructures of the fusion zone, HAZ, and BM in the PWHT-ed and Crept weldments were characterized to study microstructural evolutions in the Type I cracking. The specimen PWHT-ed at 840 °C for 2 hours before creep test were characterized by EBSD analysis. Figure 5.15 demonstrates the IPF of each region. Overall the FZ exhibits a martensitic structure. Thick bulk grains with solid colours are also observed in the FZ. This intercritical structure feature indicate a partial austenitization has occurred in the FZ. Unlike the lath-like grains in the FZ, grains in the CGHAZ, FGHAZ, ICHAZ, and BM is more close to equiaxed grains. EBSD measured grain size and GB frequency of each region are tabulated in Table 5.1. Comparing grain size of each region, the FZ has the finest grain size of 1.60  $\mu\text{m}$  and the largest frequency of LAGBs. The CGHAZ, FGHAZ, ICHAZ, and BM nearly have the same grain size of 2.6–2.7 $\mu\text{m}$ . Their LAGB fractions are also lower than that of FZ. The facts of larger grain size and lower LAGB frequency indicate the HAZ and BM have been highly tempered with significant recrystallization and grain growth in the PWHT. The fine martensitic structure feature in the FZ means it has been highly-austenized during PWHT.

To verify the structure evolutions mentioned above, the KAM maps are post-processed and shown in Figure 5.16. Distribution of the KAM values of each region is presented in Figure 5.16. It is shown that the FZ has a significantly high stored strain energy with a normalized KAM value of 0.78°. A highly-inhomogeneous KAM distribution is observed. This high strain region is caused by the martensitic structures observed in Figure 5.15a. However, the HAZ and BM exhibit quite low strain energies as shown in Figure 5.16. The normalized KAM value of the HAZ and BM is only between 0.26°–0.37°. The high-KAM regions in the HAZ and BM are identified as martensite phases, which indicates austenitization has occurred during PWHT. The fraction of martensite is still low.

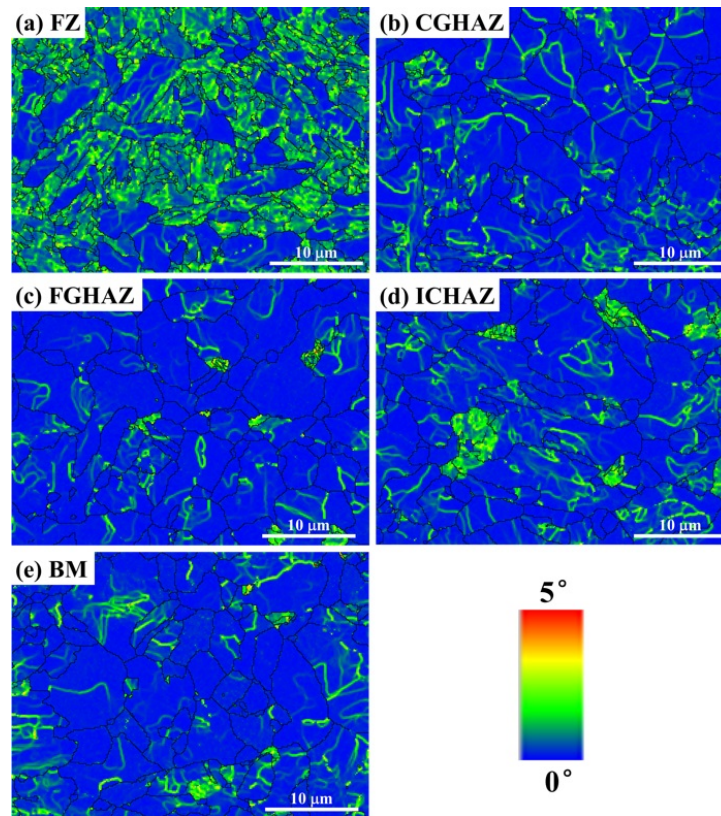


**Figure 5.16:** EBSD analysis on the specimen PWHT-ed at 840 °C for 2 hours: (a) FZ; (b) CGHAZ; (c) FGHAZ; (d) ICHAZ; (e) BM.

**Table 5.2:** EBSD KAM and GAM analyses on the specimen PWHT-ed at 840 °C for 2 hours.

Location	FZ	CGHAZ	FGHAZ	ICHAZ	BM
Normalized KAM value (°)	0.78	0.29	0.26	0.37	0.28
Deformed grain frequency (%)	45.5	3.7	2.7	7.8	3.4
Substructured grain frequency (%)	42.5	57.7	50.8	62.8	49.5
Recrystallized grain frequency (%)	12.0	38.5	46.6	29.4	47.1

GAM evaluation shows similar results in Table 5.2 . The FZ has the highest fraction (45.5 %) of deformed grains which are martensite. The deformed grains in the HAZ and BM are below 8 %. Fraction of recrystallized grains shows a opposite trend. The HAZ and BM has

a high frequency of recrystallized grains.

Based on the analysis above, it is implied that after PWHT at at 840 °C for 2 hours, there are dramatically different structures in the FZ and HAZ/BM. The FZ exhibits an intercritical structure of hard martensite with high stored strain energies and soft ferrite grains with low stored strain energies. The CGHAZ, FGHAZ, ICHAZ, and BM become a union and have similar structures of coarse equiaxed ferrite grains with low strain energies, which means they have been highly-tempered during PWHT. These uniform structures differentiate the weld into two parts, the FZ and the rest, no longer the inhomogeneous multi-layered structures. The sub-regions in the HAZ have been homogenized. Therefore it is predicted that during creep condition, the FZ and HAZ/BM will behave with different creep strength degradations and creep cavity nucleation.

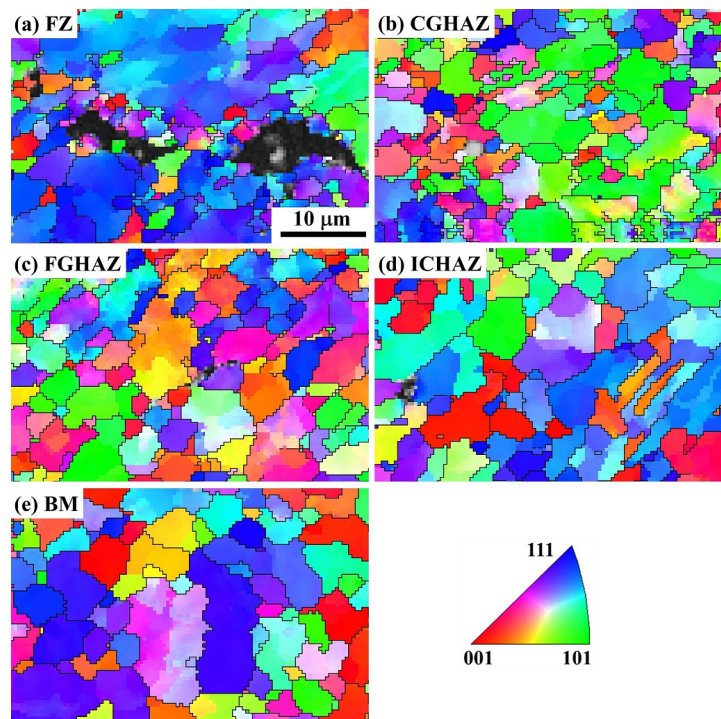


**Figure 5.17:** EBSD analysis on the crept specimen (PWHT-ed at 840 °C for 2 hours): (a) FZ; (b) CGHAZ; (c) FGHAZ; (d) ICHAZ; (e) BM.

Microstructure of the crept-weld with a Type I cracking was analyzed with EBSD. The

EBSD IPFs in Figure 5.17 present grain structures of each region. The first observation is the FZ exhibits an inhomogeneous grain size distribution. Both coarse and fine equiaxed grains are observed adjacent to creep cavities (black region). The grain size distribution in the HAZ and BM are more homogeneous. These structure features are consistent with the SEM observation in Figure 5.14.

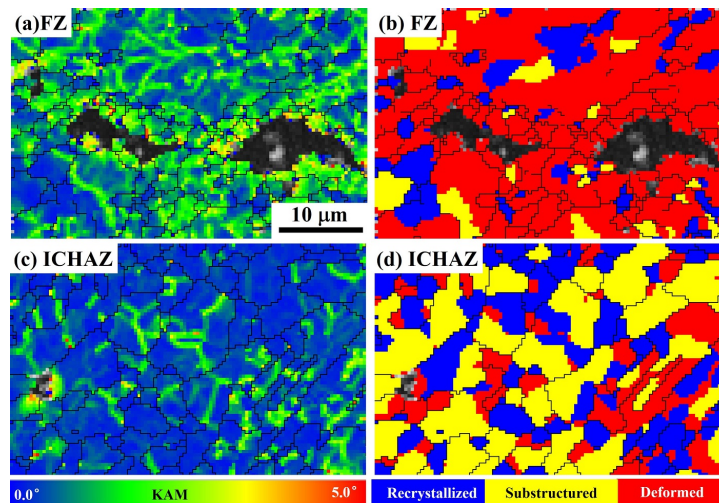


**Figure 5.18:** EBSD KAM and GAM analysis on the crept specimen (PWHT-ed at 840 °C for 2 hours): (a), (b) FZ; (c), (d) ICHAZ.

The KAM and GAM maps of the FZ and ICHAZ in Figure 5.18 uncover more details of the Type I cracking. High local strain distributes in the FZ, especially along creep cavities. The majority of grains in the FZ are identified as the deformed grains. The former creep-susceptible region ICHAZ exhibits a low strain level, except the regions surrounding a cavity. The grains in the ICHAZ are identified as either recrystallized grains or substructured (half-recrystallized) grains.

It is summarized that in the Type I cracking, the FZ with an inhomogeneous grain size distribution and high local strain variations becomes the preferred creep-damaged region. The HAZ and BM exhibit similar structures of a uniform grain size distribution and a low local strain level. ICHAZ is no longer the most creep-susceptible region.

## 5.2 Discussion

### 5.2.1 PWHT, microstructure, and hardness

The PWHT temperature exhibits a greater impact on the structural evolutions and hardness distribution in each region of the welds. Tempering effect is the dominating one for both the fusion zone and HAZ when the PWHT is conducted at 600 °C and 760 °C. However, the PWHT at 600 °C cannot provide a sufficient tempering. A large hardness difference (about 100 HV0.5) still exists between the coarse-grained HAZ and IHAZ even when the PWHT time is increased to 8 hours. Morphology of grains in the HAZ in Figure 5.6 has no significant change and maintains a similar structure to the as-welded structures. The PWHT at 760 °C shows a great tempering effect on homogenizing the hardness gradient within the HAZ and narrowing the gap between the HAZ and fusion zone, as shown in Figure 5.5.

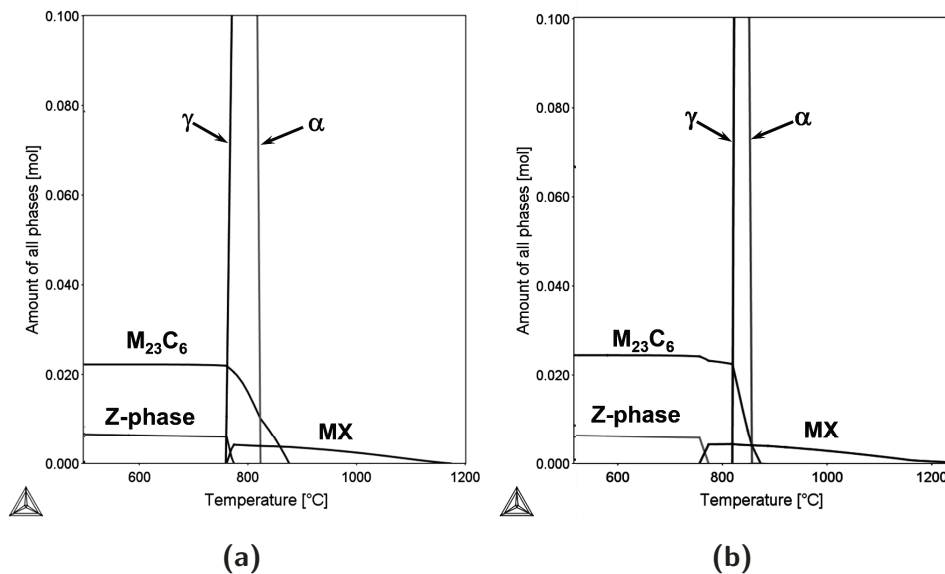


**Figure 5.19:** Phase fraction as a function of temperature calculated by ThermoCalc: (a) Weld metal; (b) BM.

The hardness in the fusion zone and HAZ shows an opposite trend after PWHT at 820 °C and 840 °C, as shown in Figure 5.5. The fusion zone hardness increases to 330 HV0.5

for PWHT 820 °C for 8 hours and 400 HV0.5 for PWHT 840 °C for 8 hours, respectively. However, the HAZ hardness decreases to the lowest value (around 210 HV0.5) after PWHT at 820 °C for 8 hours and at 840 °C for 2 hours. The mismatch of the critical  $A_1$  temperature (ferrite-to-austenite transformation temperature) between the filler metal and base metal may be used to clarify this fact. The predicted phase fractions as a function of temperatures of the base metal and the filler metal are shown in Figure 5.19. The calculated  $A_1$  temperatures for the filler metal and base metal are 770 °C and 818 °C, respectively. When the PWHT is conducted at 820 °C, austenitization occurred during heating in the fusion zone, but not in the HAZ. These transformed austenite grains transformed into un-tempered martensite during cooling, which resulted in a hardness increase in the fusion zone, as shown in Figure 5.5. Meanwhile, the HAZ experienced a further tempering instead of austenitization (820 °C is high than the original tempering temperature 786 °C) and therefore a greater reduction in hardness. The highly-homogenized HAZ and base metal share a uniform hardness of 240 HV0.5, as show in Figure 5.4d. Figure 5.7 shows the austenitization just started in the HAZ after PWHT at 840 °C for 2 hours, however, the fusion zone has already been partially austenitized. When the holding time increased to 8 hours, the martensitic transformation from the newly-formed austenite plays an important role in increasing the hardness in the HAZ.

It is concluded that when the PWHT temperature is lower than the  $A_1$ , increasing the temperature results in a higher hardness homogenization effect on the HAZ. When the PWHT temperature is close to the  $A_1$ , the greatest tempering effect leads to the lowest hardness of the HAZ. When the PWHT temperature is higher than the  $A_1$ , the holding time becomes an important factor for controlling the hardness in the HAZ by promoting the austenitization and precipitate dissolution.

### 5.2.2 Transition of creep rupture locations

The Type IV cracking is observed as the major failure mode in the specimens after creep tests. When the PWHT temperature is below or equal to the  $A_1$  (818 °C) of the base metal, the tempering effect only homogenizes the HAZ hardness, but the creep-susceptible softened region still exists, as shown in Figure 5.3 and Figure 5.4. The creep-damaged zones in the Figure 5.10 and Figure 5.11 show a high location consistency with the soften region identified in Figure 5.3 and Figure 5.4. This softened region underwent faster grain growth of ferrite and precipitate coarsening under the creep condition. The matrix grain size increased from 1.2  $\mu\text{m}$  in the as-welded condition to 3.1  $\mu\text{m}$  after the creep test condition in the specimen (PWHT-ed at 760 °C for 2 hours). The precipitates coarsened from an average size of 179 nm in the as-welded condition to 246 nm after the creep test condition in the specimen (PWHT-ed at 760 °C for 2 hours). Coarsened precipitates, mainly  $M_{23}C_6$  carbides, act as the preferential nucleation sites for the cavities in the Type IV cracking. Some finite element modeling works [20, 28] reported the fine-grained HAZ/ICHAZ experienced the highest stress during creep tests. This highest stress condition promotes the largest deformation flow in the softened region, which provides the highest driving force for cavity nucleation. The fusion zone experienced only tempering process when PWHT temperatures are 600 °C and 760 °C. A higher hardness in the PWHT-ed fusion zone indicates that its high strength (creep resistance) is still higher than that of the HAZ.

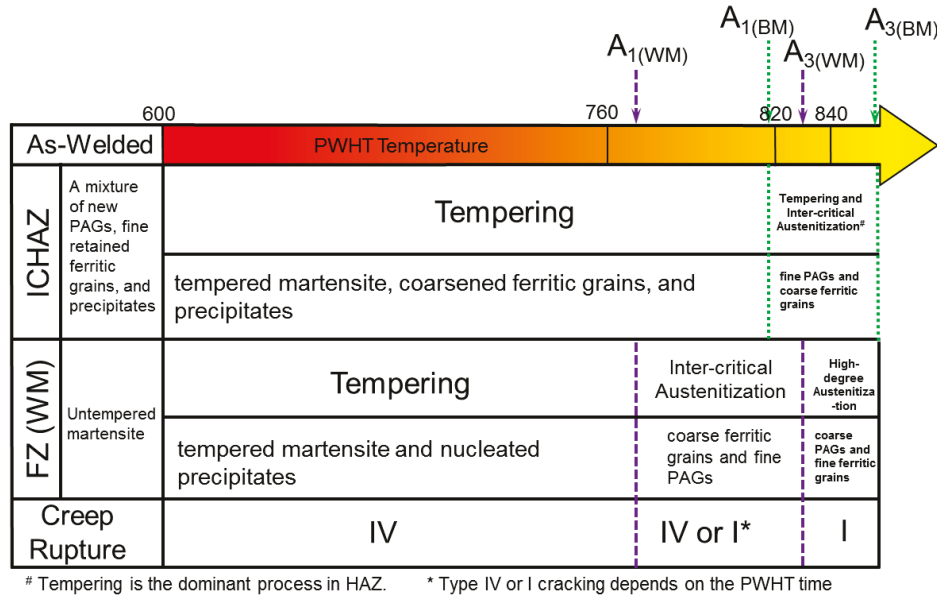


**Figure 5.20:** An illustration of effects of PWHT temperatures on microstructure evolutions of the HAZ and FZ and creep rupture mode of the weldments. The temperature unit in the figure is °C.

The observed creep rupture location has changed from the Type IV cracking in the ICHAZ to the Type I cracking in the fusion zone under PWHT at 820 °C and 840 °C (above  $A_1$  (818 °C) of the base metal). This implies that the fusion zone became the creep-susceptible region in the welds instead of the ICHAZ. To understand this transition, a hypothesis about the effects of different PWHT temperatures on the fusion zone and the ICHAZ has been put forward, which is illustrated in Figure 5.20. The structural evolutions of the fusion zone and the ICHAZ under different PWHT temperature ranges are compared.

Based on our previous observations [125,126], the microstructure of the as-welded ICHAZ is a mixed structure of new prior-austenite grains, fine retained ferritic grains and undissolved precipitates. The structure of the fusion zone is nearly a full-martensitic structure. When the PWHT temperature (600 °C and 760 °C) is below the  $A_1$  temperature (770 °C) of the fusion zone, there is only tempering effect on both the fusion zone and ICHAZ, which causes tempering of matrix grains and nucleation/coarsening of precipitates. In this case, the ICHAZ

remains as the creep-susceptible region in the welds.

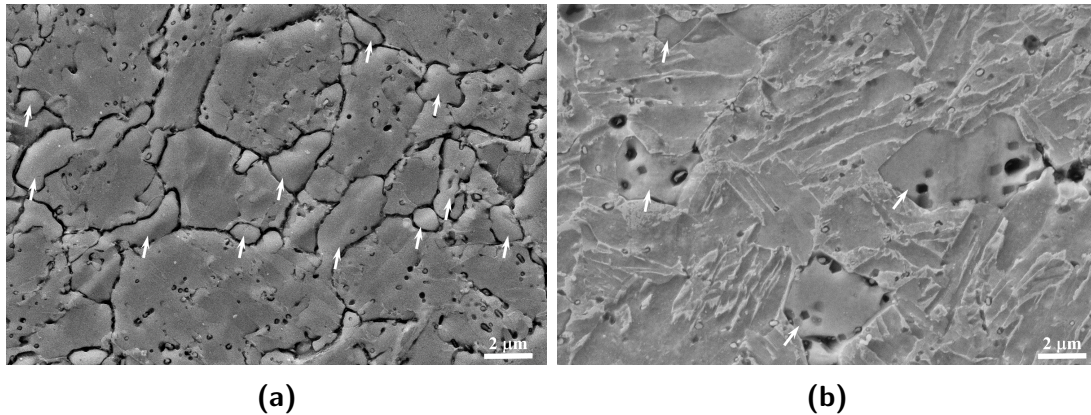


**Figure 5.21:** Microstructure of (a) as-welded ICHAZ and (b) the FZ after PWHT at 840 °C for 2 hours. The untransformed ferritic grains are marked by white arrows in the figures.

Due to the mismatch of the critical  $A_1$  and  $A_3$  temperatures between the fusion zone and base metal, PWHT at the same elevated temperatures (820 °C and 840 °C) causes different structural evolutions in the fusion zone and ICHAZ, respectively. The PWHT temperature 820 °C (around the  $A_1$  of the base metal) is between the  $A_1$  (770 °C) and  $A_3$  (830 °C) temperatures of the fusion zone. The PWHT temperature 840 °C is also located between  $A_{C1}$  and  $A_{C3}$  temperatures of the fusion zone due to the up-shift of  $A_1$  and  $A_3$  temperatures caused by non-equilibrium fast heating during the PWHT. Therefore, it is proposed that the fusion zone becomes a new “ICHAZ” due to an intercritical austenitization during the PWHT at 820 °C and 840 °C. This intercritical austenitization results in an “intercritical” structure in the fusion zone. Figure 5.21 shows structures of the as-welded ICHAZ and the fusion zone after PWHT at 840 °C for 2 hours. They both have two kinds of grains, the newly-transformed prior austenite grains and old untransformed ferritic grains (marked by white arrows). The local strain distribution in the fusion zone, evaluated by the EBSD kernel average misorientation (KAM) map in Figure 5.22, further confirmed the fusion zone’s intercritical feature. The untransformed ferritic grains exhibit a low stored-strain energy (low KAM values) and the new martensite transformed from the new PAGs has a high stored-strain

energy (high KAM values).

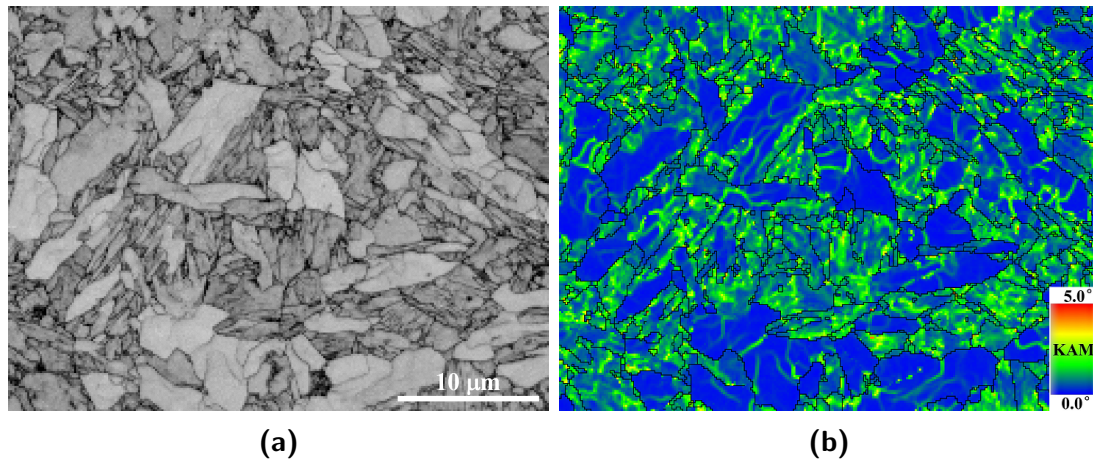


**Figure 5.22:** EBSD analysis on the FZ after PWHT at 840 °C for 2 hours: (a) Band contrast (BC) map; (b) Kernel average misorientation (KAM) map.

The main reason responsible for this non-uniform intercritical austenitization is probably the difference of the transformation driving force from the microsegregation caused by the non-equilibrium solidification in the fusion zone. The non-equilibrium solidification due to the rapid cooling of welding leads to microsegregation of alloying elements, especially Chromium, in the fusion zone. The chemical potential of austenitization differs from the alloying-rich regions and alloy-depleted regions. Zhang et al. [121] reported an inhomogeneous distribution of Cr in the as-welded P91 weld metal causes a gradient activity of carbon which affects the carbon diffusion. The carbon diffusion behavior is believed to be associated with the austenitization rate in the fusion zone.

When the PWHT temperatures are 820 °C (below the  $A_{c1}$  of the base metal), tempering is the only process occurring in the ICHAZ. The HAZ sub-zones, coarse-grained HAZ, fine-grained HAZ, and ICHAZ, behave similarly and form a uniform (highly-tempered) structure as they all have the same chemistry from the base metal, as shown in Figure 5.7. When the PWHT temperature reaches to 840 °C between  $A_1$  (818 °C) and  $A_3$  (856 °C) temperatures of the base metal, both tempering and austenitization occurs in the HAZ as well. Figure

5.1 and Figure 5.2 indicate that tempering is still the dominant process in the HAZ for 2 hours-hold and austenitization becomes the leading process in the HAZ for 8 hours-hold. No matter which process occurs, the HAZ sub-zones and base metal behavior similarly and still form a union.

Our previous study [126] and others [86, 115] have proved the ICHAZ is the creep-susceptible in the welds and responsible for the Type IV cracking under high-temperature creep tests. From the structure point of view, it is believed that this fusion zone with intercritical features become the new creep-susceptible in the welds after PWHT at 820 °C and 840 °C and is directly responsible for the Type I cracking. The large amount of coarse oxides in the fusion zone preferentially act as the cavity nucleation sites, as shown in Figure 5.14b.

The next question that needs to be discussed is the role of PWHT holding time in this creep rupture mode transition. Based on the observation, the Type I cracking only occurred when the PWHT at 820 °C for 8 hours, but not for 2 hours. It is likely that a longer time is needed to generate a high-degree intercritical austenitization for the Type I cracking since the martensite-to-tempered martensite and tempered martensite-to-austenite transformations are time-dependent processes. It is known that the un-tempered martensite is the main phase in the fusion zone after welding. During PWHT, un-tempered martensite firstly becomes tempered martensite by eliminating dislocations. The movement of dislocations is a diffusion-controlled process which is thermal-activated and time-consuming. The tempered martensite-to-austenite transformation is diffusive as well. However, when the PWHT temperature reaches 840 °C, the diffusive tempered martensite-to-austenite transformation has been enhanced because of the increased diffusion coefficients, and the austenitization can finish in a shorter time. Therefore, the Type I cracking already occurred in the specimen PWHT-ed at 840 °C for 2 hours.

## 5.3 Conclusions

Transition of Type IV cracking to Type I Cracking in post-weld heat-treated Grade 91 steel weldments after creep tests was observed and studied. The conclusions of this work are summarized as follows:

(a) The PWHT temperature is the dominant parameter that governs microstructural evolution and hardness distributions in sub-regions in the weldments. The creep-susceptible region in the ICHAZ generated by the welding thermal cycles cannot be eliminated by PWHT at temperatures below the critical  $A_1$  temperature of the base metal, even when a uniform hardness distribution in the HAZ has been achieved. The identified creep-susceptible region shows a high location consistency in the Type IV cracking.

(b) The creep-susceptible region in the weldments has shifted from the ICHAZ to the fusion zone after the heat-treatment at temperatures between the  $A_1$  and  $A_3$  temperatures of the weld metal. The generated intercritical structure of untransformed ferrite and transformed austenite grains in the fusion zone may also cause creep rupture at the fusion zone, also known as the Type I cracking.

# Chapter 6

## Finite Element Analysis of Creep Behavior of Grade 91 Steel Weldments

### 6.1 Results

#### 6.1.1 Modeling of steady-state creep of the PWHT-ed welds

A two-dimensional model is built to simulate stress and strain distributions in the PWHT-ed cross-weld samples during high-temperature creep tests. Based on the previous chapter, the effect of PWHT temperature on creep rupture of the welds is more dominant. Thus three samples after PWHT at different temperatures, 760 °C, 820 °C, and 840 °C are studied for comparison. The PWHT holding time is 2 hours for all three samples. The simulated creep test is also conducted at 650 °C with a stress of 70 MPa.

Geometry of the built 2-D model is shown in Figure 6.1. The model contains the fusion zone (weld metal), HAZ, and base metal. The dimension of each region is based on the cross-weld specimen size. The groove angle of welds is 60°. The HAZ are further divided into three sub-regions, the CGHAZ, FGHAZ, and ICHAZ, based on the observed structures in the previous chapters. Thickness of the CGHAZ, FGHAZ, and ICHAZ in the horizontal direction are 0.8 mm, 1.6 mm, and 0.4 mm, respectively. It should be noted that there is no physical boundaries within the HAZ, and between HAZ and BM. The triple points on the top

and bottom edge may cause some local errors of the simulation due to stress concentration from geometry. However, in the macro-scale level, it is believed this 2-D model is sufficient to study stress and strain distribution in the cross-weld specimens.

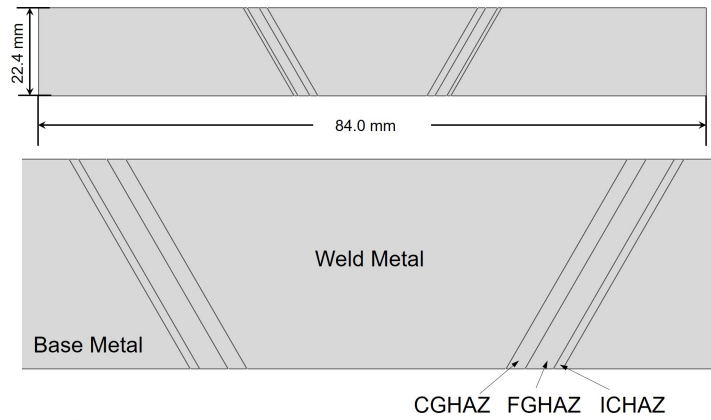


**Figure 6.1:** Geometry of the 2-D cross-weld model.

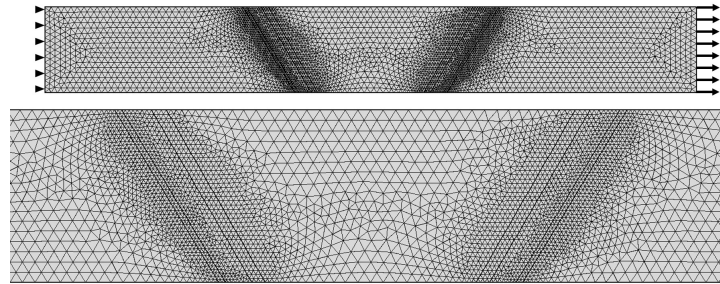


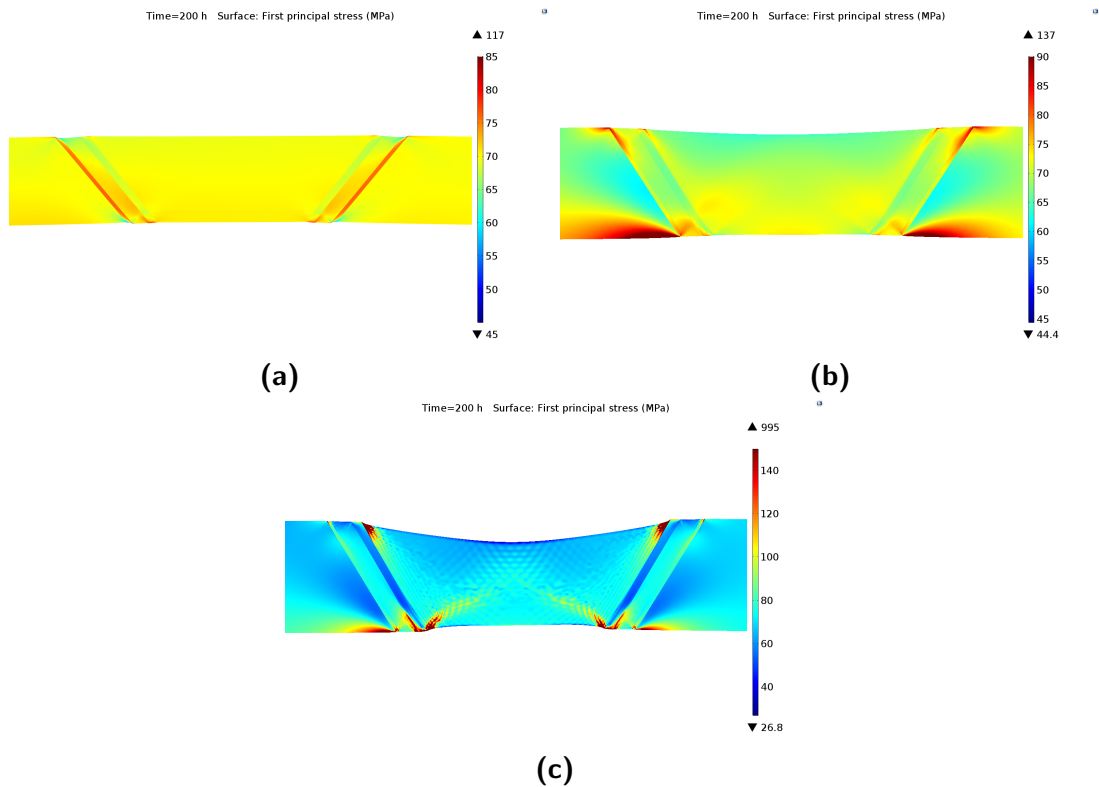
**Figure 6.2:** Physics-based mesh and boundary conditions used in the 2-D cross-weld model.

Based on results of experimental creep tests, the primary creep stage ( $t < 20$  h) of the tested welds is only a small portion of the total creep time. The Norton-Bailey creep law ( $\dot{\epsilon}_c = A\sigma^n m t^{m-1}$ ), a time-hardening formulation, is used for the primary creep stage. Based on the measured creep curve, the shift time  $t$  from primary creep to secondary creep is set as 20 h, and the  $m$  value is fitted from experimental creep curves for each PWHT-ed condition. In the secondary creep ( $t \geq 20$  h), the applied creep constitutive law is the Norton's law ( $\dot{\epsilon}_c = A\sigma^n$ ). Ideally, gradient material properties should be used for the sub-regions of the

HAZ. However, it is difficult to obtain those gradient data for each region. Instead, average property values are applied for each sub-region in the HAZ. Measurement of those average property data at high temperatures is rarely reported. One available data set was measured by our group. High-temperature creep properties for each region were determined by stress-relaxation tests and reported in a previous work [90]. The material parameters used for this simulation are listed in Table 6.1. The Poisson's ratio of 0.29 was used for all parts. For this 2-D model, the plane strain condition is used for the simulation. A physics-controlled mesh with 8070 free triangular elements was used for the model. The mesh size in the HAZ was further refined, as shown in Figure 6.2. A fixed constraint was applied on the left edge. A pressure force of 70 MPa was applied on the right edge.

**Table 6.1:** Material property parameters, including Norton parameters  $A$  ( $\text{MPa}^{-n}\text{s}^{-1}$ ) and  $n$ , Young's modulus  $E$  (MPa) at  $650\text{ }^\circ\text{C}$  are used for FE model in Figure 6.1. These parameters were determined by stress-relaxation tests in a previous work of our group [90]. The samples were PWHT-ed at various temperatures for 2 hours.

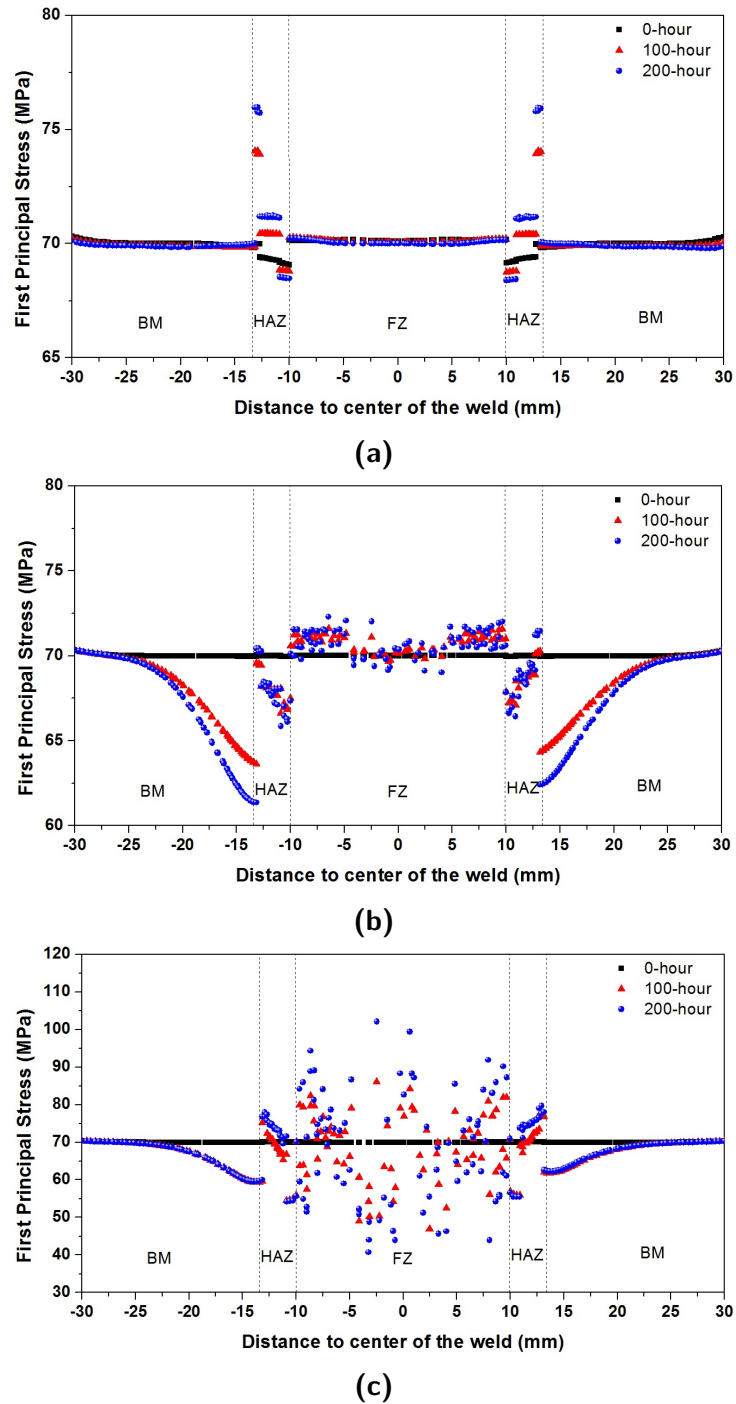
PWHT	Parameters	BM	FZ	CGHAZ	FGHAZ	ICHAZ
760 °C	A	5E-28	2E-30	1E-50	8E-33	2E-33
	n	10	11	21	13	14
	E	14193	10242	26615	25394	9491
820 °C	A	2E-19	1E-20	2E-28	7-E23	2E-17
	n	5	7	11	8	5
	E	14587	13400	14429	13572	12840
840 °C	A	3E-20	1E-17	1E-23	6E-17	2E-16
	n	5	6	7	5	5
	E	14128	12745	12645	11606	12096



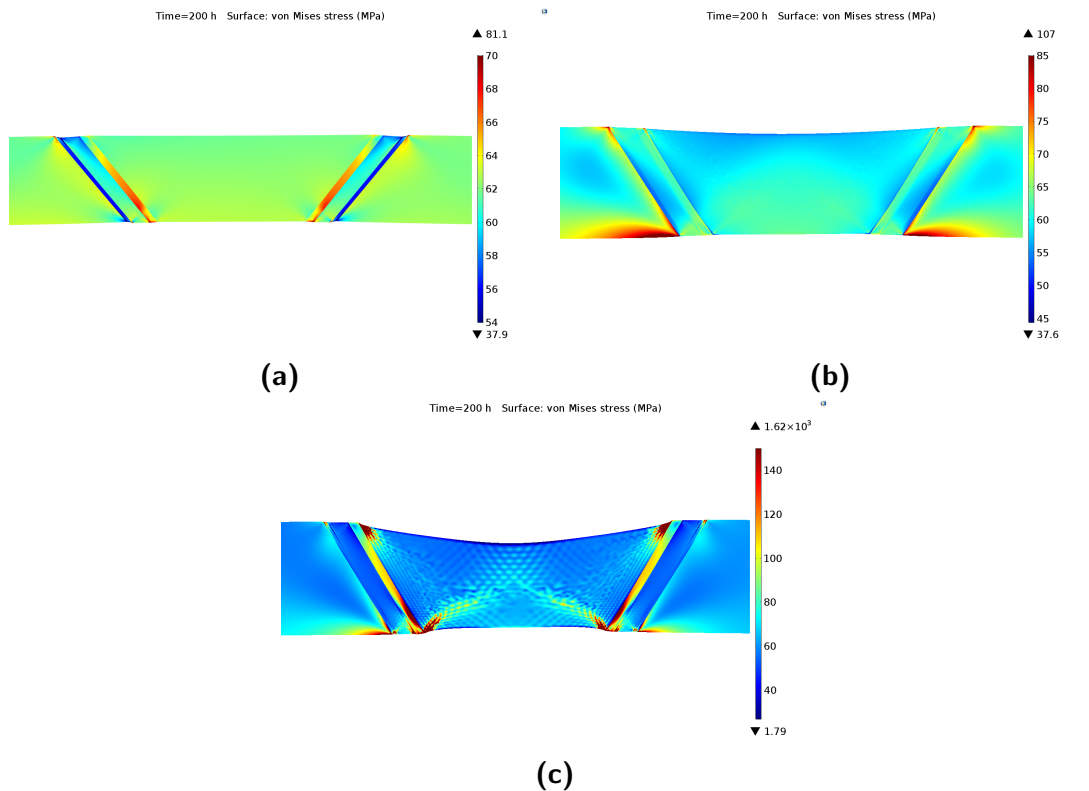
**Figure 6.3:** First principal stress distribution in the welds: (a) PWHT at 760 °C; (b) PWHT at 820 °C; (c) PWHT at 840 °C.

Figure 6.3 shows a snapshot (creep time: 200 h) of the first principal stress distribution in the three welds. The first principal stress distribution across the mid-thickness of the welds is shown in Figure 6.4. Figure 6.3a exhibits that the FZ and BM show comparable stress values of 70 MPa. The ICHAZ on the outer edge of the HAZ experiences the highest first principal stress ( $\sim 76$  MPa) and the CGHAZ close to FZ has the lowest first principal stress ( $\sim 68$  MPa) in the weld PWHT-ed at 760 °C. The first principal stress in the ICHAZ and CGHAZ shows an opposite increase-decrease trend as the creep time increases. Differences of the first principal stress distribution in the weld PWHT-ed at 820 °C are shown in Figure 6.3b and Figure 6.4b. The FZ and ICHAZ experience a principal stress just above 70 MPa. A region with a low first principal stress is located in the BM adjacent to the HAZ. The stress in FGHAZ and CGHAZ is below 70 MPa. The stress distribution remains the same in the

FZ and HAZ at 100 h and 200 h. In the weld PWHT-ed at 840 °C, the first principal stress scatters from 40 MPa to 100 MPa in the FZ. The ICHAZ shows a stress value above 70 MPa.

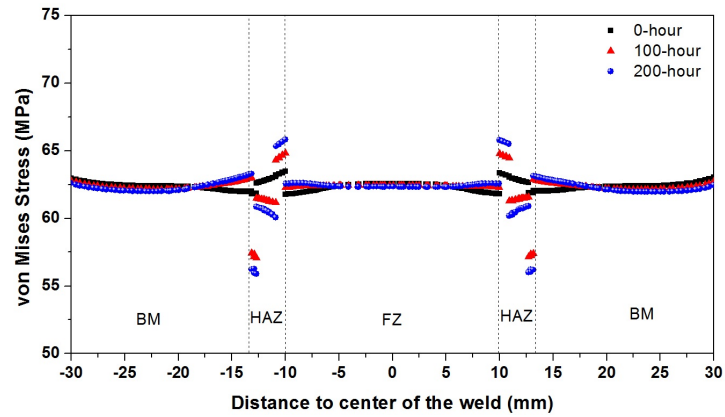


**Figure 6.4:** First principal stress distribution across the mid-thickness of the welds: (a) PWHT at 760 °C; (b) PWHT at 820 °C; (c) PWHT at 840 °C.

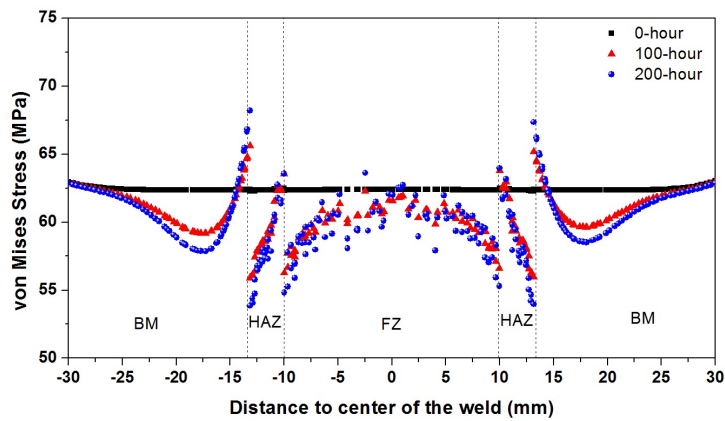


**Figure 6.5:** Von Mises stress distribution in the welds after creep tests for 200 h: (a) PWHT at 760 °C; (b) PWHT at 820 °C; (c) PWHT at 840 °C.

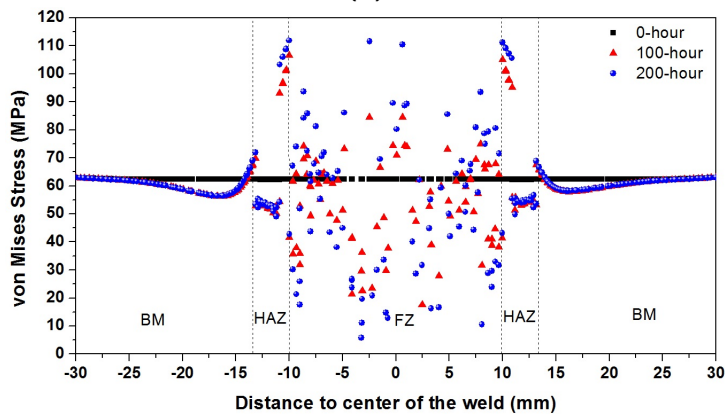
Figure 6.5 shows a snapshot (creep time: 200 h) of von Mises stress distribution in the three welds. The von Mises stress distribution across the mid-thickness of the welds is shown in Figure 6.6. In the weld PWH-ed at 760 °C, the CGHAZ exhibits the highest von Mises stress and the ICHAZ shows the lowest value. Stress difference between the two region increases with creep time. In the weld PWHT-ed at 820 °C, the CGHAZ still shows the highest von Mises stress within the HAZ. The interface between the ICHAZ and BM has the largest von Mises stress. The edges of the FZ adjacent to the CGHAZ exhibit low von Mises stress values. In the weld PWHT-ed at 840 °C, the CGHAZ exhibits the highest von Mises stress ( $\sim 110$  MPa). The von Mises stress varies from 20 MPa to 110 MPa in the FZ.



(a)



(b)



(c)

**Figure 6.6:** Von Mises stress distribution across the mid-thickness of the welds: (a) PWHT at 760 °C; (b) PWHT at 820 °C; (c) PWHT at 840 °C.

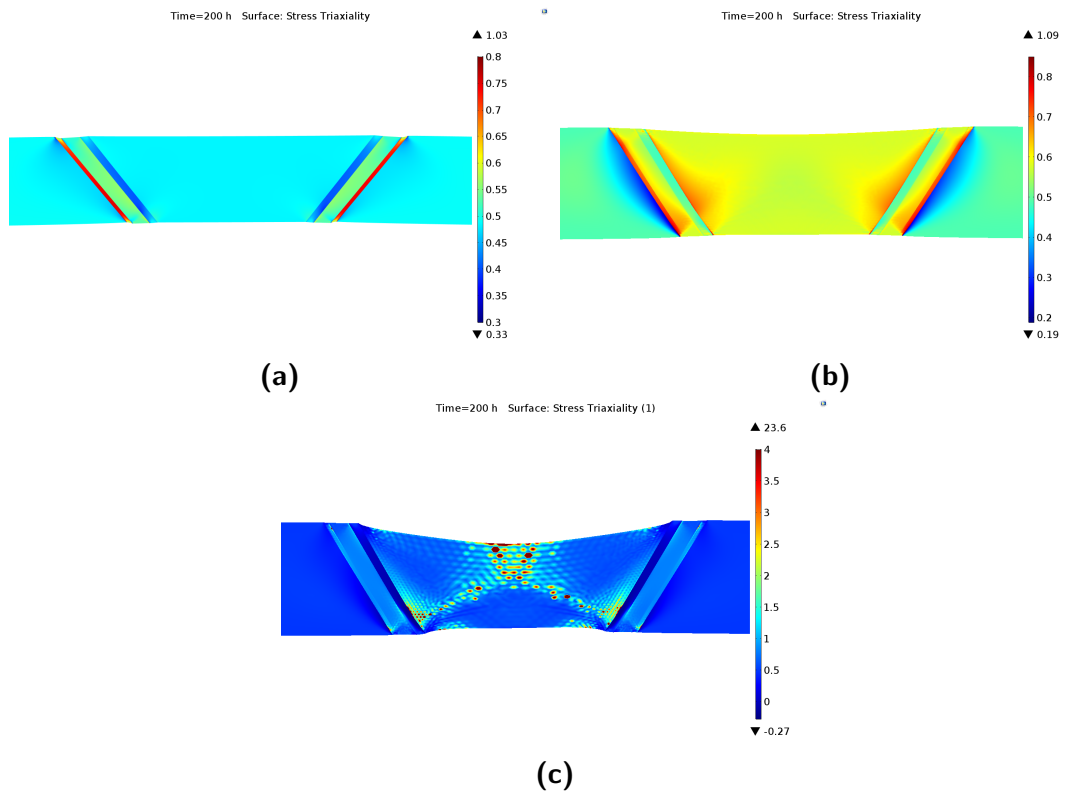
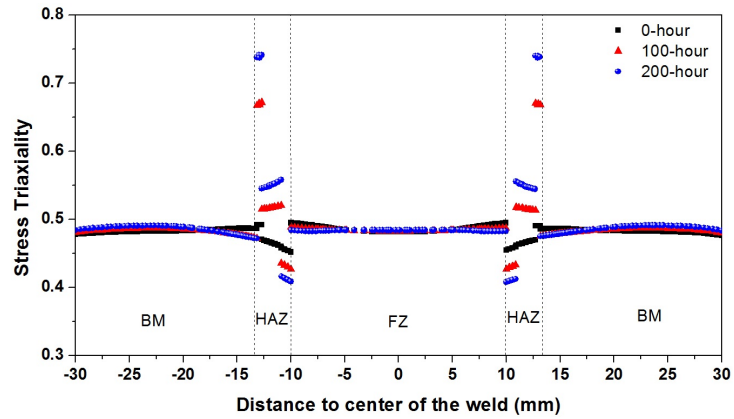
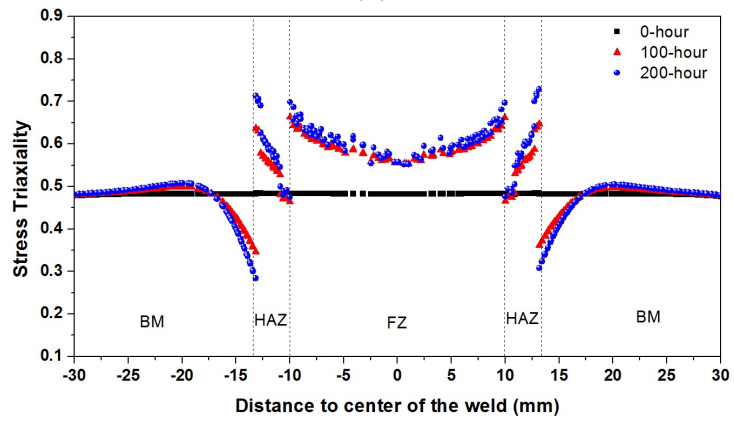


**Figure 6.7:** Stress triaxiality distribution in the welds after creep tests for 200 h: (a) PWHT at 760 °C; (b) PWHT at 820 °C; (c) PWHT at 840 °C.

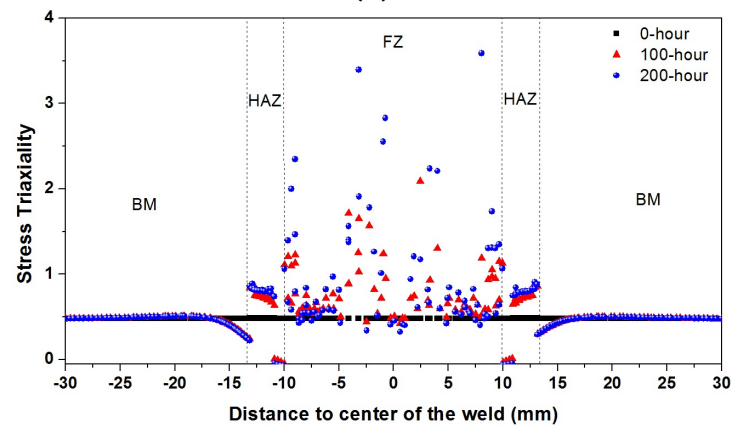
Figure 6.7 shows a snapshot (creep time: 200 h) of stress triaxiality distribution in the three welds. The stress triaxiality distribution across the mid-thickness of the welds is shown in Figure 6.8. In the weld PWHT-ed at 760 °C, the FZ and BM show comparable stress triaxiality values. The CGHAZ has the lowest stress triaxiality and the ICHAZ exhibits the highest stress triaxiality. In the weld PWHT-ed at 820 °C, high stress triaxiality exists in the FZ and HAZ, as shown in Figure 6.7b and Figure 6.8b. The ICHAZ still shows the highest stress triaxiality value. A region with the lowest stress triaxiality is observed on the BM adjacent the ICHAZ. In the weld PWHT-ed at 840 °C, the FZ has high stress triaxiality. Points with significantly high stress triaxiality are observed in the FZ. The FGHAZ and ICHAZ show comparable stress triaxiality values. The CGHAZ exhibits quite low stress triaxiality values.



(a)



(b)



(c)

**Figure 6.8:** Stress triaxiality across the mid-thickness of the welds: (a) PWHT at 760 °C; (b) PWHT at 820 °C; (c) PWHT at 840 °C.

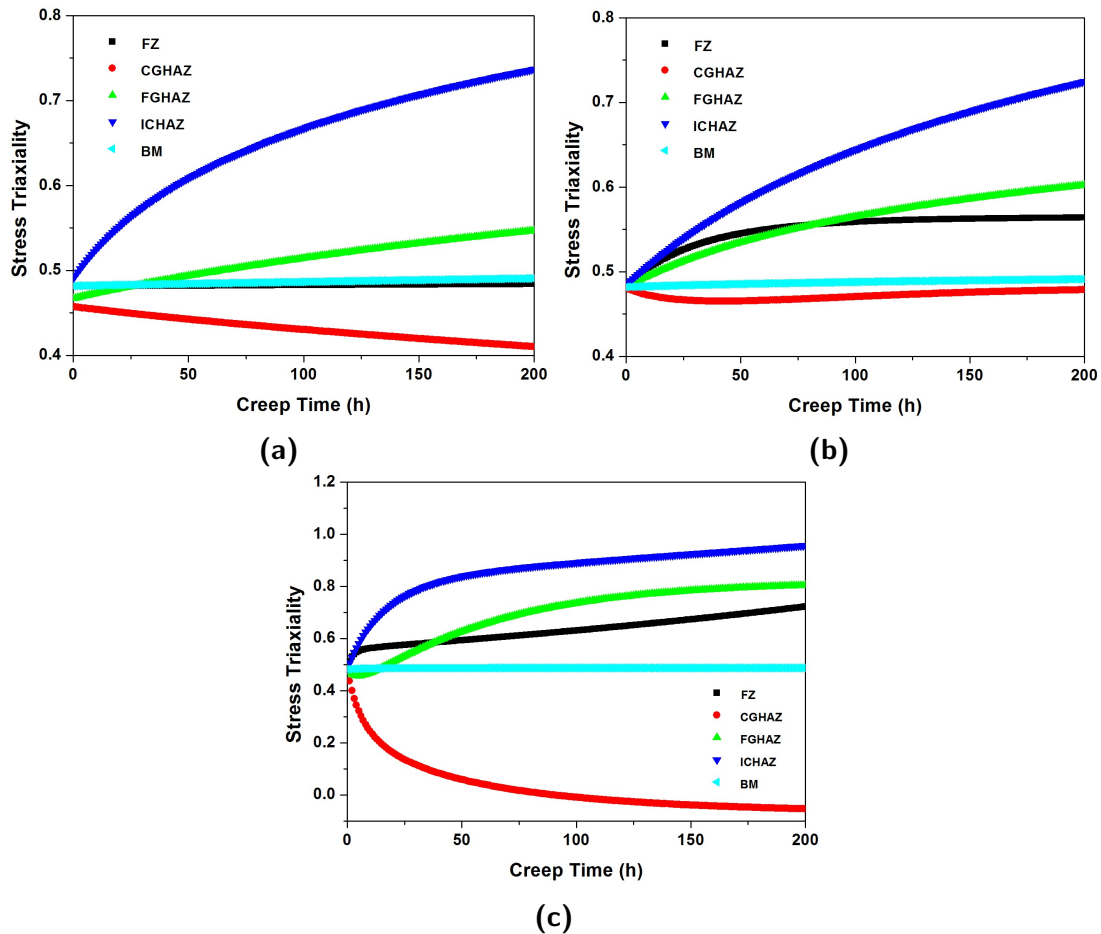


**Figure 6.9:** Stress triaxiality in the centre point of each region as a function of creep time: (a) PWHT at 760 °C; (b) PWHT at 820 °C; (c) PWHT at 840 °C.

The stress triaxiality in the center point of each region as a function of creep time is plotted in Figure 6.9. Overall, the ICHAZ exhibits the highest stress triaxiality and increases fastest with the creep time. The CGHAZ shows the opposite trend. The BM keeps relatively constant stress triaxiality value of 0.48. The stress triaxiality of the FZ increase quickly in the weld PWHT-ed at 820 °C and 840 °C. It should be pointed out that the lower stress triaxiality (lower than the ICHAZ) of the centre point in the FZ of the weld PWHT-ed at 840 °C in Figure 6.9c does not reflect the general stress triaxiality distribution in this case. Figure 6.8c shows the FZ exhibits a higher stress triaxiality than the HAZ.

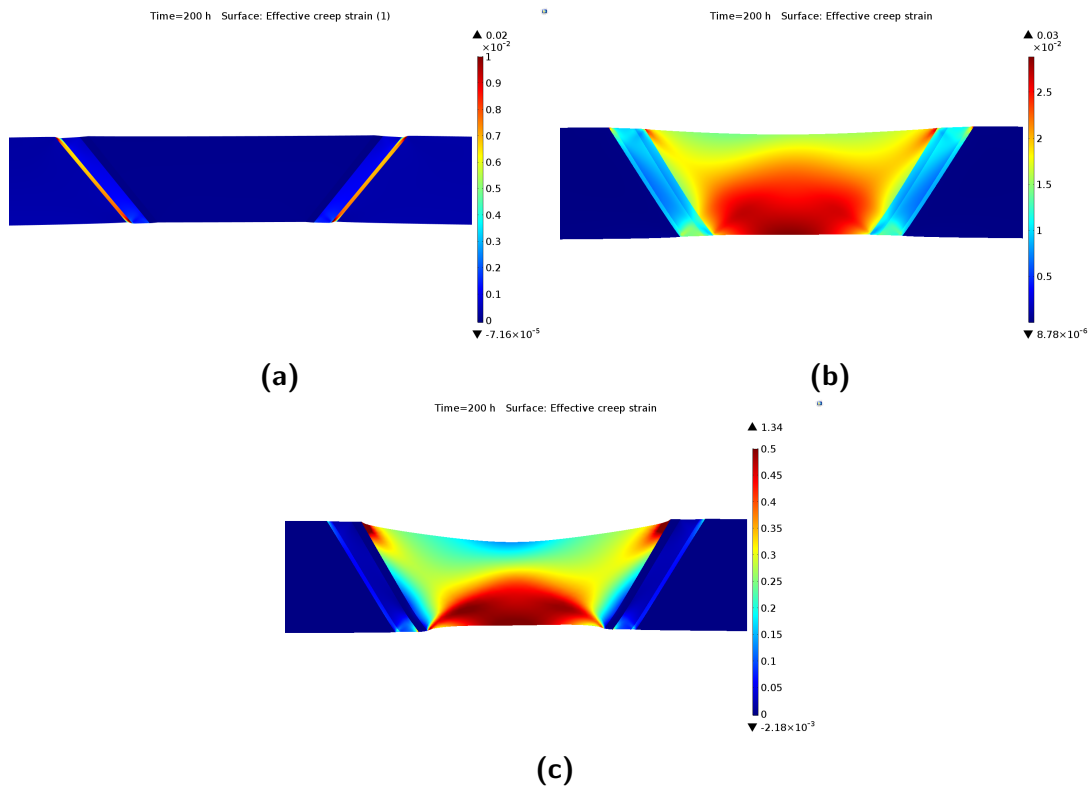
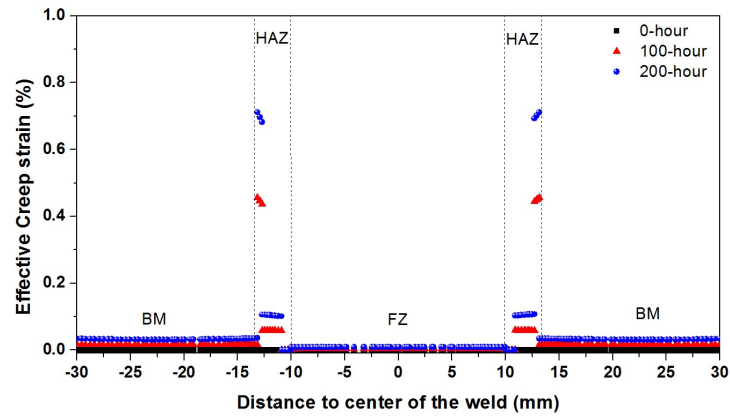
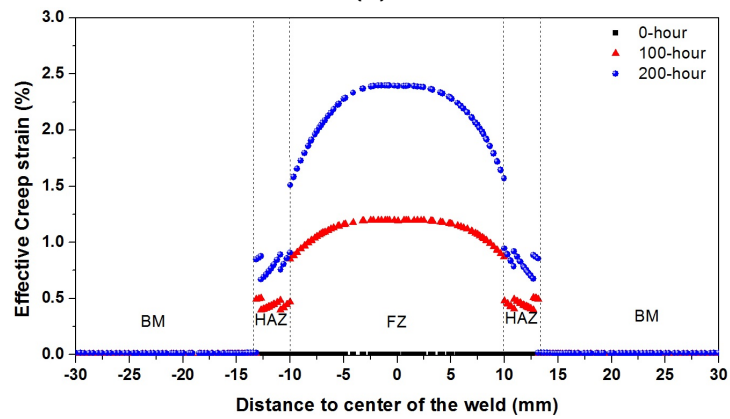


**Figure 6.10:** Effective creep strain in the welds after creep tests for 200 h: (a) PWHT at 760 °C; (b) PWHT at 820 °C; (c) PWHT at 840 °C.

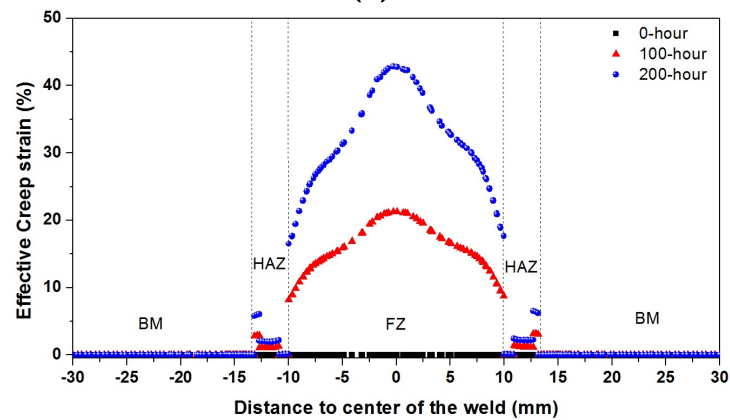
The effective creep strain is defined as [127]:  $\varepsilon_e^c = \sqrt{\frac{3}{2} \varepsilon_{ij}^c \varepsilon_{ij}^c}$ , where  $\varepsilon_{ij}^c$  are the components of creep strain tensor. Effective creep strain in the welds after creep tests for 200 h is shown in Figure 6.10. In the weld PWHT-ed at 760 °C, the ICHAZ exhibits the highest effective creep strain, compared to other regions. The strain values are quite small (below 1%). In both the welds PWHT-ed at 820 °C and 820 °C, the FZ has the highest effective creep strain. The difference, as shown in Figure 6.11, is that in the weld PWHT-ed at 820 °C effective creep strain difference between the FZ and HAZ is much smaller than that in the weld PWHT-ed at 840 °C.



(a)



(b)



(c)

**Figure 6.11:** Effective creep strain distribution across the mid-thickness of the welds: (a) PWHT at 760 °C; (b) PWHT at 820 °C; (c) PWHT at 840 °C.

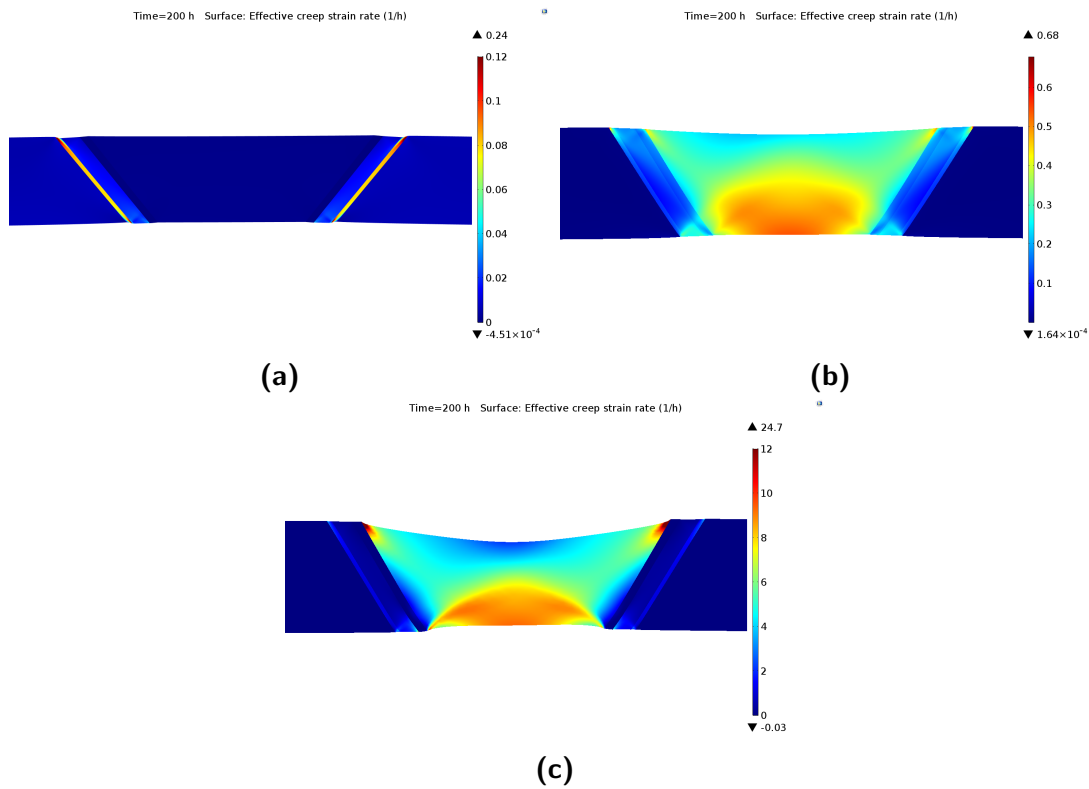


**Figure 6.12:** Effective creep strain rate in the welds after creep tests for 200 h: (a) PWHT at 760 °C; (b) PWHT at 820 °C; (c) PWHT at 840 °C.

The effective creep strain is defined as [127]:  $\dot{\epsilon}_e^c = \sqrt{\frac{1}{2} \dot{\epsilon}_{ij}^c \dot{\epsilon}_{ij}^c}$ , where  $\dot{\epsilon}_{ij}^c$  are the components of creep strain rate tensor. The snapshot of effective creep strain rate in the welds after creep tests for 200 h is shown in Figure 6.12. Generally, the effective creep strain rate shows a similar trend with the effective creep strain in Figure 6.10. In the weld PWHT-ed at 760 °C the ICHAZ has the highest effective creep strain rate. In the weld PWHT-ed at 820 °C strain rate in the FZ is slightly higher than that in the HAZ. However, the FZ's strain rate is dramatically higher than that in the HAZ. Figure 6.13 shows the strain rate in the HAZ decreases with the creep time in the weld PWHT-ed at 760 °C. However, the strain rate in the other two welds seems to keep constant with the increasing creep time.

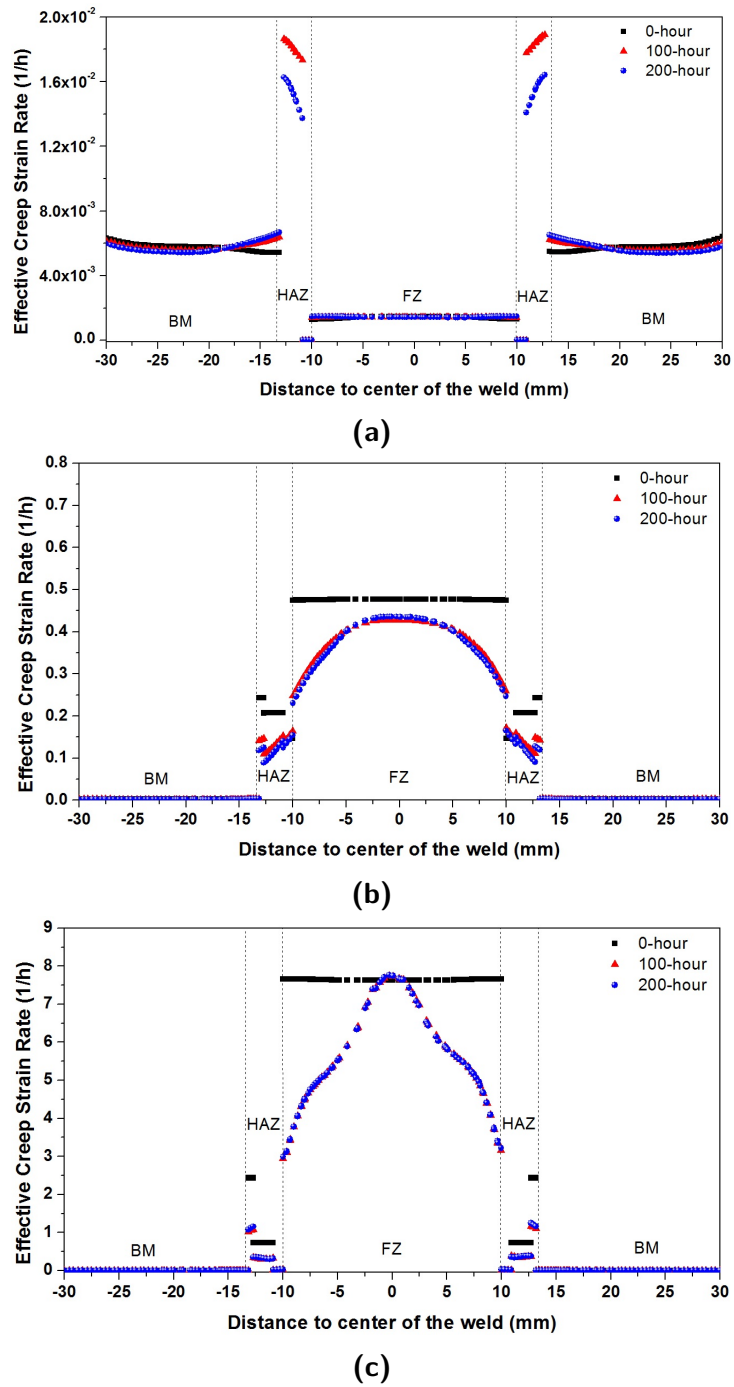


**Figure 6.13:** Effective creep strain rate across the mid-thickness of the welds: (a) PWHT at 760 °C; (b) PWHT at 820 °C; (c) PWHT at 840 °C.

### 6.1.2 Preliminary study of local stress distribution in a crept ICHAZ

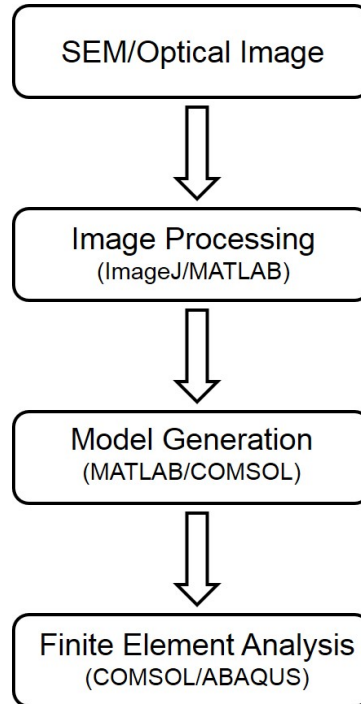


**Figure 6.14:** A flow chart shows the steps for generating microstructure-based models for finite element analysis.

Based on the experimental observations in previous chapters, more creep cavities nucleated in the ICHAZ in the Type IV cracking. Cavities were observed to be associated with grain boundaries and coarse boundary precipitates. It is well believed that these boundary precipitates cause local stress concentration on the grain boundaries, which promotes nucleation of cavities. To further clarify this statement, a microstructure-based model is ideal to be used.

A flow chart in Figure 6.14 presents steps for generating a microstructure-based model for FE analysis. The model was built from an observed structure in the ICHAZ, as shown in Figure 6.15a. The HAZ specimen was from the cross-weld sample (PWHT-ed at 760 °C for 2 hours) fractured with the the Type IV cracking after creep tests. The structure contains highly-grown matrix ferrite grains, and coarsened precipitates. Imaging processing through ImageJ and Matlab was used to highlight precipitates and grain boundaries, as shown in

Figure 6.15b. After that, a microstructure-based geometry was generated and imported into the Comsol simulation software.

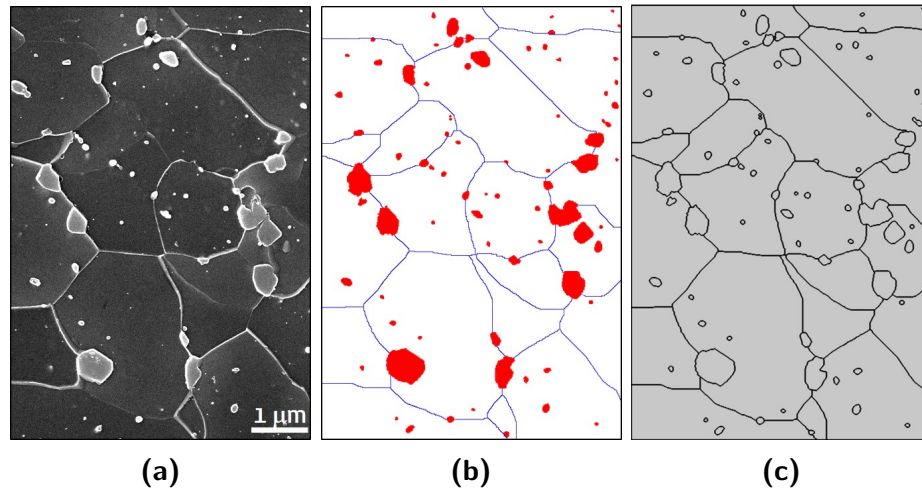


**Figure 6.15:** (a) SEM image shows typical microstructure of the ICHAZ in the specimen (PWHT-ed at 600 °C for 2 hours) after creep tests for 650 hours; (b) Post-processed graph (right) highlights the grain boundaries and distributed precipitates; (c) Geometry of the microstructure-based model.

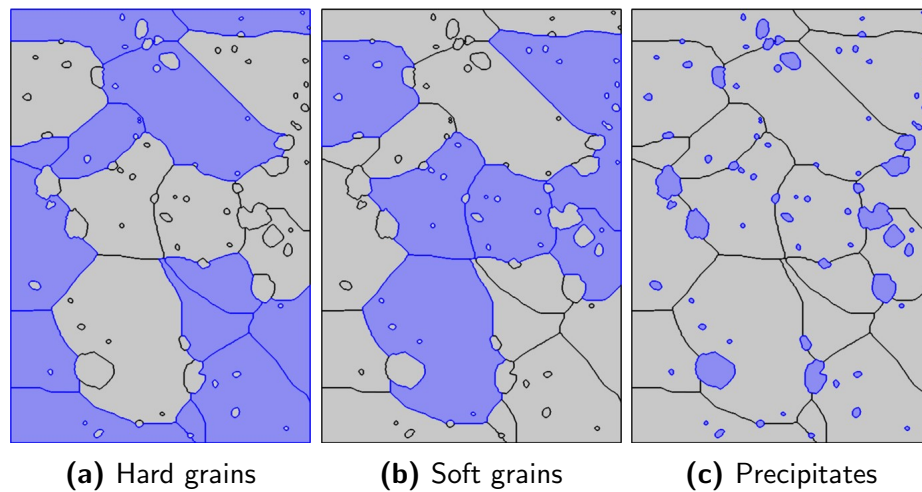


**Figure 6.16:** Three structural components with various strengths, including hard grains, soft grains, and precipitates, used in the microstructure-based model.

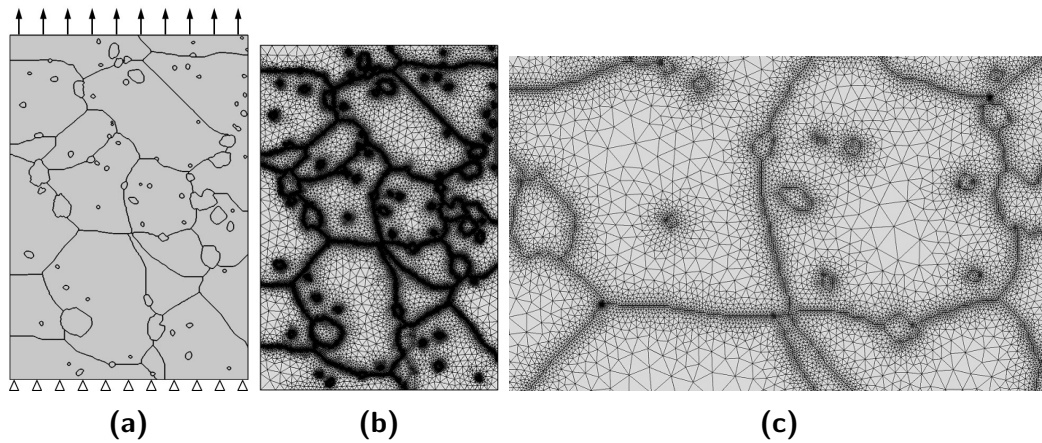


**Figure 6.17:** Boundary conditions and mesh used in the microstructure-based model.

To simulate micro-mechanics response of grain structures, crystal plasticity model is the ideal model. However, the difficulty is that creep properties of single crystal at evaluated creep temperatures and applied stresses are currently not available. Instead, averaged material properties from polycrystals was measured by stress relaxation tests, as shown in Table 6.1. Thus a simplified model by using these averaged properties was built to study local stress distribution under creep condition. Based on the previous observations, the ICHAZ has a mixed structure of hard grains, soft grains, and precipitates. Therefore, three structural components, including soft grains, hard grains, and precipitates, were considered in this microstructure-based model, as shown in Figure 6.16. The FGHAZ properties measured by stress-relaxation tests for the 760 °C-PWHT-ed sample were used as materials properties for those hard grains. And the ICHAZ properties were used for those soft grains. Those precipitates are treated as Cr-rich  $M_{23}C_6$  carbides. Properties (Young's modulus of 340 GPa and Poisson's ratio of 0.30) of precipitates are estimated from reported values in Ref. [128] and an empirical linear equation. Boundary conditions used in the model is shown in Figure 6.17a. A pressure stress of 70 MPa was applied on the top and the bottom is fixed. Symmetry boundaries were also used in the left and right edges. The plane strain condition is also used in this simulation. Mesh of the model are shown in Figure 6.17a and 6.17b. A physics-controlled mesh with 244765

free triangular elements is used in the model. Refined mesh is used for grain boundaries and precipitates.

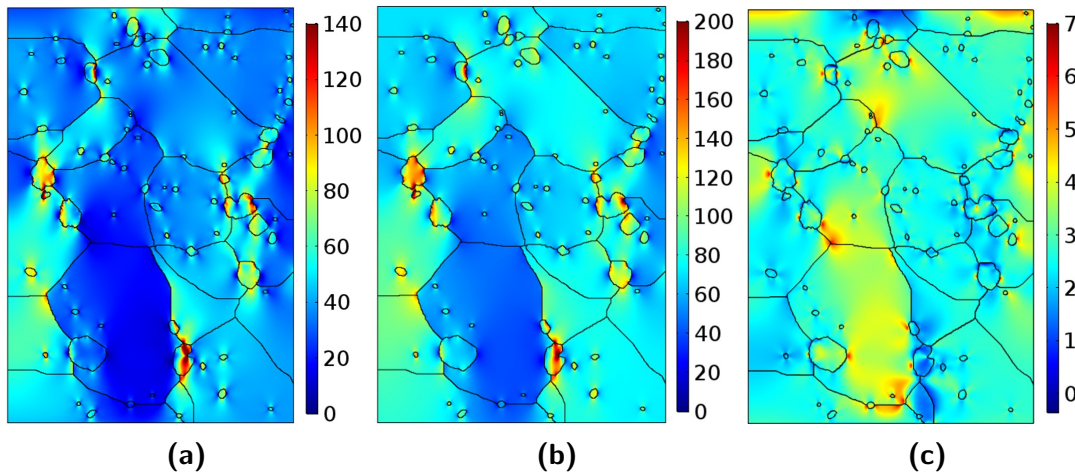


**Figure 6.18:** Von Mises stress (MPa), first principal stress (MPa), and stress triaxiality distributions in the structure.

Distributions of the simulated von Mises stress, first principal stress, and stress triaxiality in the structure are presented in Figure 6.18. Generally, similar distributions of von Mises stress and first principal stress are observed in the structure. The first principal stress level is higher than the von Mises stress. Local stress concentration as high as 200 MPa is observed to be associated with precipitates. A higher stress level ( $> 70$  MPa) exists in some of precipitates and adjacent regions. High stress levels ( $> 100$  MPa) are also observed in some triple points of grain boundaries. Figure 6.18c shows the stress triaxiality distribution in the structure. It is seen that points with high stress triaxiality as high as 7 are observed. Their locations are different from the points with high stress levels. Some grain boundary triple points close to precipitates show high stress triaxiality. These points are considered as the likely-nucleation sites for creep cavities.

## 6.2 Discussion

Based on the results of FE analysis, distributions of stress, stress triaxiality, strain, and strain rate in the welds vary with the PWHT temperatures, which eventually results in different creep rupture modes, including the Type IV cracking and Type IV cracking. The next question to answer is which one is the key factor leading to different creep rupture modes.

It is widely accepted that the Type IV cracking occurs in the FGHAZ or ICHAZ. According to the structural analysis in previous chapters and the modelling results, the ICHAZ should be the critical region, or creep-susceptible region in the Type IV cracking. In the weld PWHT-ed at 760 °C the ICHAZ exhibits the highest effective creep strain (rate) and the highest stress triaxiality. It is known that creep deformation (strain) is driven by stress in the materials, which seems to be a good indicator of creep failure. However, there is an opposite trend of von Mises stress and first principal stress in the CGHAZ, FGHAZ, and ICHAZ. Thus it is difficult to predict creep performance with a single stress. Instead, the stress triaxiality is likely to be a reliable index of evaluating creep behavior of multiple regions in the welds.

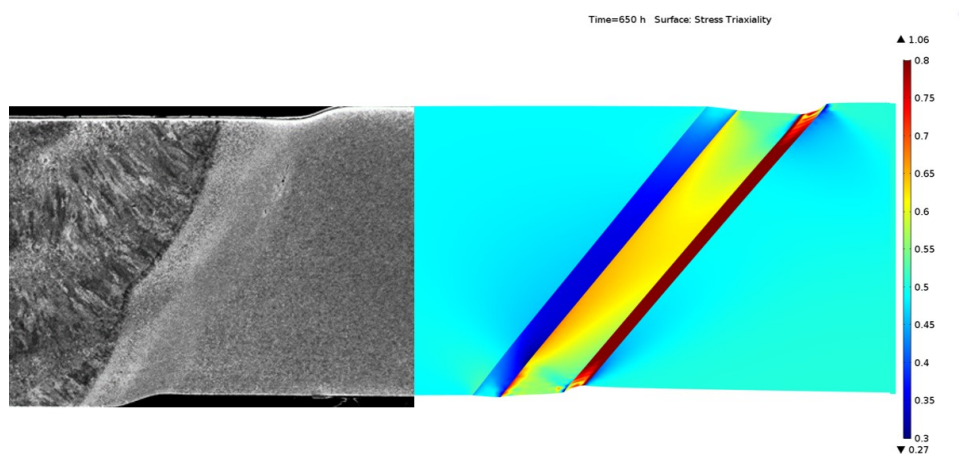


**Figure 6.19:** Optical image of a Type IV cracking and stress triaxiality in the cross-weld model.

Figure 6.19 shows a typical Type IV cracking in a weld and the stress triaxiality distribution in the HAZ of the cross-weld model. The local necking in the ICHAZ correlates with the

highest stress triaxiality and the largest local deformation. Beside this, another common observation in the Type IV cracking is that the initial cracks are located in the mid-thickness of the welds. To understand this, the stress triaxiality across the ICHAZ along the thickness direction is obtained and shown in Figure 6.20.

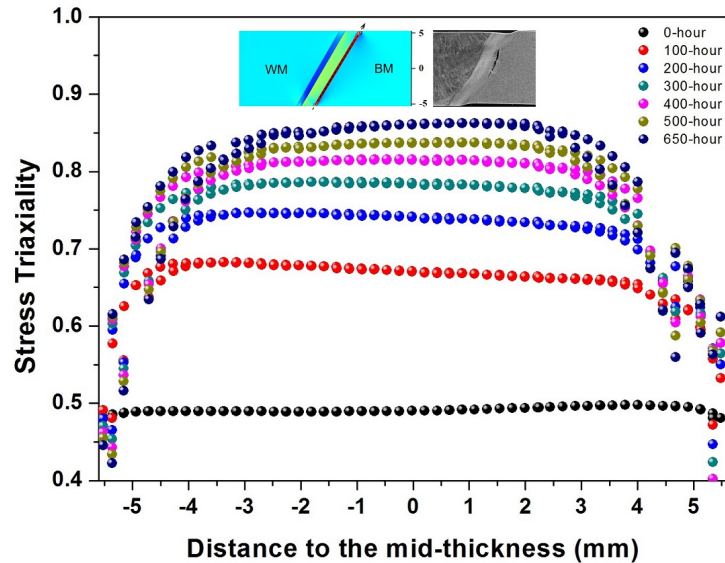


**Figure 6.20:** Stress triaxiality distribution in the ICHAZ in the thickness direction (PWHT-ed at 760 °C).

Figure 6.20 clearly shows that the stress triaxiality on the edges is lower than that in the mid-thickness. Meanwhile, the stress triaxiality value increases with creep time. The shape of the stress triaxiality curve bends toward the mid-thickness. All these features indicate the mid-thickness of ICHAZ always experienced the highest stress triaxiality during creep test, which eventually promotes nucleation of cracks in the Type IV cracking. In the weld PWHT-ed at 820 °C the ICHAZ still exhibits the highest stress triaxiality and the Type IV cracking is observed in this specimen as well, even the FZ shows a higher creep strain.

Stress triaxiality can be also used to evaluate creep fracture of the Type I cracking. Figure 6.4c and Figure 6.6c show that the first principal stress and von Mises stress vary significantly around the initial stress values (creep time is 0 h). It is difficult to draw a conclusion that

stress in the FZ is high or low than the HAZ. However, the stress triaxiality in Figure 6.8 clearly shows that the FZ has higher stress triaxiality values than the HAZ, which indicates the FZ is most likely to fracture in a Type I cracking in the weld PWHT-ed at 840 °C.

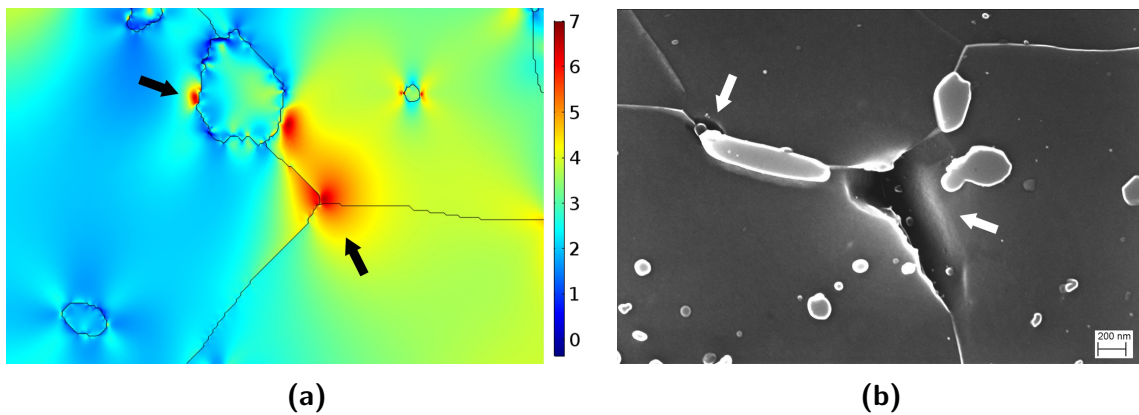


**Figure 6.21:** (a) Stress triaxiality in the structured-based model; (b) A creep cavity nucleated in a grain boundary triple intersection.

From the microstructure point of view, nucleation of cracks is a process of accumulating creep cavities. Growing and inter-connection of creep cavities lead to formation of micro-cracks. Therefore, the relation between stress triaxiality distribution and nucleation of creep cavities may be worthy of checking. Figure 6.21 shows an example of stress triaxiality distribution in the microstructure-based model and an observed creep cavity in the ICHAZ. It is obvious shown that the coarse precipitate near the triple point of grain boundaries causes a high stress triaxiality in the triple point. A region with a high stress triaxiality value is also observed at the interface between precipitate and matrix grain. SEM image in Figure 6.21b presents a similar case. A small cavity nucleated at the end of the rod-like precipitates. Grain boundary fold at triple points promotes nucleation of creep cavities. Therefore, stress triaxiality has a close relationship with cavity nucleation during creep tests.

## 6.3 Conclusions

Stress and strain distribution in the PWHT-ed welds during creep tests were studied by finite element analysis. The ICHAZ, exhibiting the highest first principal stress, the largest stress triaxiality, and the highest creep strain/strain rate, has been verified as the most creep-susceptible region when the PWHT temperature is below  $A_1$  temperature of base metal. The fusion zone becomes the new creep-susceptible region with the largest stress triaxiality and the highest creep strain/strain rate when the PWHT temperature is between  $A_1$  and  $A_3$  of the weld metal. Stress triaxiality in the mid-thickness of the ICHAZ increases with creep time, resulting in formation of cracks in the mid-thickness during the Type IV cracking. Microstructure-based modelling was attempted to simulate local stress distribution in the ICHAZ. Results show that stress triaxiality has a close relationship with creep cavity nucleation.

# Chapter 7

## Summary and Future Work

### 7.1 Summary

The work presented in this dissertation focuses on studies of microstructural evolution and creep behavior of heat-affected zone in Grade 91 steels. The main findings are summarized as follows:

Structural heterogeneities in the as-received Grade 91 pipe base metal and rapid heating/cooling in fusion arc welding lead to inhomogeneous structures in sub-regions of the HAZ. The as-welded HAZ of the pipe welds is divided into a narrow CGHAZ, a wide FGHAZ, and a narrow ICHAZ. The CGHAZ consists of coarse PAGs with a substructure of martensite laths, uniformly-distributed fine  $M_{23}C_6$  precipitates and a higher fraction of MX carbonitrides. Fine equiaxed PAGs with coarse undissolved Cr-rich  $M_{23}C_6$  carbides and fine newly-nucleated  $M_{23}C_6$  carbides are observed in the FGHAZ. The ICHAZ shows a mixed structure of newly-formed PAGs and retained tempered martensite. The undissolved Cr- $M_{23}C_6$  carbides in the FGHAZ and ICHAZ consume alloying elements, especially C and Cr. Dissolution of Cr- $M_{23}C_6$  carbides can not significantly promote grain growth of austenite during rapid heating, but can efficiently lower the  $M_s$  temperature and increase martensite hardness.

Islands of  $\delta$ -ferrite along the prior austenite grain (PAG) boundaries and tempered martensite constitute the typical microstructure of the as-received heavy section base metal. The

as-welded HAZ of this heavy section is divided into a narrow CGHAZ, a wide FGHAZ, and a wide ICHAZ. The ICHAZ exhibit the highest structural heterogeneities with the finest grain size, the largest local strain distribution, and a large frequency of the deformed grains. Micro-segregation of the ferrite stabilizing elements in the  $\delta$ -ferrite grains, originated from the initial base metal, thermodynamically stabilizes its presence in the HAZ after welding. Dilatometry study implies that significant dissolution of  $\delta$ -ferrite only occurs in the CGHAZ region.  $\delta$ -ferrite grains cannot be fully dissolved in FGHAZ and ICHAZ regions. Decomposition of the  $\delta$ -ferrite grains in the HAZ favors precipitation of dense carbides along the boundaries with the adjacent tempered martensite matrix, which is harmful to the creep resistance of the HAZ.

The mechanism of Type IV cracking is understood from a new perspective of the local chemistry in a grain-scale level. Type IV cracking occurred in a narrow creep-susceptible region, in the ICHAZ of Grade 91 weldment. The as-welded soft zone in the weldment is positively identified as the ICHAZ. Non-uniform chromium distributions in the austenite grains and martensitic packets of the base metal cause a heterogeneous austenitic transformation in the ICHAZ during welding, which results in a mixed structure of newly-formed austenite grains, undissolved precipitates, and a number of untransformed tempered martensite. During PWHT and creep tests, Cr-depleted untransformed grains preferentially grew, which results in lower creep strength. Coarsened Cr-rich  $M_{23}C_6$  carbides at the grain boundaries have provided preferred nucleation sites for creep cavities. Deformation of the weak Cr-depleted grains accelerated the coarsening of the nucleated cavities, which eventually resulted in the observed Type IV cracking. Finite element analysis further verifies that the ICHAZ, exhibiting the highest first principal stress, the largest stress triaxiality, and the highest creep strain/strain rate, is the most creep-susceptible region when the PWHT temperature is below  $A_1$  temperature of base metal. Stress triaxiality in the mid-thickness of the ICHAZ increases with creep time, resulting in formation of cracks in the mid-thickness during the Type IV cracking. In

the mesoscale level, nucleation of creep cavities along the grain boundaries is caused by high stress triaxiality values.

Transition from Type IV cracking to Type I cracking in post-weld heat-treated Grade 91 steel weldments after creep tests was observed and studied. The PWHT temperature is the dominant parameter that affects the microstructural evolution and hardness distributions in the weldments. The creep susceptible region in the HAZ generated by the welding thermal cycles cannot be eliminated by PWHT at temperatures below the critical  $A_1$  temperature of the base metal, even when a homogenized hardness distribution in the HAZ can be achieved. This creep susceptible region, showing a high location consistency, is the location for Type IV cracking. An intercritical structure of untransformed ferrite and transformed austenite grains in the fusion zone after PWHT at temperatures between the  $A_1$  and  $A_3$  temperatures of the weld metal leads to creep rupture at the fusion zone, also known as Type I cracking. The creep susceptible region in the weldments has shifted from the ICHAZ to the fusion zone after the heat-treatment at an intercritical temperature between the  $A_1$  and  $A_3$  temperatures of the weld metal. Results of finite element analysis indicate that the FZ becomes the new creep-susceptible region with the largest stress triaxiality and the highest creep strain/strain rate when the PWHT temperature is beyond  $A_1$  temperature of base metal.

This research builds a close relationship between local microstructural evolutions in the heat-affected zone and creep rupture behavior of Grade 91 steel weldments. The results provide a practical guidance for industries to design welded structures of pressure vessels and superheaters, optimize welding and post-weld heat treatment processes, and predict creep lifetime of high-temperature components in advanced fossil fired power plants.

## 7.2 Future Work

There is no doubt that Grade 91 steels will still be widely used in next generation of advanced fossil-fuel fired power plants. To ensure the pipe integrity and maximize creep lifetime of the welded components at higher service temperatures, future research work can be conducted from the following two aspects:

- Using microstructure-based models, coupling with characterized structure parameters, to predict creep performance of the welded components. Meanwhile, more experimental work should be conducted to obtain more materials properties for further model verification and calibration.
- Besides the conventional normalizing and tempering heat treatments, additional customized heat treatments of the base metal before welding can be a promising approach to improve creep resistance of the heat-affected zone and extend lifetime of the weldments.

# Bibliography

- [1] F. Lin, S. Cheng, and X. Xie. Ultrasupercritical power plant development and high temperature materials applications in China. *Energy Materials*, 3(4):201–207, 2008.
- [2] A.D. Gianfrancesco. *Materials for Ultra-supercritical and Advanced Ultra-supercritical Power Plants*. Woodhead Publishing, 2016.
- [3] A. Shirzadi and S. Jackson. *Structural Alloys for Power Plants: Operational Challenges and High-temperature Materials*. Woodhead Publishing Series in Energy Series. Elsevier Science & Technology, 2014.
- [4] F. Abe, T.U. Kern, and R. Viswanathan. *Creep-Resistant Steels*. Series in Metals and Surface Engineering. Woodhead Publishing, 2008.
- [5] J.A. Siefert and S.A. David. Weldability and weld performance of candidate austenitic alloys for advanced ultrasupercritical fossil power plants. *Science and Technology of Welding and Joining*, 19(4):271–294, 2014.
- [6] F. Kluger, C. Hölzel, J. Marion, and A. Skea. Alstom development of A-USC steam power plants. *2nd IEA CCC Rome, Italy*, October 14 2014.
- [7] S.A. David, J.A. Siefert, and Z. Feng. Welding and weldability of candidate ferritic alloys for future advanced ultrasupercritical fossil power plants. *Science and Technology of Welding and Joining*, 18(8):631–651, 2013.
- [8] P.J. Ennis and A. Czyska-Filemonowicz. Recent advances in creep-resistant steels for power plant applications. *Sadhana*, 28(3):709–730, 2003.
- [9] R. Viswanathan, J.F. Henry, J. Tanzosh, G. Stanko, J. Shingledecker, B. Vitalis, and R. Purgert. US program on materials technology for ultra-supercritical coal power plants. *Journal of materials engineering and performance*, 14(3):281–292, 2005.
- [10] F. Masuyama. Advanced Power Plant Developments and Material Experiences in Japan. In J. Lecomte-Beckers, M. Carton, F. Schubert, and P. J. Ennis, editors, *Materials for Advanced Power Engineering 2006: Part I*, pages 175–187. Forschungszentrum Jülich GmbH, 2006.

- [11] D.J. Abson and J.S. Rothwell. Review of Type IV cracking of weldments in 9-12%Cr creep strength enhanced ferritic steels. *International Materials Reviews*, 58(8):437–473, 2013.
- [12] J.A. Francis, W. Mazur, and H.K.D.H. Bhadeshia. Review Type IV cracking in ferritic power plant steels. *Materials Science and Technology*, 22(12):1387–1395, 2006.
- [13] F. Masuyama and J.P. Shingledecker. Recent status of asme code on creep strength enhanced ferritic steels. *Procedia Engineering*, 55:314–325, 2013.
- [14] W.D. Callister and D.G. Rethwisch. *Materials Science and Engineering*, volume 5. John Wiley & Sons NY, 2011.
- [15] H.J. Frost and M.F. Ashby. *Deformation Mechanism Maps: the Plasticity and Creep of Metals and Ceramics*. Pergamon press, 1982.
- [16] S. Murty, K.L. and Gollapudi and I. Charit. Newtonian viscous creep in metals. *Transactions of the Indian Institute of Metals*, 63(2-3):85–91, 2010.
- [17] T. Shrestha, M. Basirat, I. Charit, G.P. Potirniche, K.K. Rink, and U. Sahaym. Creep deformation mechanisms in modified 9Cr–1Mo steel. *Journal of Nuclear Materials*, 423(1):110–119, 2012.
- [18] R. Irving. Iron age. June 25, 1982.
- [19] K. Kimura. *9Cr-1Mo-V-Nb steel*, pages 126–133. Springer Berlin Heidelberg, Berlin, Heidelberg, 2004.
- [20] *ASTM A213/A213M-17 Standard Specification for Seamless Ferritic and Austenitic Alloy-Steel Boiler, Superheater, and Heat-Exchanger Tubes*. ASTM International, West Conshohocken, PA, 2017.
- [21] *ASTM A335/A335M-15a Standard Specification for Seamless Ferritic Alloy-Steel Pipe for High-Temperature Service*. ASTM International, West Conshohocken, PA, 2015.
- [22] T.C. Totemeier, H. Tian, and J.A. Simpson. Effect of normalization temperature on the creep strength of modified 9Cr-1Mo steel. *Metallurgical and Materials Transactions A*, 37(5):1519–1525, 2006.
- [23] C.R. Das, S.K. Albert, A.K. Bhaduri, G. Srinivasan, and B.S. Murty. Effect of prior microstructure on microstructure and mechanical properties of modified 9Cr-1Mo steel weld joints. *Materials Science and Engineering A*, 477:185–192, 2008.
- [24] K. Haarmann, J.C. Vaillant, W. Bendick, and A. Arbab. *The T91/P91 Book*. Vallourec and Mannesmann Tubes, 1999.

- [25] T. Maki, K. Tsuzaki, and I. Tamura. The morphology of microstructure composed of lath martensites in steels. *Transactions of Iron and Steel Institute of Japan*, 20(4):207–214, 1980.
- [26] S. Morito, X. Huang, T. Furuhashi, T. Maki, and N. Hansen. The morphology and crystallography of lath martensite in alloy steels. *Acta Materialia*, 54(19):5323–5331, 2006.
- [27] Z. Nishiyama. *Martensitic Transformation*. Academic Press, INC, 1978.
- [28] S. Morito, H. Tanaka, R. Konishi, T. Furuhashi, and T. Maki. The morphology and crystallography of lath martensite in Fe-C alloys. *Acta Materialia*, 51(6):1789–1799, 2003.
- [29] H. Kitahara, R. Ueji, N. Tsuji, and Y. Minamino. Crystallographic features of lath martensite in low-carbon steel. *Acta Materialia*, 54(5):1279–1288, 2006.
- [30] A.H. Pham, S. Ohba, T. Morito, and T. Hayashi. Energetic stability of boundary between variants in lath martensite. *Journal of Alloys and Compounds*, 577:583–586, 2013.
- [31] H.K. Danielsen and J. Hald. Behaviour of Z phase in 9–12% Cr steels. *Energy Materials*, 1(1):49–57, 2006.
- [32] H.K. Danielsen. *Z-phase in 9-12% Cr Steels*. PhD thesis, Department of Manufacturing, Engineering and Management, Technical University of Denmark, 2007.
- [33] J. Hald. Microstructure and long-term creep properties of 9-12% Cr steels. *International Journal of Pressure Vessels and Piping*, 85(1-2):30–37, 2008.
- [34] K. Sawada, M. Bauer, F. Kauffmann, P. Mayr, and A. Klenk. Microstructural change of 9% Cr-welded joints after long-term creep. *Materials Science and Engineering A*, 527(6):1417–1426, 2010.
- [35] C.G. Panait, W. Bendick, A. Fuchsmann, A.F. Gourgues-Lorenzon, and J. Besson. Study of the microstructure of the Grade 91 steel after more than 100,000 h of creep exposure at 600 °C. *International Journal of Pressure Vessels and Piping*, 87(6):326–335, 2010.
- [36] C.G. Panait, A. Zielińska-Lipiec, T. Koziel, A. Czyrska-Filemonowicz, A.F. Gourgues-Lorenzon, and W. Bendick. Evolution of dislocation density, size of subgrains and MX-type precipitates in a P91 steel during creep and during thermal ageing at 600 °C for more than 100,000 h. *Materials Science and Engineering A*, 527(16-17):4062–4069, 2010.

- [37] P. Mayr, T.A. Palmer, J.W. Elmer, E.D. Specht, and S.M. Allen. Formation of delta ferrite in 9 wt pct Cr steel investigated by in-situ X-ray diffraction using synchrotron radiation. *Metallurgical and Materials Transactions A*, 41(10):2462–2465, 2010.
- [38] K. Kimura, K. Sawada, Y. Toda, and H. Kushima. Creep strength assessment of high chromium ferritic creep resistant steels. In *Materials science forum*, volume 539, pages 3112–3117. Trans Tech Publ, 2007.
- [39] S. Kobayashi, K. Sawada, T. Hara, H. Kushima, and K. Kimura. The formation and dissolution of residual  $\delta$  ferrite in ASME Grade 91 steel plates. *Materials Science and Engineering: A*, 592:241–248, 2014.
- [40] K. Maruyama, K. Sawada, and J. Koike. Strengthening mechanisms of creep resistant tempered martensitic steel. *ISIJ International*, 41(6):641–653, 2001.
- [41] F. Abe. Precipitate design for creep strengthening of 9% Cr tempered martensitic steel for ultra-supercritical power plants. *Science and Technology of Advanced Materials*, 9(1):013002, 2008.
- [42] J. Lu, O. Omotoso, J.B. Wiskel, D.G. Ivey, and H. Henein. Strengthening mechanisms and their relative contributions to the yield strength of microalloyed steels. *Metallurgical and Materials Transactions A*, 43(9):3043–3061, 2012.
- [43] N. Hansen. Hall–Petch relation and boundary strengthening. *Scripta Materialia*, 51(8):801–806, 2004.
- [44] J. Pešička, R. Kužel, A. Dronhofer, and G. Eggeler. The evolution of dislocation density during heat treatment and creep of tempered martensite ferritic steels. *Acta Materialia*, 51(16):4847–4862, 2003.
- [45] M. Taneike, K. Sawada, and F. Abe. Effect of carbon concentration on precipitation behavior of  $M_{23}C_6$  carbides and MX carbonitrides in martensitic 9Cr steel during heat treatment. *Metallurgical and Materials Transactions A*, 35(4):1255–1262, 2004.
- [46] C.R. Das, S.K. Albert, A.K. Bhaduri, and B.S. Murty. Effect of boron addition and initial heat-treatment temperature on microstructure and mechanical properties of modified 9Cr-1Mo steels under different heat-treatment conditions. *Metallurgical and Materials Transactions A*, 44(5):2171–2186, 2013.
- [47] F. Abe, M. Taneike, and K. Sawada. Alloy design of creep resistant 9Cr steel using a dispersion of nano-sized carbonitrides. *International Journal of Pressure Vessels and Piping*, 84(1):3–12, 2007.
- [48] H. Magnusson and R. Sandström. Influence of aluminium on creep strength of 9–12% Cr steels. *Materials Science and Engineering: A*, 527(1):118–125, 2009.

- [49] J. Parker, J. Siefert, and J. Shingledecker. The benefits of improved control of composition for creep–strength enhanced ferritic steel Grade 91. *EPR Report 3002003472*, 8, 2014.
- [50] S.H. Song, Y.W. Xu, and H.F. Yang. Effect of impurity tin on the creep properties of a P91 heat-resistant steel. *Metallurgical and Materials Transactions A*, 45(10):4361–4370, 2014.
- [51] X. Yu, S.S. Babu, H. Terasaki, Y. Komizo, Y. Yamamoto, and M.L. Santella. Correlation of precipitate stability to increased creep resistance of Cr-Mo steel welds. *Acta Materialia*, 61(6):2194–2206, 2013.
- [52] Y. Liu, S. Tsukamoto, K. Sawada, and F. Abe. Role of boundary strengthening on prevention of type IV failure in high Cr ferritic heat-resistant steels. *Metallurgical and Materials Transactions A*, 45(3):1306–1314, 2014.
- [53] F. Abe, M. Tabuchi, S. Tsukamoto, and T. Shirane. Microstructure evolution in HAZ and suppression of Type IV fracture in advanced ferritic power plant steels. *International Journal of Pressure Vessels and Piping*, 87(11):598–604, 2010.
- [54] F.R. Larson and J. Miller. A time-temperature relationship for rupture and creep stresses. *Transactions ASME*, 74:765, 1952.
- [55] M. Tamura, F. Abe, K. Shiba, H. Sakasegawa, and H. Tanigawa. Larson–Miller constant of heat-resistant steel. *Metallurgical and materials transactions A*, 44(6):2645–2661, 2013.
- [56] T. Shrestha, M. Basirat, I. Charit, G.P. Potirniche, and K.K. Rink. Creep rupture behavior of Grade 91 steel. *Materials Science and Engineering A*, 565:382–391, 2013.
- [57] F. Masuyama. Creep rupture life and design factors for high-strength ferritic steels. *International journal of pressure vessels and piping*, 84(1):53–61, 2007.
- [58] F.C. Monkman and N.J. Grant. An empirical relationship between rupture life and minimum creep rate in creep-rupture tests. *ASTM Proceeding*, 56:593–620, 1956.
- [59] K. Kimura, H. Kushima, and K. Sawada. Long-term creep deformation property of modified 9Cr–1Mo steel. *Materials Science and Engineering: A*, 510:58–63, 2009.
- [60] P. Shingledecker, M.L. Santella, and R.L. Klueh. *ETD Seminar on New Steels. UK, London*, 2007.
- [61] F. Masuyama. Hardness model for creep-life assessment of high-strength martensitic steels. *Materials Science and Engineering: A*, 510:154–157, 2009.

- [62] J.A. Siefert, J.P. Shingledecker, and J.D. Parker. Optimization of Vickers hardness parameters for micro-And macro-indentation of Grade 91 steel. *Journal of Testing and Evaluation*, 41(5):778–787, 2013.
- [63] W.F. Newell Jr. Welding and postweld heat treatment of P91 steels. *Welding journal*, 89(4):33–36, 2010.
- [64] K.K. Coleman and W.F. Newell Jr. P91 and beyond. *Welding Journal*, 86(8):29–33, 2007.
- [65] Creep strength enhanced ferritic (csef) steel welding guide. *EPRI Report (Document ID: 1024713)*, 2011.
- [66] P. Ravi Vishnu. *Solid-State Transformation in Weldments*, volume 6, pages 70–87. ASM International, 1993.
- [67] W.F. Savage, E.F. Nippes, and E.S. Szekeres. Study of weld interface phenomena in a low alloy steel. *Welding Journal*, 55(9):260, 1976.
- [68] P. Mayr. *Evolution of microstructure and mechanical properties of the heat affected zone in B-containing 9% chromium steels*. Doctoral thesis, Graz University of Technology, 2007.
- [69] L. Li, A. Deceuster, and B. Griffiths. Effect of postweld heat treatment on the toughness of heat-affected zone for Grade 91 steel. *Welding Journal*, 92(03):80–87, 2013.
- [70] K. Easterling. *Introduction to the Physical Metallurgy of Welding*. Butterworth-Heinemann Ltd, 1992.
- [71] V.T. Paul, S. Saroja, P. Hariharan, A. Rajadurai, and M. Vijayalakshmi. Identification of microstructural zones and thermal cycles in a weldment of modified 9cr-1mo steel. *Journal of materials science*, 42(14):5700–5713, 2007.
- [72] P. Mayr, C. Schlacher, and S. Mitsche. Critical issues with creep exposed ferritic-martensitic welded joints for thermal power plants. *International Conference of the IIW*, pages 417 – 425, 2011.
- [73] D. Li, K. Shinozaki, H. Kuroki, H. Harada, and K. Ohishi. Analysis of factors affecting Type IV cracking in welded joints of high chromium ferritic heat resistant steels. *Science and technology of welding and joining*, 8(4):296–302, 2003.
- [74] T. Watanabe, M. Tabuchi, M. Yamazaki, H. Hongo, and T. Tanabe. Creep damage evaluation of 9Cr-1Mo-V-Nb steel welded joints showing Type IV fracture. *International Journal of Pressure Vessels and Piping*, 83(1):63–71, 2006.

- [75] D.J. Smith, N.S. Walker, and S.T. Kimmins. Type IV creep cavity accumulation and failure in steel welds. *International Journal of Pressure Vessels and Piping*, 80(9):617–627, 2003.
- [76] T. Sakthivel, K. Laha, M. Vasudevan, M. Koteswara Rao, and S. Panneer Selvi. Type IV cracking behaviour of modified 9Cr-1Mo steel weld joints. *Materials at High Temperatures*, 33(2):137–153, 2016.
- [77] J.A. Siefert and J.D. Parker. A well-engineered approach for establishing the minimum allowable post-weld heat treatment for power generation applications of Grade 91 steel. *EPRI Report (Document ID: 3002005350)*, 2015.
- [78] R. Blume, K.E. Leich, H. Heuser, and F.W. Meyer. Welding of modified 9% Cr steel. *Stainless Steel Europe*, pages 49–53, April 1995.
- [79] AWS. *D10.10/D10.10M: Recommended Practices for Local Heating of Welds in Piping and Tubing*. Miami, Florida: American Welding Society, 2009.
- [80] ASME. B31.1-power piping. *The American Society of Mechanical Engineers*, 2007.
- [81] M.E. Abd El-Azim, O.H. Ibrahim, and O.E. El-Desoky. Long term creep behaviour of welded joints of P91 steel at 650 °C. *Materials Science and Engineering A*, 560:678–684, 2013.
- [82] H.J. Schueller, L. Hagn, and A. Woitscheck. Risse im schweissnahtbereich von formstuecken aus heissdampfleitungen-werkstoffuntersuchungen. *Der Maschinenschaden*, 1:1–13, 1974.
- [83] M.F. Ashby, C. Gandhi, and D.M.R. Taplin. Overview No. 3 Fracture-mechanism maps and their construction for fcc metals and alloys. *Acta metallurgica*, 27(5):699–729, 1979.
- [84] J.A. Siefert and J.D. Parker. Evaluation of the creep cavitation behavior in grade 91 steels. *International Journal of Pressure Vessels and Piping*, 138:31–44, 2016.
- [85] R. Viswanathan. *Damage mechanisms and life assessment of high temperature components*. ASM international, 1989.
- [86] J.D. Parker. Factors affecting Type IV creep damage in Grade 91 steel welds. *Materials Science and Engineering A*, 578:430–437, 2013.
- [87] F. Abe. Creep behavior, deformation mechanisms, and creep Life of Mod.9Cr-1Mo steel. *Metallurgical and Materials Transactions A*, 46(12):5610–5625, 2015.
- [88] J.D. Parker and G.C. Stratford. Strain localization in creep testing of samples with heterogeneous microstructures. *International journal of pressure vessels and piping*, 68(2):135–143, 1996.

- [89] T. Ogata, T. Sakai, and M. Yaguchi. Damage characterization of a P91 steel weldment under uniaxial and multiaxial creep. *Materials Science and Engineering: A*, 510:238–243, 2009.
- [90] L. Li, B. Silwal, and A. Deceuster. Creep rates of heat-affected zone of Grade 91 pipe welds as determined by stress-relaxation test. *International Journal of Pressure Vessels and Piping*, 146:95–103, 2016.
- [91] Y. Liu, S. Tsukamoto, T. Shirane, and F. Abe. Formation mechanism of Type IV failure in high Cr ferritic heat-resistant steel-welded joint. *Metallurgical and Materials Transactions A*, 44(10):4626–4633, 2013.
- [92] Y. Liu, S. Tsukamoto, K. Sawada, M. Tabuchi, and F. Abe. Precipitation behavior in the heat-affected zone of boron-added 9Cr-3W-3Co steel during post-weld heat treatment and creep deformation. *Metallurgical and Materials Transactions A*, 46(5):1843–1854, 2015.
- [93] T. Shirane, S. Tsukamoto, K. Tsuzaki, Y. Adachi, T. Hanamura, M. Shimizu, and F. Abe. Ferrite to austenite reverse transformation process in B containing 9% Cr heat resistant steel HAZ. *Science and Technology of Welding & Joining*, 14(8):698–707, 2009.
- [94] Y.Y. Song. Thermodynamic study on B and Fe substituted  $\text{Cr}_{23}\text{C}_6$  using first-principles calculations, 2010.
- [95] S.T. Kimmins and D.J. Smith. On the relaxation of interface stresses during creep of ferritic steel weldments. *The Journal of Strain Analysis for Engineering Design*, 33(3):195–206, 1998.
- [96] K. Shinozaki and H. Kuroki. Stress-strain analysis of creep deterioration in heat affected weld zone in high Cr ferritic heat resistant steel. *Materials Science and Technology*, 19(9):1253–1260, 2003.
- [97] S. Goyal, K. Laha, K.S. Chandravathi, P. Parameswaran, and M.D. Mathew. Finite element analysis of type IV cracking in 2.25 Cr–1Mo steel weldment based on micro-mechanistic approach. *Philosophical Magazine*, 91(23):3128–3154, 2011.
- [98] *ASTM A182/A182M Standard Specification for Forged or Rolled Alloy and Stainless Steel Pipe Flanges, Forged Fittings, and Valves and Parts for High-Temperature Service*. ASTM International, West Conshohocken, PA, 2016.
- [99] L. Li. *Effect of Post-Weld Heat Treatment on Creep Rupture Properties of Grade 91 Steel Heavy Section Welds*. Utah State University, 2012.
- [100] *AWS A5.28/A5.28M: Specification for Low-Alloy Steel Electrodes and Rods for Gas Shielded Arc Welding*. Miami, Florida: American Welding Society, 1996.

- [101] AWS A5.29/A5.29M: *Specification for Low Alloy Electrodes for Flux Cored Arc Welding*. Miami, Florida: American Welding Society, 2010.
- [102] *ASTM E139 Standard Test Methods for Conducting Creep, Creep-Rupture, and Stress-Rupture Tests of Metallic Materials*. ASTM International, West Conshohocken, PA, 2006.
- [103] W.C. Oliver and G.M. Pharr. Measurement of hardness and elastic modulus by instrumented indentation: Advances in understanding and refinements to methodology. *Journal of materials research*, 19(1):3–20, 2004.
- [104] David B Williams and C Barry Carter. *Transmission Electron Microscopy: A Textbook for Materials Science*. Springer, 2009.
- [105] T. Maitland and S. Sitzman. *Electron Backscatter Diffraction (EBSD) Technique and Materials Characterization Examples*, volume 14, pages 41–75. Springer-Verlag New York, 2007.
- [106] A.J. Schwartz, M. Kumar, B.L. Adams, and D.P. Field. *Electron backscatter diffraction in materials science*, volume 2. Springer, 2009.
- [107] S.I. Wright, M.M. Nowell, and D.P. Field. A review of strain analysis using electron backscatter diffraction. *Microscopy and microanalysis*, 17(03):316–329, 2011.
- [108] J.H. Cho, K.H. Oh, A.D. Rollett, J.S. Cho, Y.J. Park, and J.T. Moon. Investigation of recrystallization and grain growth of copper and gold bonding wires. *Metallurgical and materials transactions A*, 37(10):3085–3097, 2006.
- [109] Y. Wang and L. Li. Microstructure evolution of fine-grained heat-affected zone in Type IV failure of P91 welds. *Welding Journal*, 95(1):27s–36s, 2016.
- [110] M.D. Abràmoff, P.J. Magalhães, and S.J. Ram. Image processing with imagej. *Biophotonics international*, 11(7):36–42, 2004.
- [111] *ASTM A1033-10 Standard Practice for Quantitative Measurement and Reporting of Hypoeutectoid Carbon and Low-Alloy Steel Phase Transformations*. ASTM International, West Conshohocken, PA, 2015.
- [112] J.W. Gibbs, C. Schlacher, A. Kamyabi-Gol, P. Mayr, and P.F. Mendez. Cooling curve analysis as an alternative to dilatometry in continuous cooling transformations. *Metallurgical and Materials Transactions A*, 46(1):148–155, 2015.
- [113] A. Kamyabi-Gol, S.J. Clark, J.W. Gibbs, S. Sridhar, and P.F. Mendez. Quantification of evolution of multiple simultaneous phase transformations using dilation curve analysis (DCA). *Acta Materialia*, 102:231–240, 2016.

- [114] S. Morito, H. Saito, T. Ogawa, T. Furuhashi, and T. Maki. Effect of austenite grain size on the morphology and crystallography of lath martensite in low carbon steels. *ISIJ international*, 45(1):91–94, 2005.
- [115] K. Laha, K.S. Chandravathi, P. Parameswaran, K.B.S. Rao, and S.L. Mannan. Characterization of microstructures across the heat-affected zone of the modified 9Cr-1Mo weld joint to understand its role in promoting Type IV cracking. *Metallurgical and Materials Transactions A*, 38(1):58–68, 2007.
- [116] S.K. Albert, M. Matsui, T. Watanabe, H. Hongo, K. Kubo, and M. Tabuchi. Variation in the Type IV cracking behaviour of a high Cr steel weld with post weld heat treatment. *International Journal of Pressure Vessels and Piping*, 80(6):405–413, 2003.
- [117] H.S. Yang and H.K.D.H. Bhadeshia. Austenite grain size and the martensite-start temperature. *Scripta materialia*, 60(7):493–495, 2009.
- [118] A. Garcia-Junceda, C. Capdevila, F.G. Caballero, and C. G. De Andres. Dependence of martensite start temperature on fine austenite grain size. *Scripta Materialia*, 58(2):134–137, 2008.
- [119] F. Abe, T. Horiuchi, M. Taneike, and K. Sawada. Stabilization of martensitic microstructure in advanced 9Cr steel during creep at high temperature. *Materials Science and Engineering A*, 378(1-2):299–303, 2004.
- [120] C. Coussement, A. Dhooge, M. de Witte, R. Dobbelaere, and E. van der Donckt. High temperature properties of improved 9% Cr steel weldments. *International Journal of Pressure Vessels and Piping*, 45(2):163–178, 1991.
- [121] Y. Zhang, P.H. Shipway, and F. Boue-Bigne. Characterisation of creep-weak zones (white bands) in grade 91 weld metal. *Science and Technology of Welding and Joining*, 14(6):542–548, 2009.
- [122] K. Sawada, T. Hara, M. Tabuchi, K. Kimura, and K. Kubushiro. Microstructure characterization of heat affected zone after welding in Mod.9Cr-1Mo steel. *Materials Characterization*, 101:106–113, 2015.
- [123] G. Kirchner, T. Nishizawa, and B. Uhrenius. The distribution of chromium between ferrite and austenite and the thermodynamics of the  $\alpha/\gamma$  equilibrium in the Fe-Cr and Fe-Mn Systems. *Metallurgical and Materials Transactions B*, 4(1):167–174, 1973.
- [124] J.B. Austin and R.H.H. Pierce Jr. Linear thermal expansion and transformation phenomena of some low-carbon iron-chromium alloys. *AIME Trans.*, 116(0):289–308, 1935.
- [125] Y. Wang, R. Kannan, and L. Li. Characterization of as-welded microstructure of heat-affected zone in modified 9Cr-1Mo-V-Nb steel weldment. *Materials Characterization*, 118:225–234, 2016.

- [126] Y. Wang, R. Kannan, and L. Li. Identification and characterization of intercritical heat-affected zone in as-welded Grade 91 weldment. *Metallurgical and Materials Transactions A*, 47(12):5680–5684, 2016.
- [127] D.C. Stouffer and L.T. Dame. *Inelastic deformation of metals: models, mechanical properties, and metallurgy*. John Wiley & Sons, 1996.
- [128] Y.Z. Liu, Y.H. Jiang, J.D. Xing, R. Zhou, and J. Feng. Mechanical properties and electronic structures of  $M_{23}C_6$  (M= Fe, Cr, Mn)-type multicomponent carbides. *Journal of Alloys and Compounds*, 648:874–880, 2015.